AN ANALYSIS OF THE ARCTIC OCEAN NET SURFACE HEAT FLUX AND ITS COMPONENTS FROM ATMOSPHERIC REANALYSES AND SURFACE OBSERVATIONS

By

Meghan Nicole Helmberger

B.A., Clark University, 2012

M.S., Clark University, 2013

A thesis submitted to the

Faculty of the Graduate School of the

University of Colorado in partial fulfillment

of the requirement for the degree of

Doctor of Philosophy

Department of Geography

2023

Committee Members

Mark Serreze

Peter Blanken

Carson Farmer

John Cassano

Alice DuVivier

Helmberger, Meghan Nicole (Ph.D., Department of Geography)

An Analysis of the Arctic Ocean Net Surface Heat Flux and its Components from Atmospheric Reanalyses and Surface Observations

Thesis directed by Dr. Mark Serreze

As the Arctic Ocean loses its sea ice cover, one expects a larger ocean heat gain from the net surface flux throughout the spring and summer; meaning that there is more energy to transfer from the ocean to the atmosphere in the autumn and winter. Recent work has shown that increased oceanic heat content at the end of summer delays autumn ice growth, with implications for marine shipping and other economic activities. Depending on patterns of seasonal sea ice retreat and weather conditions, the spring-summer heat uptake and autumn-winter heat loss can be highly variable from year to year as well as across regions. The main goal of this work is the validation of reanalysis data, examination of net surface heat flux patterns, and estimation of an idealized net surface heat flux value. To date, there has been little research addressing net surface heat flux specifically.

Recognizing this gap, this dissertation systematically analyzes how net surface heat flux (April-August) varies over time. In order to evaluate this across the Arctic Ocean and the marginal seas, three reanalyses were used (CFSR, ERA5, and MERRA-2), acknowledging the scarcity of measurements across the region. Following the initial steps in the project, shortwave and longwave radiation values were examined from the three reanalayses. Four variable comparisons were

undertaken showing differences between the reanalyses, exemplifying the areas of disagreement. A statistical analysis showed high correlations across the Arctic Ocean at the 95% confidence level for all variables between ERA5, CFSR, and MERRA-2.

Downwelling shortwave radiation that was collected on board the *RV Araon* in August 2018 from the Bering Strait and the Chukchi Sea showed that there is general agreement between all datasets and observations. Additionally, data from the SHEBA and MOSAIC expeditions were used to evaluate reanalysis accuracy, which allowed for the comparison of all radiation components used in calculating net surface heat flux. Since there are differences between the reanalyses, evaluating accuracy of individual components of the surface energy flux against observations was vital.

Comparisons of the net surface heat flux and ocean heat from from the reanalyses used in this study showed, as expected, positive trends in seasonal ocean heat gain from the net surface flux, but there was disagreement between values with large variability from year to year. Yet, over time, the net surface heat flux calculated from each reanalysis shows similar temporal patterns.

DEDICATION

To all those surviving in the wake of great adversity.

ACKNOWLEDGEMENTS

First, I would like to acknowledge the native communities in the Arctic, who have extensive knowledge of the region and are facing current and future hardship as the climate continues to rapidly change. Additionally, I would like to acknowledge the Ute, Arapaho, and Cheyenne nations whose land the National Snow and Ice Data Center and the University of Colorado Boulder now sit.

I would like to thank my fiancé, Greg Schafer, who I met just before I did my comprehensive exams (a very stressful time in a PhD student's life) and who has stuck by me through all the coding problems and late nights. Thank you for all your support and providing many delicious meals. Next, I would like to thank my parents who have always supported me in my educational endeavors and have encouraged my interest in science and general curiosity. A few people that need to be mentioned are Erika Schreiber, Tasha Snow, Aroob Abdelhamid, Gabby Subia Smith, and Erin Conner without whom I would have not made it through this. From all the check ins to the café and zoom work sessions, you all have helped me push through to the end.

Finally, I would like to thank my advisor, Dr. Mark Serreze, who has provided feedback, encouragement, and support all these years.

Table of Contents

LIST OF FIGURES

LIST OF TABLES

CHAPTER 1: INTRODUCTION AND BACKGROUND

1.1 Motivation

Surface air temperatures are rising globally, and the Arctic region is warming at a stronger rate due, in considerable part, to a declining sea ice cover (Schneider and Held, 2001; Comiso et al., 2008; Screen and Simmonds, 2010; Serreze and Barry, 2011; Stroeve et al., 2012); this is called Arctic Amplification (Serreze and Francis, 2006; Serreze and Barry, 2011). Higher temperatures melt sea ice, replacing a once highly reflective surface with a dark and absorbent surface (open water). As this positive feedback loop continues, more energy is absorbed by the upper ocean. Before sea ice can form again in the autumn and winter, this ocean heat must be lost to the atmosphere. As the Arctic loses its sea ice cover, exacerbated by Arctic amplification, it becomes more accessible to shipping and resource extraction while becoming less reliable for Indigenous communities and animals dependent on the ice for hunting and other activities. Given that there will still be large seasonal and interannual variability in ice conditions for years to come, there is a growing need for more accurate regional sea ice predictions at seasonal lead times (Serreze et al., 2016).

Sea ice extent is one of the key metrics that scientists use to assess the health of the Arctic sea ice cover. Satellite observations starting in 1979 show that sea ice extent is declining in all months of the year; but particularly in September. September is when the sea ice extent reaches its minimum within a year, usually in the middle of the month. Throughout the period of satellite observations (1979-present), March sea ice extent has declined by 2.7% per decade while September

extent has declined by 13% per decade relative to the 1981-2010 average (Fetterer et al., 2017). The lowest extent minimum on record was in September 2012 (3.387

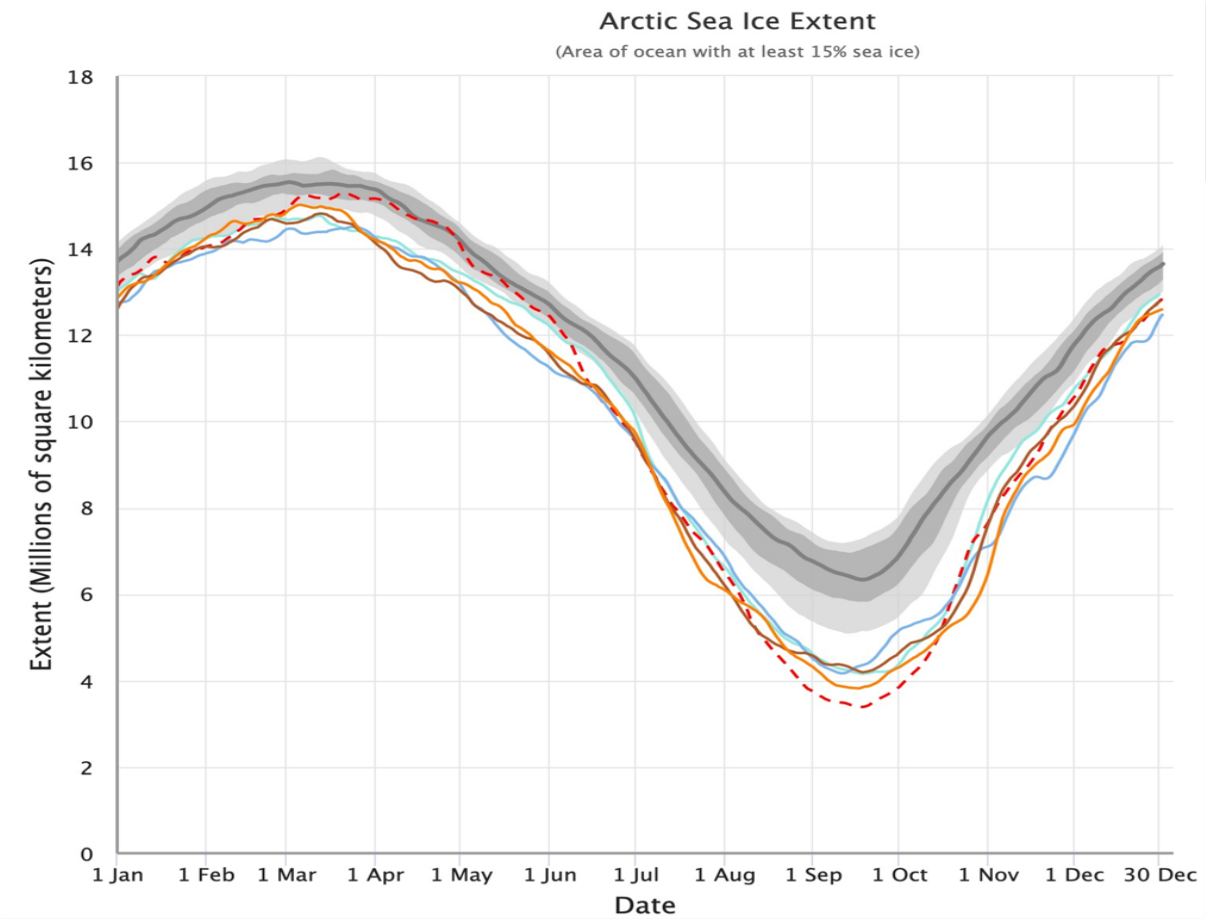

Figure 1.1: Annual cycle of sea ice extent. The 1980-2010 Median extent and the corresponding interquartile and interdecile ranges are in grey in contrast to the 2012 record minimum (red dash). The second lowest minimum is 2020 (orange) and 2007 (green), 2016 (blue), and 2019 (brown) are tied for third record minimum. Image courtesy of the National Snow and Ice Data Center.

million km^2), breaking the previous record set in 2007 (4.55 million km^2), and second lowest sea ice extent minimum was recorded in 2020 (3.818 million km^2) (Figure 1.1). Coupled with the shrinking sea ice extent are declines in sea ice thickness and concentration (Fetterer et al., 2017; Notz and Stroeve, 2016; Cavalieri and Parkinson, 2012). With a thinner and less compact ice cover, more energy can

transfer through the ice and the ice becomes more mobile. Although much of the ice loss is due to thermodynamic melting, ice is transported out of the Arctic, primarily through the Fram Strait (Kwok, 2009; Smedsrud et al., 2011; Langehaug et al., 2013; Wei et al., 2019). More heat in the ocean delays autumn freeze-up; preventing first year ice from forming until later in the season. With later freeze-up, the resultant thinner ice pack enters the following winter season. Reduced ice cover contributes to more moisture and heat in the lower atmosphere which produces more cloud cover and contributes to downwelling longwave radiation, again contributing to more sea ice melt and reduced growth (Kay and Gettelman, 2009).

As already introduced, Arctic sea ice loss can be linked to warming of both the atmosphere and ocean (Johannessen et al., 2016; Tokinaga et al., 2017). To expand on this, as the ice cover declines, exposing low albedo water, greater seasonal (spring through summer) heat gain increases the energy stored in the surface mixed layer (approximately the top 20 meters) of the Arctic Ocean; the subsequent loss of this heat to the atmosphere in autumn and winter is a strong driver of Arctic Amplification. Perovich et al. (2007) estimated that this increase in energy storage in the upper ocean was occurring across 89% of the Arctic Ocean; that value has likely increased. With this increase in upper ocean energy storage and more open water, there is an increased chance for larger turbulent heat, resulting in more water vapor and cloud cover in autumn (Kay and Gettleman, 2009). Although energy inputs to the surface strongly drive seasonal sea ice melt, basal melting (the melting at the bottom surface of the ice floe) is important. Prior

to the start of sea ice formation in the fall, the heat gained in the ocean mixed layer through spring and summer must be released back to the atmosphere and to outer space in order to reach the freezing point (Carmack et al., 2015). This helps explain the observed delay between maximum surface energy input and minimum sea ice extent (Serreze and Barry, 2014). Since there is now more heat in the ocean mixed layer at summer's end than there used to be, autumn ice growth is delayed.

Seasonal sea ice prediction is vital for planning in shipping, tourism, and resource extraction (Jung et al., 2016; Smith & Stephenson, 2013). Coupled global climate models, ice-ocean models, and statistical models are widely used for answering seasonal-scale questions about the Arctic region, yet limitations arise due to biases in the models, lack of ability to predict weather conditions beyond ~10 days, and a lack of understanding of earth system interconnectivity; this dissertation aims to actress this issue. Wayand et al. (2019) found that many global climate models (GCMs) rapidly lose forecast skill in ~5 weeks, then have a much slower skill loss out to 30 weeks; partially due to what sea ice concentration data the models use for initialization. Additionally, GCMs typically have the hardest time predicting sea ice concentration along the sea ice margin (Wayand et al., 2019). Sea ice forecasting generally produces more accurate values when the end-of-summer extents do not diverge largely from the expected trend (Stroeve et al., 2014). The predictions are more accurate when sea ice forecast models are initialized prior to the onset of melt; generally referred to as the early summer predictability barrier (Sigmond et al., 2013; Blanchard-Wrigglesworth et al., 2011;

Day et al., 2014; Wayand et al., 2019). As there are many issues with seasonal sea ice predictability, exploring further connections with heat exchange between the atmosphere, ocean, and sea ice is essential. The link between seasonal heat uptake and autumn ice formation described above could be a strong source of predictability (Lenetsky and Serreze, 2021; Serreze et al., 2016).

While these fundamental physical processes are well recognized, little quantitative information exists on the magnitudes, variability, and trends in seasonal ocean heat uptake and release. When models are initialized with different sea ice conditions, some can accurately predict sea ice extent over short timescales (a few days) while others predict more accurately over longer time scales (weeks). The problem is that any one model cannot predict accurately on short and long timescales together (Waynard et al., 2019). As many global climate models and coupled ice-ocean models are not much better than statistical models at predicting sea ice extent at more than 2-month lead times, improvements need to be made (Wayand et al., 2019; Blanchard-Wrigglesworth et al., 2011). Although other studies have found better predictive accuracy on longer time scales (Sigmond et al., 2013; Wang et al., 2013), the model that had the best success predicting accurately 5 months out used a coupled ocean-sea ice model that was forced by atmospheric reanalyses (Chevallier et al., 2013); which emphasizes the importance of including ocean heat. Using reanalysis data to initialize predictive models will include the bias from the reanalysis. Models used in studies by Sigmond et al. (2013) and Wang et al. (2013), were initialized using ocean heat data but they were constrained which

could impact the initial sea ice conditions represented in the model (Kwok, 2011). If sea ice models can be initialized with more accurate ocean mixed layer heat content data, this could lead to improved predictions of the timing of autumn sea ice formation (Serreze et al., 2016).

Driven by the need to improve sea ice predictability, this dissertation aims at better quantifying the seasonal net surface heat flux across the Arctic Ocean and its uncertainty using atmospheric data from multiple atmospheric reanalyses. As part of this effort, comparisons were made between the individual components of the surface energy budget between each reanalysis and with available surface observations to evaluate which reanalysis is best at capturing heat gain and release via the net surface flux. Since reanalysis data are commonly used to initialize sea ice models, it is important to know which model is most accurately representing the environment. Although many studies treat reanalyses as "observations", surface flux values are still largely model based, especially over the Arctic Ocean. Due to this, it is vital to "ground truth" reanalyses values. The final portion of the dissertation aims to show which reanalysis compares best to observational datasets. Observations taken from ship-board measurements in three different time periods are used to capture the different climates that the Arctic has experienced over the last 40 years.

1.2 Outline of the Dissertation

The aim of this dissertation is to evaluate the patterns of surface energy fluxes across the Arctic Ocean and how reanalysis data relates to observational datasets. Understanding these relationships can help reduce uncertainties when using reanalysis data in sea ice extent predictions on seasonal time scales.

The remainder of this chapter includes background sections on the basic physical characteristics of the Arctic, historical study of the region, atmospheric and oceanic energy budgets, and sea ice which will provide context for the research in subsequent chapters.

This dissertation is structured as follows: Chapter 2 discusses all data sources used. Technical details, data availability, processing specifics, and known biases are all discussed. Chapter 3 focuses on the methods used to process and analyze all the data. Additionally, this chapter explains how decisions were made to define the study area, and how to conduct the temporal and statistical analyses. Results and discussion of the comparison between observations and model data are presented in Chapter 4. The results and discussion of the comparison of individual radiation components and calculations of net surface heat flux are presented in Chapter 5. Chapter 6 concludes by restating the objectives of this work, results, implications, and paths for future work.

1.3 Background

1.3.1 Physical Characteristics

There are numerous different ways to define where the Arctic begins. The Arctic circle classification (66.5^{O} N), the astronomical definition, is the latitude at which the sun does not set on the summer solstice and does not rise on the winter solstice. Another definition is the area north of the 10^{O}C July isotherm, roughly corresponding to the Arctic tree line (Figure 1.2). Other investigators have viewed the Arctic as where continuous permafrost starts. There are eight countries with territory in the Arctic Region: Canada, Finland, Greenland, Norway, Russia, Sweden, Iceland, and the United States.

A key feature of the Arctic region is that it is an ocean nearly surrounded by land (Figure 1.2), which is fundamentally different from the Antarctic region (a continental ice sheet surrounded by ocean). The Arctic Ocean is bounded to the south by the North American and Eurasian continents with three prominent areas for inflow and outflow connecting to the Pacific through the Bering Strait, and connecting to the Atlantic through Fram Strait and the Barents Sea. The connections are responsible for most of the transfer of oceanic heat in and out to the Arctic Ocean; most of the sea ice that exits the Arctic Ocean does so through Fram Strait. Near surface winter temperatures over the Central Arctic Ocean generally

do not drop as low as over the Russian Arctic tundra because the ocean releases heat throughout the winter months through leads and polynyas.

Figure 1.2: Map of the Arctic, showing multiple definitions of the Arctic. The Arctic Circle is 66.5° N. The red line is the 10° C mean July isotherm. The green line is the tree line. Image courtesy of Wikipedia. courtesy of the Perry-Castaneda Library map collection. Tree line added at NSIDC based on National Geographic 1983 information, Armstrong et al. 1978 and Young 1989).

About 50% of the Arctic Ocean is underlain by continental shelf and shallow waters, with the central Arctic Ocean as the only portion with depths greater than 1000 meters (Jakobsson, 2002). Arctic Ocean surface waters are relatively fresh, 31-32 psu (compared to a global mean ocean salinity of 34 psu), due to the inflow of water from Arctic draining rivers across North America and Russia, ice melt, and net precipitation (precipitation minus evaporation). The relatively fresh surface layer, coupled with the inflow of salty waters from the Atlantic that dives underneath the surface layer, creates a strong halocline and pycnocline that fosters the formation of sea ice and limits vertical mixing into the deeper water column.

Arctic sea ice extent has strong seasonal variability. From the satellite record, the maximum extent, at the end of winter in March, tends towards 15 million km^2 while the minimum, at the end of summer in September, tends towards 7 million km^2. However, over the last decade the sea ice minimum extent in September has decreased to an average of 3.4 million km^2 and rarely rises above the 1981-2010 mean. Each year, ice forms in open water areas and is classified as first year ice. If it survives the following summer, it is classified as multi-year ice, which varies in thicknesses between 2-5 meters. The thickest and oldest multi-year ice (which has survived multiple summers) is typically found along the Canadian Archipelago and Greenland coasts, transported there by the Beaufort Gyre and the Transpolar Drift Stream.

1.3.2 Arctic Data Sources

Spatially and temporally, the Arctic Ocean is vastly under-sampled in terms of surface observations. The distance from southern ports and the harsh conditions make the Arctic a costly place to install and maintain instrumentation; from blowing snow to crushing ice, there are many ways to destroy instruments and impact data quality. Due to these challenges, many studies have relied on global climate models, atmospheric (and ocean) reanalyses, and satellite data. The modern satellite era began in 1979, which aided in providing many more data points than surface-based programs can. However, there are many biases and parameterizations in each that must be considered.

One of the first ways that data were collected across the Arctic Ocean was by ships freezing into the sea ice and drifting with the ice. Marking the first drifting data collection on a ship, the *Fram* was frozen into the ice in the 1890s and drifted with the sea ice for three years, collecting some of the first meteorological data on sea ice motion and Arctic Ocean circulation. The ship was specially designed for this expedition and instead of being crushed, the ship was lifted up by the sea ice allowing the vessel to make the entire journey. Drifting stations and buoys are also used to collect sea ice drift and meteorological data. Although satellite data are used widely, there is a necessity for validation, using the available (however flawed) surface observations. Although ground-based measurements are flawed due to potential incorrect instrument calibrations, instrument error, and user error, they are invaluable for validating the widely used satellite datasets.

Two additional major drifting vessel projects have been executed since the 1970's that provide data relevant to the present work. The first, Surface Heat Budget of the Arctic Ocean (SHEBA), froze a ship into the ice starting in the Beaufort Sea in October 1997 and drifted northeast in the Beaufort Gyre collecting many different types of data including radiation and turbulent flux values. The SHEBA drift ended in October 1998 northeast of its starting point in the northern Chukchi Sea. The most recent and most comprehensive drifting project, Multidisciplinary drifting Observatory for the Study of Arctic Climate (MOSAiC), began in 2019; freezing into the ice north of Russia and following the Transpolar Drift Stream towards Fram Strait. MOSAiC ended in October 2020. Similar to SHEBA, MOSAiC collected a wide variety of data including radiation and turbulent flux data. These measurements are vital to validation efforts and will be used in the present study and for years to come. Along with longer expeditions, like those mentioned above, there are numerous smaller expeditions that collected data over smaller spatial and temporal scales. This dissertation uses data from one of those expeditions aboard the *RV Araon*. This ice breaker collected data in the Chukchi Sea in August 2018.

Another method for collecting local observational data is by installing permanent instruments at meteorological stations, typically on land. There are networks in each Arctic country that produce freely sourced data, yet they do not extend over the sea ice. Despite the large number of organizations coordinating pan-Arctic monitoring efforts (e.g., United States Arctic Observing Network, Interagency

Arctic Research Policy Committee, Sustained Arctic Observing Network, International Arctic Buoy Programme, Arctic Monitoring and Assessment Programme), little of the Arctic Ocean is regularly observed. Even when projects like SHEBA and MOSAiC are able to set up weather stations on the ice, the instrumentation is at risk of being lost.

Satellite passive microwave remote sensing has enabled continuous monitoring of sea ice extent and concentration. For sea ice concentration, brightness temperature, which is a measurement of microwave radiation that a surface emits in different frequencies and polarizations, is measured and then processed through algorithms to produce sea ice concentration estimates. These sensors provide a continuous (over time and space) dataset in all weather conditions, irrespective of polar darkness or cloud cover.

Although passive microwave remote sensing has created many opportunities for polar researchers, a number of factors introduce inaccuracies in the data. As snow and ice warm and melt, the grain sizes change, affecting the brightness temperature and often results in the underestimation of sea ice in the area (Ivanova et al., 2015; Rosel et al., 2012b; Markus and Dokken, 2002; Comiso and Kwok, 1996; Steffen and Schweiger, 1991; Cavalieri et al., 1990). When sea ice melts in the summer, melt ponds form on top of the ice; to the sensor it looks like open water and there is no way to differentiate between melt ponds and open ocean in these wavelengths (Landy et al., 2014; Webster et al., 2015; Divine et al., 2015; Kern et al., 2020). Although these biases do not greatly affect summer sea ice extent (based

on all pixels with at least a 15% ice cover), it does affect the estimation of sea ice area which is based on concentration (Kern et al., 2020).

Atmospheric reanalyses provide global coverage of atmospheric variables and surface energy fluxes. Reanalyses are retrospective weather models that use fixed physics and assimilate observational data to constrain model output. They provide information at all grid points across the globe (at different resolutions). One of the largest challenges using reanalyses in place of surface observations is that they all come with their own set of biases and errors. Using multiple reanalyses can mitigate this issue.

There are a number of regional reanalyses optimized for the Arctic region like the Arctic System Reanalysis (ASR) that spans from 1999 to 2012 and the Copernicus Arctic Regional Reanalysis (CARRA), which focuses on the European Arctic and extends from 1998 to 2019. Although developing Arctic-focused reanalyses is extremely important, they have some limitations and they usually are not updated on a regular basis.

Modern global reanalyses include MERRA-2 (Modern-Era Retrospective Analysis for Research and Applications, version 2), ERA-5 (ECMWF Reanalysis, Version 5), and CFSR (Climate Forecast System Reanalysis), to name a few. As each reanalysis is produced by a different entity, they each come with differences and biases, especially in how different variables are parameterized. All reanalyses are continuously updated with new versions, and released periodically in order to minimize error and bias.

1.3.3 Basics of the Atmospheric and Ocean Energy Budgets

An important way to understand the climate of the Arctic region, which lies at the heart of the present study, is to look at the atmospheric and oceanic energy budgets. The atmospheric energy budget includes four main components: the change in atmospheric energy storage (composed of internal energy, potential energy, latent heat energy, and kinetic energy), the net radiation balance at the top of the atmosphere, the net poleward transport of atmospheric energy, and the net surface heat flux. Although when averaged across annual means, the change in atmospheric energy storage is nearly zero, when observed on a seasonal scale, there are large storage changes. In the spring in the Arctic, the incoming solar energy begins to increase adding energy to the atmosphere and Earth's surface, which continues through the summer months. Then, in the fall through the winter, the atmosphere loses energy as the amount of incoming solar radiation declines to zero. The average incoming solar radiation at the surface in the summer in the Arctic region and the tropics are between 220 and 235 W/m^2 and 340 W/m^2, respectively.

Similarly, the ocean warms throughout the summer season (positive storage changes), then during the fall and winter months, the ocean releases heat, warming the atmosphere; the ocean and the atmosphere are coupled through the net surface flux. The loss of energy at the top of the atmosphere is mostly balanced by the poleward transport of energy from lower latitudes and the input of heat from the

underlying ocean column. The combination of the three components produces a small annual mean net upward surface flux, heating the atmosphere (Porter et al., 2010; . However, the Arctic net surface heat flux, which is of special interest to the present study, varies widely by season; positive in spring and summer (net surface heat flux is downward), negative in autumn and winter (upward, ocean heat loss) (Serreze et al., 2007). It varies strongly by region.

Expressed formally, the energy budget equation for a column of atmosphere extending from the surface of the earth to the top of the atmosphere is:

$$(1)\ AE\ \partial t = -FA+R_{top}+F_{surf}$$

Which states that the change over time in energy storage in a column of atmosphere ($AE\ \partial t$) is determined by the sum of convergence of the horizontal energy flux (-FA), radiation at the top (R_{top}), and the net surface heat flux (F_{surf}). If the sum of the three components on the right are positive, the atmospheric column is gaining energy. The present work focuses on the last term of Equation 1, F_{surf} (Serreze & Barry, 2014), which is defined as:

$$(2)\ F_{surf} = -(R_{surf} + Q_H+Q_E)$$

which states that the net surface heat flux is the sum of the net radiation at the surface (R_{surf}, the sum of the net longwave and net shortwave radiation at the surface), the turbulent sensible heat flux (Q_H), and the turbulent latent heat flux (Q_E). The terms on the right are positive downward; adding the negative sign adheres to the convention of positive upward, into the atmospheric column.

One major factor that impacts the surface energy flux and its components which will be addressed in the present study is cloud cover. Intrieri et al. (2002) showed that for the majority of the year, clouds warm the surface, except a small period during the summer when the albedo effect outweighs the clouds' impact. This contrasts with lower latitudes where overall clouds have a cooling effect; this occurs because of the difference in shortwave radiation that reaches the surface in the Arctic compared to lower latitudes (Perovich, 2018). Except for the middle of the summer, the cloud radiative forcing is largely positive over the Arctic Ocean (clouds warm the surface), yet its impact on the surface energy balance depends on the interactions between the solar flux above the clouds, the cloud albedo, and surface albedo. The cloud radiative effect (or forcing) can be expressed as:

$$(3)\ \text{Longwave Forcing} = LW_{all} - LW_{clear}$$

$$(4)\ \text{Shortwave Forcing} = SW_{all} - SW_{clear}$$

Where LW_{all} and SW_{all} are the net longwave and net shortwave solar fluxes under "all sky" conditions and LW_{clear} and SW_{clear} are the fluxes for clear-sky conditions. Positive values are warming the surface and negative values indicate cooling of the surface. Clouds generally reduce the amount of solar radiation that reaches the surface because of their albedo but they tend to increase the amount of longwave radiation to the surface.

Underneath the atmospheric column, there is a column of ocean water, which could include ice and overlying snow cover. Its energy balance is represented in the following Equation (5):

$$(5)\ OEt = t(L_i+S_o) = -F_{sfc}- \ F_o+F_i$$

which states that the change over time in energy storage in a given column of ocean (OEt) is represented by the latent heat storage in any floating sea ice and overlying snow cover (L_i) and the sensible heat storage in ocean water (S_o). This is also equal to the sum of the negative heat flux (F_{sfc}), the horizontal convergence of the oceanic sensible heat flux (F_o), and the horizontal heat divergence of the latent heat flux of sea ice (F_i). Looking at equations 1 and 5 together, we see that the net budgets of the atmosphere and the ocean are directly connected through the net surface heat flux.

The Arctic Ocean is strongly density stratified and governed by temperature and salinity which determines density (Figure 1.3). Globally, upper ocean density stratification is determined by temperature, with higher temperatures at the surface. Yet in the Arctic Ocean, with the lower water temperatures, the stratification is governed largely by salinity, lower salinity means lower density so that the fresher waters are found at the surface. The halocline determines the pycnocline, which produces a very stable stratification at the surface and inhibits vertical mixing. This stability occurs in the surface mixed layer and is essential for sea ice growth.

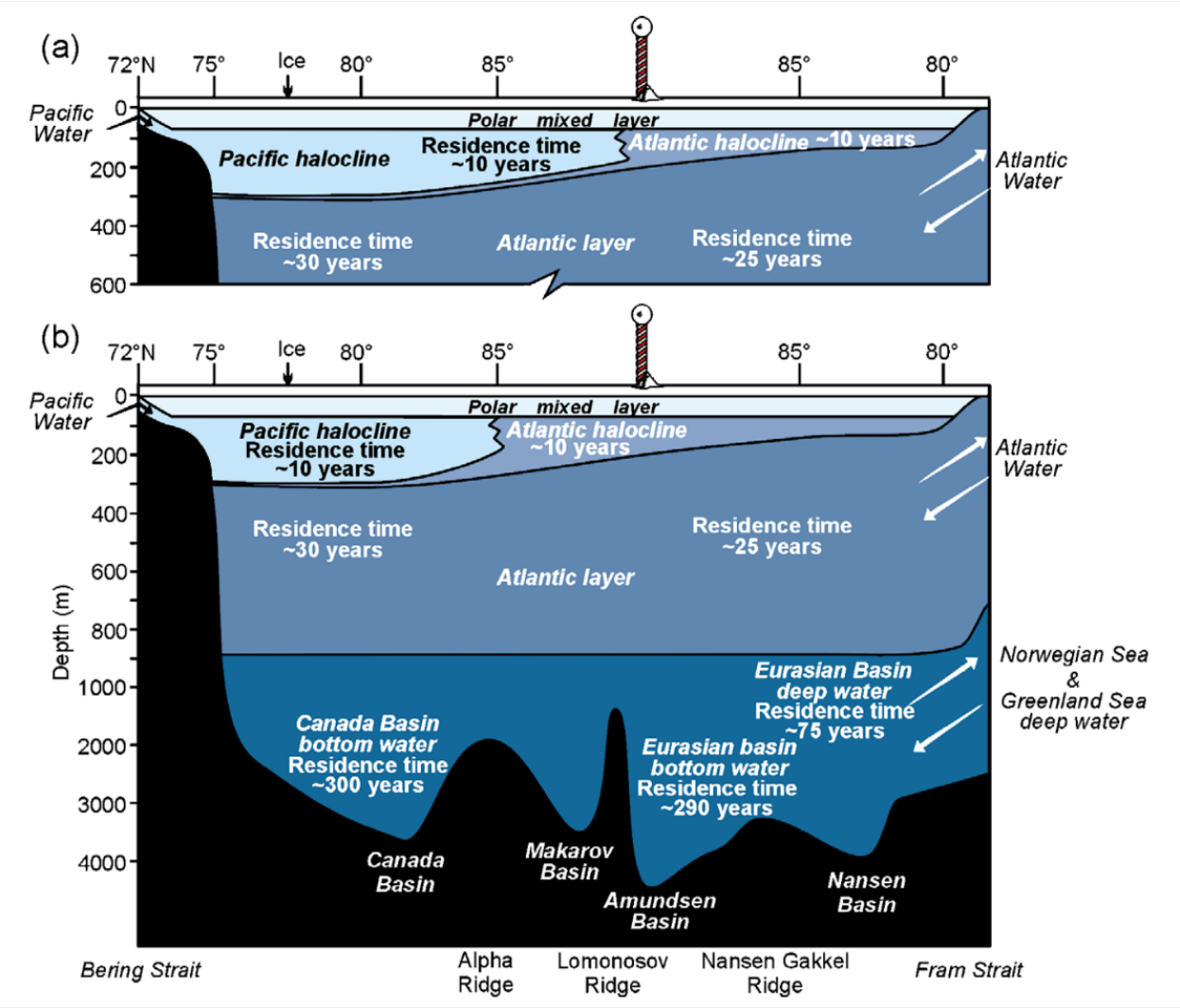

Figure 1.3: The stratification of the Arctic Ocean showing the polar mixed layer, the Pacific and Atlantic domains of influence and the haloclines. The arrow at top center shows the displacement of the Atlantic Pacific front during the high Arctic Oscillation index of the early 1990s. From Macdonald et al., 2005.

The surface mixed layer of the Arctic Ocean extends down to 10-40 m, is relatively fresh with a typical bulk salinity of 24.7 psu and has an approximate temperature of -1.8° C. This fluctuates with the season as ice freezes and melts, but as introduced earlier, the freshness is maintained largely by net precipitation and inflow of fresh water from major rivers around the Arctic. Below this is the Atlantic

layer, which is saltier and warmer (temperatures above 0°C) than the surface. These waters flow into the Arctic through Fram Strait and the Barents Sea from the north Atlantic. Additionally, Pacific water flows into the Arctic through the Bering Strait, bringing warm fresh water that sits between the surface mixed layer and the Atlantic waters. The Pacific water halocline helps prevent vertical mixing of the Atlantic waters and contributes to the surface mixed layer staying cold and fresh. Understanding the stability of the surface mixed layer is vital to explaining how ice forms in a salty body of water.

1.3.4 Arctic Sea Ice Characteristics

As the Arctic region heads into the winter months, the atmosphere and ocean lose energy to outer space. When the surface mixed layer of the ocean reaches about -1.8°C (the salinity adjusted freezing point), sea ice begins to form. Sea ice can be divided into several basic categories; first year ice, multi-year ice, seasonal ice, and fast ice. First year ice and seasonal ice usually occur in the marginal seas where there tends to be more open water; the growth and melt of these ice types largely contribute to the seasonal variation in sea ice extent. Sea ice forms in the following stages: frazil ice (3-4mm long), grease ice (slurry), and pancake ice (0.3 to 3 m diameter). Under calm wind conditions, the frazil crystals will form a continuous solid ice cover (1-10 cm thick) yet if the ocean is rough, the solid ice formation is inhibited. Following the beginning stages of sea ice formation, the ice will continue to thicken thermodynamically at the base of the ice floe. Typically, first year ice

grows up to about 2 meters thick, except in areas of ridging and rafting, where the dynamic activity creates thicker ice.

Ice thickness is an important component in thermodynamic calculations because the penetration of solar radiation into the water column and the transmission of turbulent flux energy from the ocean to the atmosphere is directly related to the sea ice thickness. As ice grows from the bottom of an ice floe, latent heat is released into the water column. This process helps maintain a temperature gradient through the ice from the warmer ice-ocean interface to the cold ice-atmosphere interface, creating an upward conductive flux. As thickness increases, the temperature gradient declines and less heat is transmitted through the ice to the surface. As ice thickness increases, the transmission of heat slows. The majority of sea ice generally falls into one of the two thickness categories: the 3-5 m range (multi-year ice) or the 1-2 m range (first year ice).

Ice thickness and concentration in each region are influenced by ice motion. If floes diverge in winter, a lead will open and ice will quickly form over the open water creating young thin ice. If ice converges, leads will close, and ridging or rafting may occur, enabling first year ice to become quite thicker. Ridged or rafted first year sea ice is more likely to survive a melt season. Due to the Beaufort Gyre circulation and the Transpolar Drift Stream, the thickest ice, measuring as much as 6-8 m, occurs along the Canadian Archipelago and the north coast of Greenland.

1.4 Focus of the Present Work

The objective of this dissertation is to use data from three atmospheric reanlyses along with available surface observations to determine the patterns of ocean heat uptake and release across the Arctic Ocean and evaluate the relationships between net surface heat flux and changes in sea ice conditions. Using these data, the relationships between the individual surface energy budget components and the reanalysis data with observational datasets were estimated to evaluate which model is doing the best job at representing the Arctic climate. The work can be broken into the following objectives and associated research questions.

Objective 1 Compare individual surface radiation balance components (SW_u, SW_d, LW_u, SW_d) across three different reanalyses in a statistical assessment. A cloud cover comparison is included in this analysis. *Does one reanalysis stand out in terms of its depiction of any or all components? Do cloud cover patterns agree with what we expect in terms of influences of downwelling shortwave and longwave radiation?*

Objective 2 Use observational datasets from the SHEBA expedition (1997-1998), the *RV Araon* (2018), and the MOSAIC expedition (2019-2020) to validate shortwave radiation data and energy budget radiation components from three different atmospheric reanalyses. *How do fluxes from the reanalysis compare to the direct observations? Are the reanalyses doing a good job of capturing these values?*

Objective 3 Determine seasonal heat gain and loss patterns and long-term changes over the Arctic Ocean via the net surface flux and its components using reanalysis data. *What is the seasonal cycle in upper net surface heat flux and loss through the net surface flux? Is there an increase in the net surface heat flux from April-August over the 39-year period? Do periods of increased heat content at the surface occur in the same years as low sea ice concentration? How do the results vary between different reanalyses?*

CHAPTER 2: DATA AND LIMITATIONS

2.1 Reanalyses: An Overview

The reanalysis datasets used are from the Modern-Era Retrospective Analysis for Research and Applications, version 2 (MERRA-2) (Gerlaro et al., 2017), the ECMWF Reanalysis, version 5 (ERA-5) (Hersbach et al., 2020), and the NCEP/NCAR Climate Forecast System Reanalysis CFSRv1 (Saha et al., 2010) and CFSRv2 (Saha et al., 2013) summarized in Table 2.1. These three were selected because they are the top three most commonly used atmospheric reanalyses. Atmospheric reanalyses provide multivariate gridded representations of atmospheric variables at sub-daily resolutions spanning multiple decades and generated by a constant atmospheric model with fixed physics and assimilated data systems (Saha et al., 2010). This differs from operational models and assimilation systems which are constantly being refined in an effort to improve forecast skill.

Reanalyses, like operational numerical weather prediction systems, assimilate millions of data points from satellites, weather stations, aircraft, radiosondes, buoys, and ships (Dee et al., 2011). The volume of assimilation data has grown over time, expanding rapidly as satellite data became available. In the Arctic, there are limited in-situ observations for assimilation, making estimates of many surface variables (e.g. energy fluxes) heavily reliant on the model physics. Each reanalysis employs similar physics but assimilation approaches differ and many variables (notably, surface fluxes) have to be parameterized which is typically where substantial differences can be introduced between the datasets. The use of three different

reanalyses enables an assessment of the spread between depictions of surface fluxes and net surface heat flux.

Table 2.1 Summary of data sources.

Data	Source	Time Period	Resolution (spatial)
ERA5	ECMWF	1956-Present, hourly	30 x30 km
CFSR	NCEP	1979-Present, 6-hourly	38 x 38 km
MERRA-2	NASA	1980-Present, 6-hourly	50 x 50 km
RV Araon	KOPRI	August 2018, Daily	X
SHEBA	NSF[1]	1998, Hourly	X
MOSAiC	AWI/CIRES	2020, Hourly	X

2.1.1 MERRA-2

2.1.1.1 Technical Specifications

MERRA-2 is produced by NASA's Global Modeling and Assimilation Office (GMAO) (Geralo et al., 2017). One of the main components of the MERRA-2 system is the Goddard Earth Observing System (GEOS) atmospheric model. The GEOS model (50 km x 50 km resolution) uses a finite volume dynamical core with a cubed-sphere horizontal discretization at a 0.5 x 0.625 resolution on a latitude-longitude grid and has 72 vertical levels up to 0.01 hPa (Geralo et al., 2017). The cubed grid allows for uniform spacing at all locations, which mitigates the effects of distortion approaching the poles.

[1] Full list of data sources listed in the references.

The second main component of MERRA-2 is the Gridpoint Statistical Interpolation (GSI) analysis scheme (Wang, 2010; Kliest et al. 2009). The analysis scheme uses the same resolution as the atmospheric model and updates on a 6-h cycle. It uses a 3DVAR algorithm and the "first guess at appropriate time" procedure for computing "observation-minus-background" departures that have temporally accurate values (Gelaro et al., 2017). The results from this analysis are used as a correction for the background states of the MERRA-2 models. This correction controls noise and improves the use of observations (Bloom et al., 1996)

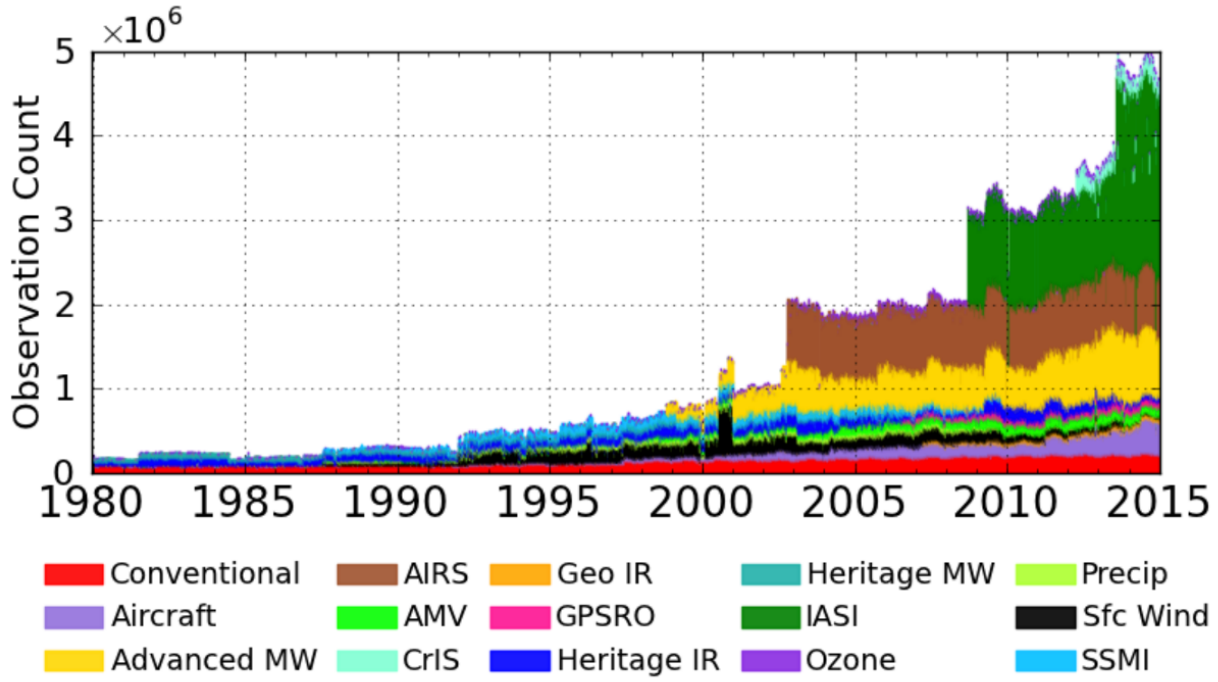

Figure 2.1: Time series of assimilated observations for MERRA-2 for 1 January 1980 – 31 December 2014. From McCarty et al., 2016.

MERRA-2 makes use of two main observational sources, conventional and satellite, summarized in Figure 2.1 and Figure 2.2. Conventional observations

primarily refer to wind or mass field data measurements (e.g., from soundings) while also including some remotely-sensed and ground based measurements (McCarty et al. 2016). The second set of observational datasets are satellite-based observations. Better use of satellite datasets is one of the major improvements made since MERRA, version 1. The incorporation of observational data into MERRA-2 helps constrain output values from the model. Although the reanalysis and assimilations systems are overall static in any reanalysis, the fact that observations quantities have evolved through time, which can influence the outputs -- a quality common to all reanalyses. Assimilating dynamic observations are important for continually improving model output. For MERRA-2 specific assimilated data, see Figure 2.1 and Figure 2.2 (McCarty et al., 2016).

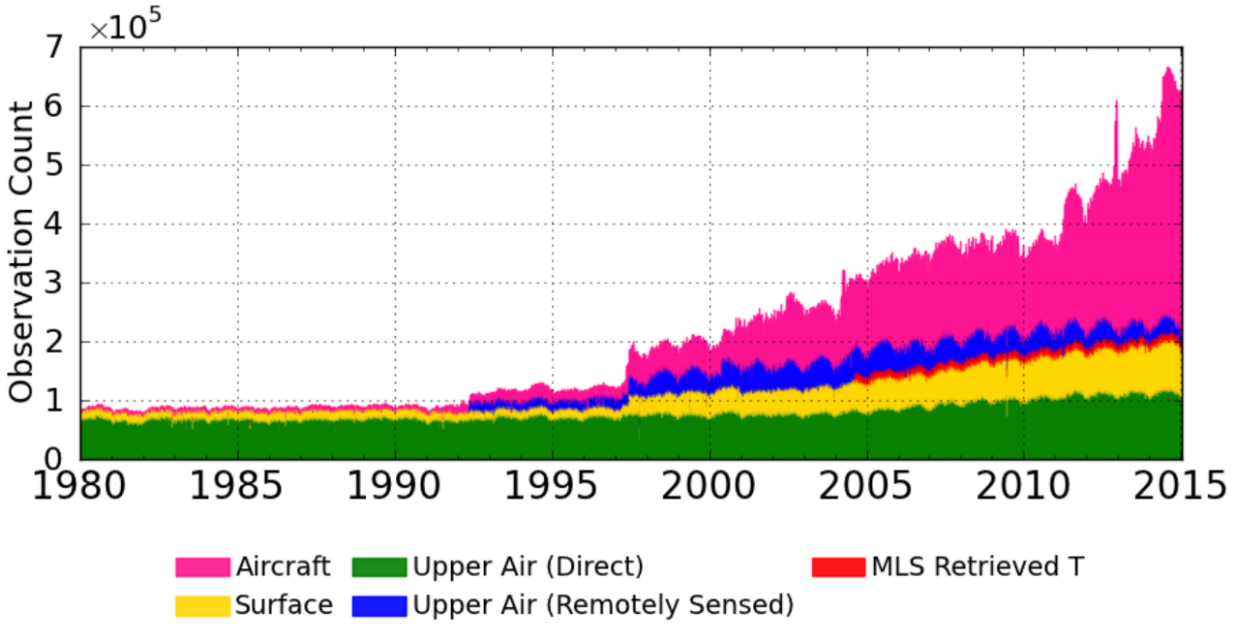

Figure 2.2: Time series of input conventional observations in MERRA-2 for 1 January 1980 – 31 December 2014. Aircraft corresponds to the group of the same

name in Figure 2.1, while all other observations are represented in the group "Conventional" in Figure 2.1. From McCarty et al., 2016.

The first component incorporated into MERRA-2 that determines the boundary layer is sea surface temperature (SST). For the first two years of the dataset (prior to 1982), MERRA-2 uses 1° SST data that was used in the Taylor et al. (2002) paper (Bosilovich et al., 2015). Between 1982 and April 2006, the SST is daily ¼° that was used in Reynolds et al. (2007). Lastly, after April 2006, the daily SST values are 1/20° from the Operational Sea Surface Temperature and Sea ice Analysis used in Donlon et al. (2012) (Bosilovich et al., 2015).

The second component determining the boundary layer in MERRA-2 is sea ice concentration (SIC). SIC is represented by a 7-cm skin layer in order to represent heat capacity incorporation to the reanalysis. The ice albedo is varying based on the SHEBA dataset collected in 1997-1998 (Bosilovich et al., 2015).

This dissertation uses radiative fluxes, turbulent fluxes, cloud cover, and sea ice fraction data at the surface at hourly time steps from MERRA-2. Cloud cover is provided as the fraction of low, medium, and high cloud cover. Low cloud cover is defined as all clouds that occur between the surface of the earth and 6,500 ft roughly occurring below 700 hPa. Medium cloud cover occurs from 6,500 ft to 13,000 ft roughly occur between 700 and 400 hPa. High cloud cover is between 13,000 ft. and 25,000 ft roughly occurring at 400 hPa. One issue with using the bounding pressures for these heights is that the values will change over high topography (Molod et al., 2015). All variables are available in their native vertical grid (72 layers) or at 42 standard interpolated pressure levels with the top of the

atmosphere defined as 0.01 hPa. Three-dimensional atmospheric variable data are provided at hourly, three-hourly, and six-hourly time steps and can be downloaded as netCDF-4 files. The data is provided at a 0.625° latitude x 0.5° longitude resolution by NASA GMAO at https://gmao.gsfc.nasa.gov/reanalysis/MERRA-2/.

2.1.1.2 Known Issues

MERRA-2 uses an automated bias correction scheme for most satellite radiance observations (Gelaro et al. 2017). Compared to MERRA, MERRA-2 has incorporated a seasonally varying sea ice albedo which has improved air temperature estimates and reduced biases in the net energy fluxes (Cullather et al. 2014). There is a considerable reduction in 2-m air temperature biases during boreal spring in MERRA-2 when compared to SHEBA measurements. Yet, in winter months over sea ice, there is a warm bias of ~1.2 C in the upper troposphere.

There is a noted high bias in summer precipitation in high latitudes as precipitation observations are not used for these regions because precipitation observations are often not accurate because of blowing snow. This could be particularly impactful on radiative and turbulent fluxes because different surface cover will change reflectivity and different amounts of moisture will change latent heat . This can contribute to biases in MERRA-2 turbulent fluxes over the Arctic region. Reichle et al. (2017) found that the observation-corrected precipitation was more realistic than the model generated values; this should be taken into consideration when looking at MERRA-2 precipitation data. Although the diurnal

cycle of the corrected precipitation has a reasonable amplitude compared to observations, the maximum precipitation (which remains the same compared to MERRA) is unrealistic (Geralo et al. 2017).

Separate from model bias corrections are corrections for assimilated observations. There is a bias correction for aircraft temperature observations that are assimilated into the reanalysis (Geralo et al., 2017). Overall, the improvement of observational bias correction has been attributed to the reduction in uncertainty for MERRA-2 (Dee et al. 2011).

2.1.2 ERA5

2.1.2.1 Technical Specifications

ERA5 is produced by the European Centre for Medium-Range Weather Forecasts (ECMWF). Compared to the earlier ERA-Interim effort, ERA5 provides higher spatial resolution outputs, assimilates more data and provides more output parameters. The outputs from ERA5 are heavily reliant on ECMWF's Integrated Forecast System (IFS). This system is a new version (Cy41r2), including many improvements, over the original model (Cy31r2) used in ERA-Interim (Hersbach et al., 2020). The IFS is a combination of a forecast model, three fully coupled atmospheric, land, and oceanic components, and a 4D-Var data assimilation system (Dee et al., 2011). The assimilation system uses a 12-hour assimilation window where all forecasts and assimilated data that fall within the window are used for the analysis.

ERA5 assimilates observations from over 200 conventional data and satellite instrument sources (Figure 2.3). The number of global observations assimilated into ERA5 increased from around 0.75 million per day average in 1979 to around 24 million per day by 2019 (Hersbach et al. 2020). Conventional observations primarily refer to wind, humidity (over land), pressure (over land and sea), upper-air temperatures, and rain measurements. Satellite instruments provide ERA5 with upper-air temperature, humidity, and ozone measurements. Similar to MERRA-2, ERA5 adjusts observations for bias. One example of bias correction that ERA5 uses is a revised cloud-detection scheme documented in Krzeminiski et al. (2009), which removes observations to reduce bias.

The first component that is used to define the lower boundary layer in the ERA5 Reanalysis is SST which comes from a level-4 gridded dataset compiled from multiple sources starting in 1950 (Hersbach et al., 2020). From January 1949 through December 1960 the SST data comes from the HadISST2.1.0.0 observations from the Met Office at the Hadley Center. From January 1961 to August 2007 the SST data is supplied by the next generation from the HADISST2.1.1.0 from the Met Office at the Hadley Center. Finally, from September 2007 onwards the SST observations are from the OSTIA dataset from the same Met Office (Hersbach et al., 2020).

The SIC used in ERA5 is also a level-4 gridded dataset compiled from 1950. From January 1949 to December 1978 the SIC observations comes from the HadISST2.0.0.0 at the Hadley Center Met office. From January 1979 to August

2007 the SIC data is the OSI SAF 409a, which is a reanalysis product. Lastly, from September 2007 onward, the SIC data is from the next generation of the reanalysis product, OSI SAF oper (Hersbach et al., 2020). The data sources for sea ice concentration in ERA5 apply a melt-pond correction which essentially removes the summertime melt pond bias (Hirahara et al., 2016).

This dissertation uses radiative fluxes, turbulent fluxes, cloud cover, and sea ice fraction data at the surface at hourly time steps. Cloud cover is provided as the cloud fraction of sky cover at low, medium, and high levels in the atmosphere. The height at each level that cloud cover was calculated changes depending on the surface pressure level.

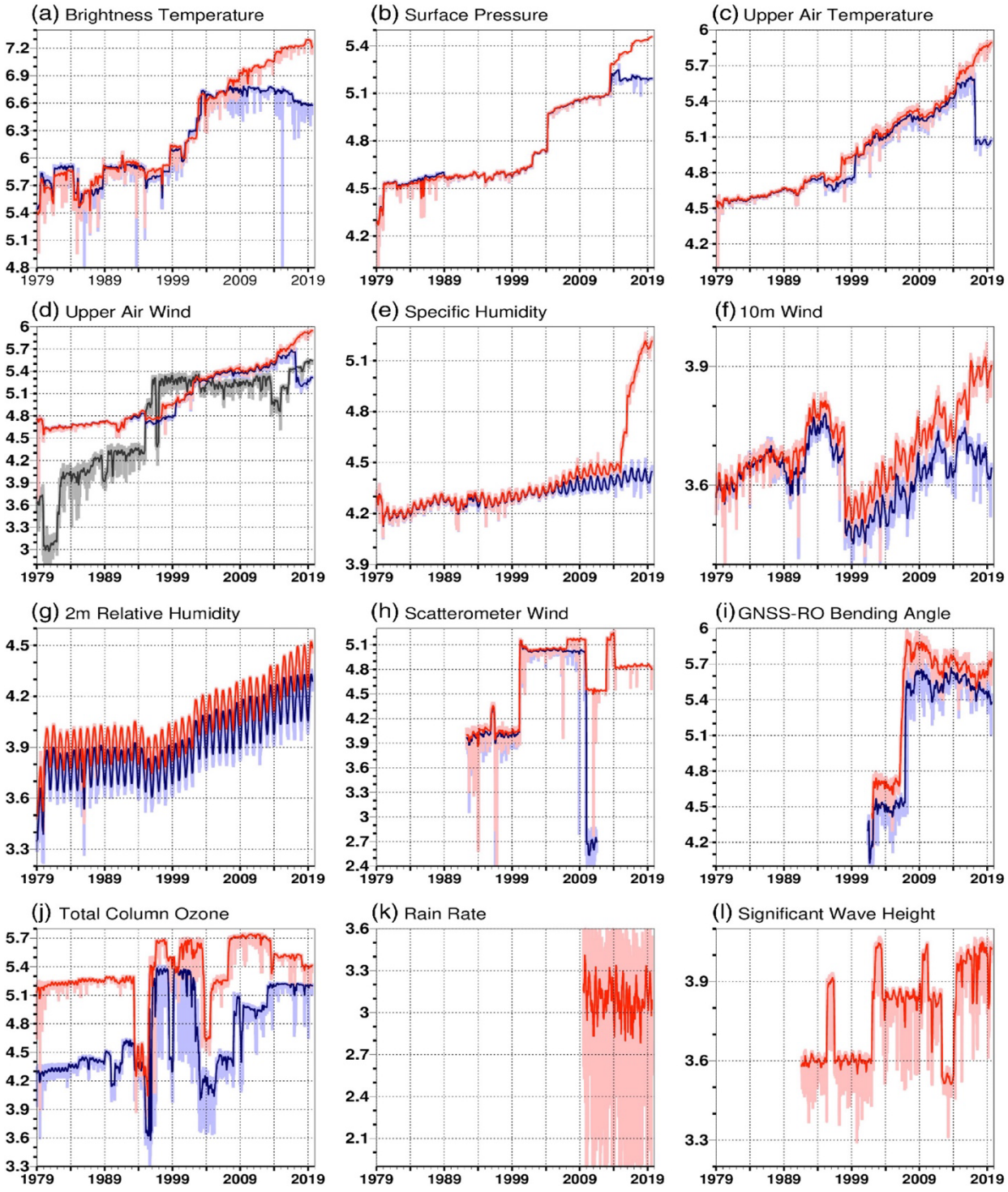

Figure 2.3: Number of daily actively assimilated observations (weak colors) and 30-day means (strong colors), both in log10 scale, for ERA-Interim (blue) and ERA5 (red) for the 12 observables for which observations are assimilated in 4D-Var and ocean wave assimilation. Numbers for (plot d) upper-air wind exclude assimilated AMV wind. Numbers of these latter are shown for ERA5 (black), while no statistics are

available for ERA-Interim. Rain (plot k) is assimilated only in ERA5. No statistics are available for (plot l) ERA-Interim significant wave height, while information on data usage in LDAS is incomplete for both reanalyses. Each 0.3 tick on the vertical axis corresponds to a factor of 2, and minor ticks (0.1) to a difference of 26%. From Hersbach et al., 2020.

The low level cloud cover pressure level has to be greater than 0.8 times the surface pressure; for example if the surface pressure is 1000 hPa, low level cloud data would occur in areas with air pressure higher than 800 hPa, which corresponds to ~ 2 km above the surface. Medium cloud cover occurs where the pressure is between 0.45 and 0.8 times the surface pressure. If the surface level is approximately 1000 hPa, the medium cloud cover would occur between 800 hPa and 450 hPa (~2km to 6km). Finally, high cloud cover is with pressure levels that are less than 0.45 times the surface pressure.

ERA5 spans from 1950 to present. The atmospheric model spatial resolution is 31 km and has 137 vertical pressure levels, defining the top as 0.01 hPa. Atmospheric data are available at all of these levels. Surface and single level data is also available. Output data are available in hourly increments and monthly averages and each variable is pre-interpolated to a regular latitude/longitude grid that is appropriate for that data. Data is available in GRIB1, GRIB2, and NetCDF formats at https://cds.climate.copernicus.eu/cdsapp - !/dataset/reanalysis-era5-single-levels?tab=form

2.1.2.2 Known Issues

All forecasts and observations in a 12-hour window are used to determine accuracy and uncertainty; yet these are not uniform across the temporal window (Hersbach et al., 2020). If the assimilated data and model are unbiased, errors follow a Gaussian curve, and observations are uniform in space and time, the analysis error will be the smallest in the middle of the window. As none of these assumptions hold in ERA5, the particular variable and location are important in determining where in the assimilation window is most accurate (Hersbach et al., 2020). To assess some of the uncertainty, evaluating a 10-member ensemble provides a sense of random uncertainty from the spread between ensemble members. Generally speaking, as one goes back in time, the uncertainty grows, and the number of assimilated observations diminishes.

A cold bias was discovered in forecasted low level temperatures across parts of the globe. To resolve this issue, the reanalysis was rerun between 2000 and 2006. Additionally, Shepherd et al. (2018) found a warm bias in the IFS model's upper stratosphere. No data source is without uncertainty, and these examples are to show that reanalyses are no exception.

Additionally, melt ponds are not considered in the ERA5 surface cover across the Arctic Ocean. Sea ice concentration, sea ice albedo, and open water albedo are calculated independently (Pohl et al., 2020). Along with these two considerations, it is well known that the turbulent fluxes in ERA5 are not well captured, especially in the Polar regions (Kong et al., 2022).

2.1.3 CFSR

2.1.3.1 Technical Specifications

The original version of CFSR was released by the National Centers for Environmental Prediction (NCEP) in August 2004. There are two versions, spanning different time periods. Version 1 produced data from 1979 through 2010 while Version 2 covers 2011 to present. CFSR Version 1, was mainly created to establish initial conditions and calibrations for the second version (Saha et al., 2014). Both versions of this reanalysis are a combination of four systems: 1) NCEP-Department of Energy (DOE) Global Reanalysis 2 (R2), which provides the initial conditions for the atmospheric and land surface; (2) a global ocean data assimilation system (GODAS), which is used for the ocean initial conditions; (3) NCEP's Global Forecast System (GFS), which is the atmospheric model run for a lower resolution; (4) and the Modular Ocean Model, version 3, (MOMs) from the Geophysical Fluid Dynamics Laboratory (GFDL) (Saha et al., 2014).

There are a number of improvements between Version 1 and Version 2 of CFSR. The same Rapid Radiation Transfer Model (RRTM) was used in both versions (adapted from AER Inc. Mlawer et al. 1997; Iacono et al. 2000; Clough et al. 2005) but some important changes were made; namely to address the variability of layered clouds (Saha et al. 2014). Another major change was the addition of the three-layer interactive sea ice model. These alterations to the reanalysis were vital to improving the surface energy budget since cloud cover and sea ice have significant impacts on the radiative and turbulent fluxes. Similar to MERRA-2 and

ERA5, CFSR assimilates data from many different sources, both surface-based observations and satellite data. Table 2.2 shows a complete table of all the radiance instruments that are assimilated in CFSRv1 and the time periods they were used.

The first variable used for boundary conditions are a daily ¼° SST observation from the AVHRR infrared satellite and the AVHRR and AMSR sensors on the NASA Earth Observing System Satellite.

The second is sea ice conditions, which come from an interactive sea ice model that is 3 layers and includes dynamic and thermodynamic components (Wu et al., 2005). The three layers are made up of two equally thick sea ice layers and a snow layer. This model includes leads and takes the melt pond effect into consideration on the summertime albedo. Unfortunately, some issues with the results are as follows: the sea ice is too thick in the initial conditions, and the sea ice is too extensive in the spring and summer (Saha et al., 2010 & 2014).

As with other reanalyses, the variables used from CFSR are radiative fluxes, turbulent fluxes, cloud cover, and sea ice fraction. Cloud cover is again provided as the cloud fraction of sky cover at low, medium, and high levels in the atmosphere. Unlike for ERA5, the descriptions of cloud cover heights are not described in a readily available source.

Table 2.2: Radiance instruments in CFSRv1 and the time period each was assimilated. From Saha et al., 2010.

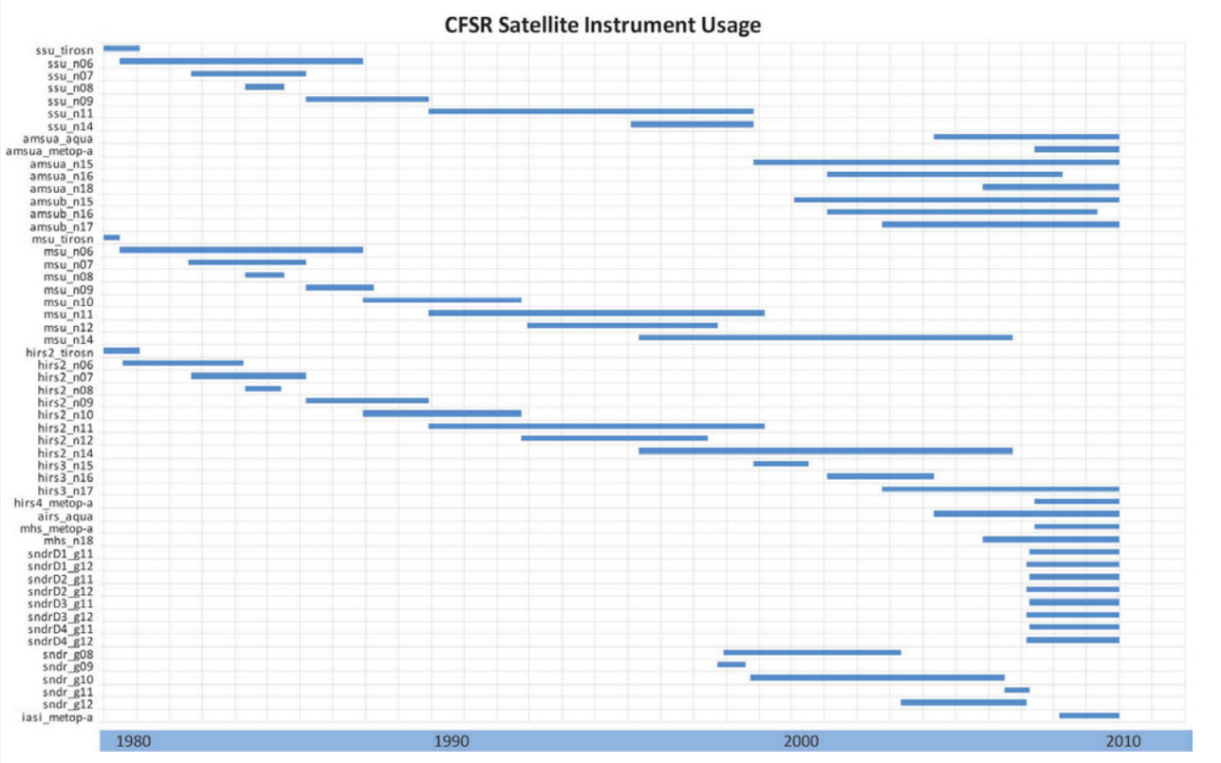

Data are available at hourly time steps and are averaged into 6-hourly variables that can also be downloaded. CFSR has an atmospheric resolution of ~38 km with 64 pressure levels extending from the surface up to 0.24 hPa. The ocean and land resolutions are 0.33° longitude by 0.33° latitude. All data from CFSR version 1 can be found at https://rda.ucar.edu/datasets/ds093.1/#!access and all data from CFSR version 2 can be found at https://rda.ucar.edu/datasets/ds094.1/#!access. Both versions can be downloaded as NETCDF files from both versions.

2.1.3.2 Known Issues

Known problems in CFSR Version 2 stem from three sources: data ingested into the model, design limitations, and systematic errors. Overall, analysis of CFSR Version

2 output indicated that it is a better model than the original version. Yet, there are some regions with large systematic errors for 2-meter temperature and sea surface temperature; systematic errors are the approximate differences in the predicted and observed climatology over a common period. Saha et al. (2010) found that there are known issues and inconsistencies with the observational data/initial states that are ingested into the forecast model; the other two reanalyses used in this study use many of the same observational sources and suffer from the same problem. One of the main system limitations is that the atmosphere and ocean models are uncoupled, limiting interactions between the two.

Saha et al. (2014) suspect that there is a significant sea ice thickness bias in the CFSR Version 2 model that causes the sea ice in the initial conditions to be too thick ultimately causing sea ice extent in spring and summer to be larger than it should be. As there is no sea ice thickness data to assimilate, at the time of construction of this model, this variable is relying entirely on parameterization. Even though CFSR Version 2 roughly captured the observed seasonal cycle, long-term trends, and interannual variability, it still has large errors in its representation of sea ice mean states and anomalies. Due to these shortcomings, CFSR Version 2 has applied a bias correction placing it among the best prediction models (Saha et al. 2014). Similarly, to the other two reanalyses, it is well known and accepted at this point that the turbulent fluxes in the reanalyses are not well represented.

2.1.4 **Reanalysis Land Mask Differences**

One issue that can apply to the entirety of the reanalysis data is the difference in land masks. In MERRA-2 the land mask is defined based on fractional tiles from the 1km Global Land Cover Characteristics dataset. ERA5 is defined by using a satellite derived 300m resolution dataset (ECMWF, 2023). CFSR does not describe how the land mask data is determined. A land mask comparison was conducted showing that there are very few differences between the three reanalyses. There are a few small differences around near Svalbard and Novaya Zemlya on the Russian/Scandinavian side of the Arctic Ocean (Figure 2.4).

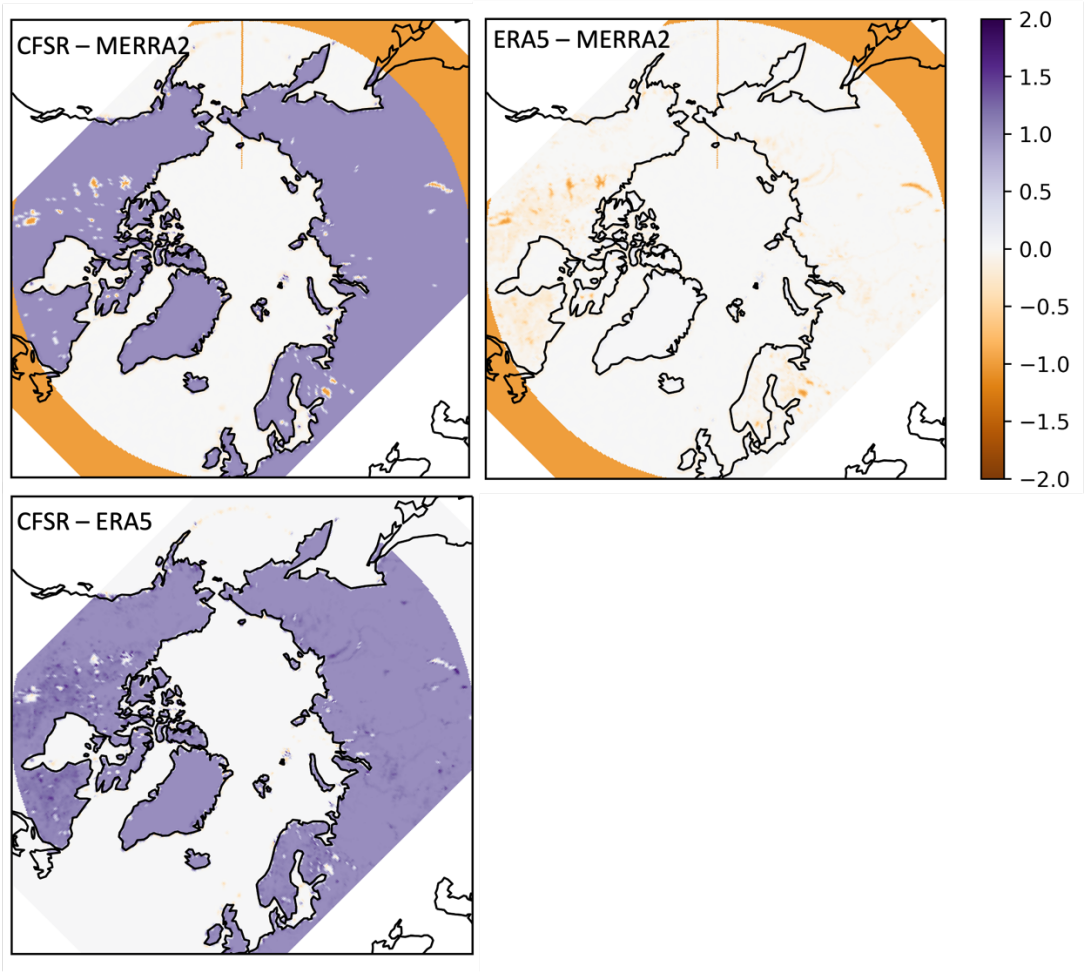

Figure 2.4: Land mask differences between CFSR, ERA5, and MERRA-2. Purple shows the largest positive differences. Zero denotes ocean pixels, all other values denote land presents.

CFSR has some land values of 2 because the land mask from CFSR v1 and CFSR v2 were combined. Orange shows large negative differences. The second noted reanalysis is subtracted from the first reanalysis to calculate these differences.

2.2 Surface Observations

To evaluate surface fluxes from the three reanalyses, outputs were compared to three different observational sources; the Surface Heat Budget of the Arctic Ocean (SHEBA) expedition, a collaborative cruise aboard the *RV ARAON*, and the Multidisciplinary drifting Observatory for the Study of the Arctic Climate (MOSAiC) expedition summarized in Table 2.1. Each expedition operated in different regions of the Arctic, at different times of the year, and for different lengths of time.

2.2.1 SHEBA

2.2.1.1 Technical Specifications

SHEBA was a program funded by the National Science Foundation to study atmospheric, sea ice, and ocean processes in the Arctic and improve predictive capacity. The research focused on gaining understanding of the ice-albedo feedback and cloud-radiation feedback mechanisms (Uttal et al., 2002).

A team of ~200 scientists, rotating throughout the year, boarded the Canadian Coast Guard icebreaker, the *Des Groseilliers*, and froze into the ice, drifting 570 km from the Beaufort Sea north of Prudhoe Bay northwest to the top of the Chukchi Sea (75°N, 142°W to 80°N, 162°W) (Uttal et al., 2002). The ship was in

the ice with a surrounding drifting station for one year from October 1997 to October 1998. The ship drift track can be found in Figure 2.4.

The SHEBA team took measurements from the surface and down into the ocean pycnocline (~0.5 km below the surface) which serves as an observational proxy for a single global climate model grid cell. Data were measured at three different spatial scales: local, which was less than 10 km from the sea ice station, aggregate scale (10-100 km), which included ice thickness distribution, mesoscale cloud systems, and high-resolution general circulation, and basin scale (1000 km+). Three scales were used so local and aggregate scales could be analyzed within a basin wide context.

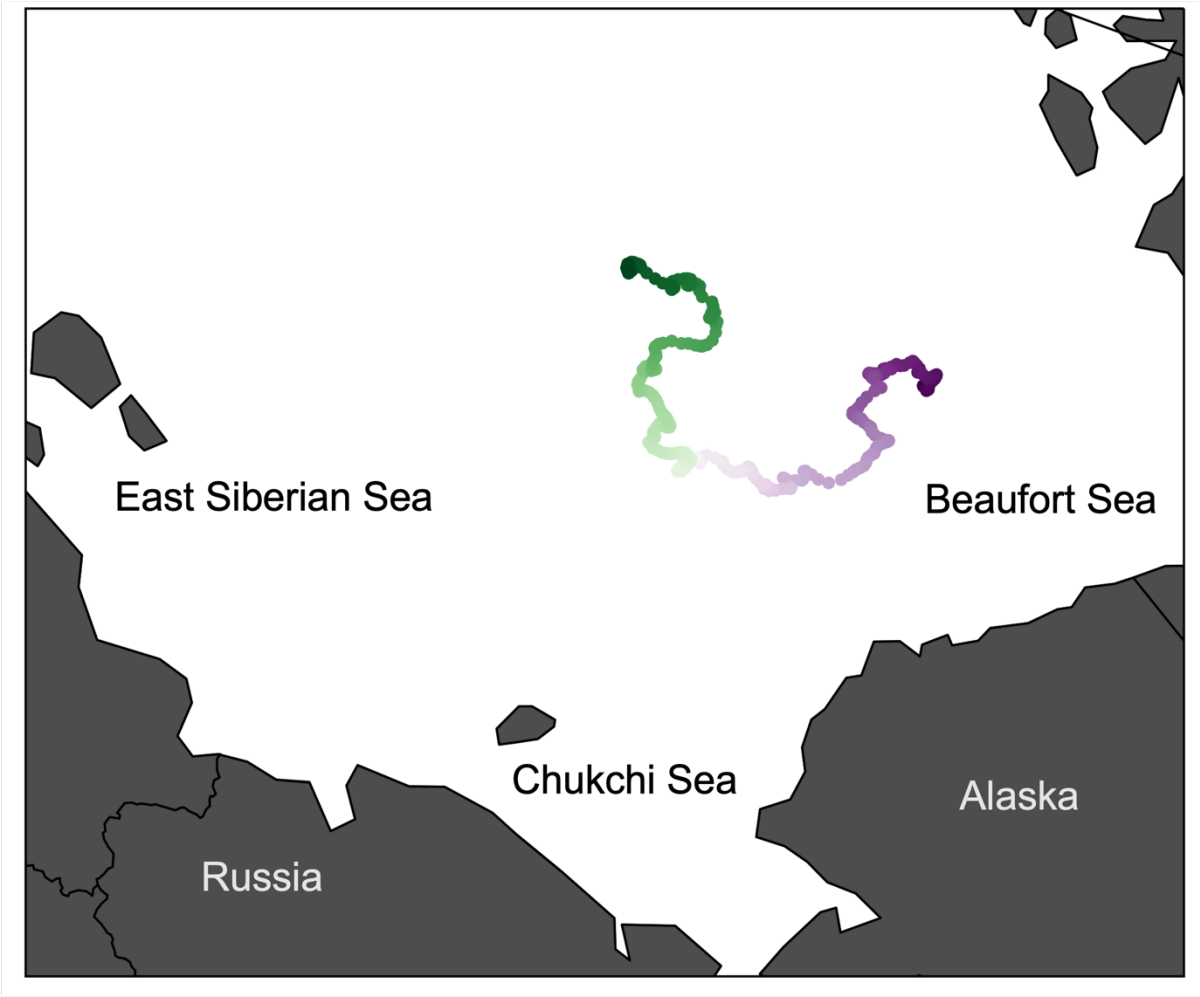

Figure 2.4: Ship track for SHEBA expedition from September 1997 – November 1998. The expedition started at the purple points and ended at the green points.

The SHEBA expedition collected a wide variety of data including but not limited to: cloud properties (including crystal/droplet sizes, optical depths, water content, and cloud boundaries), radiation fluxes (both longwave and shortwave), turbulent fluxes of latent and sensible heat fluxes, snow depth, ice thickness, ocean salinity, water temperature, and ocean currents. A few examples of instruments

used for that data collection are radar, lidar, and radiometers. A full list of instruments is provided in Table 2.3.

The National Aeronautics and Space Administration (NASA) First International Satellite Cloud Climatology Project (ISCCP) Regional Experiment (FIRE) -- Arctic Clouds Experiment (ACE; Curry et al. 2001) conducted an extensive aircraft campaign over the ice camp from April to July 1998. Additionally, the Department of Energy's Atmospheric Radiation Measurement (ARM) division collected cloud and radiation information from a continuously operating surface in Utqiagvik, Alaska (Uttal et al. 2002). Other collaborations included the Japanese Marine and Science (JAMSTEC) buoy program, the RADARSAT Geophysical Process System (RGPS), and the Alaska SAR Facility (ASF).

Table 2.3: Annual cycle measurements from the SHEBA expedition. From Uttal et al., 2002.

Instrument	Collection start date	Collection end date	Data product
Deep ocean SeaCat CTD	12 Oct 1997	21 Sep 1998	Ocean depth, temperature, salinity, conductivity, density
Doppler sonar	26 Nov 1997	2 Oct 1998	Upper-ocean current
YoYo CTD (Seabird 911+)	11 Oct 1997	1 Oct 1998	Ocean temperature, conductivity, salinity, density
Dual-thermistor thermal	7 Oct 1997	22 Sep 1998	Thermal microstructure dissipation rate dissipation package
Turbulence mast	9 Oct 1997	26 Sep 1998	Ocean current speed/direction, temperature, salinity, salinity flux, turbulent heat flux, Reynolds stress
ARGOS drifter buoys (microCAT)	2 Oct 1997	2 Oct 1998	Conductivity, salinity, temperature, position
Buoys (thermistors)	14 Oct 1997	10 Feb 1998	Air and snow temperature, position
Buoys (thermistors)	26 Oct 1997	1 Oct 1998	Ice thickness
Snow gauges	11 Oct 1997	1 Oct 1998	Snow depth
Thermistors	13 Oct 1997	1 Oct 1998	Snow and ice temperature
Stress meters			Ice stress
GPS	1 Oct 1997	11 Oct 1998	Ice camp position and heading
Surface weather reports	29 Oct 1997	9 Oct 1998	Cloud-base height, visibility, cloud fraction, wind speed and direction, air temperature, dewpoint, pressure, pressure tendency, weather conditions
Nipher-shielded snow gauge	29 Oct 1997	9 Oct 1998	Liquid water equivalent precipitation
Optical rain gauge	1 Oct 1997		Precipitation rate
Portable Mesonet (PAM) stations	1 Nov 1997	1 Oct 1998	Pressure, temperature, relative humidity, wind speed and direction, broadband shortwave and longwave fluxes up and down
Scintillometer	20 Oct 1997	2 Aug 1998	Refractive index structure, inner scale of turbulence
10-m towers (thermometers, prop anemometers)	9 Oct 1997	1 Oct 1998	Temperature, dewpoint, wind speed and direction at 2 and 10 m, pressure
20-m tower (thermometers, anemometer)	1 Oct 1997	1 Oct 1998	Temperature, relative humidity, wind speed sonic and direction, friction velocity, sensible heat flux, surface and snow/ice temperature
Eppley radiometers	1 Oct 1997	1 Oct 1998	Broadband shortwave and longwave fluxes, down and up
35-GHz cloud radar	20 Oct 1997	1 Oct 1998	Radar reflectivities, Doppler velocities and spectral widths
523-nm depolarization lidar	1 Nov 1997	8 Aug 1998	Lidar backscatter, depolarization ratios
GLAS (Vaisala) rawinsonde	16 Oct 1997	15 Oct 1998	Pressure, temperature, relative humidity, wind speed and direction, position

2.2.1.2 Known Issues

There are a number of instrumental based errors that occurred during the SHEBA expedition, although none of them largely impacted the results. There are errors of a few tenths of a degree in surface temperature caused by the pyranometer case and dome (Persson et al., 2002). Additionally, downward shortwave radiation measurements occurred at a number of different places using different instruments that produced different values ranging from 1 – 3 W (Persson et al., 2002).

Throughout the winter months, the average snow depth near the 20-m tower was 30 cm, the surface was fairly uniform and the albedo was high, yet it all changed when melt began. Once melt onset occurred, the surface became highly variable with bare ice, melt ponds, and open water which decreased albedo drastically. Surface changes on a sub-grid cell scale such as documented by SHEBA are not incorporated into models at this time because they would need much higher resolution to do so. As illustrated by Uttal et al. (2002), one of the biggest challenges faced by SHEBA was the large subgrid scale horizontal variability in ice, ocean, cloud cover, and near-surface heat and mass fluxes. The SHEBA team worked on addressing these issues by collecting enough data on spatial variability so local measurements could be scaled up to characterize processes and interactions occurring on larger scales.

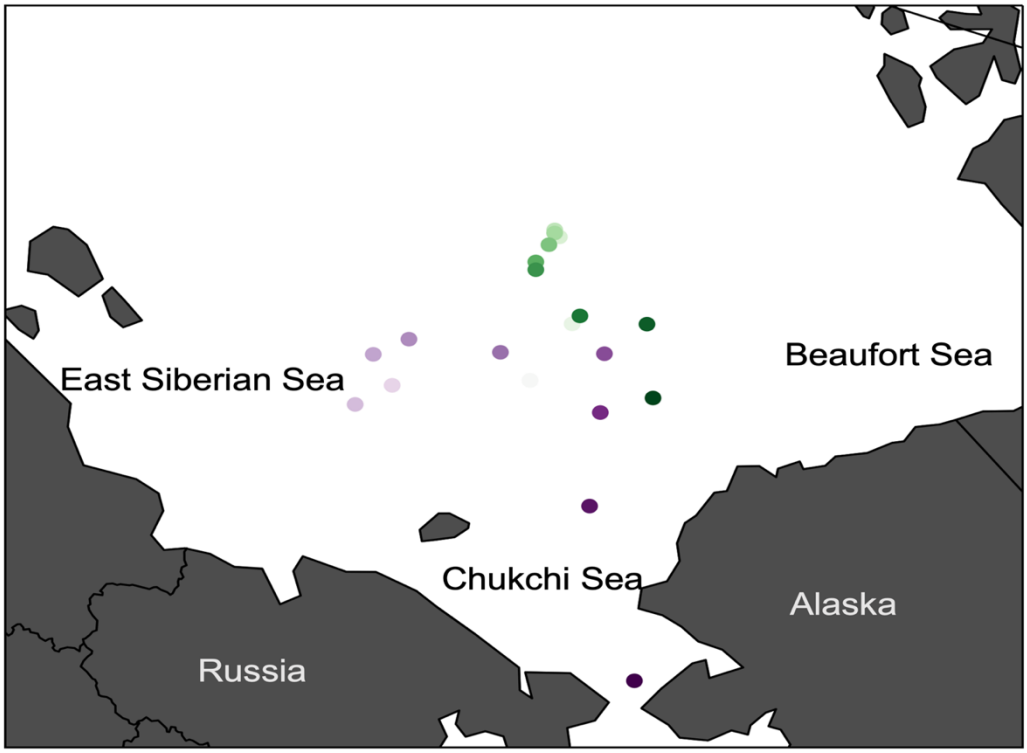

Figure 2.5: *RV Araon* ship track in August 2018. The expedition started at the purple points and ended at the green points.

2.2.2 *RV Araon* Downwelling Shortwave Measurements

2.2.2.1 Technical Specifications

The cruise aboard the *RV Araon* was a collaboration between the Korea Polar Research Institute (KOPRI) and the Nansen Center in Norway. The expedition focused on understanding the physical, chemical, and biological properties of ocean water and sea ice in the Chukchi Sea. A total of 44 scientists from 8 different countries and 20 institutes, universities, and companies left Nome, Alaska on August 4th 2018 and returned to Utqiagvik, Alaska on August 26th 2018. The ship track is shown in Figure 2.5.

This dissertation uses downwelling shortwave radiation from this expedition. Downwelling shortwave radiation measurements were taken with a Hukseflux SR30 Pyranometer installed on the top deck of the ship by Dr. Alia Khan (~18 meters above the sea ice) as shown in Figure 2.6. The pyranometer was connected to a CR1000x data logger that stored the data on a memory card. Measurements were sampled at two second intervals and were averaged to 15-minute, hourly, 6-hourly, and daily averages. Measurements began at 64°N north of Nome, Alaska and continued through the Bering Strait into the Chukchi Sea and up to the ice edge at 79°N (Figure 2.5).

The Hukseflux SR30 measures solar radiation received by a plane surface from a 180° field of view angle in W/m^2. The pyranometer uses a recirculating ventilation and heating system, which uses lower wattage than a traditional ventilation system, to keep the dome ice and rime free.

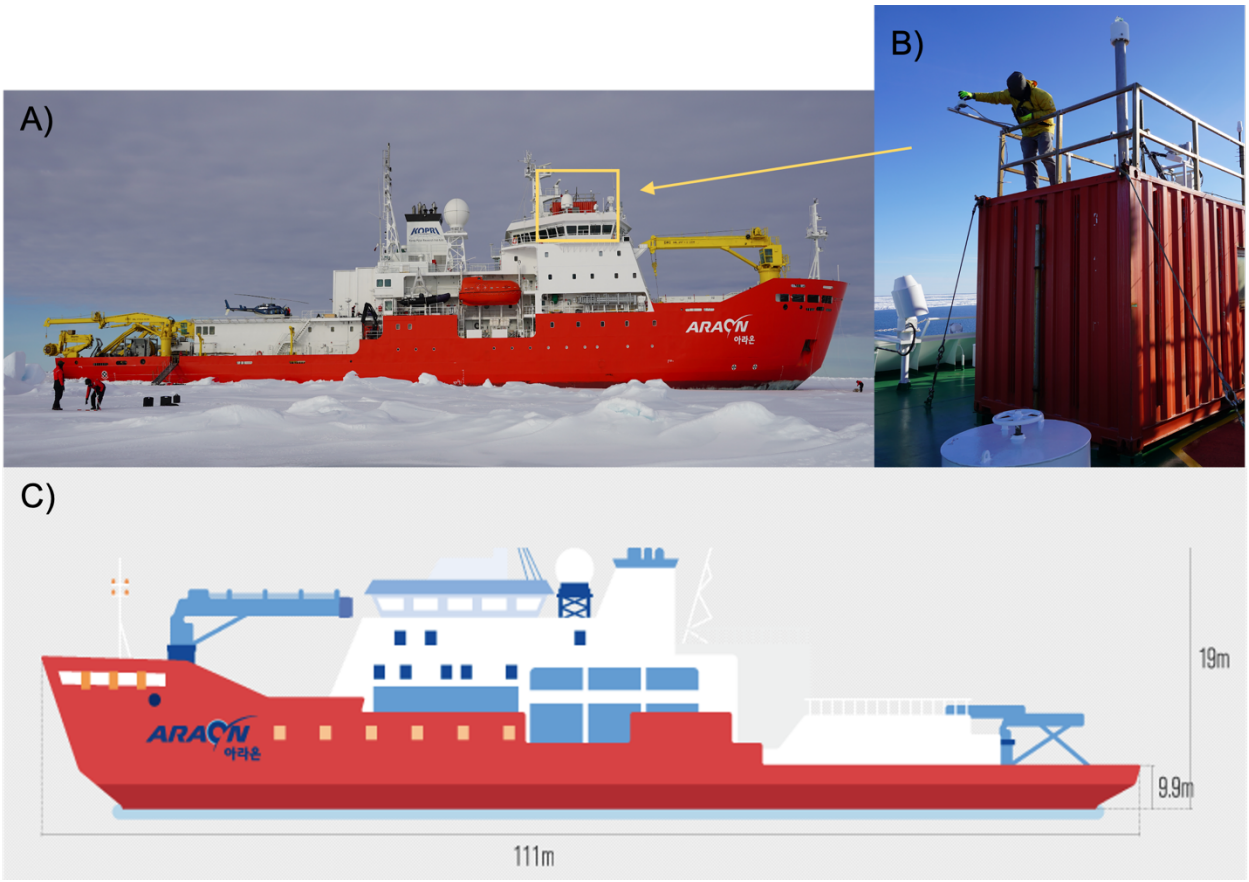

Figure 2.6: location of the pyranometer (A and B, photo credit: Dr. Alia Khan) and diagram of *RV Araon* ship dimensions (C) from https://www.kopri.re.kr/eng/html/infra/02030101.html.

2.2.2.2 Known Biases

A number of issues arise when using pyranometers on a ship in the Arctic. There are two noted uncertainties internal to the Hukseflux SR30, the first is a calibration error of less than 1.2% and the second is a tilt measurement uncertainty of +/- 1°. Regarding tilt, the pyranometer measures incoming solar radiation from a level, horizontal surface with a 360° horizontal and 180° vertical, unobscured viewing angle. If that is changing between measurements due to the rocking of the ship, this will alter the measurement accuracy. When consulting Campbell

Scientific, the seller of the Hukseflux SR30 recommend against using a gimbal mount because there is no good way to compensate for ship movement (ref: personal conversation between Dr. Khan and specialist).

Additionally, the coverage of the pyranometer dome by ice, snow, or rime impacts the instrumental measurement of downwelling shortwave radiation. This is a constant challenge in the Arctic, but especially on ships because ocean spray is kicked up and can settle and freeze on the dome. Since the dome is letting in shortwave radiation, if it is covered by ice, rime, or snow, the instrument is blocked from measuring shortwave radiation. Scientists would check the instrument every two days to ensure the heater was working and to clear the dome if it was covered.

2.2.3 MOSAiC

2.2.3.1 Technical Specifications

The MOSAiC expedition was led by the Alfred Wegener Institute, Helmholtz Centre for Polar and Marine Research (AWI). This was the first cruise of its kind, taking instruments near the North Pole throughout the winter months. A team of over 300 scientists, exchanged in phases over the year, representing 20 nations, worked together aboard the German icebreaker *RV Polarstern*. The research vessel froze into the ice on the Russian side of the Arctic (85° N, 137° E) in September 2019 and drifted for a year until October 2020 (Figure 2.7). From that point, the Polarstern drifted 3400 km across the Central Arctic Ocean, reaching as far north as 88°35’ North, just 156 km shy of the North Pole. This expedition produced some

of the most unique data because of how far north the ship and the ice camp traveled.

Starting on October 4, 2019, a regional network of observational sites was set up on the ice up to 50 km from where the *RV Polarstern* was drifting. Autonomous sensors were arranged to collect data to represent a grid cell of a modern climate model, similar to SHEBA. The camp was set up in this way to easily use the results to develop parameterizations for sub-grid cell scale processes in climate models. Current model parameterizations are areas that incorporate more uncertainty into climate model output because there is not enough sub-grid cell information. Alongside the ice floe camp, two German research aircraft, the Polar 5 and Polar 6, were used to collect complementary data near the central MOSAiC sites.

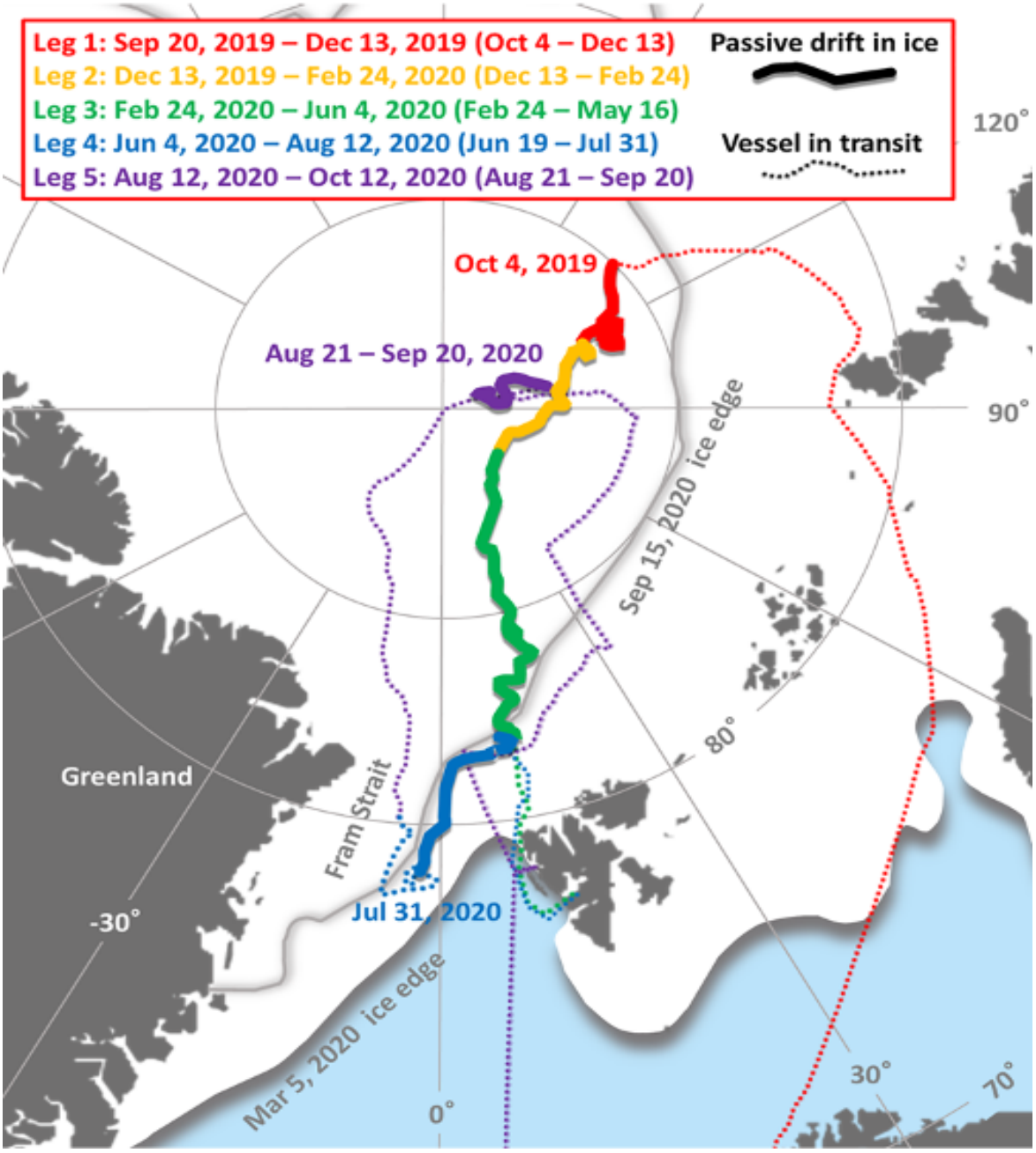

Figure 2.7: MOSAiC ship track distinguished by leg. Periods of passive drift by Polarstern (solid) and periods of transit when the vessel was underway (dotted) are distinguished. The inclusive dates for each of the 5, color-coded expedition legs are given in the legend, with the second set of dates in parentheses being the dates spent in passive drift with an ice floe. The approximate sea ice edge at the annual maximum (Mar 5, 2020) and minimum (Sep 15, 2020) is also provided. From https://doi.org/10.1525/elementa.2021.00060.f2.

The MOSAiC expedition collected a variety of data throughout the year including but not limited to: turbulence, shortwave and longwave radiation (upwelling and downwelling), temperature, humidity, pressure, water vapor, aerosols, trace gasses, and cloud properties (Shupe et al., 2022). A few examples of instrumentation used onboard the Polarstern and in the ice camp are radar, lidar, weather balloons, and unmanned aerial vehicles (UAV); the full list of energy budget instruments are in Figure 2.8.

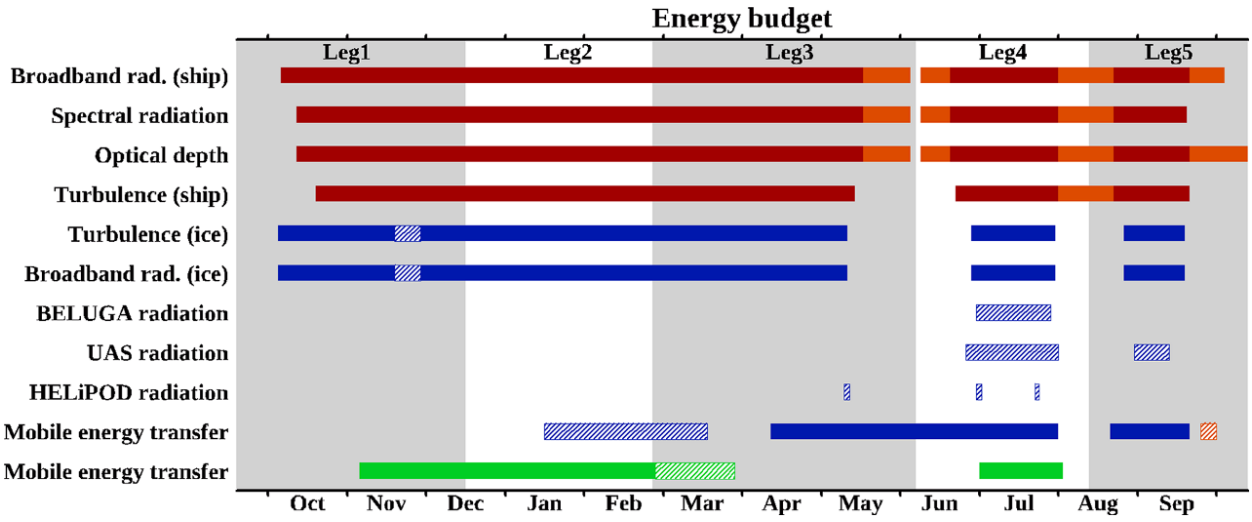

Figure 2.8: Temporal coverage of energy budget measurements in different categories. The different colors represent the following: red, onboard Polarstern while at MOSAiC ice floe; orange, onboard Polarstern while underway; blue, on sea ice in the Central Observatory; green, on sea ice in the Distributed Network. Solid bars are continuous measurements with minimal gaps. Hatched bars are intermittent or periodic measurements. The time spans from late September 2019 through early October 2020. From https://doi.org/10.1525/elementa.2021.00060.f8.

2.2.3.2 Known Issues

As this is a relatively new data set there has not yet been sufficient work to address problems or biases in the data. Many of the atmospheric measurements were taken onboard the *RV Polarstern* as it was a stable base (Shupe et al. 2022).

Yet, the vessel can adversely affect measurements of some atmospheric processes, like turbulence. To address these potential issues, the atmospheric science team also set up a number of ice camps to take complementary measurements.

Additionally, radiation measurements are usually taken as direct observations and diffuse fluxes separately, but during the MOSAiC expedition it was impractical to set up those set of instruments on the sea ice (Cox et al., 2023). There are several small offsets that occurred as noted in Wang et al., 2018 and Dutton et al., 2001 but there were no corrections implemented because of how small they were. Generally though, the instrument calibrations were implemented in order to reduce error issues (Cox et al., 2023).

CHAPTER 3: METHODS

3.1 Objective

As introduced previously, the goal of the dissertation is to estimate the amount of net surface heat flux, using the net surface flux (Equation 6), that the Arctic Ocean surface mixed layer gains on a seasonal basis using three reanalysis, including an idealized value using the best performing reanalysis for each surface flux component based on the results in Chapter 4 and Chapter 5. Analyses focus on the April through August season to capture the climatic processes occurring between the sea ice extent maximum (mid-March) and the sea ice extent minimum (mid-September). The net surface heat flux is calculated using Equation 6:

$$(6)\ F_{sfc} = R_{sfc} + Q_H + Q_E$$

Where R_{sfc}, is the sum of the upward and downward components of solar radiation and longwave radiation (the net radiation R_{sfc}: each component will be examined separately), Q_H is the turbulent sensible heat term and Q_E is the turbulent latent heat term. The convention is that the right-hand terms are positive downward (into the ice/ocean column).

It is first necessary to compare the reanalysis datasets against one another and the observational datasets. This is the focus of the analysis in Chapter 4 and Chapter 5. Lastly, a statistical analysis using t-tests and Pearson R Correlations was conducted to evaluate the datasets against one another more robustly. The study domains and additional methods used throughout the dissertation are discussed below. The statistical analysis is discussed in the last section (Section

3.6). Results presented in this dissertation were produced using software developed in Python and the datasets described in Chapter 2. Software code will be made available through GitHub for public access upon publication of this dissertation.

3.2 Study Domains

This analysis focuses on five regions: 1) The Arctic Ocean as a whole, excluding the Greenland, Iceland, and Norwegian (GIN) seas; 2) The Beaufort Sea; 3) The Chukchi Sea; 4) The Barents Sea; and 5) the polar cap, taken as the region polarward of 70 N. The GIN seas are excluded because this area has very little sea ice cover, and in this sense cannot be viewed as part of the Arctic Ocean. Study boundaries for the four focus regions listed above were approximately based on the Multisensor Analyzed Sea Ice Extent (MASIE) product boundaries from the National Snow and Ice Data Center[2] (Figure 3.1). The Beaufort Sea, the Chukchi Sea, the Barents Sea and the polar cap regions were selected as they provide contrasts between regions that are seasonally ice covered and a region that is usually ice covered year-round.

[2] https://nsidc.org/data/masie

Figure 3.1: Arctic Ocean regions with labeled seas (Groves & Francis, 2002). All regions except for the GIN seas were used for the Arctic Ocean Domain portion of the project. Regions 1, 2, and 8 were used for the regional observation comparison portion.

3.2.1 Arctic Ocean Domain

As seen in Figure 3.1, the total Arctic Ocean domain, as based on MASIE, includes the peripheral seas (Beaufort, Chukchi, Laptev, Barents, and Kara), the Canada Basin, North Pole sector, Central Arctic, and the central Arctic Ocean which is defined as the ocean that is north of all land and is ice covered year-round (Serreze and Barry, 2014). The Beaufort Sea sector extends north of Alaska, with the eastern boundary just west of Point Barrow. It is partially underlain by continental shelf. While the Beaufort Sea is influenced by the inflow of Pacific waters, ice conditions are strongly tied to variability in the circulation of the Beaufort Gyre. The Mackenzie River (one of the four largest rivers entering the Arctic Ocean) empties into the Beaufort Sea, influencing ocean surface salinity and ultimately sea ice growth (Serreze and Barry, 2014).

3.2.2 Chukchi Sea Domain

Ice conditions in the Chukchi Sea (2) are strongly influenced by variability in the inflow of warm Pacific waters through the shallow Bering Strait (Serreze et al. 2016). Serreze et al. (2016) documented pronounced trends towards later freeze-up dates and earlier ice retreat dates. This region is a gateway for ships entering or exiting the Arctic Ocean through the Bering Strait, as well as a focus for resource exploration.

3.2.3 Barents Sea Domain

The Barents Sea region is at the northern edge of the North Atlantic storm track. Roughly half of the North Atlantic warm ocean current enters the Arctic Ocean through this region. The warm water keeps the southern portion ice free, even in winter. The persistence of year-round open water in this area in recent years has been manifested in pronounced positive anomalies in winter surface temperature in recent years (Polyakov, et al., 2017). The Barents Sea offers a contrast to the other two marginal sea regions (Beaufort and Chukchi) because of how much warm ocean water and air is transported through this region.

3.2.4 Central Arctic Domain

Except for 2012, the central Arctic Ocean maintains sea ice year-round. Much of the heat exchange between the atmosphere and ocean occurs in leads, polynyas, and in areas of thin ice. However, the central Arctic Ocean is vastly understudied because of its remoteness and many satellites used for Arctic data collection do not provide coverage extending to the North Pole. The cost associated with traveling to the central Arctic Ocean, combined with the installation and maintenance cost for instrumentation is very prohibitive.

3.2.5 Polar Cap Domain

Calculations are also performed for a simple polar cap domain that extends from 70° N to 90° N (area of 15.4×10^6 km^2) which enables direct comparison to

energy budget studies such as those by Serreze et al. (2007) and Trenberth and Stepaniak (2003). Only ocean points are included in these calculations even though there are only a few land masses in the polar cap in order to keep consistent with the rest of the analysis.

3.3 Individual Flux Components from Reanalyses

3.3.1 Objectives

The goal of this portion of the dissertation is to evaluate the differences and similarities between the three reanalyses discussed in Chapter 2 (CFSR, ERA5, and MERRA-2). This will provide insight into what is causing the differences between the reanalyses and what potential biases need to be accounted for going forward in this study. The results of this portion of the analysis (detailed in Chapter 4) act as a base for the portion of the study discussed in Chapter 5.

3.3.2 Radiation and Turbulent Flux Calculations

Daily surface energy budget components were downloaded from ERA5, CFSR, and MERRA-2 at sub-daily timesteps (6-hourly and hourly, respectively) from 1980 through 2018. MERRA-2 does not provide upwelling shortwave directly, so net shortwave and downwelling shortwave were used to calculate the upwelling shortwave radiation. Similarly, ERA5 does not directly provide upwelling longwave radiation, so net longwave and downwelling longwave radiation were used to

calculate the upwelling longwave radiation. The variables used in this section of analysis are upwelling and downwelling shortwave radiation, upwelling and downwelling longwave radiation, and the turbulent latent and sensible heat fluxes.

ERA5 variables are in J/m^2 so they are summed because J/m^2 is an accumulation of energy and then converted to W/m^2 (which is a power unit) for a daily value that is comparable with MERRA-2 and CFSR. To convert from joules to watts over a model timestep, one must divide joules by the total seconds in each timestep. ERA5 daily values were divided by 86400 seconds. No conversions were applied to CFSR and MERRA-2 because their values were already in W/m^2.

For each of the three reanalyses, daily means were calculated at each grid point (node), then monthly averages were calculated from the daily data and an average for the melt season (April through August) was calculated from the monthly data. All temporal averaging was done with reanalysis data on their native grid. Additionally, while still on their native grids, data over the GIN seas and land were masked out, using the land masks provided by each reanalysis but that were slightly different from one another as the reanalysis native grids are not identical.

After the processing described above, the data values were bilinearly interpolated to the EASE 2.0 25km equal-area grid (used at the National Snow and Ice Data Center for its passive microwave sea ice products). This interpolation method is used because it employs a weighted average of the four nearest pixels in the original file and is better for continuous data compared to other interpolation

methods, such as nearest neighbor. Finally, each set of seasonal data across the Arctic Ocean was averaged to one number for each year, creating a time series, and plotted on a line graph with all reanalyses. The same data processing workflow was used for all the radiation components from all reanalyses.

3.3.3 Cloud Cover Calculations

Low, medium, and high cloud cover was also downloaded from CFSR, ERA5, and MERRA-2 at sub-daily timesteps and processed similarly; masking out values over land and the GIN seas, then interpolating the data to the EASE grid. These values were averaged to produce low, medium, and high cloud cover at daily, monthly and seasonal (Aug-Sept) time steps. Cloud cover is provided as either a percentage or a decimal of coverage of each grid cell. Prior to plotting values, ERA5 and MERRA-2 data were multiplied by 100 to produce whole numbers that could be compared directly to CFSR.

3.4 Reanalyses vs. Observational Datasets

3.4.1 Objectives

To refresh the reader, this portion of the analysis is aimed at further clarifying the differences and similarities between the three reanalyses and using observational data to validate the reanalysis data. Data collected in the Chukchi Sea, Beaufort Sea, and central Arctic Ocean from three separate expeditions

(SHEBA, Araon, MOSAiC) were used for comparison with fluxes from the three reanalyses discussed in Chapter 2.

3.4.2 *RV Araon* Comparison

This comparison used daily downwelling shortwave radiation values from the three reanalysis products and those collected aboard the *RV Araon* in August of 2018. *Daily RV Araon* values were then paired with the reanalysis values at closest grid node based on latitude and longitude on the original reanalysis grids. These paired values are presented in scatter plots. Mean and standard deviation of each dataset were also calculated.

3.4.3 SHEBA and MOSAiC Comparisons

Shortwave radiation and longwave radiation components were downloaded from the SHEBA and MOSAiC expeditions and paired with the reanalysis data at the closest grid node based on the original reanalysis resolutions. As with the *RV Araon* data, scatter plots are used to make comparisons between the observational datasets and the reanalyses. Means and standard deviations were also calculated.

3.5 Seasonal Heat Gain Comparisons

3.5.1 Objectives

The final aim of this dissertation is to estimate seasonal heat gain from the net surface heat flux over the Arctic Ocean as a whole and over sea ice and open water. If one can calculate a more accurate amount of heat gain in the ocean, this will be useful for improving seasonal sea ice predictions. This section of the dissertation uses previously calculated daily averages from each reanalysis to calculate heat gain values from the net surface flux for each grid node across the Arctic Ocean as well as estimates combining component fluxes from the different reanalyses, based on assessment of which fluxes from which reanalyses performed the best. This is measured using T-tests and Pearson-r correlations to determine which reanalysis has the best relationship with the observational datasets.

3.5.2 Seasonal Heat Gain Estimations

Sea ice fraction was downloaded from MERRA-2 and CFSR, hourly and 6-hourly, respectively. ERA5 provides sea ice concentration twice daily. Similar to the energy flux values, the sea ice concentrations were averaged to daily concentration values prior to subsetting. Sea ice fraction or concentration was used from each individual reanalysis because the differing parameterizations and model physics might have led to different sea ice location or concentration, between the reanalyses.

Once the daily net surface heat flux and sea ice concentration values were calculated for each grid cell, the daily net surface heat flux values were sub selected using sea ice concentration variables to separate the daily net surface heat flux values over ice and open water. Open water is defined as any grid cell that has a sea ice concentration of 15% or less in MERRA-2 and CFSR. This may introduce some complications when comparing values with ERA5 values because ERA5 considers open water at or below 20% concentration.

The daily net surface heat flux values were then summed for each month from April through August to calculate monthly ocean heat gain from the surface flux for each year. April was selected as the first month for the heat gain calculations because it is the first full month after the March sea ice extent maximum. August was selected as the end point because it is the last full month prior to the seasonal sea ice minimum in September.

After calculating monthly net surface heat flux values for each node, all values from April through August were summed to produce a seasonal net surface heat flux value and the subsets over sea ice or open water. The subsetting is done to determine what energy is potentially used to sea ice or whether it could be stored in the surface mixed layer for later in the season.

Finally, a climatology was calculated for each reanalysis which was used to calculate anomalies for each year. For each reanalysis, the net surface heat flux anomalies were averaged to one number per year; these were then used to plot 40-

year time series plots. Trends were plotted with slope lines for visual comparison (Figures 5.12-5.14).

3.6 Statistical Analyses

3.6.1 Objective

Statistical analyses were performed to quantify differences between each reanalysis and between the observations and reanalyses.

3.6.2 Statistical Analysis Details and Equations

Statistical analyses focused on the two tailed t-test and Pearson's r correlations. T-tests look at the difference between two means, can be used to test how different the reanalyses are from one another for cloud cover, the six individual surface flux components, and net surface heat flux. Statistical significance was calculated using critical t values and significance was measured at a 95% confidence interval. Maps were produced of these results. Statistical significance was calculated at 95% confidence intervals. The correlation coefficient was used to calculate the r^2 value because r often overstates the relationship when used on its own. Maps were produced of these results.

3.6.3 Direct Comparisons

For data calculated in Section 3.3, the first set of t-tests were calculated using five years of daily values from April 1st to August 31st between 1993 and 1997. This first analysis period includes 1996, which was a record-setting year for high September sea ice extent. The second set of t-tests were performed on 5 years of daily values from April 1 to August 31 between 2009 and 2013, which includes 2012, the recording setting year for low September sea ice extent. The choice of five year periods was due to limits in computational power. Detrended data were used for the correlation portion of the analysis using a 5-year climatology to largely eliminate the warming signal throughout the ~40 year record.

Tables of all means, standard deviations, t-values, correlation coefficients, r^2, and significance values can be found in Chapter 4 and Chapter 5.

For data calculated in Section 3.4, all statistical analyses were performed comparing each reanalysis to each observational dataset. The specific comparisons that were run used daily surface flux components values of upwelling and downwelling shortwave radiation, and upwelling and downwelling longwave radiation. A table of all means, standard deviations, t-values, correlation coefficients, r^2, mean difference bias, RMSE, and significance values are presented later.

Finally, for the data calculated in Section 3.5, seasonal net surface heat flux means were used in the t-test analysis. The main tests were run for the first ~20 years of the dataset (1979 or 1980 to 1999) and the last 10 years of the dataset (2008-2018). Given the strong downward trend in September sea ice extent, this

amounts to a comparison of means from years with generally low September sea ice values to years with generally high September sea ice extent, capturing the two different climates of the Arctic.

CHAPTER 4: REANALYSIS COMPARISONS

4.1 Introduction

This chapter examines downwelling shortwave and longwave radiation, upwelling shortwave and longwave radiation, turbulent fluxes, and cloud cover (total, low, medium, and high) to evaluate how each reanalysis performs relative to the others. The focus is on differences between seasonal means for the period 1993-1997 and 2007-2013 using t-tests and spatial correlations. Detailed comparisons are made with direct observations in Chapter 5, and comparisons between the three reanalyses are made here to help set the stage for Chapter 6.

4.2 Spatial Distribution

Nine variables from three different reanalyses (CFSR, ERA5, and MERRA-2) were used in this comparison across the Arctic Ocean. The following figures depict the seasonal averages from April to August 1993-1997 of downwelling shortwave radiation, downwelling longwave radiation, upwelling shortwave radiation, upwelling longwave radiation, latent heat, sensible heat, high cloud cover, medium cloud cover, and low cloud cover.

4.2.1 Radiative Fluxes

The majority of this analysis consists of comparisons of data from 1993-1997. There were not many differences between the results from 1993-1997 and results from 2009-2013, which can be found in Appendix II.

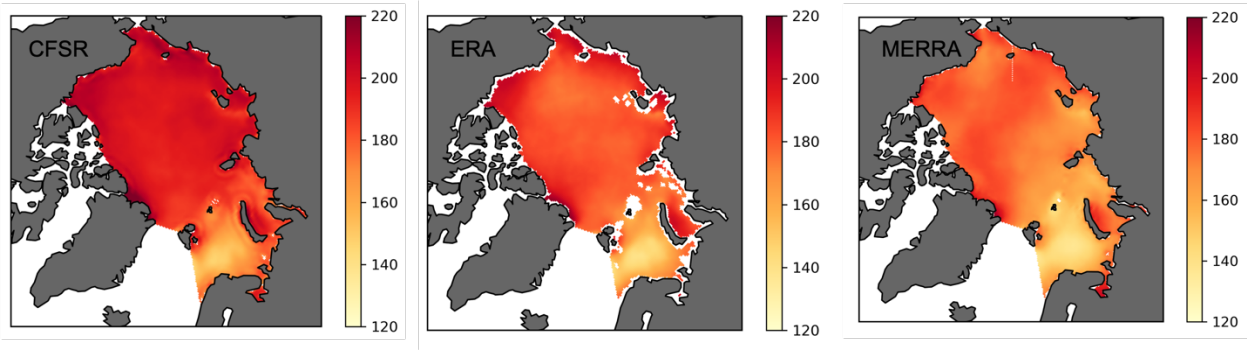

Figure 4.1: Seasonal downwelling shortwave radiation average in W/m^2 from CFSR, ERA5, and MERRA-2 between April-August 1993-1997.

Figure 4.1 shows seasonal downwelling shortwave radiation values from the three reanalyses. The downwelling shortwave radiation from the CFSR reanalysis has higher values across the entire region when compared to the other two reanalyses, which implies less cloud cover or lower optical cloud thickness in CFSR than the other reanalyses. ERA-5 is in the middle and MERRA-2 has the smallest downwelling shortwave radiation values. There are similar spatial patterns across all three products. Particularly of note is the Barents Sea, which has consistently lower downwelling shortwave values compared to the rest of the Arctic Ocean region. The Barents Sea region is known to be a particularly cloudy part of the Arctic Ocean because of frequent passage of extratropical cyclones (Serreze and Barry, 2014), which bring clouds that ultimately blocking more incoming solar radiation. A statistical analysis of these relationships is discussed later in this chapter.

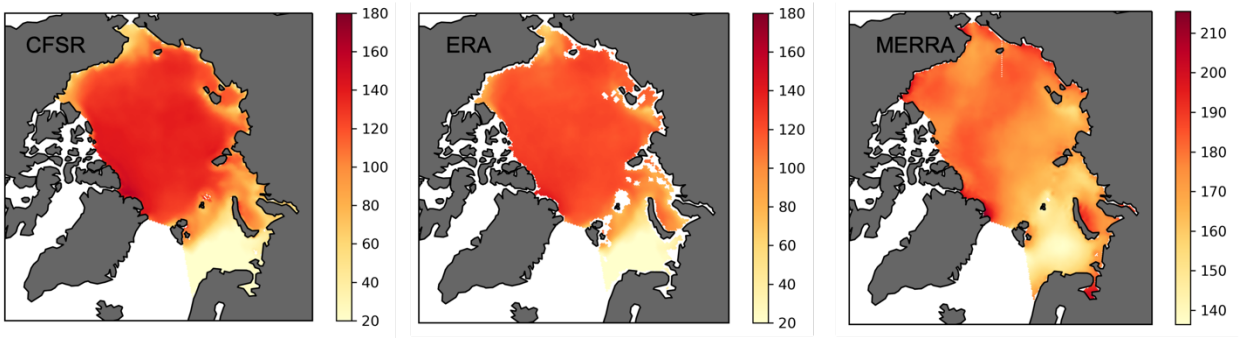

Figure 4.2: Seasonal upwelling shortwave radiation averages in W/m^2 from CFSR, ERA5, and MERRA-2 between April-August 1993-1997.

Figure 4.2 shows the upwelling shortwave radiation across the Arctic Ocean from the three reanalyses. Not surprisingly, given the large downwelling component, CFSR has the largest upwelling shortwave radiation. ERA5 again is in the middle, and MERRA-2 has the smallest upwelling shortwave radiation. The Barents Sea is the region with the smallest upwelling shortwave radiation in all of the models, which is likely related to the relatively small downwelling component in this cloudy part of the Arctic. Another factor contributing to the smaller upwelling shortwave radiation in the Barents Sea is the lower sea ice concentration that would lead to lower surface albedo; the Barents Sea usually only has seasonal sea ice, which does not cover the entire region (Serreze and Barry, 2014). Oddly, though, MERRA-2 has higher upwelling shortwave radiation values in the Barents Sea compared to CFSR and ERA5. A unique feature of MERRA-2 is there are large values of upwelling shortwave radiation directly along the coasts in Canada, the US, and Russia, that are not present in the other two reanalyses. The differences

along the coast lines in MERRA-2 are likely due to how the reanalysis parameterizes sea ice extent and the land mask MERRA-2 uses.

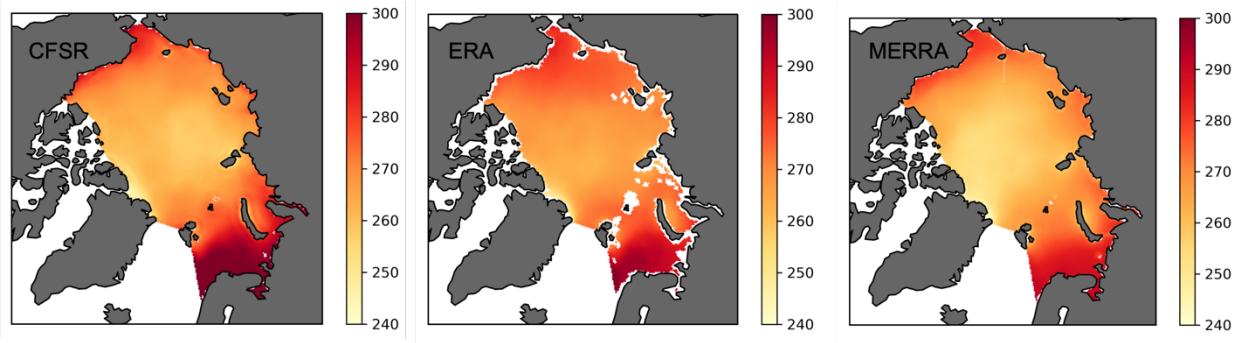

Figure 4.3: Seasonal downwelling longwave radiation averages in W/m^2 from CFSR, ERA5, and MERRA-2 between April-August 1993-1997.

The downwelling longwave radiation (Figure 4.3) patterns largely are opposite to downwelling shortwave radiation since both depend strongly on the contrasting effects of cloud cover. Generally, there is less downwelling longwave radiation across the central Arctic Ocean and more downwelling longwave radiation in the Barents Sea. This is because clouds, especially liquid water or mixed phase clouds, are effective longwave absorbers and emitters and there are more clouds in this area. Cloud phase (liquid, ice, or mixed) does not inherently impact longwave radiation because the relationship between particle size and longwave radiation is similar (Francis, 1999; Shupe and Intrieri, 2004). Shupe and Intrieri (2004) found that liquid water clouds have a larger impact on longwave radiation than clouds with ice particles because although ice clouds have larger particles, the liquid water cloud particles are more dense. Thus, cloudier regions, particularly those with liquid

water clouds, expected in the warmer parts of the Arctic like the Barents Sea, have higher values of downwelling longwave radiation.

Other important components to consider that may not be correct in the reanalyses are cloud temperature and cloud height, which play an important role in the cloud emissivity (Shupe and Intrieri, 2004). ERA5 has the largest values across the central Arctic and in the Chukchi Sea, while CFSR has the largest values for downwelling longwave radiation in the Barents Sea. CFSR's large values in the Barents Sea region suggests more thick cloud cover (or perhaps differences in cloud microphysics) compared to the other reanalyses; such differences in clouds and therefore radiation components between the reanalyses will have strong impacts on computed net surface flux.

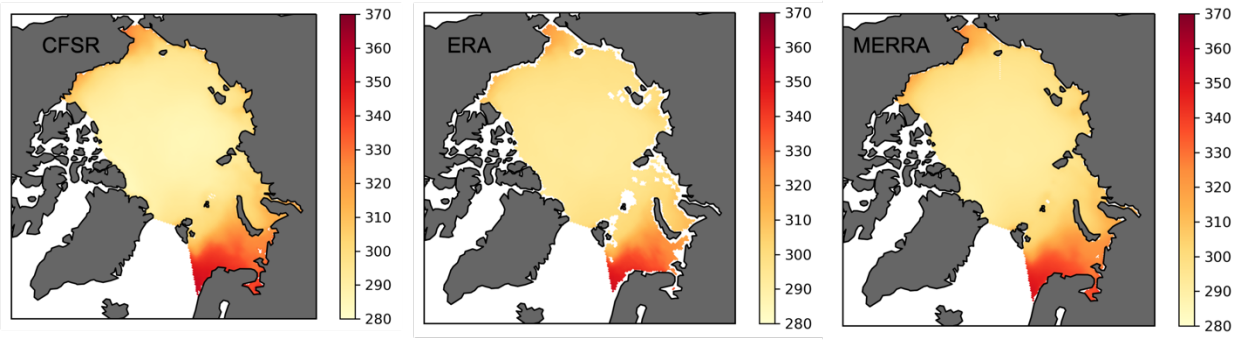

Figure 4.4: Seasonal upwelling longwave radiation averages in W/m^2 from CFSR, ERA5, and MERRA-2 between April-August 1993-1997.

Upwelling longwave radiation (Figure 4.4) shows little variation between the reanalyses and the fields are quite flat across the majority of the Arctic Ocean, with values hovering around 290-320 W/m^2. The similarity is due to the strong influence

of a melting ice surface during the summer months, when much of the surface of the Arctic Ocean remains close to 0°C. Assuming blackbody emission and a surface temperature of 0° C yields a radiation flux of 316 W/m^2, close to what is seen in Figure 4.4. The one exception is the Barents Sea which has values between 340 and 360 W/m^2; predominantly in the southern portion. This is largely different from the rest of the Arctic Ocean because there is significantly less sea ice in the Barents Sea and so the surface flux is not tied to melting sea ice but instead related to the sea surface temperature, which is higher.

4.2.2 Turbulent Fluxes

It is well documented that the turbulent fluxes -- sensible and latent heat -- are not well captured in atmospheric reanalyses (Graham et al., 2019; Zhang et al., 2023). Even direct observations have large uncertainty because they rely on surface temperature and moisture gradients (Zhang et al., 2023); observations largely depend on eddy covariance flux calculations. Figure 4.5 shows seasonal latent heat flux values across the Arctic Ocean.

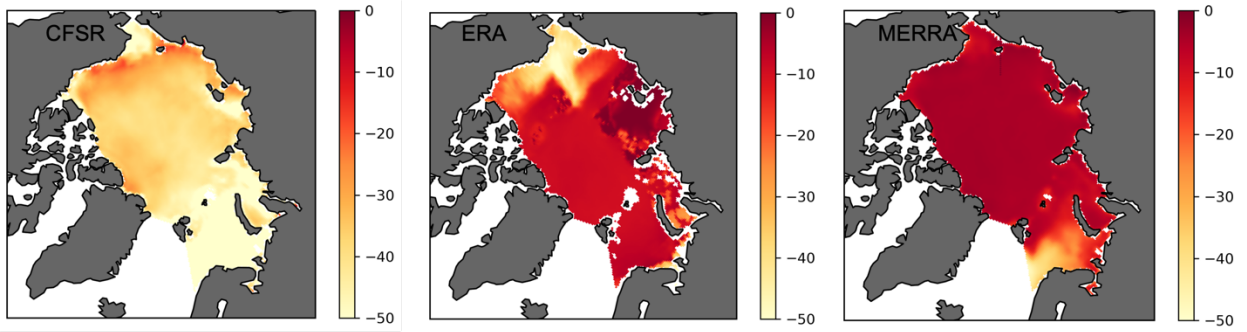

Figure 4.5: Seasonal latent heat averages in W/m^2 from CFSR, ERA5, and MERRA-2 between April-August 1993-1997.

CFSR has the greatest magnitude of negative fluxes across the Arctic Ocean with values ranging from of 30-50 W/m^2. Note that negative values indicate energy flux upward and into the atmosphere, and the negative values also indicate a decrease in specific humidity with height. At face value, these latent heat flux values seem unrealistically large given physical reasoning and when compared to SHEBA values that range from 0 W/m^2 to -7 W/m^2 (Serreze and Barry, 2014) throughout the year. Small values are expected given that the saturation vapor at the surface during melt is fixed to the value corresponding to the melting point, greatly limiting the vertical vapor gradient. Values can be larger pre-melt and post-melt, but will still tend to be greatly limited by the presence of the ice cover. ERA5 has smaller magnitude and arguably more realistic negative (upward) fluxes and shows some regional variation, especially noticeable in the Chukchi and Beaufort Seas, where open water in summer can foster a large vertical vapor gradient. However, MERRA-2, which uses basically the same ice mask as ERA5, shows more uniform values across the central Arctic Ocean. Most fluxes are negative quite small

in magnitude, though larger magnitude negative fluxes occur over the Barents Sea. In summary, there are some very large differences between the reanalysis latent heat fluxes, sometimes on the order of 30 W/m^2, which will have large impacts on the computed net surface flux.

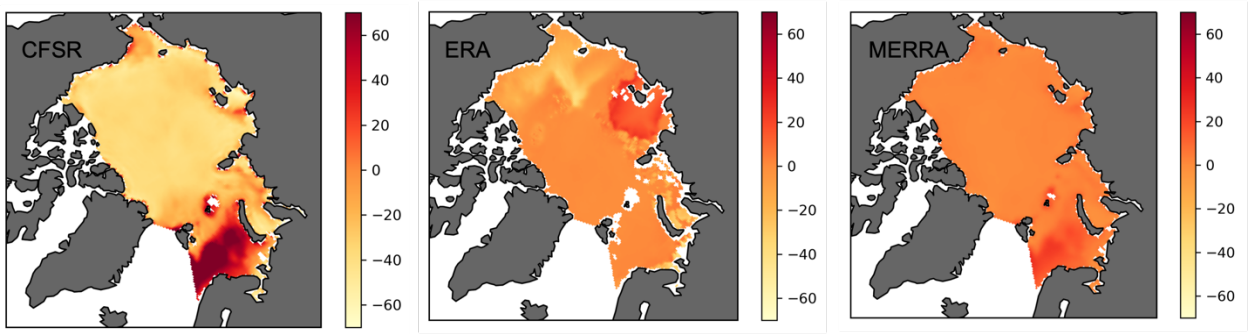

Figure 4.6: Seasonal sensible heat averages in W/m^2 from CFSR, ERA5, and MERRA-2 between April-August 1993-1997.

As seen for latent heat fluxes, seasonal sensible heat flux values (Figure 4.6) show a similar story of large differences between the three reanalyses. CFSR depicts mostly negative values (upward energy transfer) across the Arctic Ocean, yet in the Barents Sea there are moderate positive (downward energy transfer) values. CFSR has the most positive fluxes of the three reanalyses in the Barents Sea region. Positive values imply that the surface is at a lower temperature than the overlying atmosphere, i.e. there is a near surface temperature inversion. Note, in this regard in the summer months, the generally melting sea ice surface greatly limits the temperature gradient that can develop; data from SHEBA point to summer average fluxes between -2 W/m^2 and 3 W/m^2 (Serreze and Barry, 2014).

The present analysis, however, also Includes spring, forIch the sea ice temperature can be well below the freezing point such that when stronger temperature inversions (with warm air advection) could develop. ERA5 shows small negative (upward) values across most of the Arctic Ocean including the Barents Sea, which track qualitatively with the results from SHEBA. It shows stronger negative values in the Chukchi and Beaufort Seas, but positive values (downward) in the Laptev Sea. MERRA-2 shows the most homogeneity in values, which are slightly negative over most of the Arctic Ocean. This could be due to the consistency of air temperature used in the model across the Arctic Ocean or the melting sea ice holding the surface constant. Like CFSR, in the Barents Sea MERRA-2 shows slightly positive values.

Overall, for the turbulent fluxes, there is some agreement in sign and spatial distributions of the flux, largely between ERA5 and MERRA-2. CFSR stands out as very different in these values. The Barents Sea also stands out as an area that varies in between each of the reanalyses in terms of sign and magnitude of the turbulent fluxes. There are higher fluxes in the Barents Sea because the north Atlantic storm track brings warmer air up from the equator and the sea ice concentration is lower.

4.2.3 Cloud Cover

Cloud cover plays a vital role in the surface energy budget of the Arctic. Cloud cover will primarily influence differences in downwelling shortwave radiation

and downwelling longwave radiation, and subsequently the net surface flux. Scientists do not have a completely clear understanding of how clouds influence atmosphere/surface interactions because of uncertainties in cloud microphysics; th78specialpecially the case for ice clouds (Shupe et al., 2005). This is why iI is important to see how the reanalyses depict cloud cover across the Arctic Ocean.

Figure 4.7 shows the seasonal average percentage of high-level cloud cover (corresponding to cirrus, cirrostratus, and cirrocumulus). The high cloud cover ranges from ~10% to 40%. All three reanalyses are relatively similar to one another. There are a few small differences; particularly between CFSR and ERA5. CFSR has slightly smaller levels of high cloud cover compared to ERA5. These reanalysis-based cloud cover percentages are somewhat similar to observed values of cloud cover, particularly in the winter (Gryning et al., 2021).

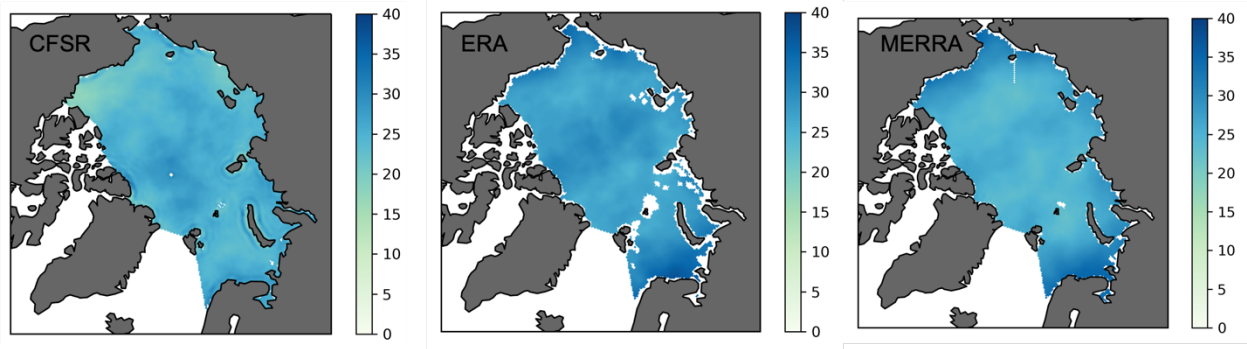

Figure 4.7: Seasonal high level cloud cover averages in percent from CFSR, ERA5, and MERRA-2 between April-August 1993-1997.

Figure 4.8 shows the seasonal average of percent medium level cloud cover (which would correspond to altostratus and altocumulus types of clouds). Overall,

medium cloud cover values range between 10% and 50%. CFSR shows the highest percentage of cloud cover across the Arctic. Regionally, the largest medium cloud cover percentages are in the Barents Sea in CFSR. ERA5 is in the middle of the three reanalyses and has fairly uniform medium cloud cover with some small regional variations. MERRA-2 has the lowest medium cloud cover by far, and there is little variation across the Arctic Ocean. As cloud cover is entirely parameterized, differences between reanalyses in cloud cover are likely due to different cloud microphysics parameterizations.

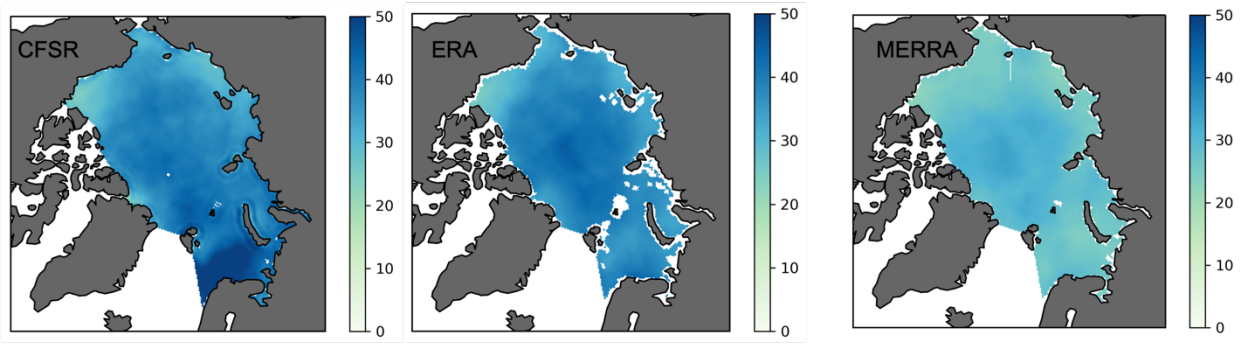

Figure 4.8: Seasonal medium level cloud cover average in percent from CFSR, ERA5, and MERRA-2 between April-August 1993-1997.

Figure 4.9 shows seasonal averages of low-level cloud cover. Low level corresponds to the lowest level Arctic stratus or fog that is prevalent in summer. Similar to medium-level cloud over, there is a wide range between the reanalyses. Values range between 50 and 100% which is a little higher than past observations show (45-75% throughout the whole year) (Serreze and Barry, 2014). Again, CFSR shows the highest low cloud percentage and there is very little variability in values

across the Arctic Ocean. MERRA-2 has the lowest values of low cloud cover across the whole Arctic, as was the case for medium-level cloud cover. Finally, ERA5 has similar values to CFSR in the central Arctic Ocean, with lower values approaching the coasts (and lower latitudes). ERA5 is the only reanalysis that has this distinctive pattern of low-level cloud cover near coasts and is likely due to the higher resolution of the results calculated in ERA5 prior to regridding.

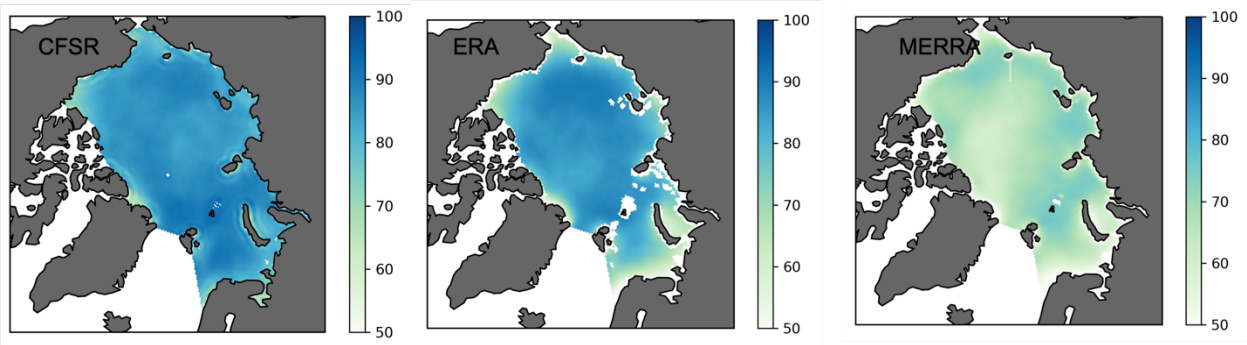

Figure 4.9: Seasonal low-level cloud cover average in percent from CFSR, ERA5, and MERRA-2 between April-August 1993-1997.

It is stressed that the comparisons between cloud cover and low, medium, and high level clouds from the reanalyses may not be direct comparisons because the reanalyses define low, medium, and high levels differently as outlined in Chapter 2. This is one area that uncertainty can be introduced in the comparison analysis.

4.3 Value Distributions

4.3.1 Radiative Fluxes

Figures that follow below show the distribution of values for each of the radiation components from the reanalyses. Some figures show the distributions of daily values between 1993-1997 and others show the distributions of daily values between 2009-2013. This is done to evaluate differences in conditions between Septembers with generally anomalously high end of summer sea ice extent (1993-1997) and Septembers with generally anomalously low end of summer sea ice extent (2009-2013).

Figure 4.10 depicts histograms for daily values for the four radiation components from the three reanalyses between 1993-1997. The overall shape of the distributions for all variables from the three reanalyses are broadly similar. There is reasonable agreement, at least in terms of distributions, between ERA5 and MERRA-2 for downwelling shortwave radiation. MERRA-2 has more low values than ERA5 and CFSR, CFSR has the highest number of values between 150-275 W/m^2. The differences between the distributions of downwelling shortwave radiation values could be due to how the reanalyses parameterize water vapor and aerosols in the air as both scatter and absorb incoming solar radiation.

In the upwelling shortwave plot, CFSR and ERA5 show many instances of very low radiation fluxes (such that downwelling shortwave must be very small, as would be the case in some areas in April), whereas MERRA-2 does not. The rest of the values share a similar distribution, except MERRA-2 has a larger number of

high values than ERA5 and CFSR. MERRA-2 has values extending up to ~400 W/m^2 while the other two reanalyses do not have any values above 300 W/m^2. The differences between the upwelling shortwave radiation values are likely due to differences in incoming shortwave radiation and the amount of sea ice cover in each reanalysis which affects albedo.

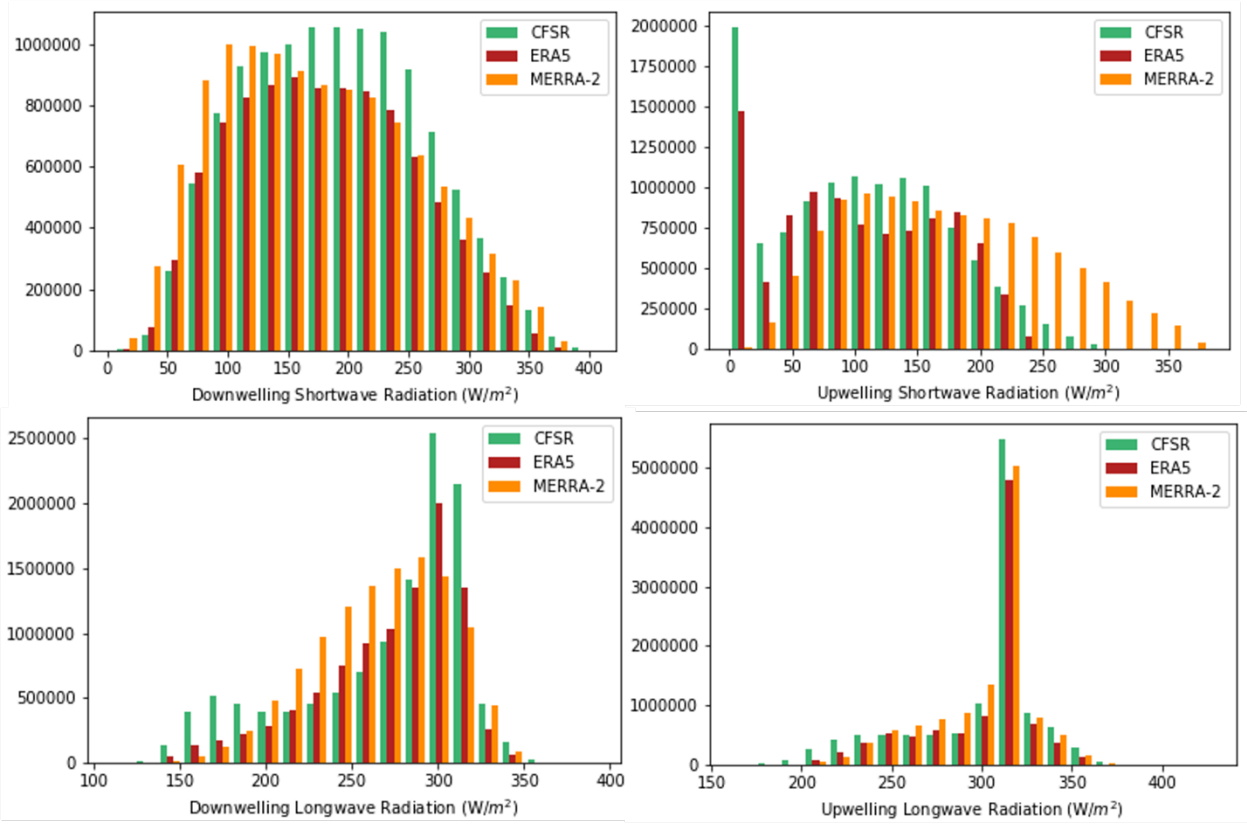

Figure 4.10: Histogram of daily radiation components across the central Arctic Ocean between April and August of 1993-1997.

The distribution of downwelling longwave radiation is sharply peaked with CFSR having more values between 150-200 W/m^2 and 300-325 W/m^2, while MERRA-2 has more values between 200-290 W/m^2. MERRA-2 likely has a lower

distribution of values for downwelling longwave radiation because of differing cloud cover and aerosol parameterizations.

Upwelling longwave distributions are very sharply peaked for all reanalyses; as discussed earlier, this points to the dominance of a melting sea ice surface in the summer months which fixes the upwelling component at 316 W/m^2 assuming blackbody emission. There are minor differences which are likely due to differences in surface cover; i.e., melting ice, melt ponds, open water, snow cover.

4.3.2 Turbulent Fluxes

Figure 4.11 shows the distribution of values of latent and sensible heat between April and August 1993-1997 across the Arctic Ocean. As expected, given the earlier discussion, most of the values are small, reflecting surface melt and (in non-melt conditions) the presence of a high concentration sea ice cover. However, there are clearly some very large outliers for both fluxes, some well over 200 W/m^2 of both positive and negative sign. CFSR has the highest occurrences of extremes between 150 W/m^2 and 400 W/m^2 in the latent heat plot; ERA5 and MERRA-2 have no values in that range. All values for MERRA-2 fall under 150 W/m^2. Very large fluxes imply large vertical temperature (for sensible heat) and vapor (for the latent heat fluxes) gradients and strong turbulence, which for upward fluxes could occur over open water in spring during a storm passage. Very large downward fluxes would require very warm advection over a cold surface. That one does not see these in MERRA-2 could reflect differences in sea ice concentration or the land masks.

The sharp peak in small values for both fluxes is in turn consistent with a melting sea ice in the summer months, which greatly limits the size of the fluxes through greatly limiting the possible magnitude of the vertical humidity and temperature gradients. There are some smaller values in CFSR and ERA5 because of little to no melting occurring in late spring (April and May).

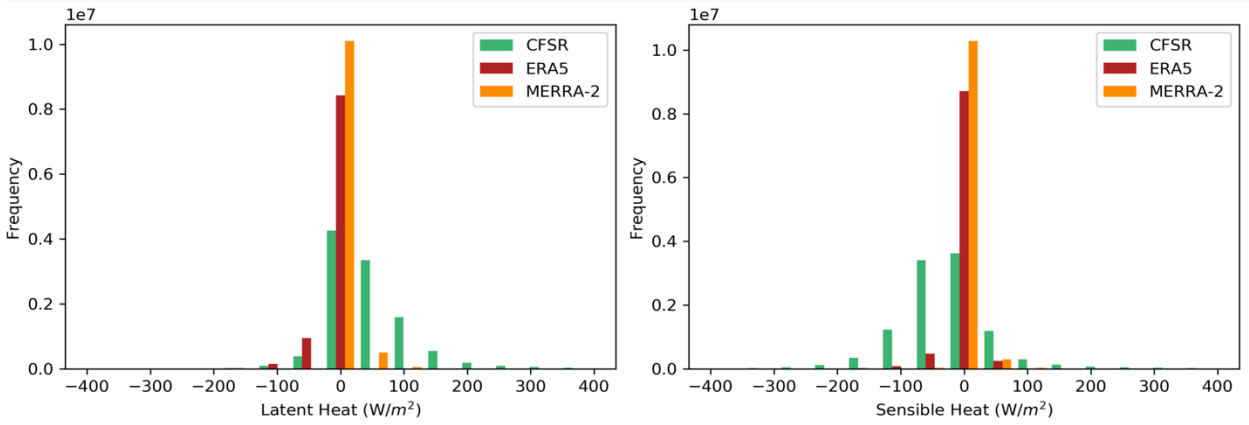

Figure 4.11: Histogram of daily turbulent components across the central Arctic Ocean between April and August of 1993-1997.

However, drawing on the spatial plots (Figures 4.5-4.6) of the turbulent fluxes, the physical modeling of some of these very sensible (as well as latent) heat large flux values must be questioned. Over an open lead and with a very cold and dry overlying air mass, or along the sea ice margin, upward (negative) fluxes of several hundred W/m^2 may occur for both the sensible and latent heat fluxes (Serreze and Barry, 2014), but such values are highly unlikely in the period of April to August over an entire grid cell let alone extensive stretches of the Arctic Ocean. Even more puzzling are the occasional large downward flux values, which would

imply a strong temperature inversion (for the sensible heat flux) and strong vapor inversion (for the latent heat flux) and strong turbulence.

4.3.3 Cloud Cover

Distribution of low, medium, and high level cloud cover from the three reanalyses between 1993-1997 are shown in Figure 4.12. Most of the high cloud cover values for the reanalyses are very small; between 0-10%. Very few are above 80%. The medium cloud cover values show a similar spike at the low values (0-10%). MERRA-2 does show larger numbers of high cloud occurrences between 17-55% when compared to the other two reanalyses. However, it shows very few values between 85-95%, while CFSR and ERA5 show much larger values. As cloud cover is entirely parameterized, this is likely due to modeling differences in each reanalysis.

Lastly, low cloud cover shows very low distributions of values below 90% cloud cover; although MERRA-2 does show higher values at all levels except between 90-100% cloud cover compared to CFSR and ERA5. CFSR has the highest values of low cloud cover between 90-100%. The differences between distributions in cloud cover are largely impacting the observed differences in the radiation component distributions. CFSR has the largest amount of low cloud cover and that could be contributing to the highest values of downwelling longwave.

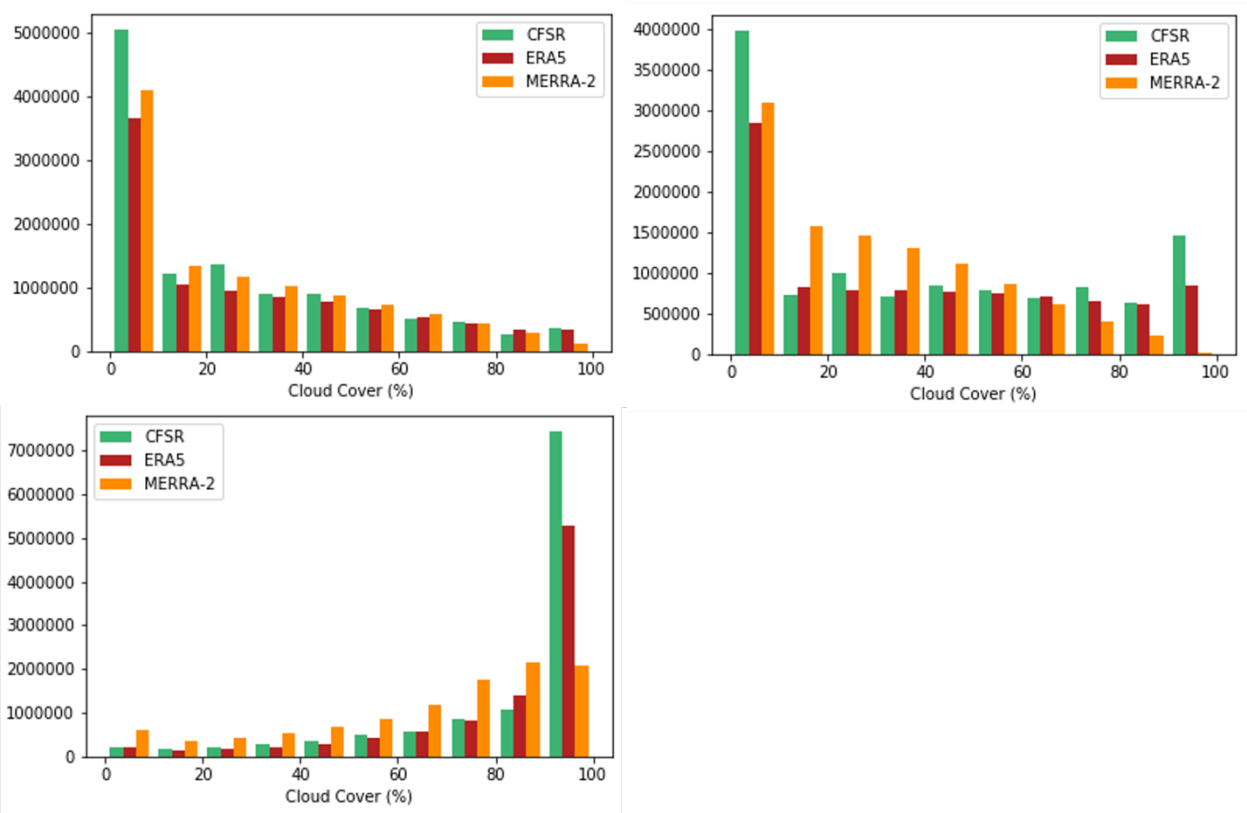

Figure 4.12: Histogram of daily cloud cover (high-top left, med-top right, low-bottom) central Arctic Ocean between April and August of 1993-1997.

4.4 Further Statistical Analysis

Digging further into the statistics the following sections identify areas of significant difference (at 95% confidence interval), based on the t-test method described in Chapter 3. Table 4.1 summarizes comparisons for all the daily surface radiation values, turbulent fluxes, and cloud cover values between each reanalysis. Trends were calculated and removed in order to get a clearer picture of the underlying relationships between the reanalyses. Figures 4.13-4.16 show the relationships between the means and the correlations between all reanalyses from the detrended data. Figures showing the cloud relationships are relegated to

Appendix II as the differences are largely insignificant between the means between each reanalysis.

4.4.1 CFSR Compared to ERA5

The maps comparing downwelling shortwave radiation from CFSR and ERA5 reveal significant differences at the 95% confidence interval in the means across the majority of the Arctic Ocean, with the largest differences in the Chukchi and Beaufort Seas (Figure 4.13). The red colors indicate that CFSR values are higher than those for ERA5, while blue means CFSR values are lower than ERA5. Upwelling shortwave radiation differences are again statistically significant across nearly all the Arctic Ocean. Downwelling longwave radiation shows that there are fewer points with significant differences between the means compared to the shortwave radiative components. There is a large area north of Canada and in the central Arctic Ocean with no significant differences. Statistically significant differences in upwelling longwave radiation cover most of the Arctic Ocean, and nearly everywhere ERA5 has higher values than CFSR.

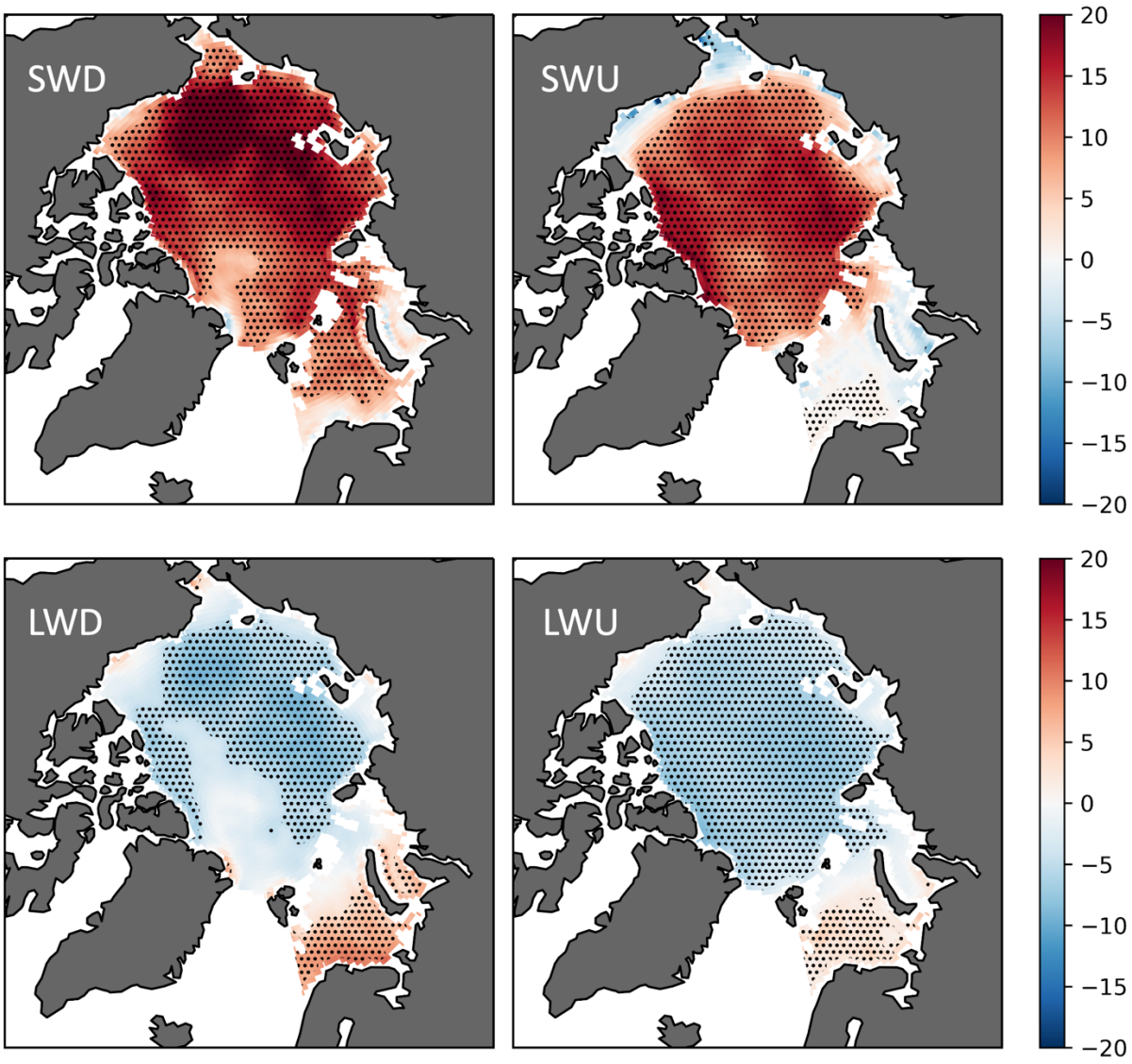

Figure 4.13: Differences between CFR and ERA5 (in continuous color) in W/m² and statistical significance at the 95% confidence interval (points) for downwelling shortwave radiation (SWD), upwelling shortwave radiation (SWU), downwelling longwave radiation (LWD), and upwelling longwave radiation (LWU) from daily values from April-August between 1993 and 1997 for CFSR and ERA5.

Recall that based on the spatial plots of means, there appeared to be little difference between the reanalysis in the upwelling longwave components due to effects of melting sea ice in the summertime. However, the results in Figure 4.13 show while the differences in seasonal means are not large, the differences are

significant. This likely largely represents differences early in the season when the ice is still frozen since once melting occurs both reanalyses surface temperatures will remain at the melting point.

One important piece to take into consideration is whether these datasets violate any potential dependencies for the T-tests and Pearson-r correlation tests. A Kwiatkowski–Phillips–Schmidt–Shin (KPSS) test is used to test for stationarity and it is assumed that the null hypothesis is that the data is stationary. Looking at the results from this test for all detrended radiation components confirmed that the data was not stationary, and the statistics varied through time; the KPSS statistics were a larger than the critical value at 1% (0.739) and p-values (0.01) were significant at the 99% confidence level.

An autocorrelation analysis was conducted to better understand whether the detrending eliminated the seasonal impacts. Durbin Watson (DW) tests were conducted on the detrended radiation variables from each reanalysis. Based on the results of these tests, the autocorrelation is highly spatially variable (Appendix II – Figures 17-19). Values near two mean that there is little to no autocorrelation while values closer to zero mean positive autocorrelation. The downwelling shortwave radiation for CFSR shows many areas of little autocorrelation after detrending. Upwelling shortwave radiation and downwelling longwave radiation show large areas of positive autocorrelation and upwelling longwave radiation results show positive correlation across the entire study domain. ERA5 shows similar patterns of

autocorrelation as CFSR. The spatial variability in autocorrelation is likely due to the variability in surface radiation values.

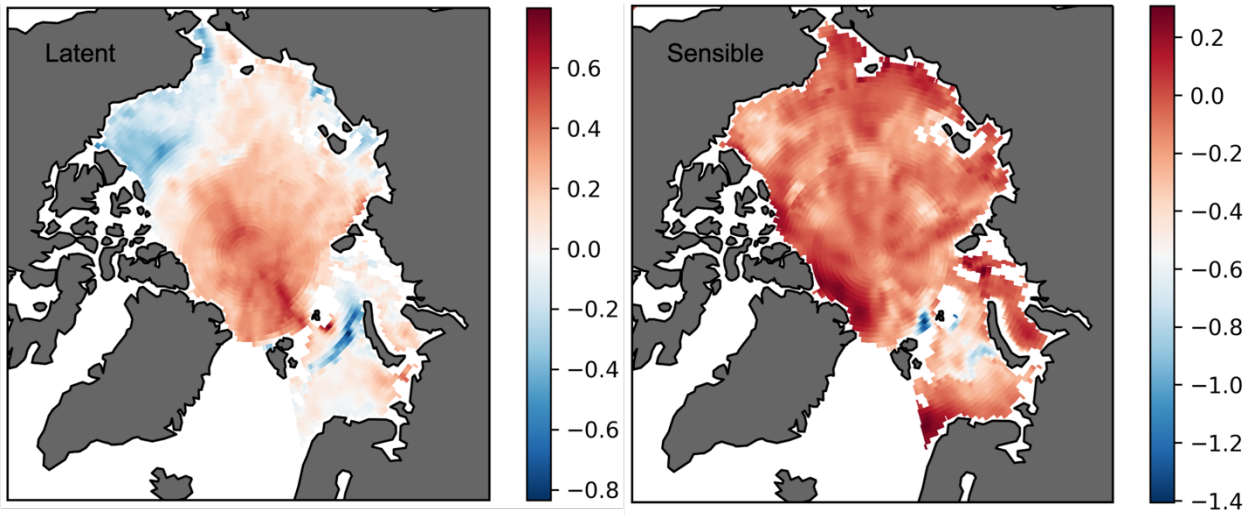

Figure 4.14: T-test results (continuous color) and statistical significance at the 95% confidence interval (points) for latent and sensible heat flux from CFSR and ERA5 from daily values from April-August between 1993 and 1997.

The results from the T-tests for latent and sensible heat from the CFSR and ERA5 comparison, show no significant differences across the entire study region (Figure 4.14); looking back at Figure 4.4 and 4.5 this seems surprising given the obvious differences in the means between the two products over large part of the ocean. In explanation, since the T-tests are run on detrended data, the observed differences are likely in trend differences, instead of in the underlying data. It could also be due to the larger variances that are seen in the latent and sensible heat fluxes making it very hard to determine statistical significance.

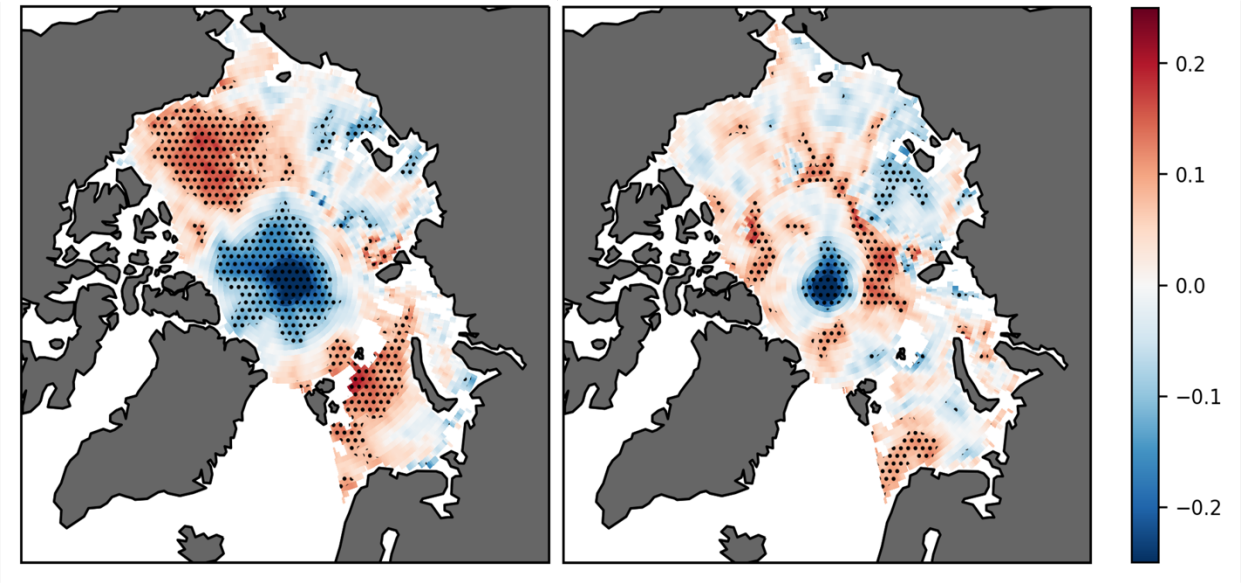

Figure 4.15: Pearson-r correlations (continuous color) and statistical significance at the 95% confidence interval (points) for latent (left) and sensible (right) heat flux from CFSR and ERA5 from daily values from April-August between 1993 and 1997.

There are nevertheless some areas where there are significant spatial correlations between the time series (Figure 4.15). The sensible heat correlations are positive in most of the Arctic Ocean, though only significantly positive at the interface between the central Arctic Ocean and the marginal seas and in the Barents Sea. The latent heat flux correlations are also positive in most locations, and significantly positive in the Beaufort and Barents Seas. These positive correlations mean that both model values increase or decrease at the same time. However, both latent heat and sensible heat show significantly negative correlations in the central Arctic Ocean; latent heat has a larger area of significantly negative correlation in the central Arctic Ocean. The negative correlations mean that the values from CFSR and ERA5 are inversely related; as one model value increases, the other model value decreases.

The correlations for cloud cover all show statistical significance across the whole Arctic Ocean; figures are in Appendix II. All radiation correlations are significantly positive at the 95% confidence interval; all figures can be found in Appendix II. The turbulent fluxes in Figure 4.15 both have regions that are significantly positively correlated and significantly negatively correlated at the 95% confidence level.

4.4.2 CFSR Compared to MERRA-2

Figure 4.16 shows the statistics of the differences between CFSR and MERRA-2 for the radiation fluxes. Red indicates that CFSR has higher values, while blue indicates that CFSR has lower values. T-tests for upwelling and downwelling shortwave radiation reveal significant differences between the two reanalyses across the entire Arctic Ocean (Figure 4.16). For upwelling and downwelling shortwave radiation, CFSR has higher fluxes across the majority of the Arctic Ocean minus a swath across the western central Arctic Ocean for downwelling shortwave radiation. In contrast, upwelling and downwelling longwave radiation have statistically significant differences only in the central Arctic Ocean and upwelling longwave radiation differences are also significant in the surrounding marginals seas. For downwelling longwave radiation, there is a strip northwest of Greenland with significant differences between CFSR and MERRA-2 and differences are significant in the Barents Sea as well, which is consistent across many T-test figures. Since large amounts of energy are transported in the ocean and

the atmosphere along the north Atlantic storm track ending in the Barents Sea, being able to quantify that energy fluxes and their impacts on the upwelling and downwelling longwave radiation and turbulent fluxes is a challenge.

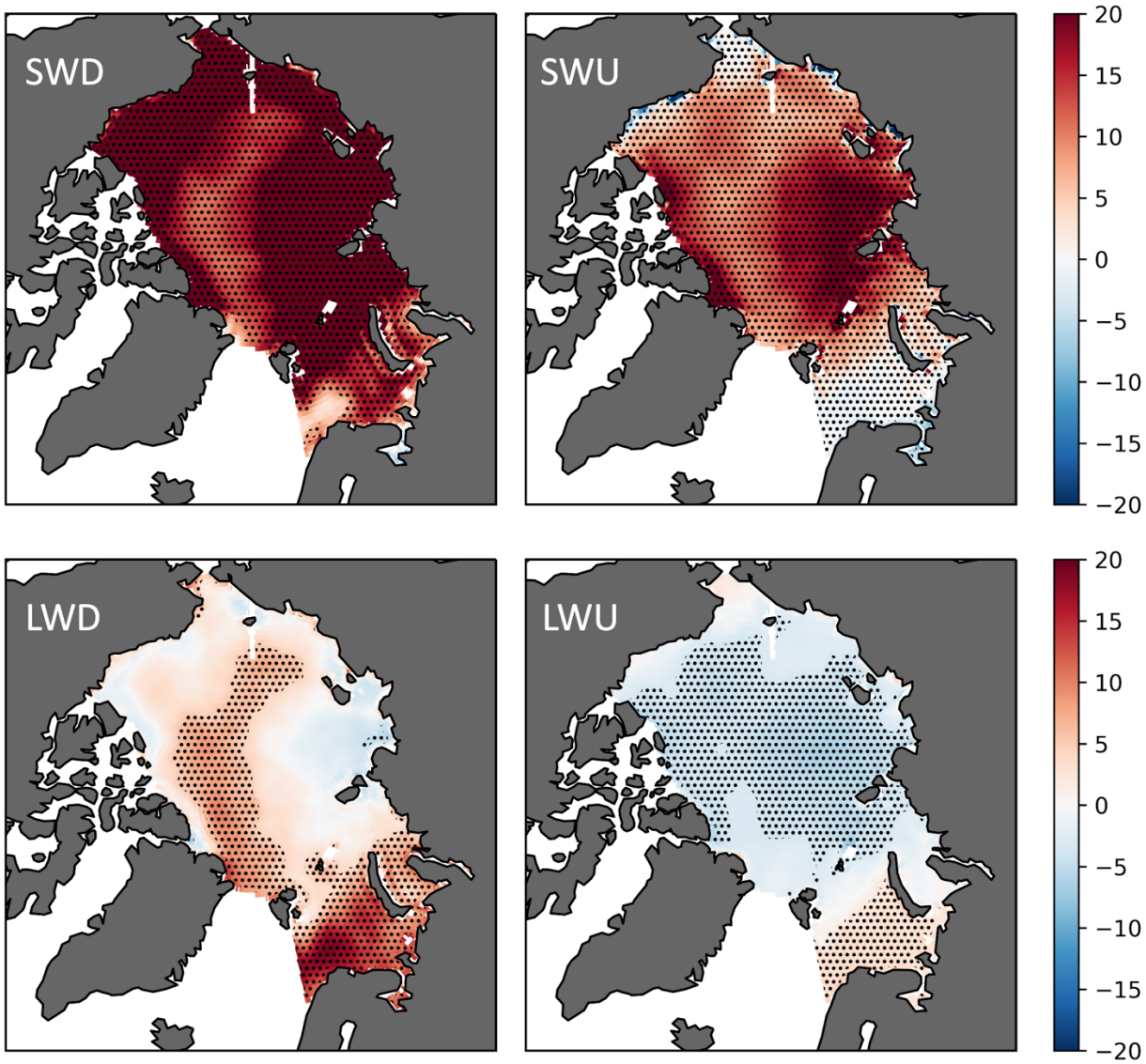

Figure 4.16: Differences between CFSR and MERRA-2 (in continuous color) in W/m^2 and statistical significance at the 95% confidence interval (points) for downwelling shortwave radiation (SWD), upwelling shortwave radiation (SWU), downwelling longwave radiation (LWD), and upwelling longwave radiation (LWU) from daily values from April-August between 1993 and 1997 for CFSR and MERRA-2.

Again, an important thing to consider statistically is whether these datasets violate any potential dependencies for the statistical tests used. The results from the KPSS test for all detrended radiation components show that the data was not stationary, and the statistics varied through time; the KPSS statistics were a larger than the critical value at 1% (0.739) and p-values (0.01) were significant at the 99% confidence level. The autocorrelation results for MERRA-2 are largely like CFSR and ERA5 with one exception. Upwelling shortwave radiation autocorrelation spatial patterns look the same as the downwelling shortwave autocorrelation spatial patterns – showing that the majority of the study domain has little to no autocorrelation.

The CFSR and MERRA-2 cloud cover comparisons yield results similar to those between CFSR and ERA5. There are no significant differences between the cloud cover means at any level (Figure 4.17), likely meaning that there is a high variance. The turbulent flux data also does not show any significant differences between the means from CFSR and MERRA-2 (Figure 4.18).

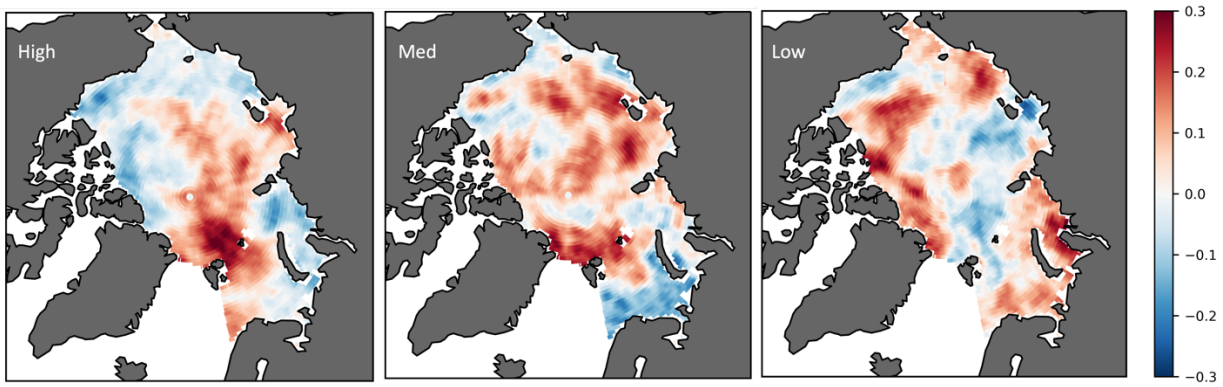

Figure 4.17: T-statistics (in continuous color) and statistical significance at the 95% confidence interval (points) for high level, medium level, and low level cloud cover from April-August between 1993 and 1997 for CFSR and MERRA-2.

All turbulent flux correlations have a mix of positive and negative statistically significant regions between CFSR and MERRA-2; figures can be found in Appendix II.

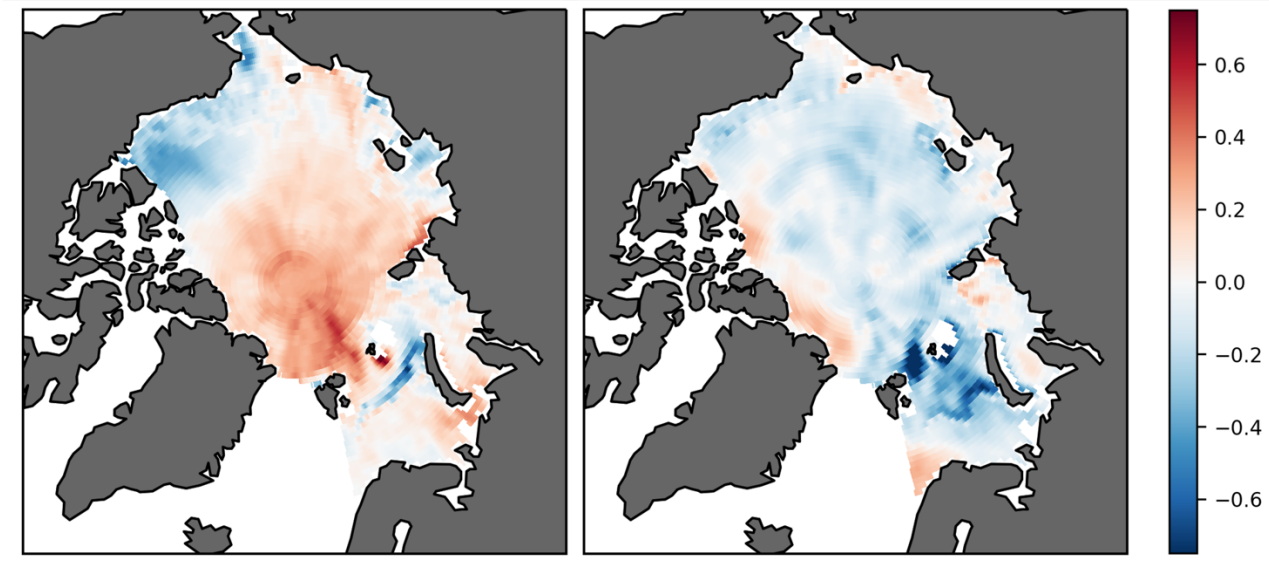

Figure 4.18: T-test results (continuous color) and statistical significance at the 95% confidence interval (points) for latent (left) and sensible (right) heat flux from CFSR and MERRA-2 from detrended daily values from April-August between 1993 and 1997.

4.4.3 ERA5 Compared to MERRA-2

Figure 4.19 shows the T-test results for the four radiative components. Similar to the results for CFSR and MERRA-2, there are statistically different downwelling shortwave radiation values across most of the Arctic Ocean and marginal seas. The majority of the T-statistics values from downwelling shortwave radiation are positive, meaning higher fluxes in ERA5, but negative values dominate in the Barents Sea meaning less incoming shortwave radiation in this region in ERA5. The upwelling shortwave radiation plot shows significant differences in means in the marginal seas but insignificant differences over the central Arctic Ocean. Downwelling longwave radiation has significantly different means across the region with the only insignificant points located along the coasts. For longwave radiation, most significant differences in red, meaning larger incoming longwave radiation values for ERA5. The T-statistics in the region showing statistical significance have values for the differences that range between 4-6 W/m^2 above the sample variances. Lastly, upwelling longwave radiation means show few significant differences across most of the Arctic Ocean, implying that ERA5 and MERRA-2 have close to the same surface (skin) temperatures. The similar upwelling longwave radiation values between MERRA-2 and ERA5 contrast with the previous comparisons between reanalyses, which did have significant differences in this field and show that CFSR values are likely an outlier from the other two reanalyses. There are three small areas of significant differences along the coast of Greenland and the northern Canadian archipelago, in the Barents Sea, and in the East Siberian Sea.

The results from theKPSS tests for all detrended radiation components show that the data was not stationary. The KPSS statistics were larger than the critical value at 1% (0.739) and p-values (0.01) were significant at the 99% confidence level. With that said, it's important to note the non-stationarity as the past values in the models may not be representative of the future values; and this applies to all of the reanalysis data for all radiation components.

Figure 4.20 reveals significantly different detrended values in the central Arctic Ocean for latent and sensible heat between MERRA-2 and ERA5. For latent heat, significant differences are mostly positive, meaning higher values for ERA5. The exception is the area near the pole. Significant differences for the latent heat flux are a mix of positive and negative. In terms of magnitude, differences in the turbulent latent heat flux between the two reanalyses range upwards of 10 W/m^2.

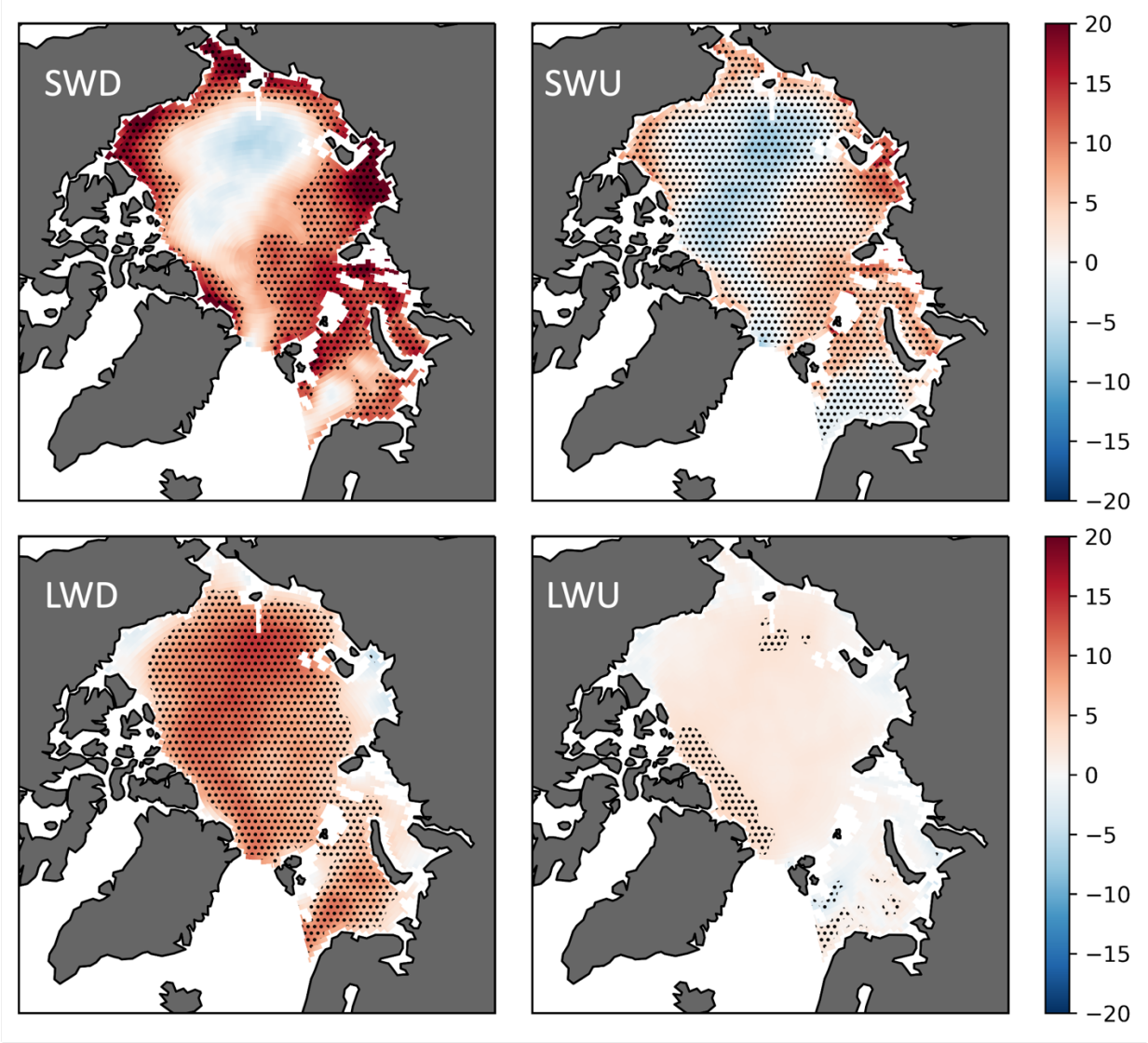

Figure 4.19: Differences between ERA5 and MERRA-2 (in continuous color) in W/m^2 and statistical significance at the 95% confidence interval (points) for downwelling shortwave radiation (SWD), upwelling shortwave radiation (SWU), downwelling longwave radiation (LWD), and upwelling longwave radiation (LWU) from daily values from April-August between 1993 and 1997 for ERA5 and MERRA-2.

The T-test results from the ERA5 and MERRA-2 comparison are very similar to those from the CFSR and MERRA-2 comparison. For latent heat, Figure 4.15 from the CFSR and ERA5 comparison shows similar significant differences over the central Arctic Ocean and some in the surrounding marginal seas (Beaufort and

Barents Seas). The sensible heat results in both comparisons shows a different pattern, with many smaller, patchy significantly different areas across the whole Arctic Ocean.

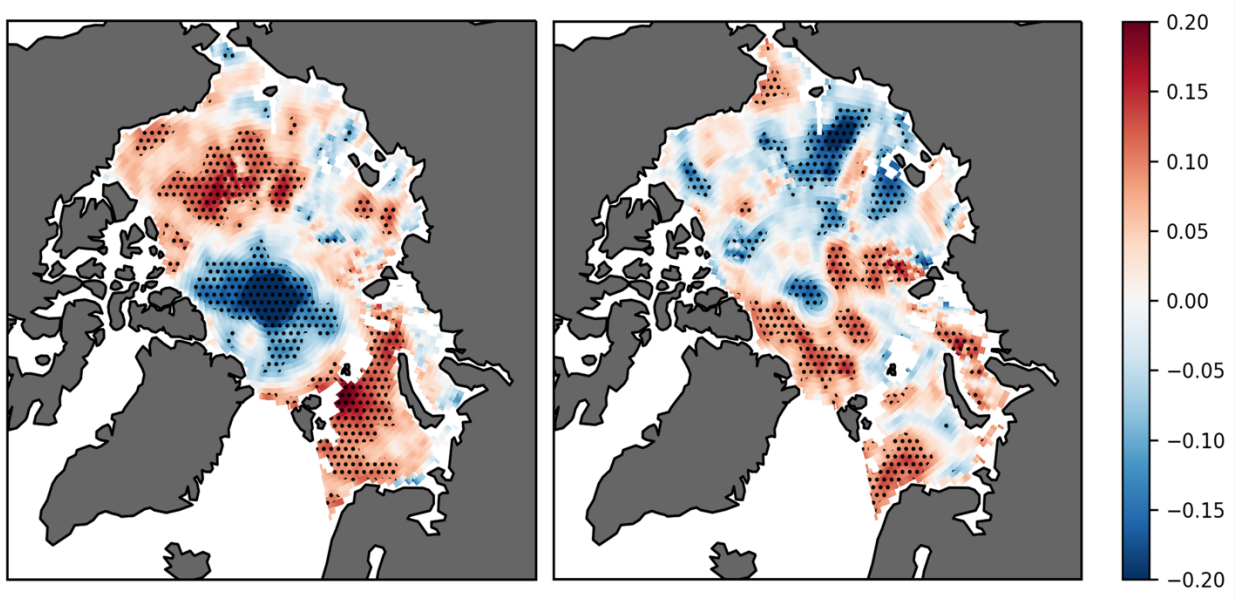

Figure 4.20: Pearson-r correlations (continuous color) and statistical significance at the 95% confidence interval (points) for latent (left) and sensible (right) heat flux from ERA5 and MERRA-2 from daily values from April-August between 1993 and 1997.

By contrast, the turbulent flux values from each reanalysis show no significant differences in the means. Nevertheless, the spatial fields are well correlated with each other. The statistics reveal no significant differences between the cloud cover means from each reanalysis but again there are significant spatial correlations between each dataset. This is somewhat unexpected as there are differences in shortwave radiation, longwave radiation, and cloud cover as seen in Figure 4.1 - Figure 4.4, Figure 4.8, and Figure 4.10.

All correlations have a mix of positive and negative statistically significant regions between CFSR and MERRA-2; figures can be found in Appendix II.

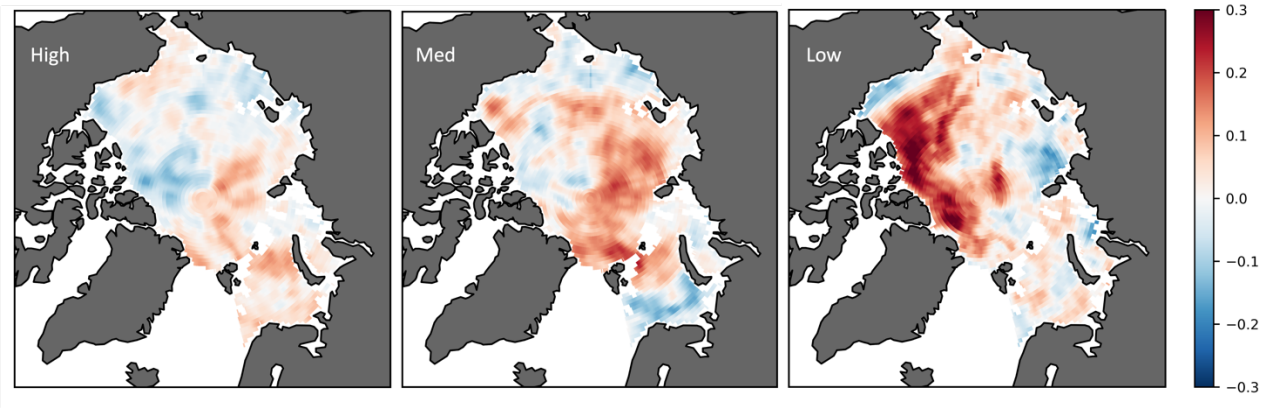

Figure 4.21: T-statistics (in continuous color) and statistical significance at the 95% confidence interval (points) for high level, medium level, and low level cloud cover from April-August between 1993 and 1997 for ERA5 and MERRA-2.

Figure 4.21 shows the T-statistics for high level, medium level, and low level cloud cover between 1993 and 1997 comparing ERA5 and MERRA-2. At the 95% confidence level there are no significant differences between the means in cloud cover at all levels, likely meaning there is also a high variance for the cloud cover data from these two sources. All correlations are statistically significant across the whole Arctic for cloud cover and those figures are in Appendix II.

4.5 Discussion

4.5.1 Spatial Distribution

While it is already apparent that there are concerns with the reanalysis turbulent heat fluxes based on the differing signs and magnitudes between reanalysis products, and unrealistically large outliers compared to available observations, it is clear from the results presented so far that depictions of most other fluxes also differ considerably between reanalyses. Comparisons with published data from SHEBA will be explored more fully in Chapter 5.

To summarize, CFSR has the highest values for both upwelling and downwelling shortwave radiation. If there is more downwelling shortwave radiation in CFSR model, there will be more shortwave radiation reflected back (upwelling shortwave radiation) to the atmosphere and out to space if the surface albedo is similar compared to the other reanalyses. MERRA-2 has the lowest values of both downwelling and upwelling shortwave radiation. Using the same reasoning, it makes sense that if there is less solar insolation reaching the surface in MERRA-2, there is also less sunlight to reflect back to the atmosphere and space. Even though there are statistically significant differences between the three reanalyses, basic patterns of upwelling and downwelling shortwave radiation, the patterns of incoming and outgoing energy agree with each other. There are also significant positive spatial correlations in the shortwave terms between the reanalyses, meaning that they are capturing similar day to day variability.

Longwave radiation distributions tell a different story. ERA5 has the highest values of downwelling longwave radiation across the central Arctic Ocean and the Chukchi Sea while CFSR has the highest values in the Barents Sea. The differences in longwave radiation most likely reflect differences in cloud cover amount and microphysics and atmospheric water content. Cloud cover differences will also affect the shortwave components through albedo effects as well as cloud absorption. In general, more low-level clouds or regions with more liquid water in the clouds will have higher values of downward longwave radiation. Thus, the longwave radiation fields suggest ERA5 has the most low level cloud cover over the Arctic, while CFSR has the most clouds in the Barents Sea. However, this result is a little different from the implications of the downwelling shortwave radiation results, which suggest MERRA-2 may be the cloudiest reanalysis rather than ERA5, as implied by downwelling longwave radiation. But the cloud cover analysis also shows that MERRA-2 has the least cloud cover. One reason for this difference may be related to different liquid water contents, cloud temperatures, and cloud heights in the clouds rather than just the percentage of cloud cover. A deeper dive into the differences in cloud microphysics would be needed to clarify these inconsistencies.

As with the shortwave terms, spatial correlations between the reanalyses in the downwelling component are still often fairly high and significant, indicating similar depictions in day-to-day variability. Upwelling longwave radiation patterns are similar between the reanalyses, and this is consistent with the effects of a melting sea ice surface in summer. However, there are statistically significant

differences which tend to be driven by the colder months (April and May) when the surface is still frozen.

CFSR shows a wide distribution of large negative values of the two turbulent fluxes across the majority of the Arctic, yet it has positive (downward) values of sensible heat in the Barents Sea, likely a result of the fairly warm open water surface found here in summer. ERA5 and MERRA-2 have more similar turbulent heat flux values with many regions showing small negative values or values of zero. However, as noted, some of the flux values appear unrealistically large compared to published summer estimates based on the SHEBA expedition (Persson et al., 2002) and raise prominent red flags about reanalysis representation of turbulent fluxes. The following chapter addresses comparisons between the reanalyses and observations in detail.

The raw spatial distribution of seasonally averaged cloud cover values shows that over the Arctic Ocean CFSR has the highest percent cover of medium and low cloud cover and MERRA-2 has the lowest values. The clouds in these reanalyses are entirely parameterized, but Arctic clouds are still not well understood and this analysis shows significant differences and/or flaws in these parameterizations for each reanalysis. High cloud cover appeared to have the same values across all reanalyses. This does not fit with the hypothesis that differentiation in cloud cover in each reanalysis is causing the differences between the radiative and turbulent fluxes.

An additional note is that cloud cover, although important to the climate system, is not the best variable for understanding the cloud-radiation interaction. Cloud optical thickness, total column cloud liquid water, and total column cloud ice water must be examined to caption clouds' relationships with downwelling radiation and turbulent fluxes. This may be the case because these variables are able to share more information about the moisture content and thickness of the cloud cover. These two pieces of information are vital for looking at the impacts on radiation and turbulent fluxes.

4.5.2 Statistical Comparisons

Many of the tests show that there are significant differences in many of the surface energy flux components from each reanalysis across the Arctic Ocean. This is likely due to the differences in model physics and parameterizations of atmospheric characteristics. These statistical tests were run on detrended data to examine the relationships that underlie any trends in the data. Since there is a good grasp of the amount of incoming solar radiation at the top of the atmosphere, it was expected that the downwelling shortwave radiation would have the most similarities between all the reanalyses, yet that is the one component with the most notable differences.

Although there were some obvious differences in the quantities of cloud cover discussed in section 4.3.3, there was an absence of statistical significance in all of the cloud cover T-test results at all levels (low, medium, and high). It is possible that the detrended data did not have differences in the quantity of values and that

is why the results from the T-tests did not show any significance. Additionally, only cloud coverage fraction was used in this analysis because it impacts optical properties and longwave radiation. There may be statistical significance if liquid water path was used as well.

In conclusion, there are differences between CFSR, ERA5, and MERRA-2 in many of the components that are used to calculate the surface energy flux or affect those components. Many of those differences are presumably driven by model parameterization differences, particularly focusing on different values for atmospheric water vapor, aerosols, and surface characteristics like open ocean and sea ice. To get a clearer picture of how accurate any of the model values are, in Chapter 5, the reanalysis data is compared more closely to observational datasets taken aboard several ship-based field campaigns across the Arctic Ocean.

CHAPTER 5: OBSERVATION VS. REANALYSIS COMPARISON ANALYSIS

5.1 Introduction

This chapter focuses on direct comparisons with available surface observations using data collected in 1998 (SHEBA), 2018 (RV Araon), and 2020 (MOSAiC). For these comparisons between reanalyses that have grid cells encompassing a relatively large area (hundreds of square kilometers) and data taken at a single point, comparisons are made between the observations to the reanalysis data at the closest grid node to the location and the same time the observations were taken.

5.2 Radiation Terms

To help set the stage, Figure 5.1 shows the difference in values of downwelling and upwelling daily shortwave radiation (left and right, respectively) from SHEBA and the three reanalyses along the SHEBA ship track. The ship track for SHEBA starts on the northern edge (top) of the figure panels beginning in April 1998 and ends at the bottom of the figure panels in August. Although there are many locations where the differences are negligible, the daily upwelling shortwave radiation values from the reanalyses and SHEBA in Figure 5.1 have distinct differences between 76°N and 78°N. As the SHEBA expedition traveled south and east the downwelling shortwave radiation differences from all the datasets had values between -100 W/m^2 and 150 W/m^2.

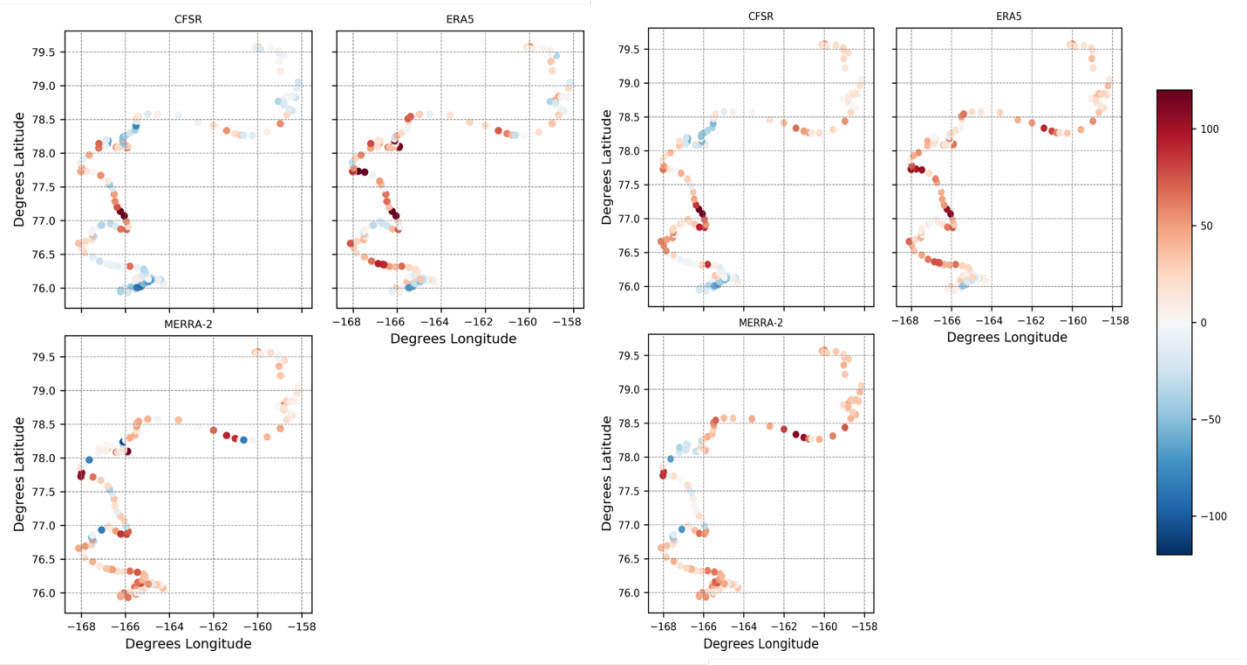

Figure 5.1: Daily downwelling shortwave radiation (left) and upwelling shortwave radiation (right) difference values in W/m² from SHEBA, ERA5, CFSR, and MERRA-2 between April and August 1998 along the SHEBA ship track.

The raw shortwave flux plots (not shown) are visually similar for all datasets. This simply follows from seasonality - values for all increase from April through June as the solar declination becomes more positive and thereafter declines in all datasets. In turn, some of the upwelling shortwave radiation values during April show small differences because the sea ice has not yet started to melt such that the surface albedo is high and fairly uniform.

Turning back to Figure 5.1, as the expedition continued, ERA5 and MERRA-2 show upwelling shortwave radiation difference values that are more different than SHEBA and CFSR shows more upwelling radiation similarities when compared to the SHEBA data. This is likely due to the onset of melt across the region where the SHEBA expedition took place and the change of surface albedo due to snow and ice

melt[3]. CFSR, additionally shows fewer differences in downwelling shortwave radiation which could relate to the similarities between the two datasets in upwelling shortwave radiation. Since SHEBA was taking measurements on the surface of the ice, it was able to capture upwelling shortwave radiation responses to finer surface details, like melt pods, open water, and thin ice unlike the reanalyses. Each reanalysis is working with parameterized data on larger resolutions rather than small scale surface details, ultimately resulting in values that do not agree with the observational dataset.

Figure 5.2 shows downwelling and upwelling longwave radiation differences between the reanalyses and SHEBA. Differences from SHEBA range between -70 W/m^2 and 70 W/m^2. Recall from Chapter 4 that there are fairly large differences between each of the reanalyses for both of these variables (150 - 350 W/m^2). That said, there could be variation between the four data sources during the temporally and spatially limited SHEBA time period. Note that small differences in the upwelling longwave radiation field may be because upwelling longwave radiation is closely linked to the surface temperature. Once melt onset begins in the late spring/early summer the surface temperature remains nearly constant at the melting point (0° C), so differences in upwelling longwave radiation difference values will be small as all reanalyses and observations correspond to surface melt conditions. It is expected that there will be larger differences between the four

[3] Snow cover is parameterized in all reanalyses. Sea ice is parameterized in CFSR and ERA5, although ERA5 has a 4 layer interactive model (Saha et al., 2014; Hersbach et al., 2010). Sea ice in MERRA-2 is based on daily satellite records (Gelaro et al., 2017).

datasets in the downwelling longwave radiation plots (left) because downwelling longwave radiation is closely linked to clouds. Cloud cover is parameterized in each reanalysis differently, yet there are large differences in downwelling longwave radiation during the SHEBA period, which implies that cloud cover and its radiative properties are similar in the reanalyses.

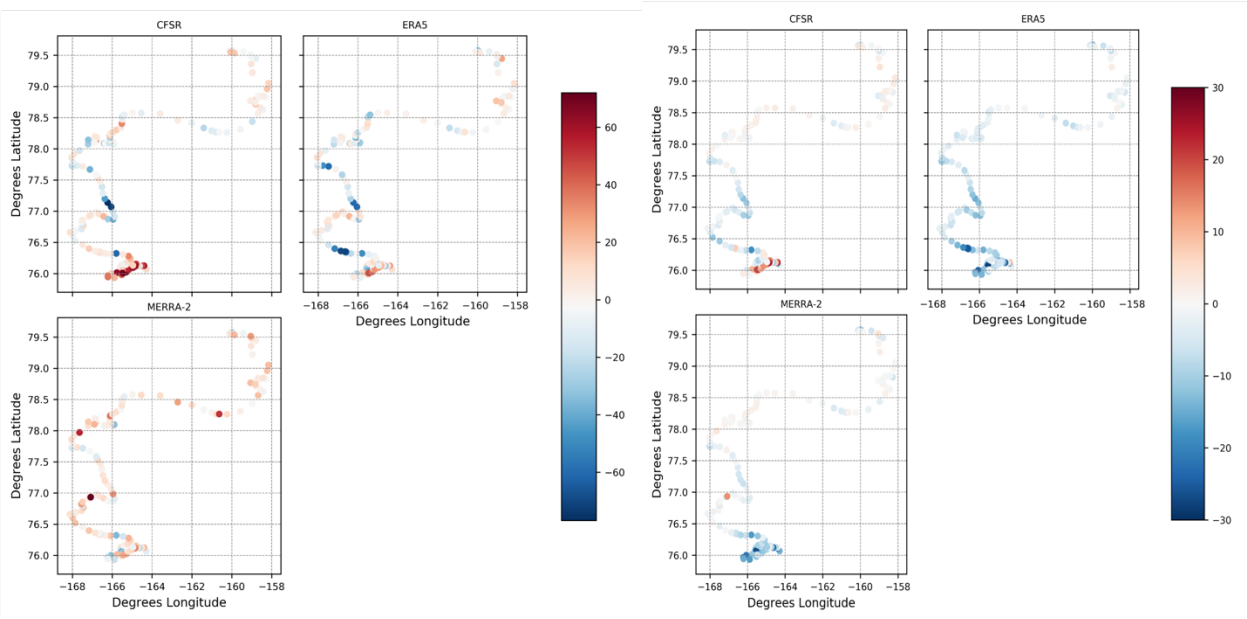

Figure 5.2: Daily downwelling longwave radiation (left) and upwelling longwave radiation (right) difference values in W/m^2 from SHEBA, ERA5, CFSR, and MERRA-2 between April and August 1998 along the SHEBA ship track in W/m^2.

Operating in a similar region to SHEBA, but two decades later, the *RV Araon* cruise started in the Bering Strait on August 5th 2018 and ended in the northern Chukchi Sea on August 25th 2018. Figure 5.3 highlights the locations and daily downwelling shortwave radiation differences compared to measurements taken aboard the *RV Araon*. Note that longitudinal values range from 0 to 360 instead of 180 to -180 as was done for the SHEBA figures.

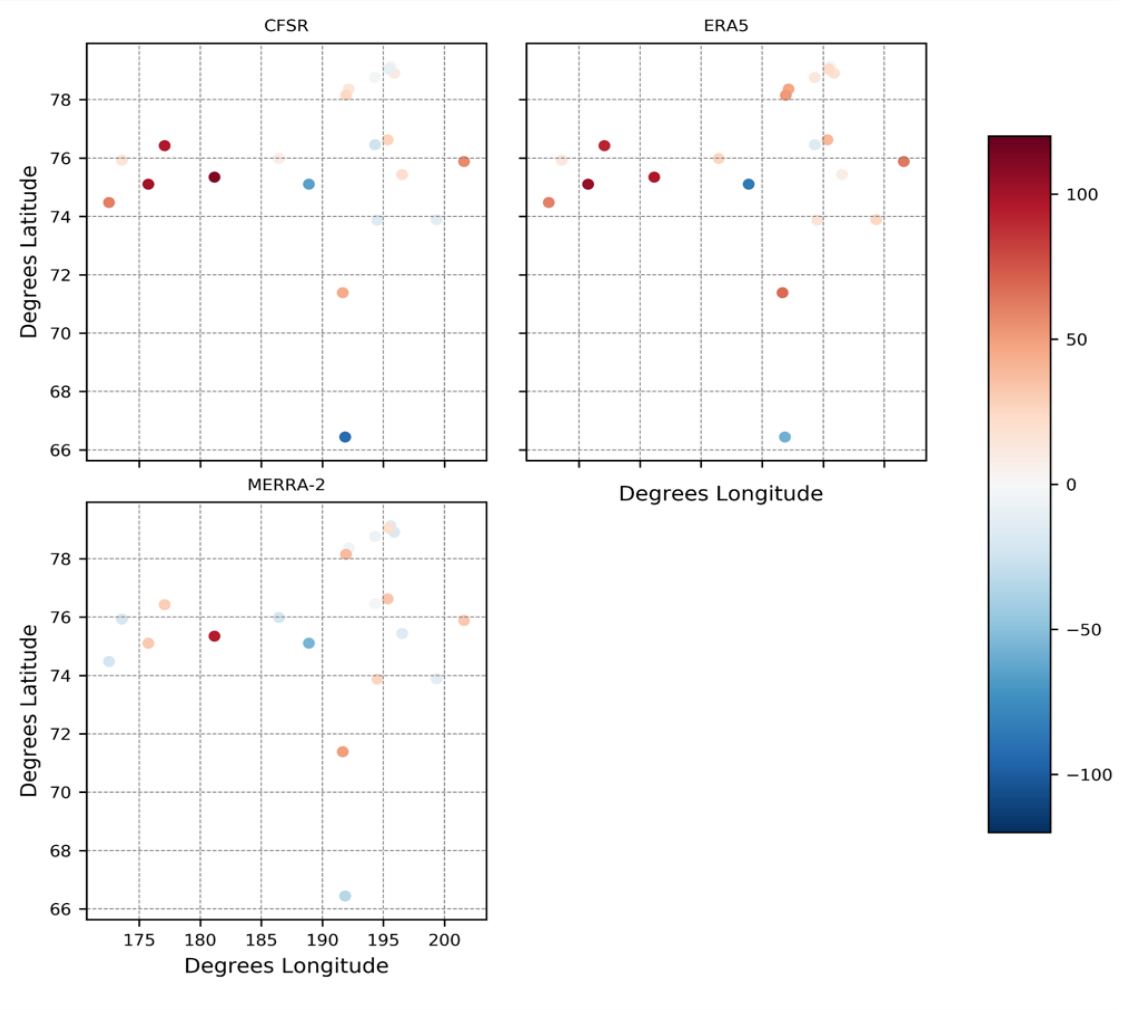

Figure 5.3: Daily downwelling shortwave radiation differences from RV Araon values in W/m² from ERA5, CFSR, and MERRA-2 in August 2018 and the RV ARAON ship track in the Chukchi Sea in W/m².

Even though the data collected aboard this expedition is limited due to the short duration of the trip, these data provide another useful comparison between the reanalyses and direct observations. Broadly, the values from the *RV Araon* and the reanalyses indicate many similarities between the datasets, yet there are some differences, especially between ERA5, CFSR, and the *RV Araon* fluxes. Particularly in the left side of the plot, the data from the *RV Araon* shows larger values while

ERA5 and CFSR show differences downwelling shortwave radiation ranging from -100 W/m^2 to 100 W/m^2 as seen in Figure 5.3 and MERRA-2 does not. Differences in downwelling shortwave radiation are primarily affected by cloud cover and atmospheric aerosols. As already noted, in reanalyses, these variables are entirely parameterized. Interestingly though, MERRA-2 has similar values to the *RV Araon* observations in the same region (left side of the plot). There are very likely some scale difference issues as well that lead to uncertainty in the results presented here.

The MOSAiC expedition started at around 89^{o}N and the ship drifted south near the North Pole. Figure 5.4 shows differences of downwelling and upwelling shortwave radiation during MOSAiC. The downwelling shortwave radiation differences for all the datasets range from -150 W/m^2 up to 200 W/m^2. The upwelling shortwave radiation differences range from -75 W/m^2 to 150 W/m^2. These are large differences. This is likely related to differences in the treatment of cloud cover and optical depth between reanalyses. Differences in the spatial scale of the observations and reanalyses likely play a large role as well.

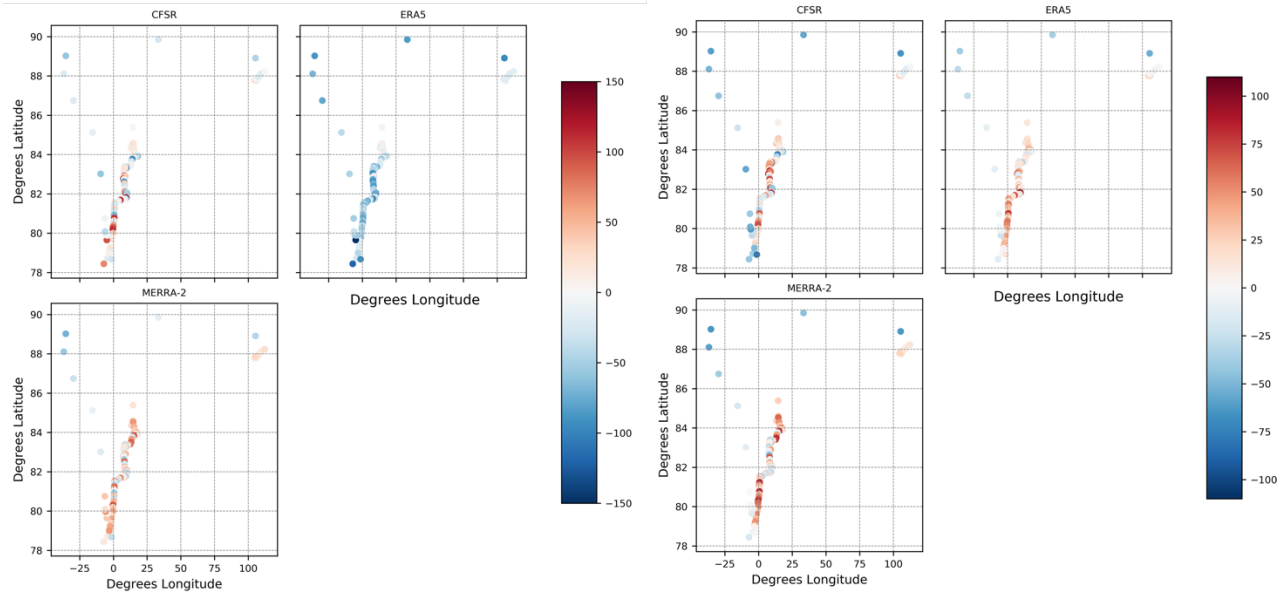

Figure 5.4: Daily downwelling shortwave radiation differences from MOSAiC data (left) and upwelling shortwave radiation differences from MOSAiC data (right) values in W/m^2 from ERA5, CFSR, and MERRA-2 between April and August 2020 along the MOSAiC ship track in W/m^2.

Downwelling and upwelling longwave radiation differences during MOSAiC follow in Figure 5.5. Similar to Figure 5.4, there are few differences between the four datasets for both variables. All downwelling and upwelling longwave radiation difference range from -70 W/m^2 to 70 W/m^2. Note that the MOSAiC ship and surrounding area was in an area of high concentration of sea ice cover for nearly the entire expedition, which limits both the magnitude of upwelling longwave radiation (few leads) and potential differences between the MOSAiC observations and reanalysis values due to the different spatial measurement scales.

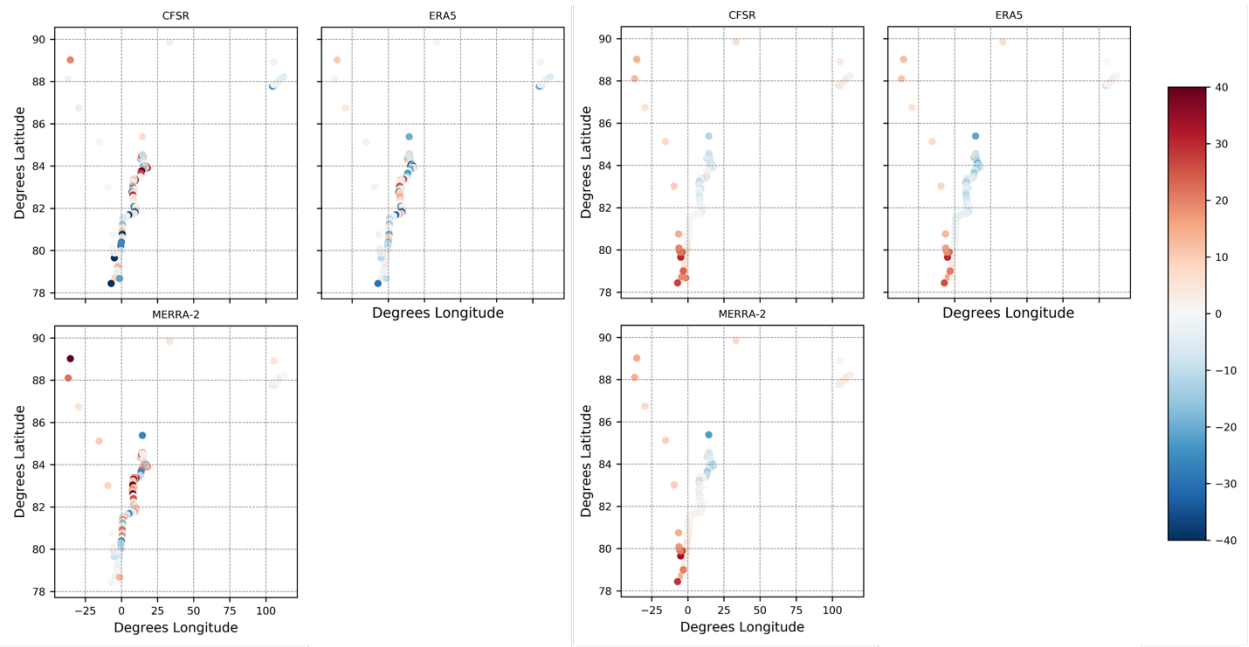

Figure 5.5: Daily downwelling longwave radiation differences from MOSAiC data (left) and upwelling longwave radiation differences from MOSAiC data (right) values in W/m² from ERA5, CFSR, and MERRA-2 between April and August 2020 along the MOSAiC ship track.

5.3 Temporal Distribution: Radiative Fluxes

Figure 5.6 summarizes the distributions of the daily radiation components during the SHEBA expedition between April 1998 and August 1998. The SHEBA observational data is shown by orange Xs and the reanalysis data are shown in purple shapes.

The upwelling and downwelling shortwave radiation components reflect the seasonal cycle. In April the Arctic is in late winter/early spring and starting to receive more solar radiation. It is assumed that the reanalyses will capture the seasonal cycle of top of atmosphere downward solar radiation. Early in the season, it appears that the overall spread of downwelling shortwave values at the surface from the reanalysis generally bracket the SHEBA observations. The same is true of

upwelling shortwave radiation early in the season, later in the season the SHEBA upwelling shortwave values are generally higher than the reanalysis values. This suggests that the albedos in the reanalysis are too low at this time because despite there being similar amounts of downwelling shortwave radiation, less shortwave radiation is reflected upward compared to observations.

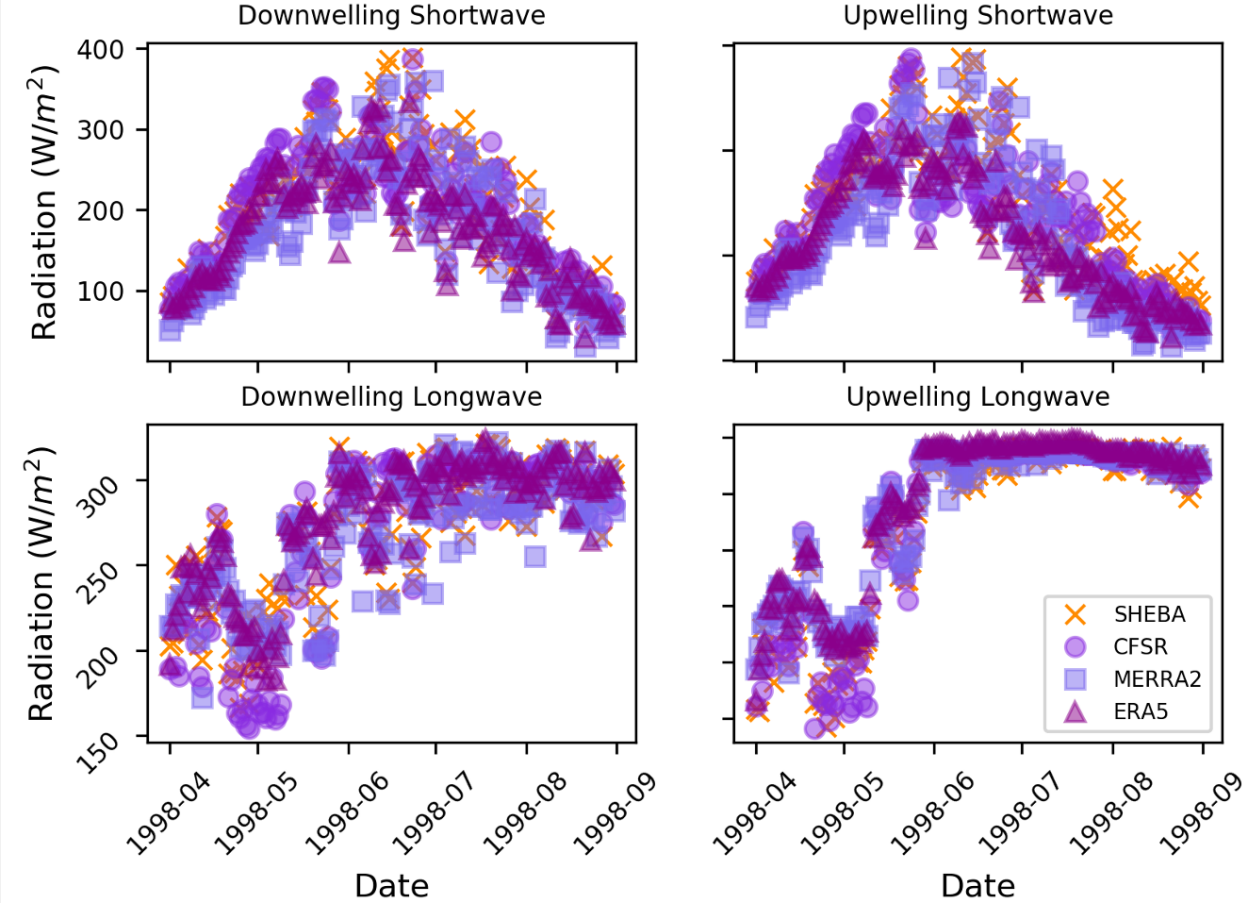

Figure 5.6: Scatterplots of daily radiation component values across the Central Arctic Ocean between April and August of 1998 from SHEBA, ERA5, CFSR, and MERRA-2

As seen in Figure 5.6, the downwelling longwave radiation components during the SHEBA period show that the spread of the reanalysis values bracket the observations, which is consistent with the results that will be discussed later with

reference to Table 5.1. The same is true for upwelling longwave. Note that later in the seasons, all data sets show little variation in upward longwave radiation due to the impact of a melting sea ice surface on stabilizing the surface temperature at the

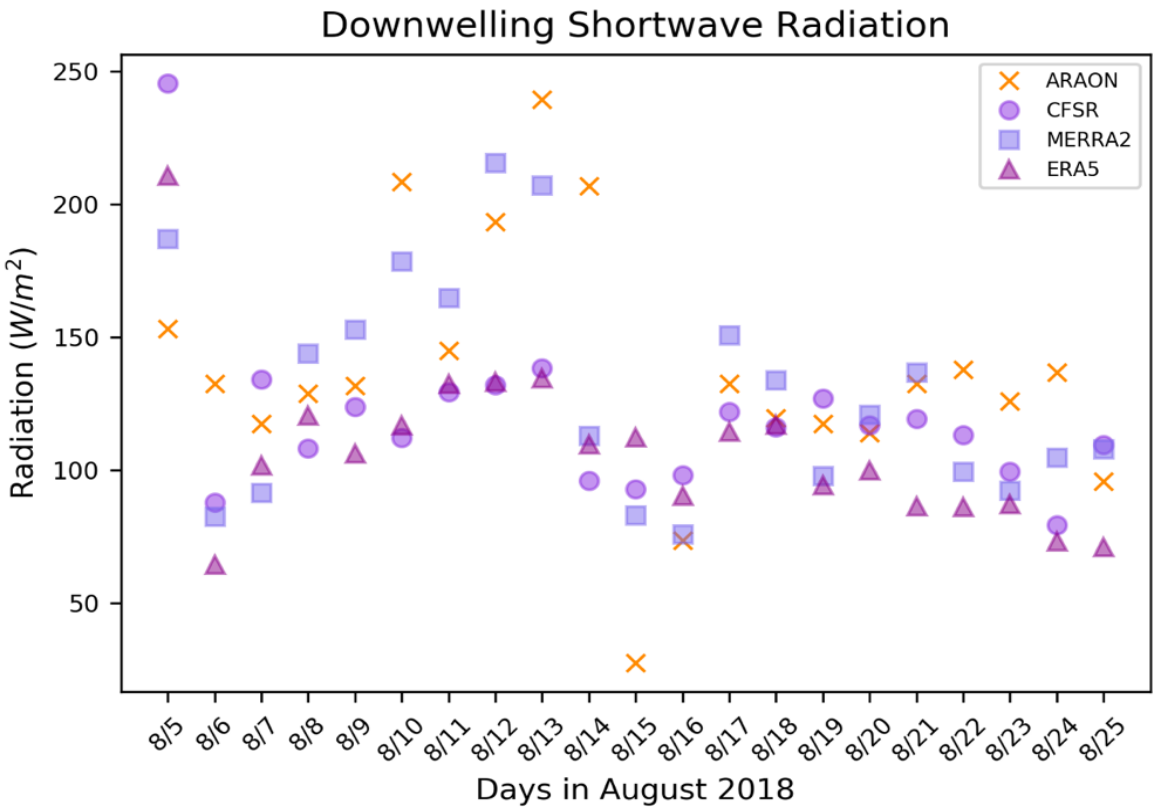

Figure 5.7: Scatterplots of daily downwelling shortwave radiation values in the Bering Strait and Chukchi Sea in August 2018 from RV ARAON, ERA5, CFSR, and MERRA-2.

melting point. Interestingly, the reanalyses capture the observed dip in the magnitude of both longwave components in May 1998. While a dip in downwelling longwave radiation values indicates a comparatively cold and less cloudy period, this feature is not readily captured in the downwelling shortwave which would be expected to increase if there were fewer clouds.

Figure 5.7 shows a scatterplot of daily downwelling shortwave radiation from the *RV Araon* (orange Xs) and the three reanalyses (three purple shapes) between August 5, 2018 and August 25, 2018. The range in reanalysis values generally captures the day-to-day downwelling shortwave radiation fluctuations in the *RV Araon* data. However, there are several days (e.g. August 15th) where the observed values are well outside the spread of the reanalysis values. This will be discussed in more detail later. The main reason for differences in downwelling shortwave radiation in observations and reanalyses is how the reanalyses treat cloud cover and atmospheric aerosols.

The four radiation components from MOSAiC (orange Xs) and the reanalyses (purple shapes) follow in Figure 5.8. Similar to data collected during the SHEBA expedition, the reanalyses are able to capture the basic observed seasonal cycle (as expected) from MOSAiC but there is some indication that the reanalysis values of both downwelling and upwelling shortwave radiation are somewhat too low, also confirmed when comparing the means in to be discussed later. Again, the differences between the reanalyses and observations are likely due to differences in parameterizations of cloud cover and aerosols, albedo, surface cover and spatial scale. Note, however, the odd spike in upwelling longwave radiation in the MOSAiC record in August that is not captured by the reanalyses. The cause for this spike is due to the breakup of the ice floe that the *RV Polarstern* was frozen into and the repositioning of the ship (Cassano – personal communication).

In summary, although there are clear differences between all the data sources for all radiation components, all reanalyses capture the basic seasonal cycles. They also capture some of the minor changes in the observed dataset. CFSR appears to have the most visually similar pattern in the raw data to the observational datasets. The patterns observed in the raw data for ERA5 and MERRA-2 are very similar and they do not capture the range in value variability throughout the year as CFSR does.

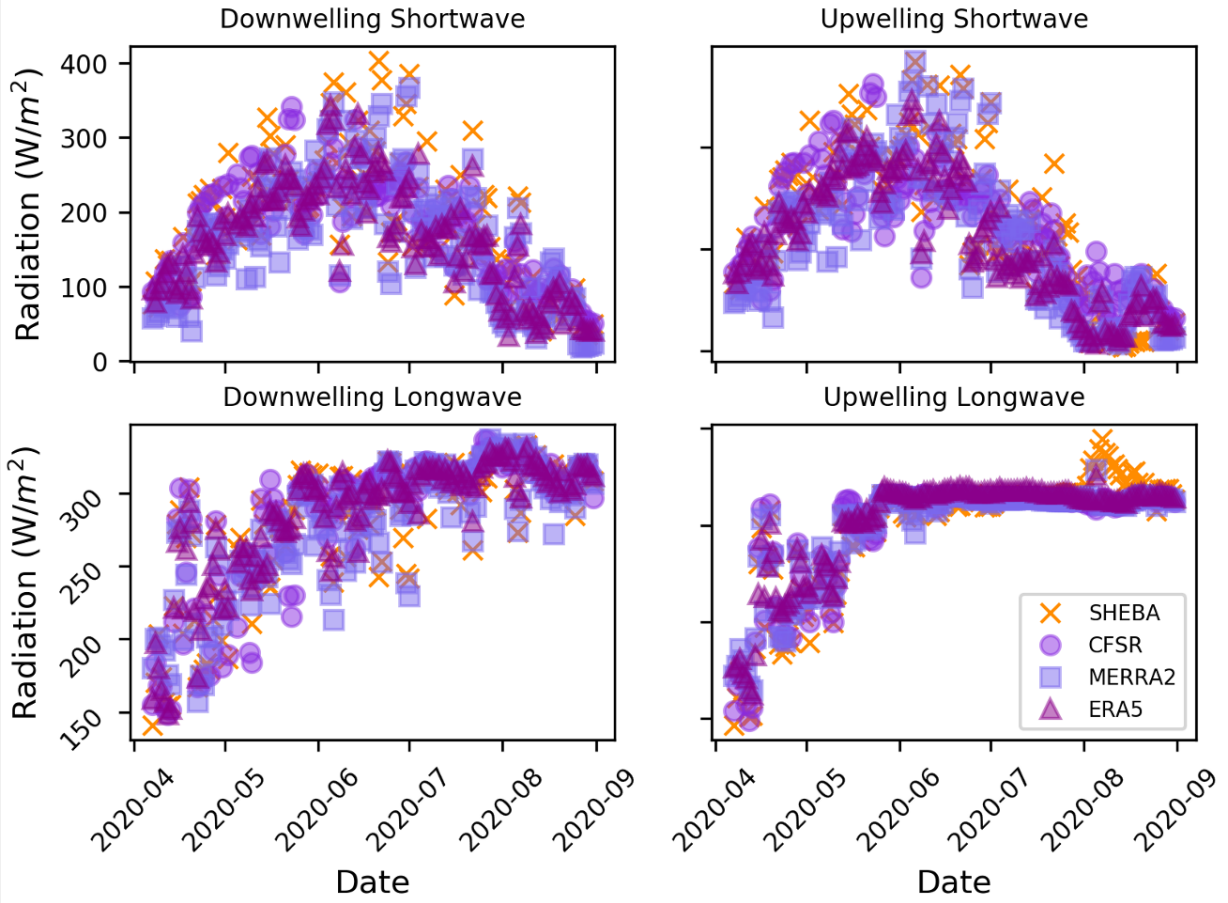

Figure 5.8: Scatterplots of daily radiation component values across the Central Arctic Ocean between April and August of 2020 from MOSAiC, ERA5, CFSR, and MERRA-2

However, looking more closely at Figures 5.6 - 5.8 and referring to Table 5.1 that follows later, it is seen that all the datasets show the seasonal cycle and there is a smaller spread between the models and SHEBA data. MERRA-2 consistently underestimates both downwelling and upwelling shortwave radiation compared to ERA5, CFSR, and SHEBA, as shown in Table 5.1. This may be due to inaccurate representation of clouds/too much cloud cover, reflecting and absorbing too much incoming shortwave radiation. Although, when all raw values were run through QQplots, which are used to test for normality, none of the datasets for the radiation variables had normal distributions. This could mean that some of these results are not capturing the full relationships that exist in the physical world.

5.4 Value Distribution: Radiative Fluxes

Figures 5.9 - 5.11 provide frequency histograms (expressed as observation counts). Figure 5.9 depicts the histograms for daily values of all four radiation components compared to the SHEBA values. The longwave radiation values are strongly skewed toward higher values (>300 W/m^2), especially upwelling longwave radiation. Based on the spatial distributions in Figures 5.1 - 5.3, it is unexpected to find that all datasets, except two small cases, have different frequency distributions. There is no one dataset that is consistently lower or higher than the other three. There is ample variation between histogram bins. Interestingly, ERA5

does not have values in the highest bins for shortwave radiation. It also has no values in the lowest bins for longwave radiation.

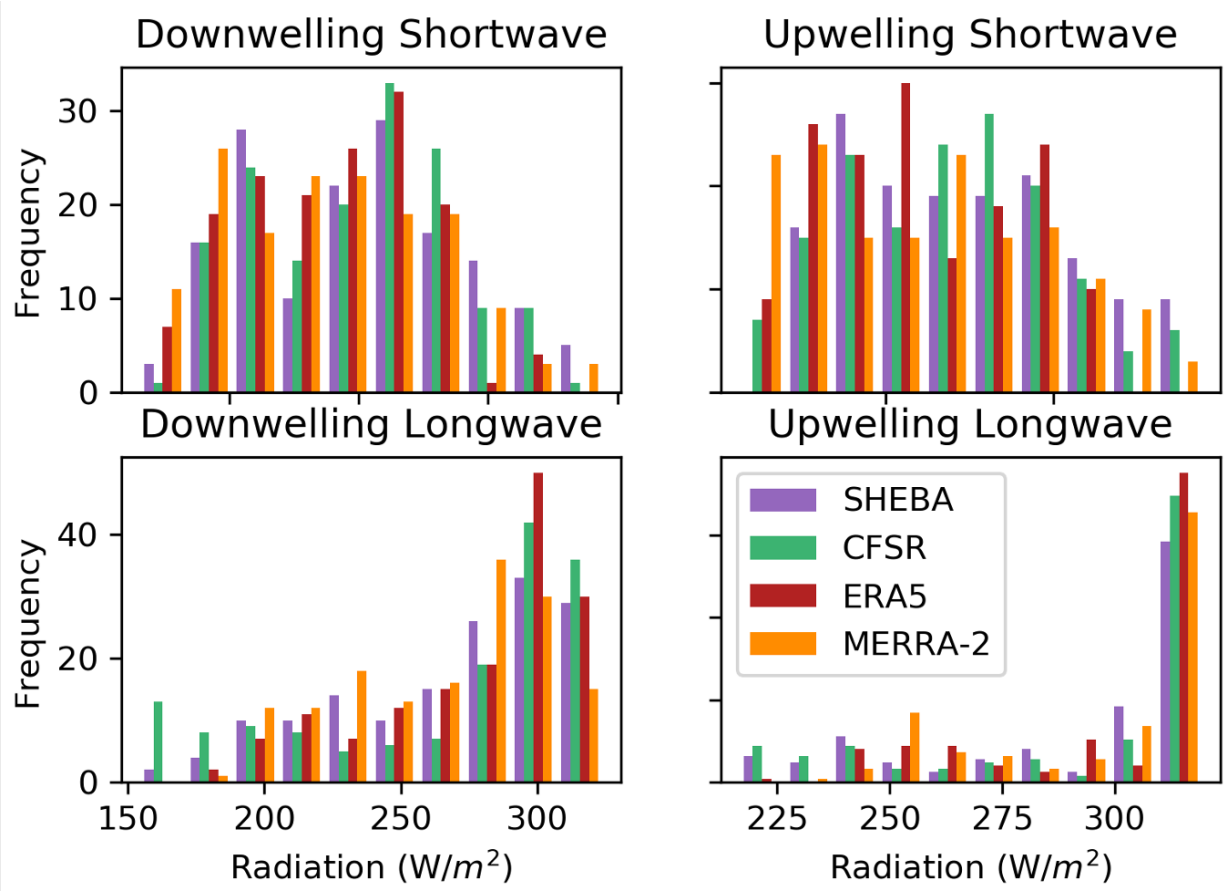

Figure 5.9: Histograms of daily radiation component values across in the Beaufort and Chukchi Seas between April and August 1998. Histograms were calculated using daily values.

Figure 5.10 shows the histograms for downwelling shortwave radiation in August 2018 from the *RV Araon* and the reanalyses. These values are slightly skewed towards lower values (between 70 W/m^2 and 150 W/m^2) compared to SHEBA, which is expected moving into the autumn season. Solar radiation declines and temperatures begin to drop. The *RV Araon* measurements have a few low values (<50 W/m^2), that the three reanalysis datasets do not capture. ERA5 and

CFSR do not capture many values higher than 150 W/m², which may be related to the differences in parameterized cloud cover and atmospheric aerosols. There are a few instances where the frequency of values in the *RV Araon* and CFSR datasets are equal, but besides those points, all datasets have different frequency distribution

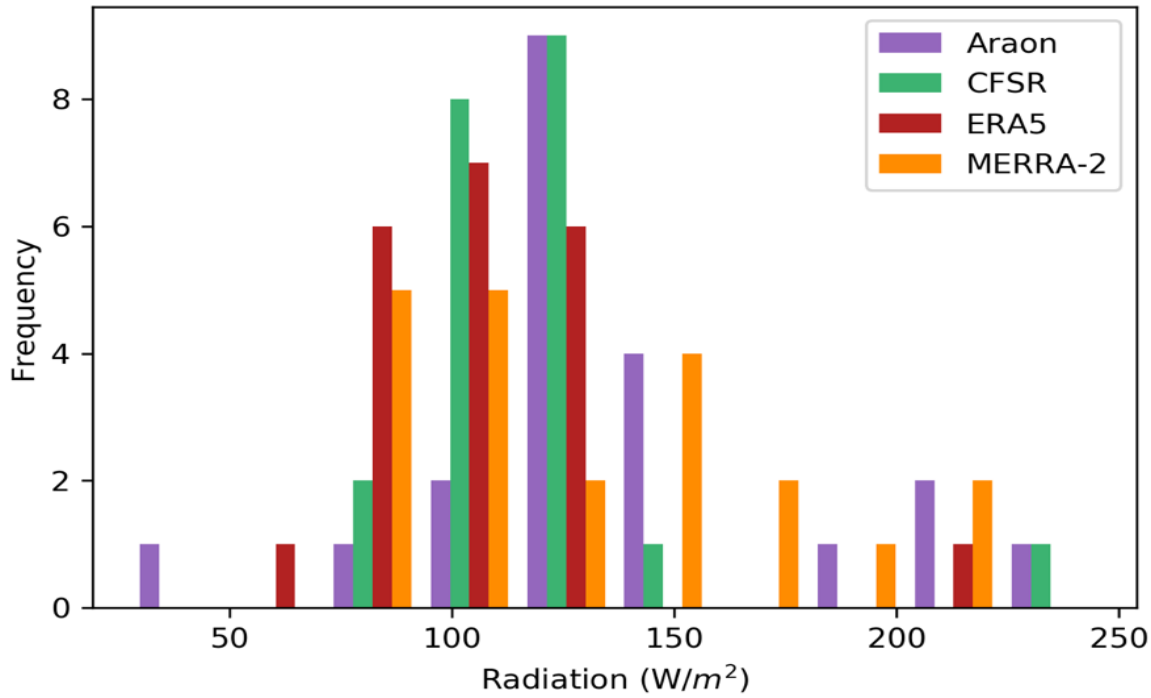

Figure 5.10: Histograms of daily radiation component values across the Chukchi Sea in August 2018. Histograms were calculated using daily values.

Figure 5.11 shows the histograms for daily values of the radiation components between April and August 2022 from the MOSAiC expedition and the reanalyses. Similar to the SHEBA comparisons in Figure 5.10, and as expected, the longwave radiation values are strongly skewed toward values over 300 W/m². The upwelling shortwave radiation values are slightly more skewed to lower values compared to the radiative components. In the downwelling shortwave figure there is

an instance just above 250 W/m^2 where all three reanalyses have the same frequency, and they are overestimating the number of those values when compared to MOSAiC. Overall, there is a wide distribution of value frequencies and there is little agreement between the observational dataset and the reanalyses.

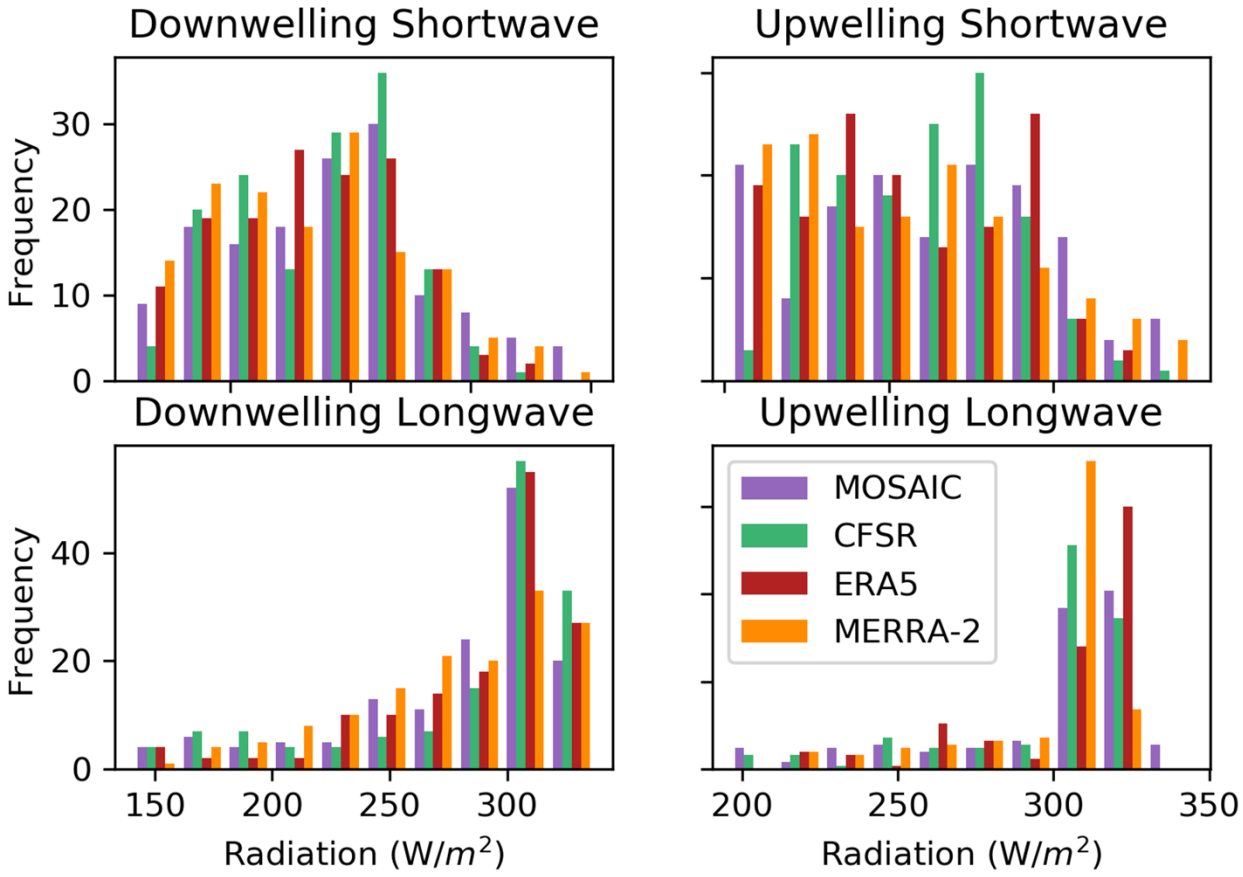

Figure 5.11: Histograms of daily radiation component values across the Central Arctic Ocean between April and August of 2020. Histograms were calculated using daily values.

In summary, there are spatial and temporal inconsistencies between the observations and the reanalyses in all regions. There are also different frequencies of value occurrences between the datasets. By contrast all reanalyses capture the overall pattern of the observational datasets. Figures 5.9 - 5.11 reveal that when

comparing individual value counts, there are inconsistencies between each dataset. Since the differences between the datasets were only established visually up to this point, a formal statistical comparison is needed.

5.5 Descriptive Statistics

Table 5.1 summarizes differences between the climatological means, standard deviations, and variances for the raw data from the four radiation components as averaged over the study domain. The reanalysis values will be missing some detail as they are one value for a large spatial (grid cell) area. Consider first a comparison between the means and standard deviations as a possible metric to determine which reanalysis performs the best.

The average downwelling shortwave values from the reanalyses compare reasonably well with the *RV Araon* mean(136.7 W/m^2), yet they are all negatively biased. The ERA5 average bias is about -30 W/m^2, the MERRA-2 mean bias is about -7 W/m^2, and the CFSR mean bias is about -19 W/m^2. Comparisons with the SHEBA mean (201.4 W/m^2) are somewhat different: the CFSR mean bias is nearly nearly zero, but the ERA5 and MERRA-2 mean biases are both greater than - 20 W/m^2. Compared to the MOSAiC mean (184.7 W/m^2), CFSR again has the smallest magnitude negative bias of -6 W/m^2, while ERA5 and MERRA-2 have large magnitude negative biases (-19 W/m^2 and -22 W/m^2, respectively).

Table 5.1: Means, standard deviations, and variances of for daily values of the four radiation components for all observations and reanalysis datasets.

Variables	Mean	Stand Dev.	Variance
RV ARAON			
Shortwave Down	136.7	45.5	2175.5
CFSR shortwave D	119.2	32.3	1091.9
ERA shortwave D	107.9	30.3	966.2
MERRA shortwave D	130.5	40.8	1750.7
SHEBA			
Shortwave Down	201.4	81.3	6644.2
Shortwave Up	147.4	64.1	4140.7
Longwave Down	269.5	40.1	1616.9
Longwave Up	290.6	31.1	971.7
CFSR shortwave D	201.5	74.1	5531.3
CFSR shortwave U	138.3	60.6	3692
CFSR longwave D	265.6	50.8	2596.3
CFSR longwave U	291.1	32.9	1087.6
ERA shortwave D	177.2	67.2	4541.5
ERA shortwave U	119.4	56.5	3207.9
ERA longwave D	277	36.6	1346.9
ERA longwave U	298	26.7	718
MERRA shortwave D	176.6	80.3	6483.8
MERRA shortwave U	122.1	70.4	4988.8
MERRA longwave D	264.9	35.9	1298.6
MERRA longwave U	295.4	25.2	638.7
MOSAiC			
Shortwave Down	184.7	84.1	5202
Shortwave Up	126.7	72.7	5202
Longwave Down	280	46.5	2418.6
Longwave Up	298.7	32.6	1261.3
CFSR shortwave D	178.1	67	4764
CFSR shortwave U	120.3	53.5	2846.8
CFSR longwave D	283.3	50	2758.6
CFSR longwave U	298.5	29.4	1010.1
ERA shortwave D	165.4	72.7	5244.9
ERA shortwave U	110	62.4	3881
ERA longwave D	285.8	41.5	1946.5
ERA longwave U	301.7	26.8	853
MERRA shortwave D	161.8	83.2	6802.5
MERRA shortwave U	109.3	71	4993.6
MERRA longwave D	276.7	43.1	2167
MERRA longwave U	298.8	26.1	795.5

These results suggest that simply based on mean biases (Table 5.2), CFSR provides the best estimates of downwelling shortwave radiation compared to all three observational campaigns. Note that overall, for downwelling shortwave radiation, the observations have higher standard deviations than the reanalyses, i.e., there is a larger spread in values in the observational datasets than shown in the reanalyses. This may relate, at least in part, to the fact that the observations are point scale measurements as opposed to being integrated values over fairly large areas and are relatively smooth fields.

The remainder of the comparisons are limited to SHEBA and MOSAiC observations since *RV Araon* only collected downwelling shortwave radiation. The upwelling shortwave values will depend on both the downwelling shortwave and the surface albedo from all datasets. The SHEBA mean upwelling shortwave radiation (147.4 W/m^2) is best matched by the CFSR mean (138.3 W/m^2), but again, ERA5 (119.4 W/m^2) and MERRA-2 (122.1 W/m^2) are too low. In part, this follows the results of the downwelling shortwave components, which were also biased low. If there is too little shortwave radiation reaching the surface then there will be less reflecting upward as well. Interestingly, the standard deviations from the three reanalyses are all fairly similar as compared to that of the SHEBA values. The MOSAiC mean upwelling shortwave radiation value of 126.6 W/m^2 is best matched by the mean from CFSR (120.2 W/m^2), which is too low. But ERA5 and MERRA-2 means are also too low by ~11W/m^2.

Downwelling longwave radiation values are a function of temperature and emissivity, with cloud cover playing a large role (clouds tend to emit approximately as blackbodies). The SHEBA downwelling longwave mean of 269.5 W/m^2 is very close to the CFSR mean of 265.6 W/m^2, but the CFSR standard deviation of 51 W/m^2 is higher than the observed values of 40 W/m^2. However, both the ERA5 mean (277 W/m^2) and the MERRA-2 mean (264.9 W/m^2) are also very similar to the observations and their standard deviations are closer to the observed SHEBA values than CFSR. The MOSAiC comparisons show a broadly similar story. The observed downwelling longwave mean of 281 W/m^2 is fairly close to the three reanalyses, and the standard deviations are also fairly similar. For the sake of calculating "best estimate" net surface heat flux values, based on both the means and standard deviations, MERRA-2 is the best performing reanalysis for downwelling longwave radiation.

Upwelling longwave radiation is a simple function of skin temperature, assuming blackbody emission and can be found using the Stefan-Boltzmann Equation. Thus, the SHEBA average of 290.6 W/m^2 hence corresponds to a mean skin temperature of -5.5° C. While too low of a surface temperature for summer when the sea ice is melting, remember that the surface will be below freezing in spring. CFSR also has a mean of 291 W/m^2, and therefore captures a similar average skin temperature to SHEBA. Both ERA5 and MERRA-2 have slightly higher means (298 W/m^2 and 295 W/m^2, respectively), yet they are still close to the observational mean. ERA5 and MERRA-2 standard deviations are very similar to

one another, but they are more than 5 W/m^2 smaller than the SHEBA standard deviation (31 W/m^2).

The MOSAiC comparisons tell a very similar story. The observed upwelling longwave values of 299 W/m^2 correspond to a skin temperature of -3.7° C. CFSR and MERRA-2 both have means that are nearly identical to the MOSAiC mean, yet the MERRA-2 standard deviation is 6 W/m^2 smaller than the observed standard deviation. In CFSR's standard deviation is only 3 W/m^2 smaller than the observed standard deviation. The ERA5 mean (302.3 W/m^2) is biased high when compared to the MOSAiC mean. Ultimately, it is a close call which dataset performs the best from this analysis, but between CFSR's mean and standard deviation matching the observations' so well, CFSR is the best performing reanalysis for upwelling longwave radiation. Again, however, this conclusion is based simply on the means, as shown earlier.

5.6 Correlations and T-Statistics

An analysis of correlations and T-statistics can help put some of the above results into additional context. As shown in Table 5.1, there are differences in the raw flux values, and it could be argued that based on the means only, CFSR is a better product. However, upon closer examination and with removing the seasonal signal, the differences in the means from the detrended data do not stand up in the T-statistics (Table 5.2). There are no statistically significant differences in the means for any radiation variable. The temporal correlations, based on detrended

daily values from the observational datasets and reanlayses, arguably tell a more interesting story. With few exceptions, the correlations are statistically significant, and many are quite high.

Using Pearson-r correlations, all r values except two are statistically significant at the 99% confidence level. In several cases, the reanalyses explain more than half of the variance in the corresponding observed records. It is reasonable to expect that downwelling shortwave radiation would have higher correlations as compared to the other flux terms because the amount of energy received at the top of the atmosphere is known. Unfortunately, this is not supported in the literature because models prescribe cloud characterizes, aerosols, and atmospheric moisture are different among reanalyses (Chakraborty and Lee, 2021). Chaudhuri and Ponte (2015) found that there was a large spread between downwelling shortwave radiation in multiple reanalyses, Longwave radiation depends on many interactions in the atmosphere, ice, and ocean leading to the expectation that it would have lower correlations; but this does not show in the results. Furthermore, the results in Table 5.2 show that an assessment of which reanalysis performs the best requires looking at more than just mean values (Table 5.1).

For downwelling shortwave radiation, from the SHEBA comparisons, CFSR and MERRA-2 correlate almost equally (0.64), yet ERA5 is a bit lower (0.57). But based on the MOSAiC results, CFSR is the worst performer (0.41). For upwelling shortwave radiation, based on SHEBA, the three reanalyses are on par with each

other, but using the MOSAiC dataset one sees that CFSR does not perform. For downwelling longwave, CFSR and MERRA-2 correlate about the same with the SHEBA dataset, while compared to MOSAiC, CFSR loses out to both ERA5 and MERRA-2. Finally, for the upwelling longwave component, all of the reanalyses correlate highly with both the SHEBA and MOSAiC records.

RMSE and mean difference biases were also calculated and are included in Table 5.2. The results for the downwelling shortwave radiation from the *RV Araon* shows that MERRA-2 values have the lowest RMSE, even though it is larger than desired (37.5). The mean difference bias is -6.2 which agrees with the calculated RMSE value.

The results comparing SHEBA values to the reanalyses show that CFSR has the lowest RMSE values for upwelling and downwelling shortwave radiation and upwelling longwave radiation. MERRA-2 has the lowest RMSE for downwelling shortwave radiation. Most RMSE values are still well above zero, showing that the reanlyses do not capture the values observed on the SHEBA expedition. The RMSE for CFSR values for upwelling longwave radiation is only 6,3, which is the lowest RMSE of all SHEBA-reanalysis comparisons. Interestingly though, CFSR has the lowest mean difference bias values for all four variables.

Comparing the reanalysis values to the MOSAiC observations shows that CFSR still has the lowest RMSE for upwelling longwave radiation. MERRA-2 also maintains having the lowest RMSE for downwelling longwave radiation. But ERA5 has the lowest RMSE for both upwelling and downwelling shortwave radiation,

which was not the case in the SHEBA-reanalyses RMSE values. CFSR has the lowest mean difference bias values for upwelling and downwelling shortwave radiation and downwelling longwave radiation while MERRA-2 has the lowest mean difference bias for upwelling longwave radiation.

Taken together, these results show that there are a number of factors that can be contributing to the differences between the reanalyses and observations. These differences are including but not limited to the differences in scale (point versus grid), different cloud cover at difference heights, cloud type, surface temperature differences, surface type, albedo, and humidity.

Table 5.2: Daily t-test, correlation values, r^2, RMSE and mean bias between observational and reanalysis datasets for downwelling shortwave, upwelling shortwave, downwelling longwave, and upwelling longwave across the respective study areas. Statistically significant values are bolded for T-stat and R^2. The bolded RMSE and mean bias values are the lowest values.

Variables	T-STAT	Corr Coeff	R2	RMSE	Mean Bias
RV ARAON					
CFSR shortwave D	0.106	0.421	0.177	52.14	-17.6
ERA shortwave D	0.027	0.402	0.161	53.85	-28.8
MERRA shortwave D	-0.159	0.674	**0.453**	**37.5**	**-6.2**
SHEBA					
CFSR shortwave D	-0.012	0.641	**0.41**	**37.03**	**0.11**
CFSR shortwave U	-0.057	0.6	**0.36**	**35.41**	**-9.12**
CFSR longwave D	-0.051	0.741	**0.55**	23.81	**-3.9**
CFSR longwave U	-0.016	0.905	**0.82**	**6.3**	**0.51**
ERA shortwave D	0.048	0.569	**0.32**	45.64	-24.17
ERA shortwave U	0.073	0.576	**0.33**	39.7	-28
ERA longwave D	0.011	0.583	**0.34**	22.41	7.8
ERA longwave U	-0.055	0.801	**0.64**	10.7	7.38
MERRA shortwave D	0.049	0.638	**0.41**	42.6	-24.9
MERRA shortwave U	0.095	0.631	**0.40**	39.15	-25.27
MERRA longwave D	-0.076	0.76	**0.58**	**18.23**	-4.6
MERRA longwave U	-0.081	0.891	**0.80**	9.05	4.8
MOSAiC					
CFSR shortwave D	0.06	0.407	**0.17**	49.6	**-6.7**
CFSR shortwave U	-0.112	0.343	**0.12**	42.15	**-6.37**
CFSR longwave D	-0.051	0.427	**0.18**	22.7	**3.4**
CFSR longwave U	0.297	0.781	**0.61**	**8.2**	-0.2
ERA shortwave D	0.327	0.755	**0.57**	**40.6**	-19.3
ERA shortwave U	0.323	0.735	**0.54**	**33.42**	-16.74
ERA longwave D	-0.413	0.674	**0.45**	18	5.8
ERA longwave U	-0.056	0.742	**0.55**	10.2	3
MERRA shortwave D	0.196	0.771	**0.60**	44.5	-22.9
MERRA shortwave U	0.173	0.736	**0.54**	37.5	-17.37
MERRA longwave D	-0.115	0.843	**0.71**	**16.2**	-3.8
MERRA longwave U	0.284	0.767	**0.59**	9.2	**0.07**

5.6.1 *RV ARAON*/Reanalyses Scatterplots

Figure 5.12 shows a scatter plot of all the detrended daily downwelling shortwave radiation data between August 5th and August 25th in 2018. MERRA-2 has the largest standard deviation (Table 5.1) of all the reanalyses, and the strongest positive correlation (0.674) with significance at a 99% confidence interval (P-value: 0.006). CFSR and ERA5 have a much milder positive linear relationship to the *RV Araon* record and the relationships are not statistically significant. Looking back at Table 5.2, the *Araon* observations are poorly correlated with ERA5 and CFSR (16% and 18%, respectively).

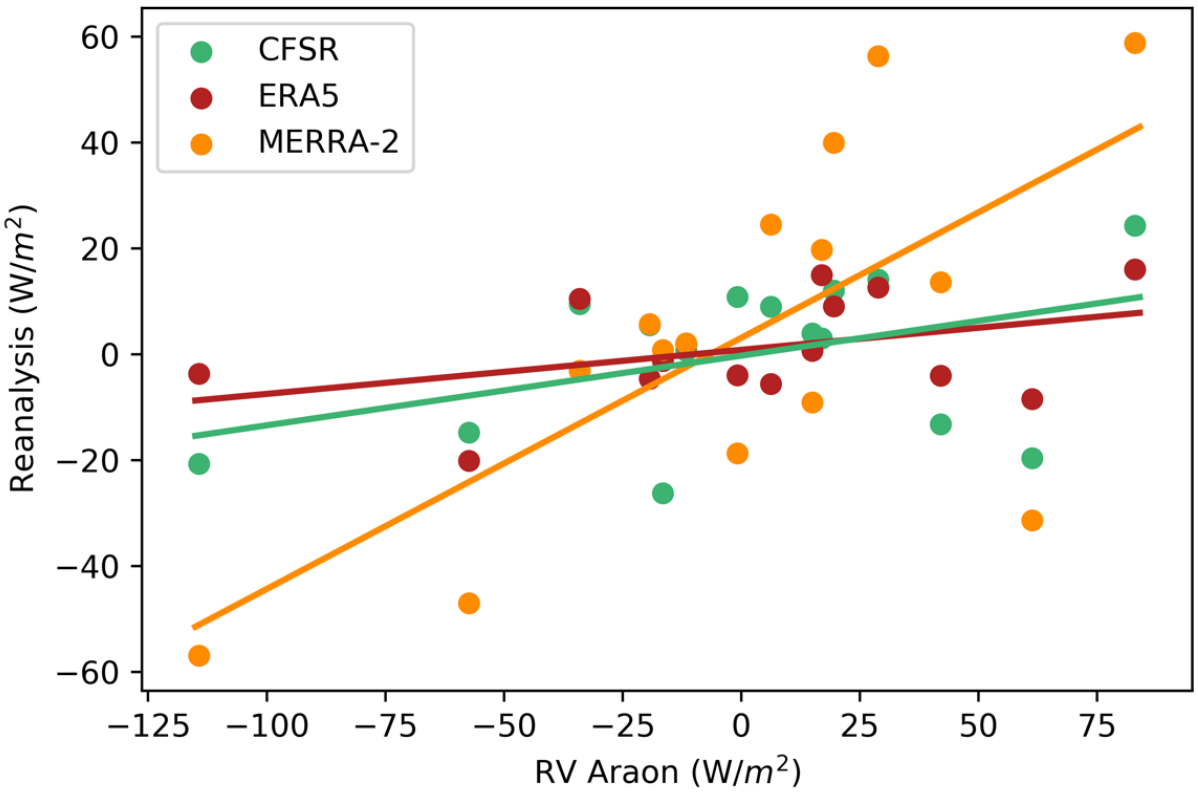

Figure 5.12: Scatterplots plotting daily downwelling shortwave from each reanalysis against the RV ARAON observational dataset to evaluate the relationship in the Bering Strait and Chukchi Sea in August 2018. CFSR data are in green, ERA5 data

are in red, and MERRA- 2 data are in orange. The linear line is a one-to-one line to visually represent what a perfect linear relationship would look like.

5.6.2 SHEBA/Reanalyses Scatterplots

Figure 5.13 shows the relationships between the three reanalyses and the SHEBA record (detrended as above). The downwelling shortwave radiation has a positive correlation, but there are some large outliers. Again, this may relate to scale issues; for example, while a given day at the SHEBA site may have been clear, it may have been cloudy on the scale of a reanalysis grid cell. The upwelling shortwave radiation scatterplot shows a wider spread around the linear line and a few outliers, not surprising given that this variable relates to both the downwelling shortwave radiation and the albedo. The longwave radiation relationships are strongly positively linear, although upwelling longwave has the strongest positive linearity.

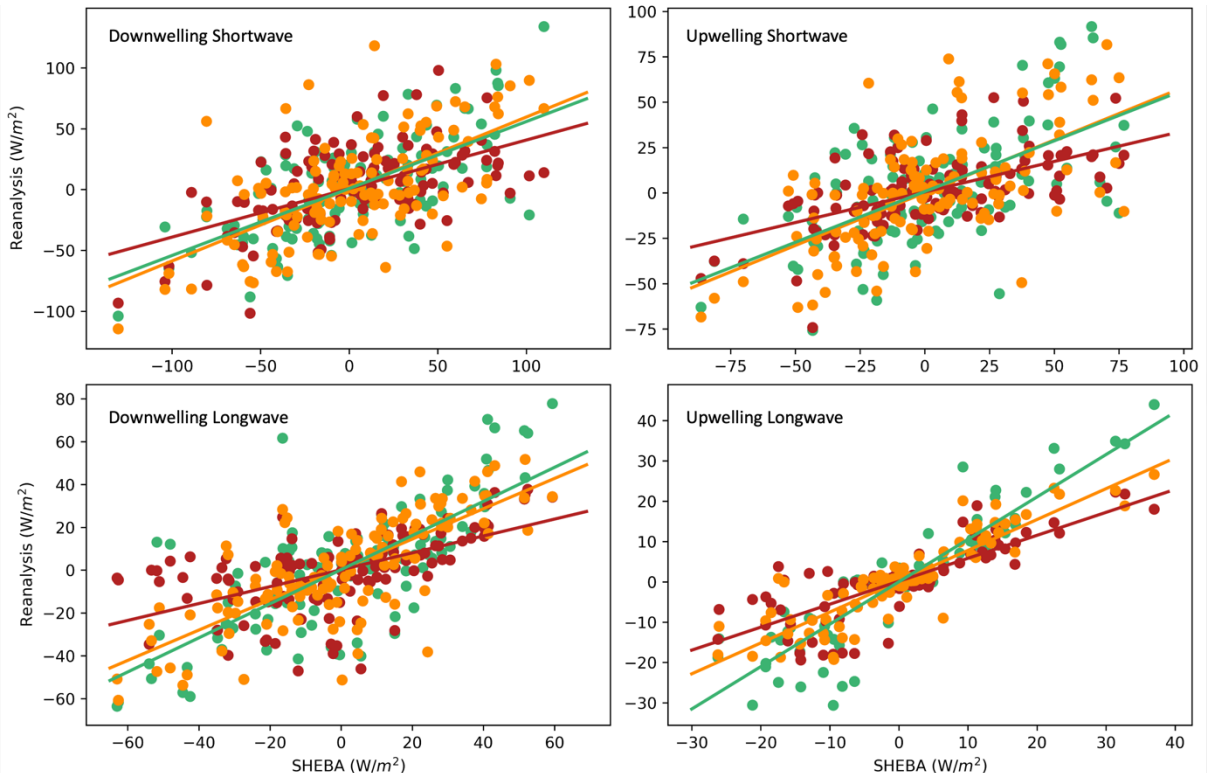

Figure 5.13: Scatterplots plotting daily downwelling shortwave, upwelling shortwave, downwelling longwave, and upwelling longwave from each reanalysis against the SHEBA observational datasets to evaluate the relationship in the Beaufort and Chukchi Seas between April and August 1998. CFSR data are in green, ERA5 data are in red, and MERRA-2 data are in orange. The linear line is a one-to-one line to visually represent what a perfect linear relationship would look like.

5.6.3 MOSAiC/Reanalysis Scatterplots

Scatterplots comparing MOSAiC observations with the reanalyses follow in Figure 5.14. Echoing results in Table 5.2, CFSR (green) does not have a strong linear relationship with the observations for downwelling shortwave radiation, yet it has a very strong linear relationship with the observations for upwelling longwave radiation.

When comparing the detrended upwelling shortwave radiation data from the reanalyses to the MOSAiC dataset, MERRA-2 and ERA5 have the strongest positive

correlations; with coefficients of 0.736 and 0.735, respectively, both are statistically significant at the 99% confidence interval (Table 5.2). Although MERRA-2 does not have perfect linear relationship with the MOSAiC data, it does have the highest variance of the three reanalyses (Table 5.1). Despite having the smallest biases, CFSR has the weakest positive linear relationship with the observations (0.343), showing that simple comparisons of means do not tell the full story.

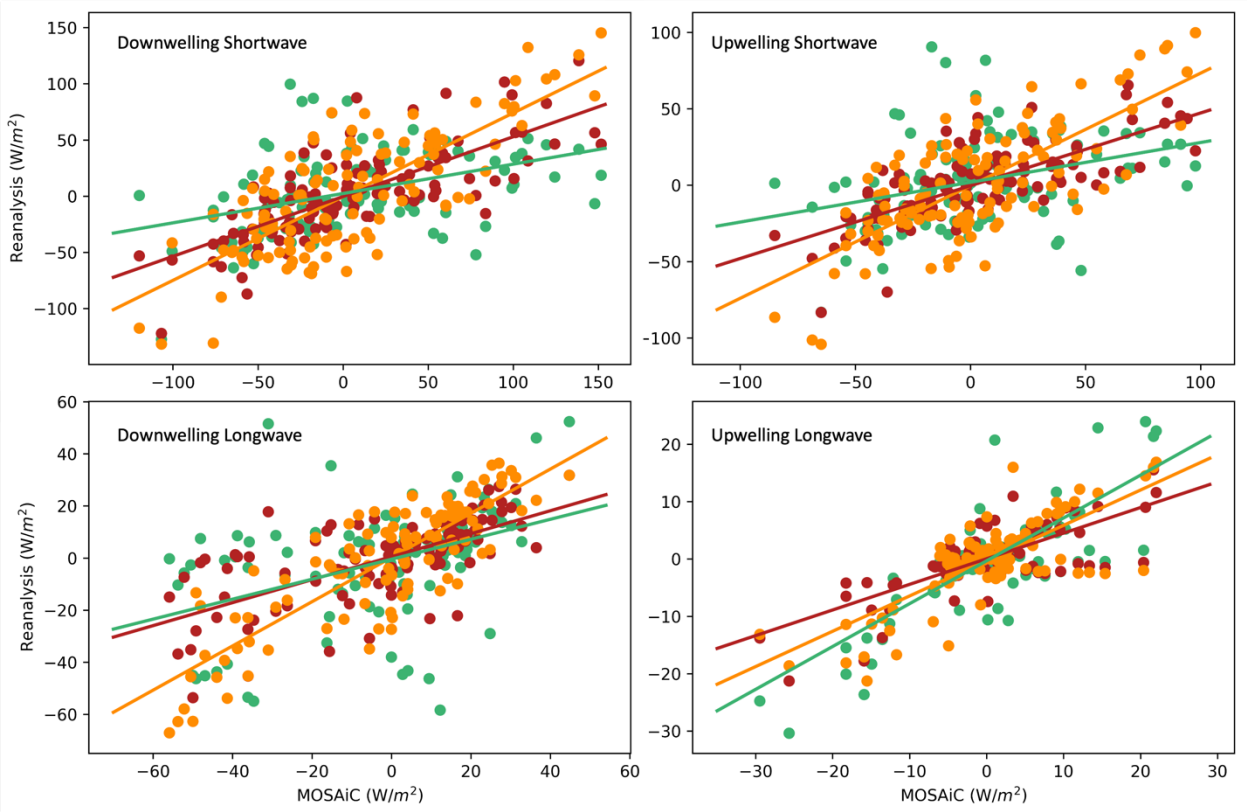

Figure 5.14: Scatterplots plotting daily downwelling shortwave, upwelling shortwave, downwelling longwave, and upwelling longwave from each reanalysis against the SHEBA observational datasets to evaluate the relationship in the Central Arctic Ocean between April and August 2020. CFSR data are in green, ERA5 data are in red, and MERRA-2 data are in orange. The linear line is a one-to-one line to visually represent what a perfect linear relationship would look like.

The detrended downwelling shortwave radiation from the reanalyses illustrates a very similar story to the detrended upwelling shortwave radiation comparison. MERRA-2 performs the best when compared to the observations (0.775). ERA5 is similar (0.755) and CFSR (0.407) is the lowest performing reanalysis. The variances for each of the reanalyses also follow this pattern.

By contrast, CFSR has the highest correlation (0.781) for upwelling longwave radiation. MERRA-2 (0.767) and ERA5 (0.742) are very close behind. As noted in Table 5.2, MERRA-2, outperforms the other two reanalyses when looking at the detrended downwelling longwave radiation data. CFSR's correlation (0.427) is half that of MERRA-2 (0.843) for downwelling longwave radiation. All correlations are statistically significant at the 99% confidence level. In comparison to the SHEBA analysis, more than 50% of all detrended reanalysis variability is also shown in the MOSAiC observations, except four: CFSR downwelling and upwelling shortwave radiation, CFSR downwelling longwave radiation, and ERA5 upwelling shortwave radiation (Table 5.2).

5.7 Conclusion

This comparison is an essential part of determining the top performing reanalysis for calculating net surface heat flux and release values in the last portion of analysis. In order to get an estimate of the net surface flux, it must first be determined which models perform best for the radiation components.

A perhaps surprising result from the analysis presented here is that ERA5 was not the top performer for any of the variables examined based on the performance metrics studied here (means, standard deviation, temporal correlations). ERA5 is the newest reanalysis,of the three and has the highest resolution of the reanalyses examined in this dissertation. Based simply on agreement between mean values of the fluxes compared to observations, it might be tempting to conclude that CFSR is overall the best performer, but as discussed, there are no statistically significant differences in the detrended means in any of the variables. Instead, MERRA-2 arguably performs the best across two of the observational datasets (*RV Araon* and MOSAiC) for downwelling shortwave radiation.

These results, however, must be tempered by recognition that there are substantial differences in the spatial patterns of the flux variables. In the absence of direct observations spanning the Arctic Ocean, one cannot say which reanalysis provides the most realistic spatial patterns. The differences in the spatial patterns will directly influence the calculated net surface flux. Another issue to consider is that the reanalysis data represent a grid cell area and the observations are point values.

It is also important to note that because the *RV Araon* dataset is much shorter than the SHEBA and MOSAiC datasets that the results using this dataset does not hold as much weight and importance as the longer expedition datasets.

Biases between the reanalyses and the *RV Araon* should not be viewed the same as the biases shown using the SHEBA and MOSAiC datasets.

CFSR has the strongest positive correlation (0.641) for downwelling shortwave radiation when compared to the SHEBA dataset. But because MERRA-2 performs best with two of the three datasets it might be better as the source for downwelling shortwave radiation when calculating the best estimate of the net surface flux and thus seasonal net surface heat flux value. Although, it is important to keep in mind that the three observational datasets took place on cruises that were limited in space and time, thus, these results should consider the potential uncertainty that the limits could introduce. MERRA-2 also performed the best for upwelling shortwave radiation with a correlation coefficient of 0.631 with SHEBA data and 0.736 with MOSAiC data. CFSR was close behind in the comparison with the SHEBA data (0.60), but MERRA-2 ultimately performed slightly better. MERRA-2 outperformed CFSR and ERA5 for downwelling longwave as well. MERRA-2's correlation coefficient with SHEBA data was 0.76 and 0.843 with MOSAiC data. One surprising note is that MERRA-2's MOSAiC correlation coefficient was double that of CFSR's correlation coefficient. Lastly, CFSR has the highest correlation coefficient for upwelling longwave radiation when compared to both SHEBA (0.905) and MOSAiC (0.781). Thus this argues that MERRA-2 data is the best choice for downwelling and upwelling shortwave radiation as well as downwelling longwave radiation. CFSR appears to be the best choice for upwelling longwave radiation.

CHAPTER 6: SEASONAL HEAT GAIN ESTIMATES

6.1 Introduction

This chapter examines the estimated seasonal heat gain from the net surface flux across the Arctic Ocean and for open water and ice areas separately from each reanalysis. The focus is to estimate heat gain values and to compare those results between each reanalysis and the "best estimate" values calculated for each year between the period 1980 and 2018.

Figures are included to illustrate the temporal differences between each reanalysis and to highlight some of the spatial differences between the specific years: 1982, 1996, 2007, and 2012. These years were selected because the September sea ice extent in 1982 and 1996 was anomalously high and the September sea ice extent in 2007 and 2012 was anomalously low, which have substantial impacts on the upwelling shortwave radiation, upwelling longwave radiation, and the turbulent fluxes.

To set the stage, Figure 6.1 shows the climatological average spatial fields of the April through August average heat gain from the net surface flux for CFSR, ERA5, and MERRA-2. The units for Figure 6.1 are Megajoules per square meter (MJ/m^2). The climatological seasonal heat gain values averages across the entire Arctic Ocean domain over the period 1980 and 2018 are 287 MJ/m^2 for CFSR, 250 MJ/m^2 for ERA5, and 202 MJ/m^2 for MERRA-2. CFSR has the largest Arctic Ocean climatological averages, thus ERA5 sits in the middle and MERRA-2 has the lowest average. Across all of the reanalyses, the region with the lowest heat gain is, not surprisingly, the central Arctic Ocean. Values increase towards the coasts and lower

latitudes, which is expected given the lower albedos and stronger downward solar radiation in these areas.

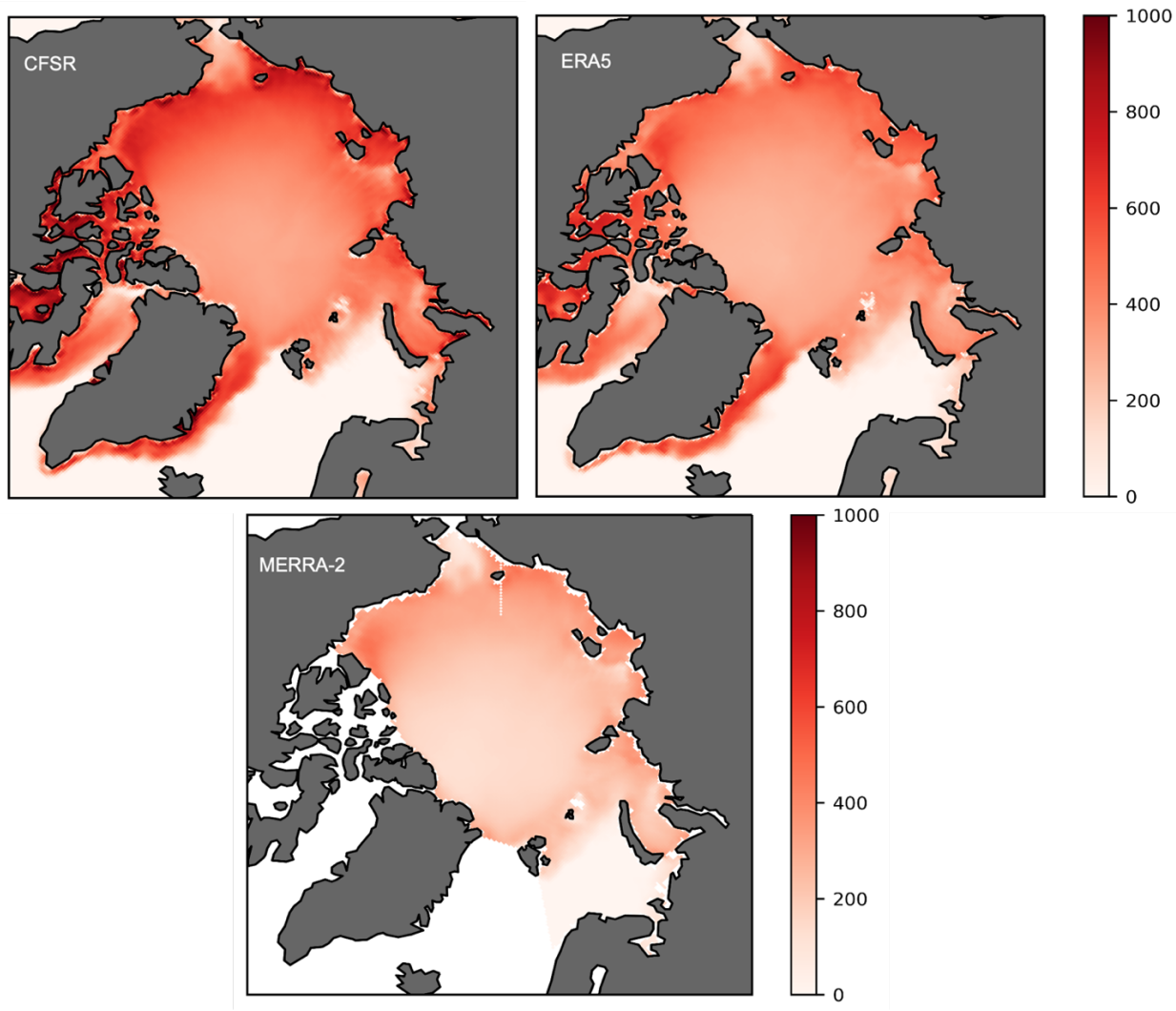

Figure 6.1: Climatological average of ocean heat gain from April to August over sea ice across the Arctic Ocean CFSR (left), ERA5 (middle) and MERRA-2 (Right). Values are shown in MJ/m^2 per each grid cell.

6.2 Heat gain comparisons

The seasonal heat gain from the net surface flux is examined for the Arctic Ocean domain as a whole and also separated into plots over sea ice and over open water. Daily sea ice concentration values were calculated for each reanalysis and

were used to subset the daily net surface heat flux values each day; this process is outlined in more detail in Chapter 3. By this subsetting method, through the season, some grid cells characterized as ice become open water grid cells. Furthermore, as the years pass, and consistent with the observed decline in sea ice concentration and extent in response to Arctic warming, more grid cells become open water, especially later in the season. Recall that the downward trends in sea ice extent are largest in late summer and early fall. These plots (Figures 6.2 and 6.3) are useful in understanding the differences between the three reanalyses. Spatial comparisons will follow later.

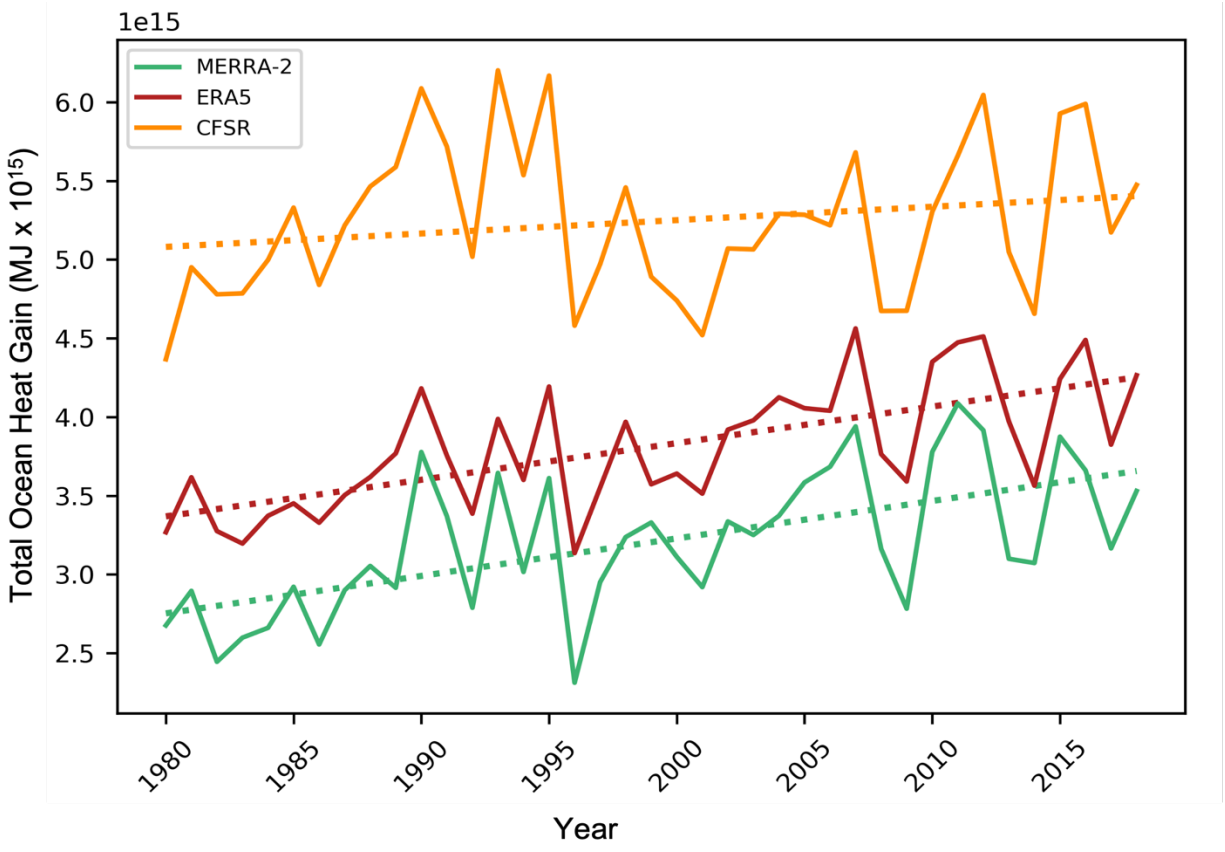

Figure 6.2: Seasonal ocean heat gain from the net surface flux for the Arctic Ocean domain as a whole from CFSR (green), ERA5 (blue), and MERRA-2 (orange) averaged per year from April to August from 1980 to 2018.

Figure 6.2 shows those values for each year across all regions in the Arctic Ocean and marginal seas over sea ice and open water. All three reanalyses have the same temporal patterns, which in general follow variations in end of summer sea ice extent. Note, for example, the low heat gain in 1996 in all the reanalyses, which had the highest September sea ice extent in the satellite record. Also seen in the time series is the much higher values in CFSR compared to ERA5 and MERRA2. Overall, there does not seem to be on model that fully agrees with another, which fits with the results discussed in previous chapters. CFSR largely has the largest values in much of the analysis presented here. ERA5 and MERRA-2 appear to agree much more both in time and space.

Of particular note is the positive trends in heat gain depicted in each of the reanalyses. This is of course expected. When a bright reflective surface (sea ice) is replaced with a dark absorbent surface (ocean water), more energy is expected at the surface. The linear trend values from CFSR, ERA5, and MERRA-2 over the analysis period are 8.5×10^{12} MJ, 2.3×10^{13} MJ, and 2.4×10^{13} MJ, respectively but only CFSR is statistically significant at the 95% level.

The results from the three reanalyses are in overall agreement with the analysis of Li et al. (2022) which focused on the net surface heat flux from ERA5, which shows a strong positive trend in the net surface flux between 1979-2018.

There are differences in study methods. The present study uses data from April through August while the Lit et al. (2022) study only focused on June, July, and August.

The study domain used by Li et al. (2002) also includes the Greenland Sea along the Greenland coast, Baffin Bay, and the Canadian archipelago (not included in the present study) and excludes the Barents Sea (included in the present study). For example, Baffin Bay has shown significant increases in sea surface temperatures during the summer months (York et al, 2020), which could contribute to the positive trends observed in Li et al. (2022).

Figure 6.3 shows the yearly seasonal heat gain between April and August over sea ice only from ERA5 (green), CFSR (purple), and MERRA-2 (orange). The values for 1981 (as an example) of 220 MJ/m^2 from MERRA-2, 360 MJ/m^2 from ERA5, and 405 MJ/m^2 from CFSR correspond to the melt of 7.32×10^{-10} km^3, 1.2×10^{-9} km^3, and 1.34×10^{-9} km^3 of ice, respectively. These values appear to be fairly small in relation to the total volume of ice in the Arctic Ocean. This may be because much of the sea ice melt is due to basal melt from heat in the ocean, especially at the end of the summer season.

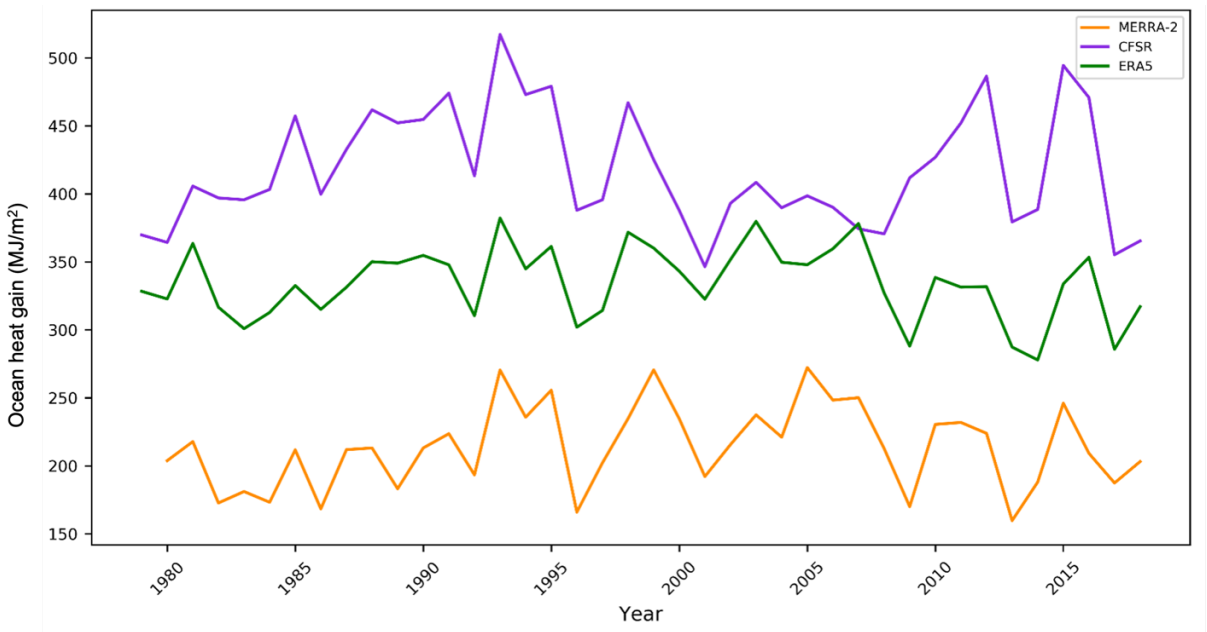

Figure 6.3: Yearly ocean heat gain from the net surface heat flux from April to August over sea ice across the Arctic Ocean from ERA5 (green), CFSR (purple), and MERRA-2 (orange).

MERRA-2 has the lowest values across the entire record, ERA5 has the middle amount of net surface heat flux and CFSR has the highest amount. The values from MERRA-2 are often less than half those from CFSR. Although the magnitude of values are vastly different in some places, the reanalyses share most of the same peaks and valleys. The contrasts between the values are due to the many issues previously discussed, namely, parameterizing differences in cloud cover, particularly cloud type, temperature, and optical thickness, differences in surface cover (ocean vs. sea ice, etc), albedo, and surface temperature. Seemingly small differences in any of individual flux components can compound into large differences in the net surface heat flux. None of the reanalyses show evidence of long-term trends in net surface heat flux over ice. There are a few areas in which high and low years do not match up between the reanalyses. Of particular note is

between 2004-2007 where MERRA-2 and ERA5 show general increases with two notable peaks, while CFSR shows the first increase but not the second decrease.

Through time, the number of grid cells represented by ice is of course decreasing. It is apparent that when the analysis is restricted solely to ice (as opposed to all grid cells as done for Figure 6.2) there are no notable trends in heat gain. Apparently, any reduction in the albedo of ice covered grid cells only, as depicted in the reanalyses, is insufficient to force a trend – because these values do not take into account the change in area covered by ice.

Remember that the net surface flux components are parameterized and those differ between the reanalyses. This can result in large differences between the estimated flux values. This may help to explain (as just one example) why peaks in heat gain after 2010 in CFSR have a much larger magnitude when compared to ERA5 and MERRA-2. Overall, MERRA-2 and ERA5 do not have the same magnitude of values but their similitude in year to year patterns reinforce that CFSR is more dissimilar. CFSR could be particularly diverging in magnitude and year-to-year patterns in the latter half of the study (2002-2018). CFSR is thus considered an outlier because its year to year patterns do not follow the other two reanalyses as closely, and it has the highest values, which relates back to the results in Chapter 5 that showed CFSR had a poor relationship with many of the observations.

Figure 6.4 shows time series plots of the estimated seasonal heat gain from each reanalysis over open water. Values from the three reanalyses are closer to one

another but still quite different. Because the albedo over open water is consistent, and that changes through time in the seasonal duration at which a grid cell is designated open water will be largely the same, the seasonal heat gains will tend to be somewhat consistent in magnitude and for the year-to-year differences. The largest magnitude difference between each of the reanalyses is between 1986 and 1998, which had relatively high sea ice extents. Note also that after 2015 MERRA-2 and ERA5 show similar patterns while CFSR stands out as quite different. Since these values are over open water, there is a stronger direct connection between the atmosphere and ocean, which may be more difficult for the reanalyses to capture.

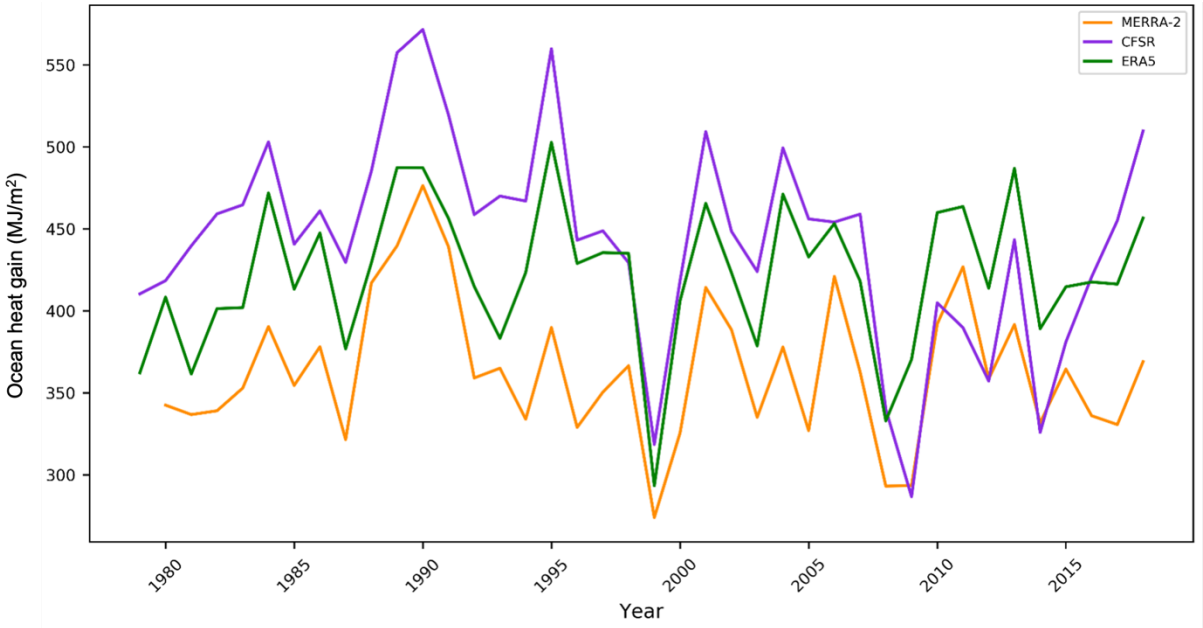

Figure 6.4: Yearly ocean heat gain from the net surface heat flux from April to August 1979 to 2018 over open water across the Arctic Ocean from ERA5 (green), CFSR (purple), and MERRA-2 (orange).

While no trends are observed when the analysis is restricted to ice, the same holds when the analysis is restricted to open water grid cells. While the number of open water grid cells is increasing with time, those grid cells that become open

water will be trending to do so later in the melt season and as such will not have along time to pick up extra energy due to the drop I albedo. Phrased a bit differently, over the years, the area of sea ice coverage over the summer has declined and the area of open water has increased, resulting in the ocean heat gain trends observed in Figure 6.2. Since Figures 6.3 and 6.4 examine the two surfaces separately, trends are not seen.

Table 6.1 shows the temporal correlations between the seasonal averages for all the reanalyses (the values shown in Figures 6.3 and 6.4). CFSR and ERA5 seasonal heat gain over sea ice are modestly correlated (r=0.56), statistically significant at the 99% confidence level (p= 0.000182). CFSR and MERRA-2 values over sea ice are weakly correlated (r=0.4) and statistically significant at the 99% confidence level (p=0.0067). Lastly, ERA5 and MERRA-2 are more strongly positively correlated (r=0.72) and statistically significant at the 99% confidence level (p=2.331e-7)

Average seasonal open water heat gain correlations are also reported in Table 6.1. CFSR and ERA5 are positively correlated but only modestly (r=0.5) and their relationship is statistically significant at the 99% confidence level (p= 0.00121). CFSR and MERRA-2 are also moderately positively correlated (r=0.43) and this relationship is statistically significant at the 99% confidence level (p=0.0060). Lastly, ERA5 and MERRA-2 are essentially uncorrelated, and their relationship does not even pass the 95% confidence interval.

Table 6.1: Correlation results between seasonal heat gain averages.

	CFSR			ERA5			MERRA-2		
	R^2	R	p	R^2	R	p	R^2	R	p
Over Sea Ice									
CFSR				0.32	0.56	**0.000182**	0.18	0.43	**0.0067**
ERA5	0.32	0.56	**0.000182**				0.52	0.72	**2.331e-7**
MERRA-2	0.18	0.43	**0.0067**	0.52	0.72	**2.331e-7**			
Over Ocean									
CFSR				0.25	0.5	**0.00121**	0.19	0.43	**0.0060**
ERA5	0.25	0.5	**0.00121**				0.01	0.11	0.4979
MERRA-2	0.19	0.43	**0.0060**	0.01	0.11	0.4979			

As a summary statement, while there are positive correlations between the time series over both open water and ice, with the reanalyses agreeing with respect to some of the years with an especially high or low heat gain, agreement cannot be considered especially impressive. Furthermore, there are large systematic differences in the means.

Why are there larger differences in magnitude and year to year pattern over sea ice as compared to calculations over open water? The likely answer is that open water albedo is fixed in each reanalysis. When the Arctic Ocean is covered in sea ice (or partially by sea ice) the albedo is parameterized and widely variable depending on the surface; sea ice albedo is 60-70%, melt pond and open ocean albedo are ~6%, and fresh snow albedo is 80-90%. The resolution of each reanalysis is on the order of tens of kilometers, they do not have the capacity to produce accurate albedos for sub

grid cell spatial scales. Albedo in each reanalysis is on a grid cell basis, which is an average value across a large area, when in reality, albedo can change quite dramatically within a few feet.

Turning back to the large differences in the overall magnitudes of the seasonal heat gain, it is reasonable to expect a strong role of sea ice albedo. Figure 6.4 shows the seasonally averaged albedo values between April and August of 1980 to 2018 across the sea ice covered areas. ERA5 has a considerably lower sea ice albedo compared to CFSR and MERRA-2 which translates into large impacts of upwelling shortwave radiation that is part of the next surface flux term. MERRA-2 and CFSR have values that vary between 55% and 70% which is within the range of the previous albedo estimates for sea ice.

Interestingly, as well as disturbing from the viewpoint of trying to come up with net surface estimates, while ERA5 has the lowest sea ice albedos of the three reanalyses, the seasonal net surface heat fluxes values are not the highest - values lie between those from MERRA-2 an CFSR. Furthermore, while the sea ice albedos from MERRA-2 and CFSR are broadly similar, MERRA-2 has, by far, the smallest net surface heat flux values.

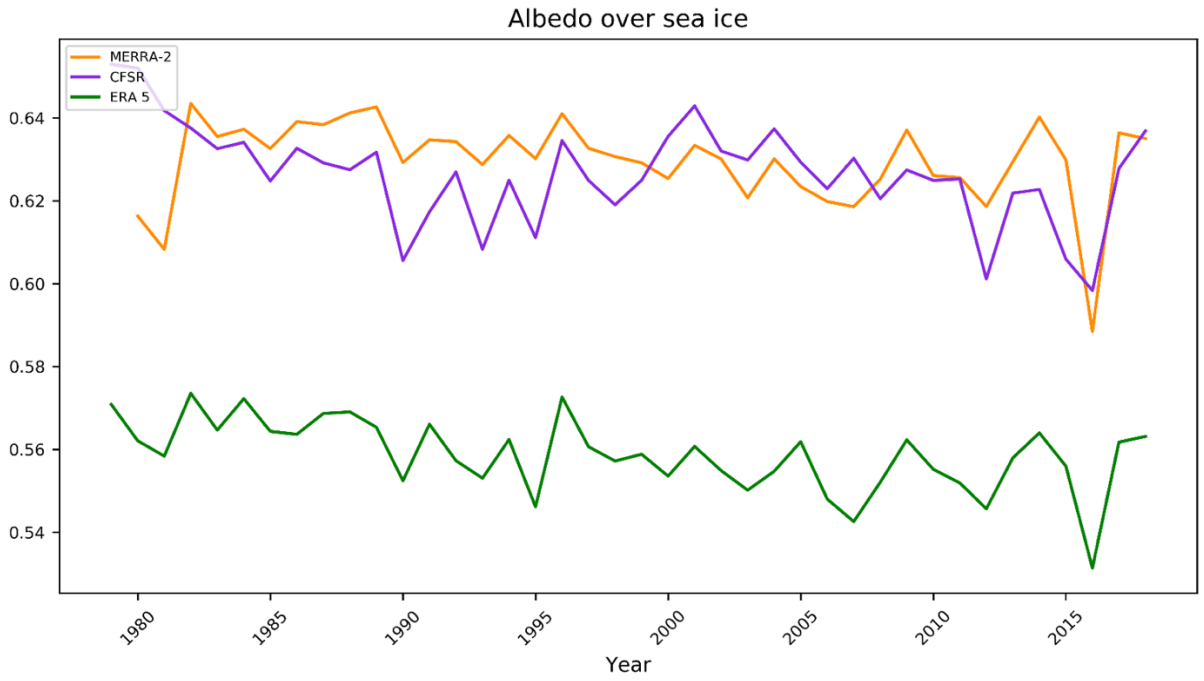

Figure 6.5: Yearly average albedo from April to August 1980 to 2018 over sea ice across the Arctic Ocean: ERA5 (green), CFSR (purple), and MERRA-2 (orange).

Figure 6.5 shows the yearly averaged albedo from April to August from 1980 to 2018 over open water. MERRA-2 has the highest albedo throughout all of the years. However, consistent with earlier discussion regarding the closer agreement between the reanalyses net surface flux values over open water, the range in albedo between the reanalyses of only about 0.05. Pohl et al., (2020) found that ERA5 albedo broadly agreed with observations but when looking at point to point comparisons, ERA5 albedo did not agree with the observations, which agrees with Figures 6.5 and 6.6.

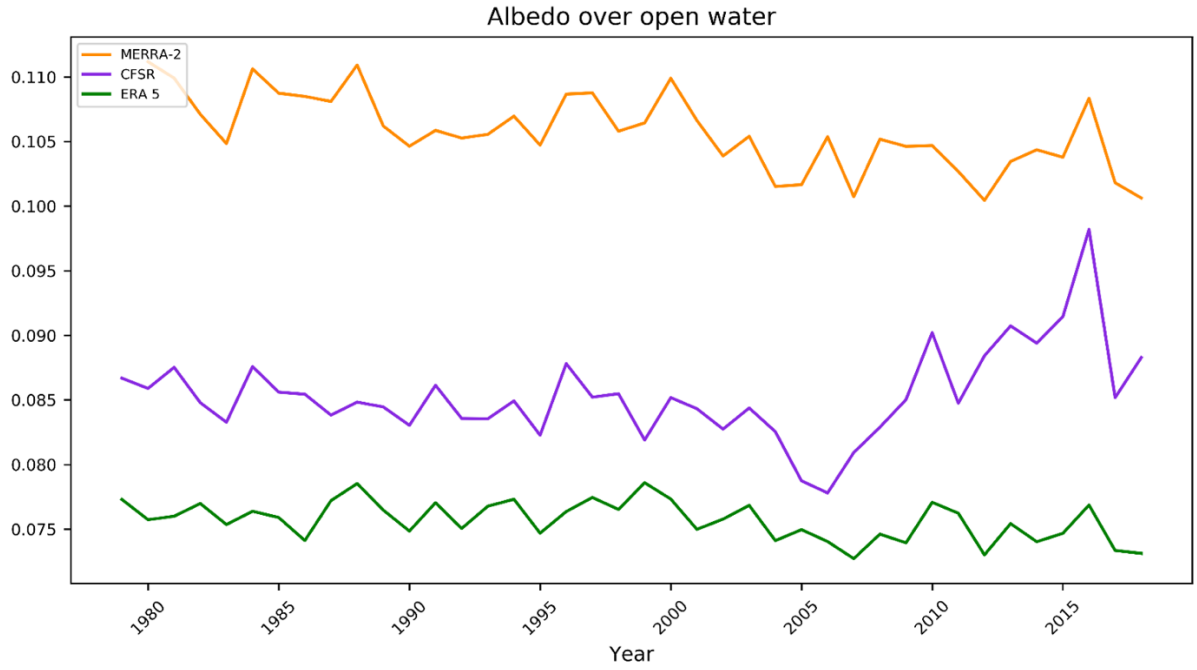

Figure 6.6: Yearly average albedo from April to August 1980 to 2018 over open water across the Arctic Ocean: ERA5 (green), CFSR (purple), and MERRA-2 (orange).

To better capture what component of the surface energy budget is impacting the spread between the accumulated heat gain values from each reanalysis, the accumulating values for net shortwave radiation, net longwave radiation, and the turbulent fluxes were calculated. Looking at the accumulated values for all the variables can help determine what other components need to be considered in future work to diagnose the problems in reanalysis data.

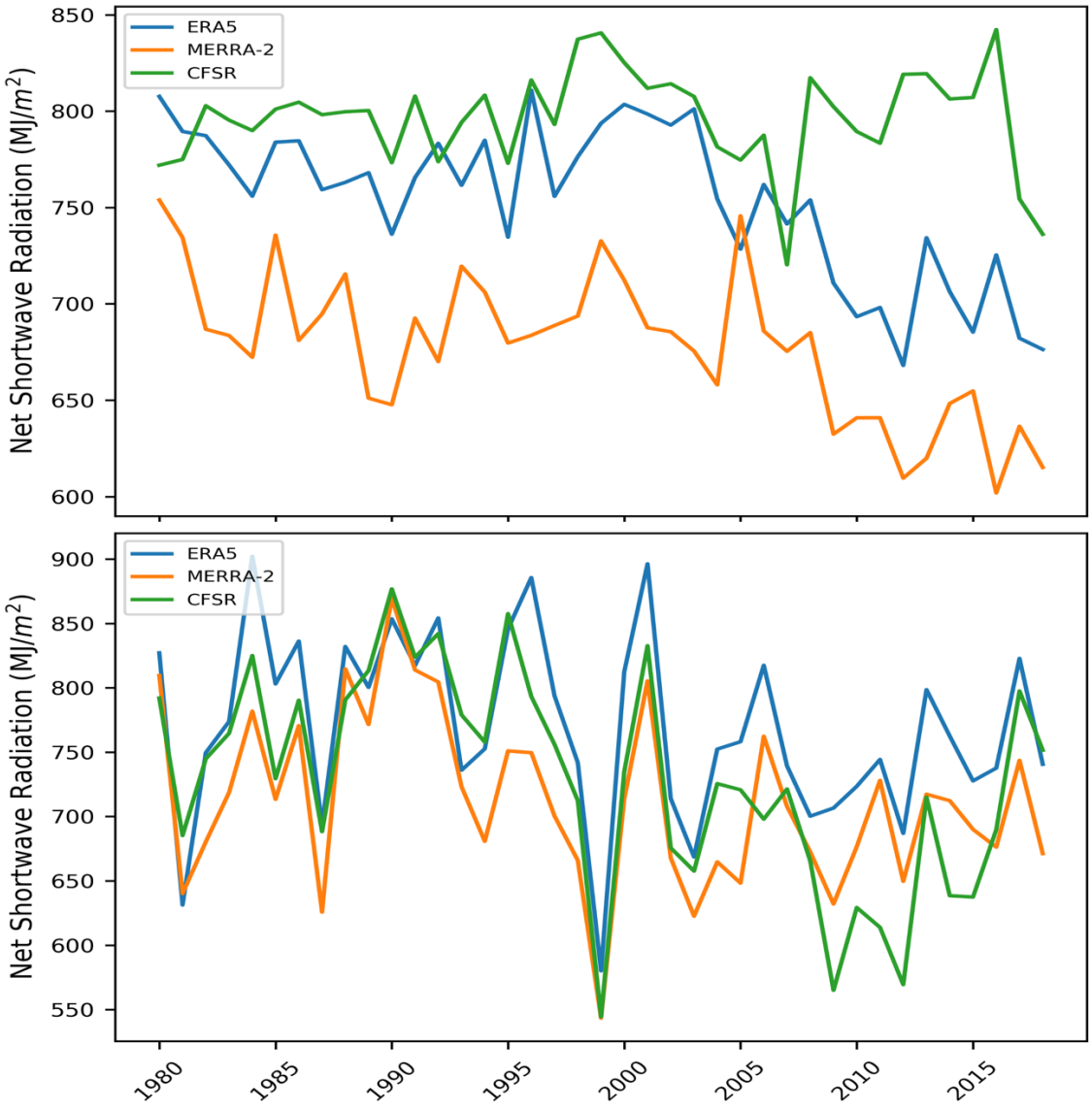

Figure 6.7: Yearly averages of accumulated net shortwave radiation from April to August 1980 to 2018 over sea ice (top) and open water (bottom) across the Arctic Ocean.

Figure 6.7 shows the accumulated net shortwave radiation over sea ice and open water across the Arctic Ocean between 1980 and 2018. ERA5 values are in blue, MERRA-2 values are in Orange and CFSR values are in Green. Looking at the top plot, MERRA-2 stands out with the lowest values for all years except one over sea ice; in some years it is particularly noticeable because MERRA-2's values are

200 MJ/m^2 different from values from CFSR. CFSR has relatively consistent values over sea ice and does not show a downward trend like ERA5 and MERRA-2 in the latter half of the record. This is likely due to the differences in cloud cover and height, cloud type, and surface albedo. As expected, there is more consistency in values between the accumulated net shortwave radiation over open water since the albedo of open water is much more consistent in value than the albedo over sea ice.

The accumulated net longwave radiation follows in Figure 6.8. Net longwave radiation over the sea ice and ocean is negative meaning that the surface is losing more heat than the atmosphere is radiating down to the earth. There are no large differences between the over sea ice and open ocean values although MERRA-2 does have the lowest accumulated net longwave radiation over sea ice. CFSR has the highest accumulated net long wave radiation over open water. The accumulated net longwave radiation values over the open water are not as consistent as the accumulated net shortwave radiation values in Figure 6.8. ERA5 and MERRA-2 values follow very similar temporal patterns while CFSR has higher values and does not follow the temporal pattern as closely. This is likely because the amount of energy emitted from the surface depends on the ocean temperature.

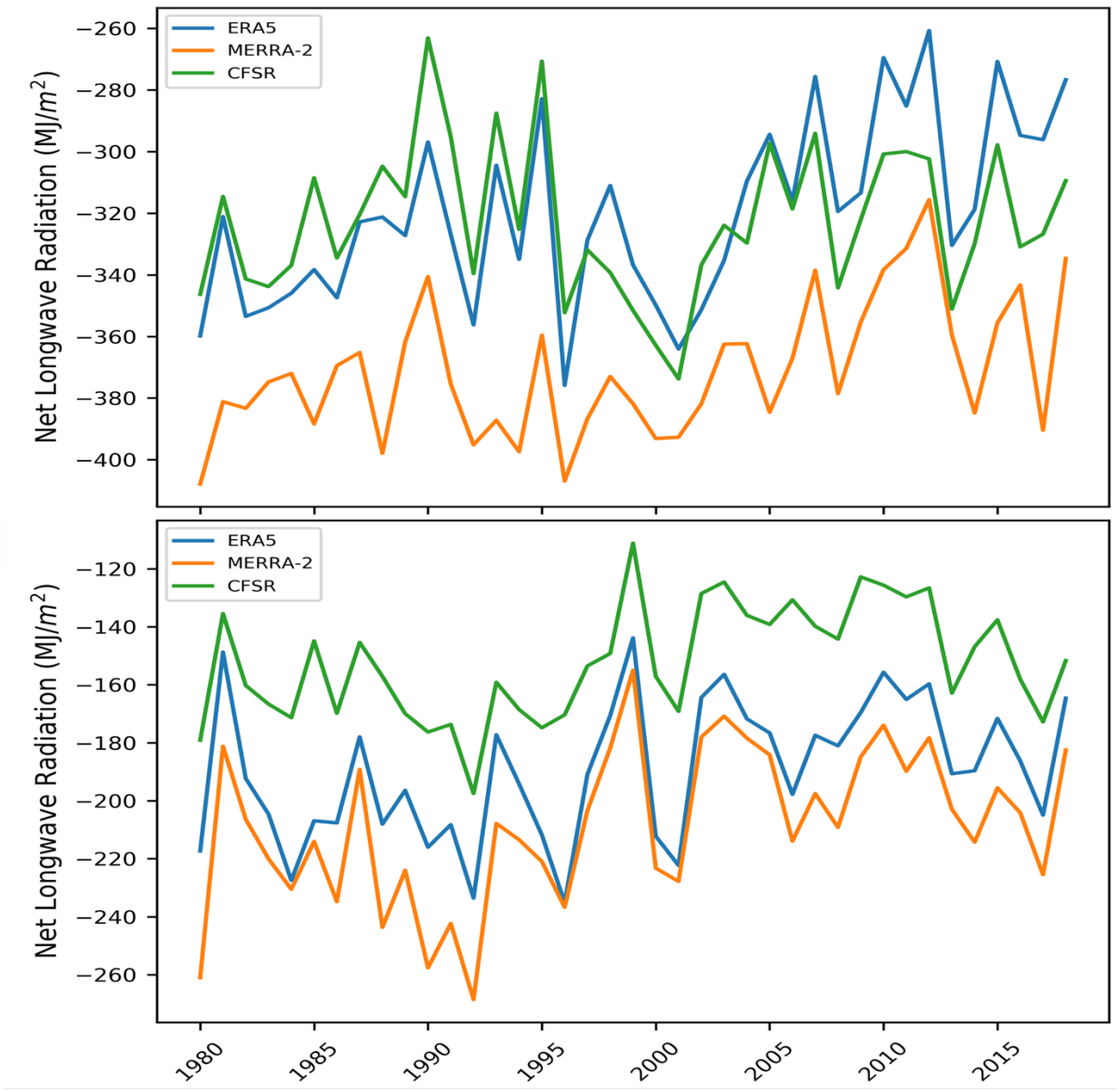

Figure 6.8: Yearly accumulated net longwave radiation from April to August 1980 to 2018 over sea ice (top) and open water (bottom) across the Arctic Ocean.

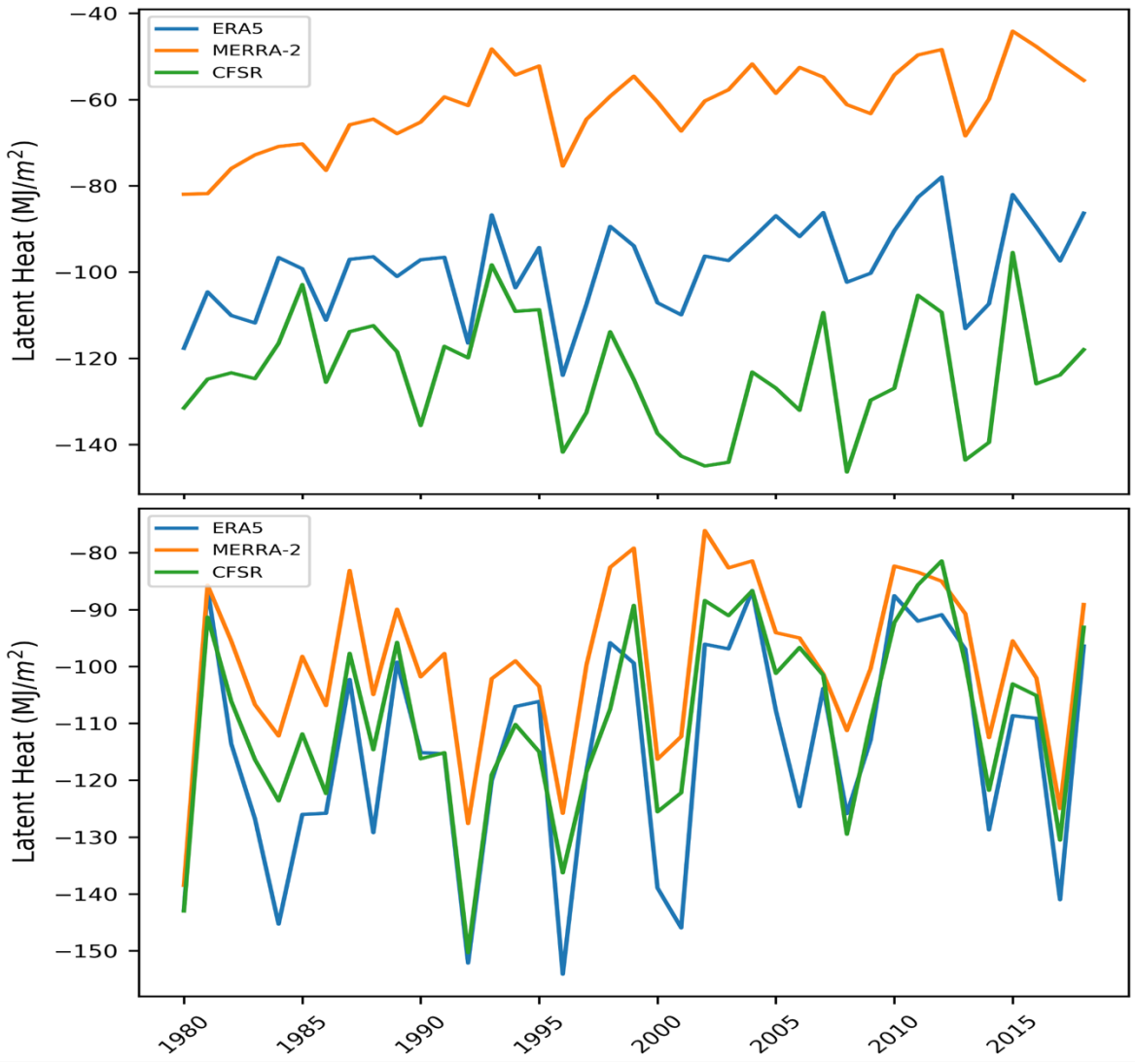

Figure 6.9: Yearly accumulated latent heat from April to August 1980 to 2018 over sea ice (top) and open water (bottom) across the Arctic Ocean.

Figure 6.9 shows the temporal patterns of the accumulated latent heat. Over sea ice, ERA5 and CFSR follow a similar temporal pattern with similar values from year to year. Yet, MERRA-2 shows a similar temporal pattern but has values that are much smaller than the other two reanalyses. These could be due to differences in sea ice melting within each reanalyses; there may be less melting in the MERRA-2 reanalysis which would be presented in the sea ice concentration/fraction data.

Over open water, the latent heat values express a very similar temporal pattern from year to year with similar values. These values are likely more consistent with one another because in the summer the melting ice holds the ocean surfer temperature very close to 0°C.

The accumulate sensible heat values over sea ice plotted in Figure 6.10 show a large spread between reanalysis values. From year to year, the reanalyses do not even show a similar temporal pattern. In this case, CFSR has the largest values ranging between 40 and 120 MJ/m^2 while ERA5 varies between -25 and 0 MJ/m^2 and MERRA-2 range from -75 and -20 MJ/m^2. This is a huge spread, and although turbulent fluxes are a small components of the net surface flux and hence the seasonal heat gain, it is important to address issues where they are known. Zhang et al. (2023) found that ERA5 aligns better with turbulent fluxes measured using the maximum entropy method, but how well they align depends on how the turbulent fluxes are calculated. This method of calculating turbulent fluxes is heavily affected by errors in the net radiative fluxes. This is stated to explain that the differences observed in the net radiation values may have an impact on the differences in sensible and latent heat over sea ice values.

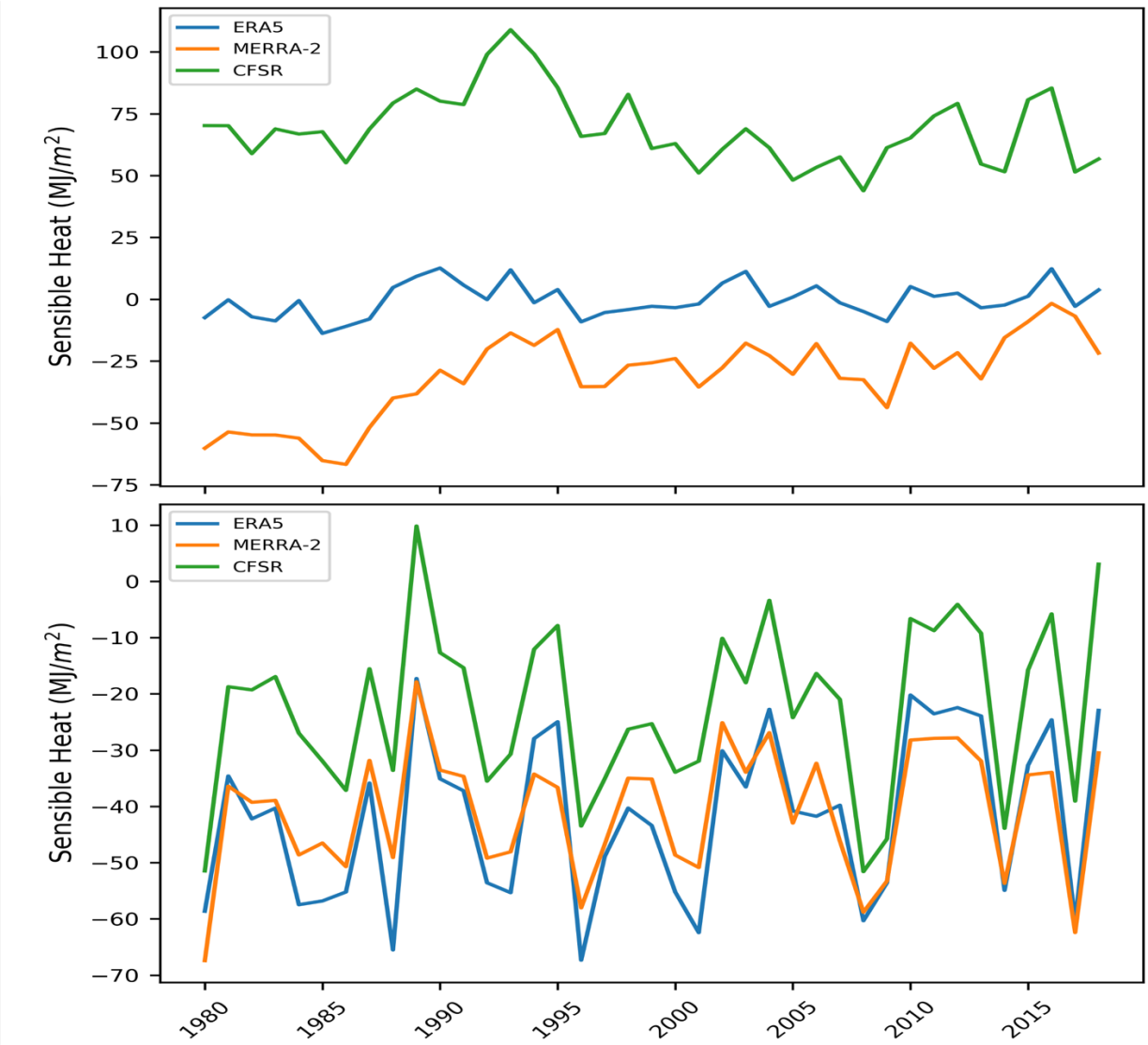

Figure 6.10: Yearly accumulated sensible heat flux from April to August 1980 to 2018 over sea ice (top) and open water (bottom) across the Arctic Ocean.

The bottom plot in Figure 6.10 shows the accumulated sensible heat flux over open water. Similar to all the plots over open water in Figures 6.7-6.9, the sensible heat values from each reanalysis have a similar temporal pattern. All the values range from -70 to 15 MJ/m^2 but all the reanalyses vary from year to year together.

Overall Figures 6.7-6.10 shows that MERRA-2 has the highest values with a decent spread from ERA5 and CFSR over sea ice for accumulated net shortwave and net longwave radiations. MERRA-2 also has the highest values over sea ice for the accumulated latent heat values. Alternatively, CFSR has the highest values for net longwave radiation over open water and the highest sensible heat values over open water and sea ice. ERA5 values either overlap/align with CFSR or MERR-2 (depending on the variable) or are in the middle.

Additional calculations were done for the polar cap domain, 70° N-90° N (Figure 6.11) to make direct comparisons with the study of Serreze et al. (2007). ERA5 has the largest magnitude of values across the entire time series for the polar cap domain. Recall that the polar cap domain is mostly ocean but contains some land. CFSR and MERRA-2 are somewhat lower and after 2007 these values overlap for the rest of the time series. Although the magnitudes are different, similar to the previous figures, the year-to-year patterns across this time series line up decently. Differences are mostly in terms of magnitude, but the differences in magnitude are large. Why ERA5 has the highest values may be because ERA5 defines open water as sea ice concentration at or below 20% instead of at or below 15% in reanalyses. This could mean that in the calculations for 70° N-90°N there is more open water in the ERA5 calculations.

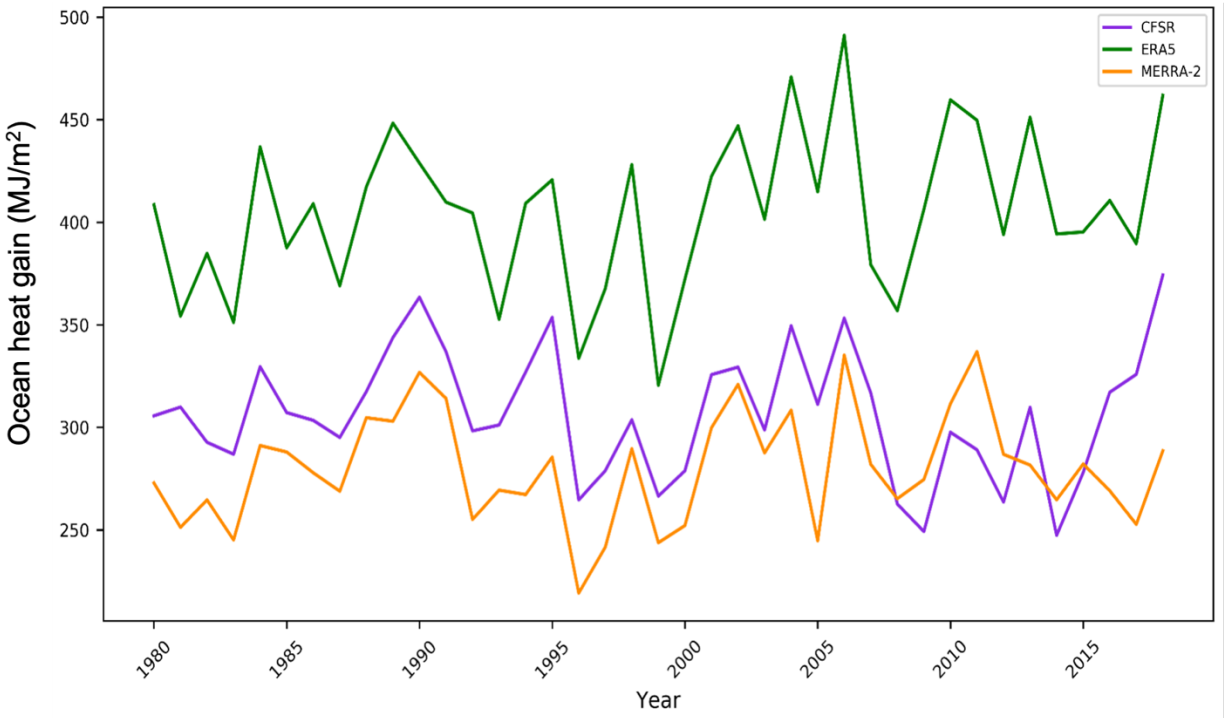

Figure 6.11: Seasonal heat gain from the net surface heat flux over the open water portion of the polar cap domain from ERA5 (green), CFSR (purple), and MERRA-2 (orange).

Conversely, Figure 6.11 shows that CFSR has the largest magnitude of heat gain over the part of the polar cap covered by sea ice. ERA5 is in the middle and MERRA-2 has the lowest heat gains. Although MERRA-2 and ERA5 values dip in 2002, CFSR had the largest decline in values that year. Yet, overall, the year-to-year pattern does match across all reanalyses. This is similar to all the previous figures as well.

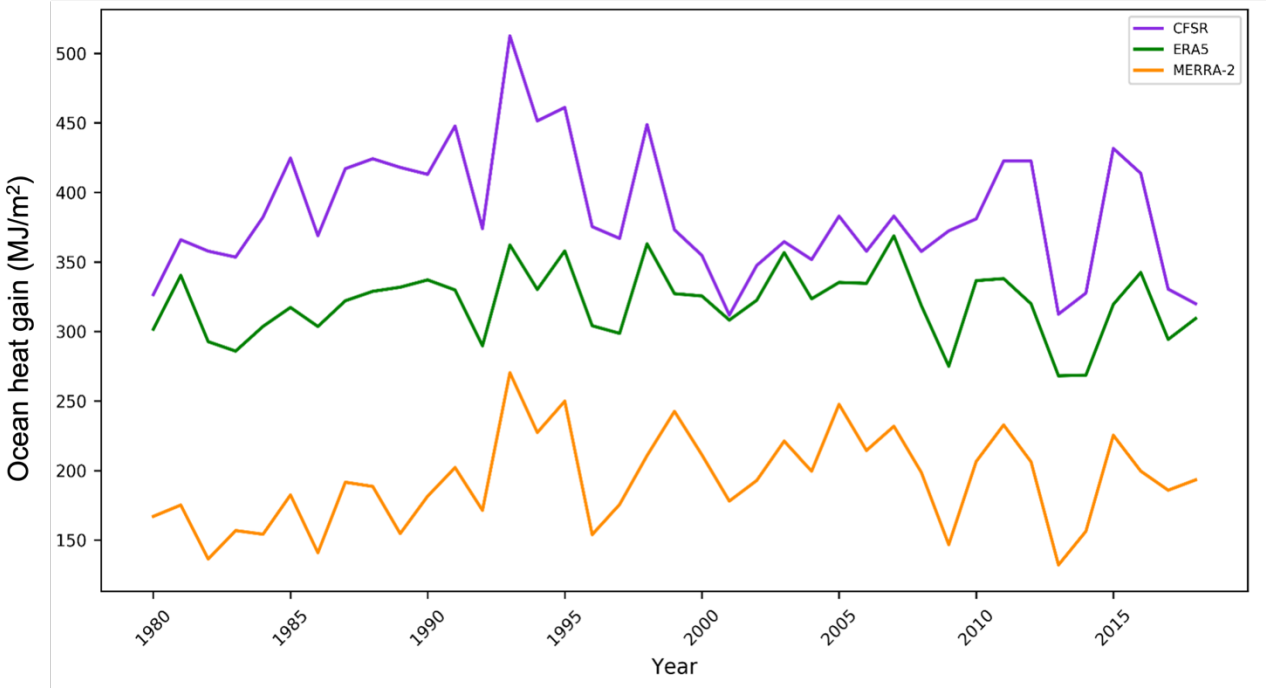

Figure 6.12: Seasonal heat gain from the net surface heat flux over the sea portion of the polar cap domain from ERA5 (green), CFSR (purple), and MERRA-2 (orange).

To bolster the comparison results for seasonal heat gain between 70° N and 90° N, Table 6.2 summarizes correlation statistics. ERA5 and CFSR (r=0.61) and MERRA-2 and CFSR (r= 0.54) values over sea ice are moderately positively correlated. ERA5 and MERRA-2 (r= 0.77) values over sea ice are strongly correlated and all comparisons are statistically significant at the 99% confidence level. Values over open water also show moderate positive correlations between CFSR and ERA5 (r=0.61) and CFSR and MERRA-2 (r= 0.53). Again, ERA5 and MERRA-2 are strongly correlated (r= 0.8) and all relationships are significant at the 99% confidence level.

Table 6.2: Correlations between seasonal heat gain from net surface heat flux between 70°N and 90°N.

	CFSR			ERA5			MERRA-2		
	R^2	R	p	R^2	R	p	R^2	R	p
Over Sea Ice									
CFSR				0.37	0.61	**3.3e-5**	0.3	0.54	**0.0004**
ERA5	0.37	0.61	**3.3e-5**				0.6	0.77	**9.23e-9**
MERRA-2	0.3	0.54	**0.0004**	0.6	0.77	**9.23e-9**			
Over Ocean									
CFSR				0.4	0.63	**1.8e-5**	0.28	0.53	**0.00046**
ERA5	0.4	0.63	**1.8e-5**				0.64	0.8	**3.4e-9**
MERRA-2	0.28	0.53	**0.00046**	0.64	0.8	**3.4e-9**			

In summary, all relationships are positively correlated over both open water and ice, with the reanalyses agreeing with respect to some of the years with an especially high or low heat gain. Agreement between reanalysis values in this region is particularly arguably fairly good.

6.3 Focus on Contrasting Years

Figure 6.13 depicts seasonal heat gain anomaly values from April to August over sea ice in 1982, 1996, 2007, and 2012 from the three reanalyses (calculated with respect to 1980 to 2018 means). Recall that the data has been separated out over sea ice and open water based on the daily sea ice concentration data from each reanalysis; based on the approach outlined at the beginning of this chapters and

introduced in Chapter 3. Despite differences in magnitude, there are similarities in the spatial patterns of anomalies. First, the two years (1982 and 1996) that have anomalously high September sea ice extent show negative anomalies across much of the central Arctic Ocean. Conversely, the years 2007 and 2012, which have especially low September sea ice extent, have large positive anomalies over the central Arctic Ocean and extending into some of the marginal seas. The central Arctic Ocean shows the most recognizable pattern between the years that have low September sea ice extents and high September sea ice extents.

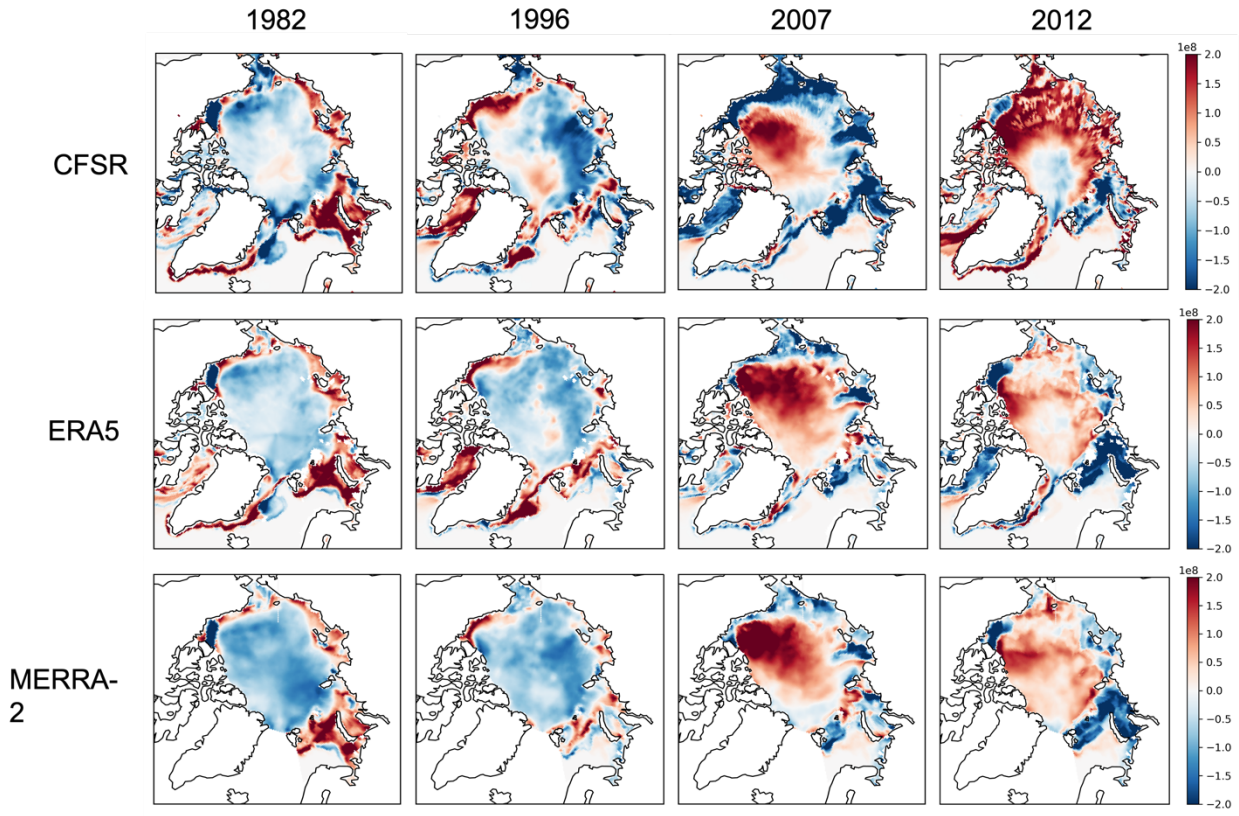

Figure 6.13: Spatial distribution of seasonal heat gain anomalies over sea ice in MJ/m^2 from April to August in 1982, 1996, 2007, and 2012 from CFSR, ERA5, MERRA-2.

Figure 6.14 shows the seasonal heat gain anomalies over open water from the same four years as Figure 6.13. Values over the central Arctic Ocean are zero because these areas are covered in perennial sea ice. Similar to the results in Figure 6.13, the years 1982 and 1996 have negative net flux anomalies in the marginal seas, signifying that there is less heat in the ocean at the end of the summer than for years with anomalously high September sea ice extents (at least as supplied by the net surface flux). By contrast, 2007 and 2012 show large seasonal net surface heat flux values in all marginal seas except the Barents Sea.

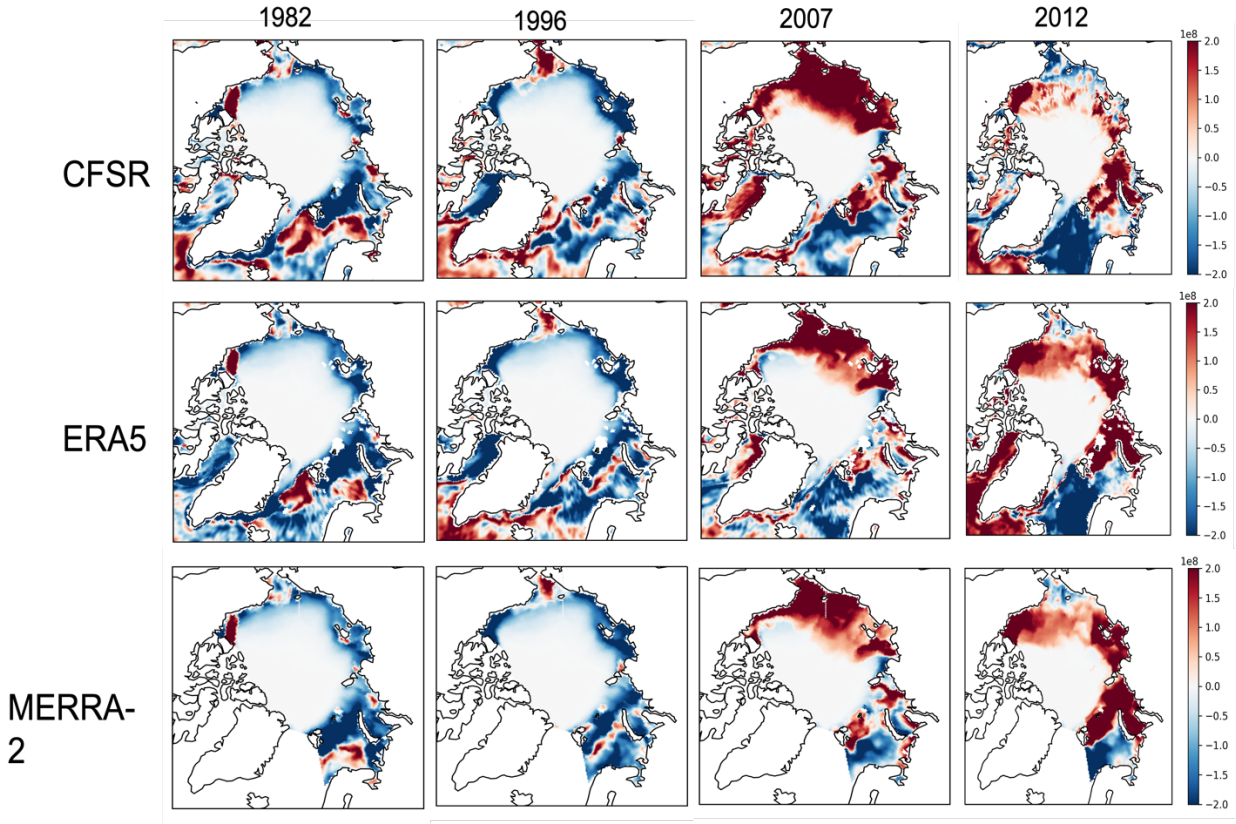

Figure 6.14: Spatial distribution of seasonal heat gain anomalies over open water in MJ/m^2 from April to August in 1982, 1996, 2007, and 2012 from CFSR, ERA5, MERRA-2.

To further quantify differences between the datasets, Figures 6.15 and 6.16 show the percent difference in heat gain between the reanalyses. Over sea ice (Figure 6.15), ERA5 and CFSR have the most similar values. In many areas, CFSR values are ~25% larger or smaller (depending on region) than ERA5. CFSR is significantly different from MERRA-2, particularly in 1982 and 1996. The smallest differences between CFSR and MERRA-2 are in 2007 while those in 2012 are larger, especially in the marginal seas. Lastly, ERA5 and MERRA-2 show differences roughly in the middle of the other two comparisons. Again though, 1982 and 1996 show larger percent differences across the whole Arctic Ocean between ERA5 and MERRA-2.

For the two years when September sea ice was anomalously low, there appears to be less spread between the reanalyses yet each comparison shows a wide variation of percent differences. It was expected that the years with anomalously high September sea ice extents would have the smallest differences because the ice limits the amount of energy that transfers between the atmosphere and ocean. Yet, we see that those years, in the subsets shown in Figure 6.15, show the largest percent differences.

Figure 6.16 shows results calculated over open water. These plots provide little evidence of one reanalysis having values either higher or lower than the reanalyses for all years. CFSR has larger values right around the ice edge when compared to ERA5, likely due to the differences in sea ice location determination.

Recall that ERA5 defines ice free as 20% or less for sea ice concentration while the rest of the reanalyses define ice free as 15% or less concentration.

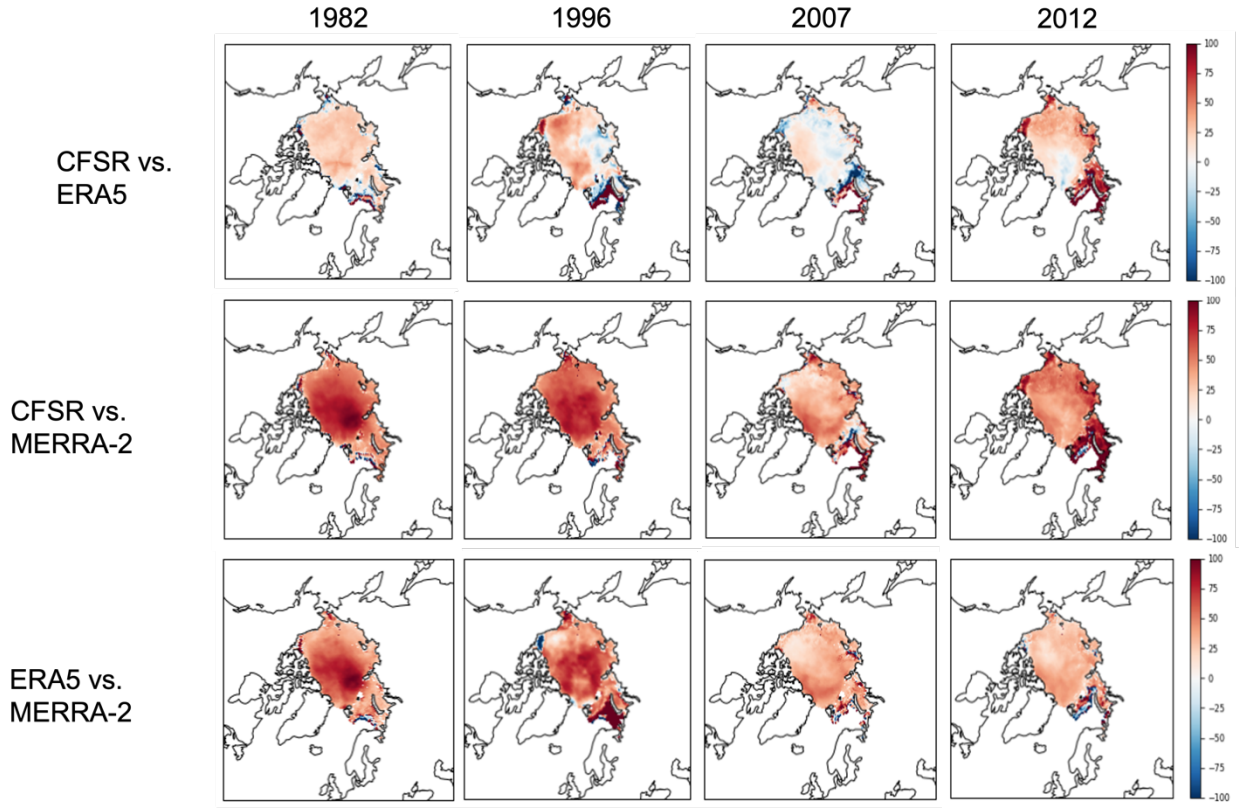

Figure 6.15: Percent differences between seasonal heat gain over ice from April to August in 1982, 1996, 2007, and 2012 from CFSR, ERA5, MERRA-2.

The 2012 values from CFSR are much lower than depicted by ERA5. There are many areas where the differences exceed 10%. The percent differences seen between CFSR and MERRA-2 have similar values to the plots featuring the differences between CFSR and ERA5. The percent differences between ERA5 and MERRA-2 are much smaller than in the other two comparisons, except in 1996. In 1982, 2007, and 2012, the percent differences are closer to 25%, except right around the ice margin. But in 1996, the differences between the two models are much larger. There are a few areas along the eastern Alaskan coast and along the

Russian coast that show ERA5 values 100% larger (twice as large) as those depicted by MERRA-2. Along the north edge of the Barents Sea, MERRA-2 values are much larger than ERA5. This region may show larger differences because there is a large amount of heat transported in the atmosphere and the ocean through the Barents Sea that may be hard to capture in a fixed physics model.

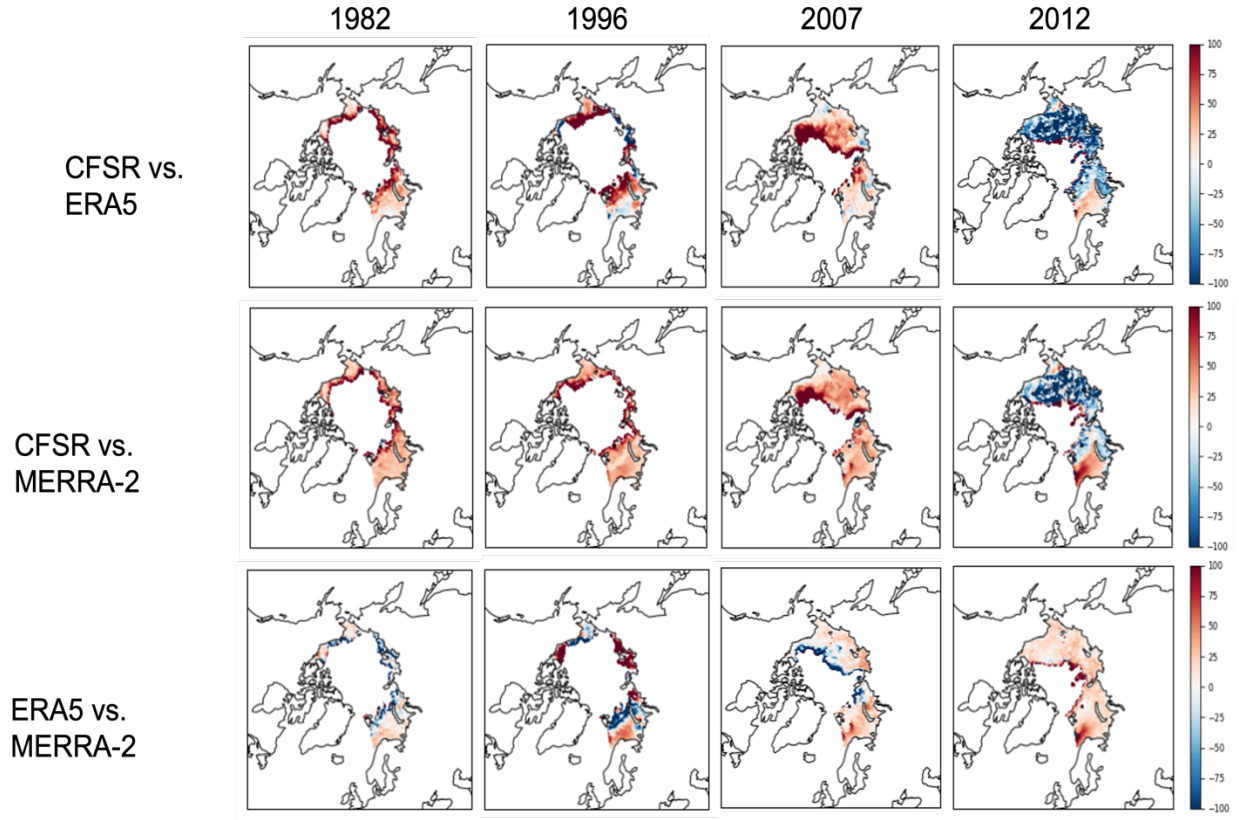

Figure 6.16: Percent differences in seasonal heat gain over ocean from April to August in 1982, 1996, 2007, and 2012 from CFSR, ERA5, MERRA-2.

6.4 Regional Comparisons

As a note, part of the analysis was to assess differences between the Barents, Beaufort, and Chukchi Seas and the central Arctic Ocean. As a reminder, the regions were selected to offer contrasting environments.

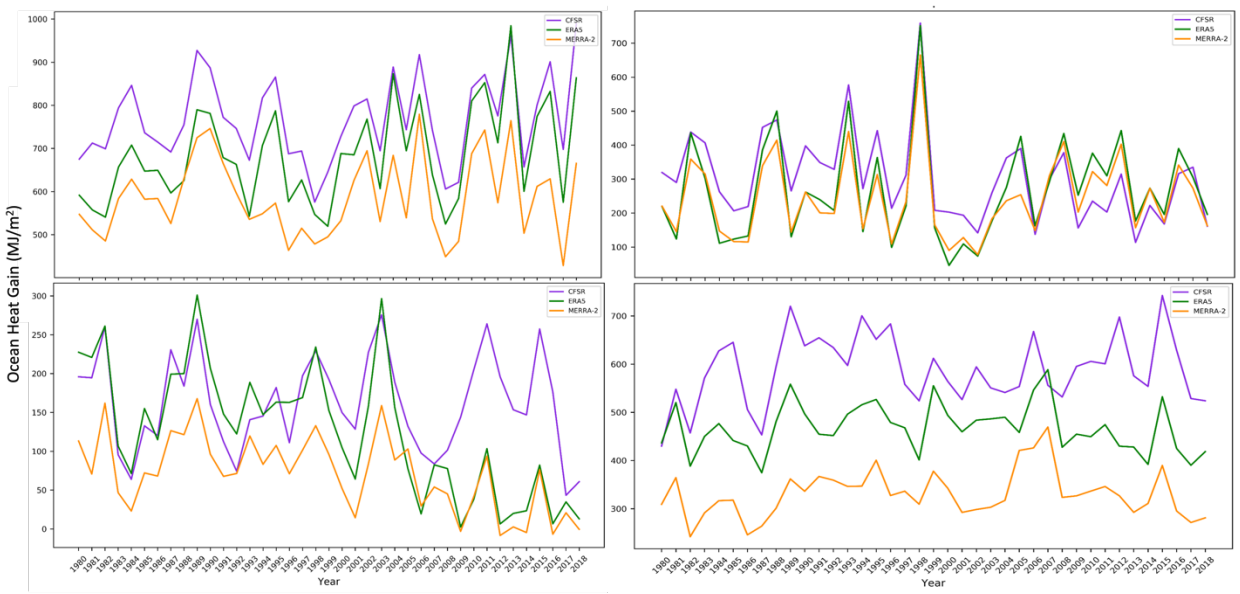

Figure 6.17: Seasonal heat gain from the net surface flux from 1979 to 2018 over open water and sea ice in the Barents (left) and Beaufort (right) Seas from the three reanalyses: ERA5 (green), CFSR (purple), and MERRA-2 (orange).

Figure 6.17 plots values over open ocean and sea ice from 1980 to 2018 in the Barents and Beaufort Seas, which lie on opposite sides of the Arctic Ocean. The top panels are for values over open water and show very similar values between all the reanalyses. There are large peaks and valleys between each year for both regions. And interestingly enough, the values in these regions are much larger than what is depicted in Figures 6.4 and 6.6. The bottom panels show values over sea ice in the Barents and Beaufort Seas. Although the Barents Sea values show some similarities, CFSR diverges from the other two reanalyses after 2007. In the Beaufort Sea, all reanalyses are spread over 400 MJ/m^2. This is an enormous range.

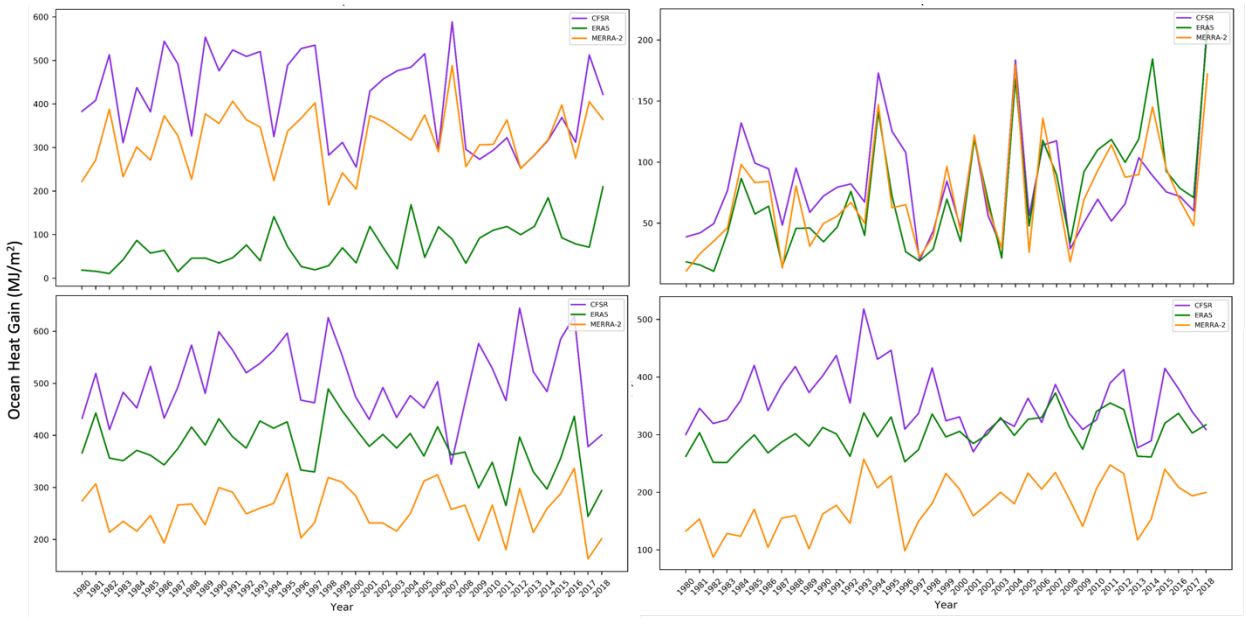

Figure 6.18: Seasonal heat gain from the net surface flux for1979 to 2018 over open water and sea ice in the Chukchi Sea and the Central Arctic Ocean as defined by the MASIE definitions from ERA5 (green), CFSR (purple), and MERRA-2 (orange).

Plots for the Chukchi Sea and Central Arctic Ocean plots over open water and over sea ice are presented in Figure 6.18. For the Chukchi Sea, the reanalyses are spread across a range of 400-500 MJ/m^2 between 100 MJ/m^2 to 600 MJ/m^2. These results are similar to those in Figure 6.17 for the Beaufort Sea over sea ice. Across the central Arctic Ocean, the net surface heat flux over the open ocean shows very similar values between all of the reanalyses. Yet over the sea ice the three

reanalyses show a large range until the year 2000. After the year 2000 CFSR and ERA5 mostly overlapped for the rest of the record.

Table 6.3: Descriptive statistics of seasonal heat gain for all reanalyses over sea ice and open water in the Barents Sea, Beaufort Sea, Chukchi Sea, and the Central Arctic Ocean, all in MJ/m^2.

	CFSR	ERA5	MERRA-2	CFSR	ERA5	MERRA-2
	Over ice			Over Ocean		
Barents Sea						
Max	275.7	301.1	167.7	989.0	984.5	779.2
Min	43.3	2.3	-8.5	575.6	519.5	428.4
Mean	163.8	129.5	70.7	765.3	680.6	586.8
Beaufort Sea						
Max	742.3	588.4	469.4	758.8	751.3	665
Min	429.9	374.5	241.9	113.8	46.0	77.6
Mean	585.2	466.5	330.5	305.2	264.8	243.1
Chukchi Sea						
Max	644.4	489.2	336.41	588.3	209.7	488.0
Min	344.5	244.1	162.6	252.1	10.5	167.8
Mean	500.5	373.6	255.9	411.2	71.4	319.9
Central Arctic Ocean						
Max	518.1	372.4	257.4	215.2	209.7	179.5
Min	270.0	251.6	87.1	19.4	10.5	10.9
Mean	357.1	300.7	176.3	81.7	71.4	72.8

Table 6.3 further highlights similarities and differences between the heat gain values from the reanalyses across four regions. In the Barents Sea over sea ice

ERA5 had the highest maximum, MERRA-2 had the lowest minimum, and CFSR had the highest average. CFSR had the highest maximum over the ocean, MERRA-2 had the lowest minimum, and CFSR had the largest average. The differences in over sea ice versus over open water are quite large. This is likely due to the limited time that the Beaufort Sea has ice cover in the spring; the majority of the year is ice free.

Similar to the Barents Sea, in the Beaufort Sea CFSR has the largest maximum, MERRA-2 has the lowest minimum, and CFSR has the largest mean values over sea ice. CFSR has the highest maximum, ERA5 has the lowest minimum value and CFSR has the highest mean over open ocean. The values over sea ice and open water are likely more similar than those seen in the Barents Sea because the Beaufort Sea has more sea ice throughout the melt season.

In the Chukchi Sea over sea ice CFSR has the largest maximum value, MERRA-2 has the lowest minimum, and CFSR has the largest mean. Over open ocean, CFSR, again, has the largest maximum, ERA5 has the lowest minimum, and CFSR has the largest mean value. These results appear quite similar to those in the Beaufort Sea because they are neighbors and have similar sea ice conditions.

Lastly, in the central Arctic Ocean over sea ice CFSR has the largest maximum, MERRA-2 has the smallest minimum, and CFSR has the largest mean. Over open water CFSR has the largest maximum, but only by a few MJ/m^2, ERA5 had the smallest minimum, and CFSR had the largest mean. Values over the open water are quite low, which is due to limited open water in this region. The central

Arctic Ocean largely remains ice covered through the year; the only open water that occurs in the central Arctic Ocean are in leads and polynyas.

6.5 Net Surface Flux and Heat Gain Estimates

Given all that has been discussed so far, is it possible to assemble a good net surface flux estimate and hence seasonal heat gain time series from the reanalyses, either for the study domain as a whole or for subregions? One approach is to take the "best of the fluxes" from the different reanalyses, based on the comparisons with the direct surface observations detailed in Chapter 5, and combine them. An obvious drawback to this approach is the violation of energy conservation.

Nevertheless, to proceed with this approach, a conclusion from Chapter 5 is that the best performing reanalysis for downwelling shortwave radiation, upwelling shortwave radiation, and downwelling longwave radiation is MERRA-2, while the best performing reanalysis for upwelling longwave radiation is CFSR. This is based on the correlations between detrended daily radiation component data between 1993 and 1997 from each reanalysis. MERRA-2 performed the best for downwelling shortwave (MOSAiC r= 0.77, ARAON r= 0.67), and upwelling shortwave radiation (SHEBA r=0.63, MOSAiC r= 0.74) with positive correlations statistically significant at the 95% confidence interval. MERRA-2 also performed the best for downwelling longwave radiation with a correlation coefficient of 0.76 for SHEBA and 0.84 for MOSAiC. CFSR outperformed the other two reanalysis for upwelling longwave radiation with a correlation coefficient of 0.91. Combining these yields the net

radiation. As described earlier, assessing the quality of the turbulent fluxes proved to be difficult. As a seasonal heat gain time series is compiled using the combined MERRA-2/CFSR net radiation and the turbulent flux values from each reanalysis of the three reanalyses.

Figure 6.19 shows results over the sea ice portion of the study domain; the purple line shows values using the turbulent fluxes from CFSR, the orange line shows values using MERRA-2 turbulent fluxes, and the green line shows those values using the ERA5 turbulent fluxes.

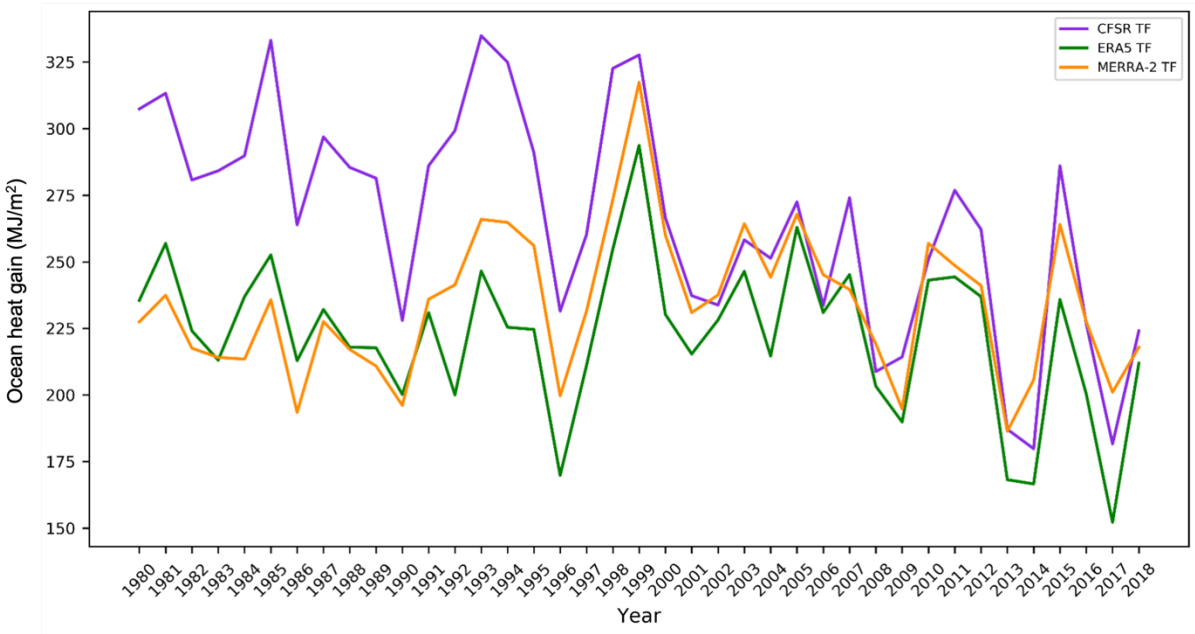

Figure 6.19: Seasonal heat gain from the net surface heat flux averages over sea ice using radiation values from MERRA-2 and CFSR and turbulent flux values from ERA5 (green), CFSR (purple), and MERRA-2 (orange) across the whole Arctic Ocean.

The values using the turbulent fluxes from CFSR and MERRA-2 align with one another rather well. In Chapter 4, the results showed that the turbulent fluxes from CFSR and MERRA-2 were quite different from one another; it is surprising that the net surface flux (net surface heat flux) values here would be so similar

when the only difference is which reanalysis the turbulent fluxes come from. The heat gain values using the turbulent fluxes from ERA5 are well below those using CFSR and MERRA-2 fluxes.

To address this point further, Figure 6.20 portrays the seasonally average sensible and latent heat fluxes across the entire study domain between April and August from 1980 to 2018. CFSR has the strongest negative (downward) values of sensible heat while ERA5 and MERRA-2 more closely reflect one another. CFSR is also very different than ERA5 and MERRA-2 for the latent heat flux; the time series is characterized by positive (upward) mean values of 45-60 W/m^2. The CFSR time series for both fluxes are also more variable.

Initial results in Chapter 4 also showed that ERA5 and MERRA-2 turbulent fluxes were more similar to each other than they were to CFSR. Turbulent fluxes are expected to be poorly captured within the reanalyses because (like the other fluxes) they are highly parameterized. Even observational measurements can be prone to considerable uncertainty, and measured values can be very site specific. Nevertheless, from basic physical considerations, the turbulent fluxes should be quite small in summer over a melting ice cover (on the order of 5 W/m^2) such as shown in the SHEBA data, as well as over open water. This is not borne out in the results from CFSR. The latent heat values in particular seem physically unrealistic. This argues that the combinations of the "best" net radiation and the CFSR turbulent fluxes to produce the net surface flux and seasonal net surface heat flux is a poor choice.

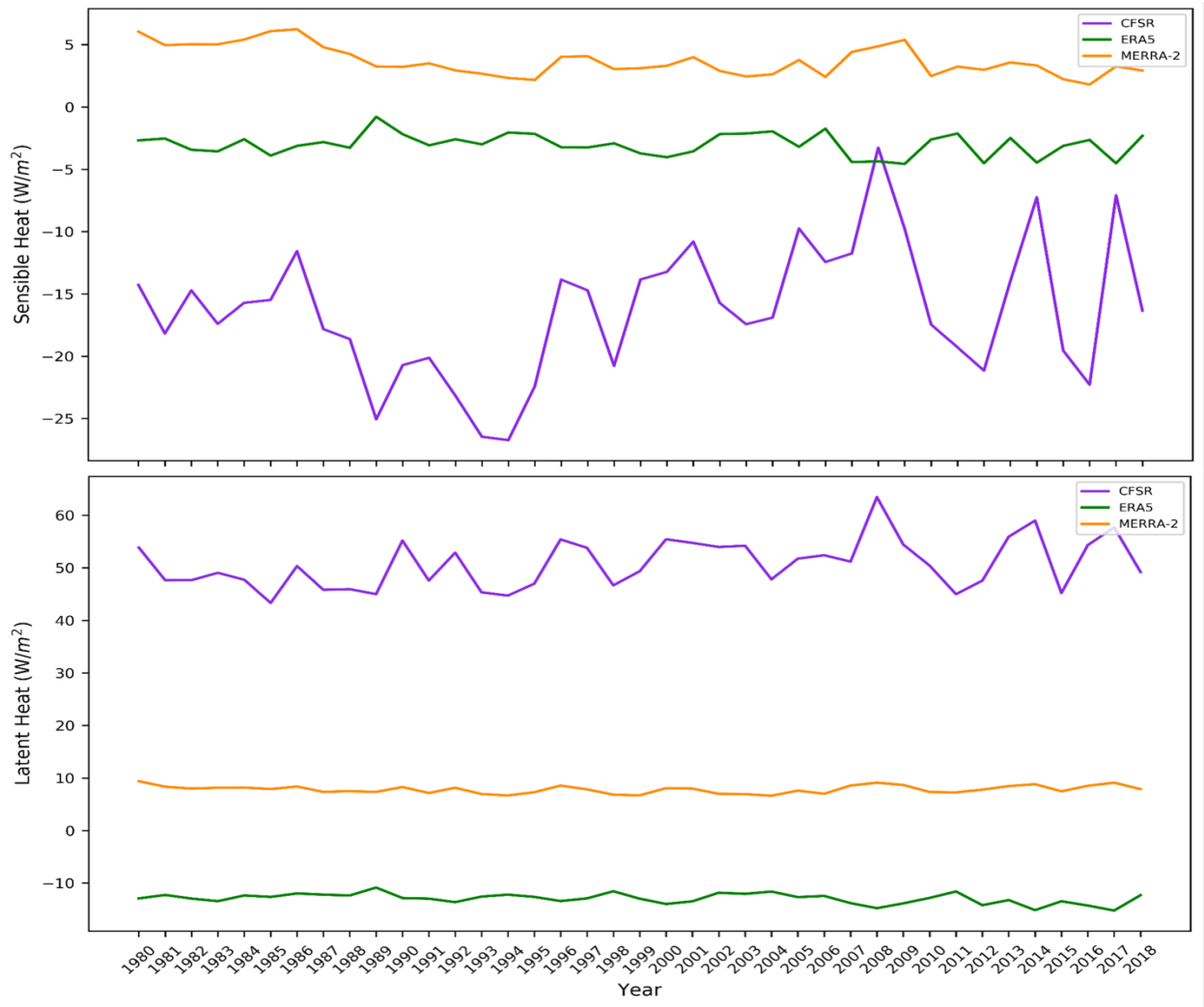

Figure 6.20: Seasonally averaged sensible (top) and latent (bottom) heat fluxes in W/m^2 across the Arctic Ocean and marginals seas between April and August from 1980 to 2018.

The corresponding seasonal heat gain estimates from this approach over open water show a much smaller spread (Figure 6.21). While this suggests that the differences between the reanalyses in the turbulent fluxes are having a smaller effect, it may also simply mean that the larger turbulent fluxes in CFSR are simply balancing biases in other flux terms.

Figure 6.21: Seasonal heat gain from the net surface heat flux averages over open water across the Arctic Ocean using radiation values from MERRA-2 and CFSR and net turbulent flux values from ERA5 (green), CFSR (purple), and MERRA-2 (orange) across the whole Arctic

Attention now turns to looking at the anomalies from the estimates just described for the four years contrasting September sea ice extents described earlier (Figures 6.22 and 6.23). In 1982, the heat gain using the turbulent fluxes from CFSR (Figure 6.22) has small positive anomalies across the central Arctic Ocean and much larger positive anomalies along the coasts. The patterns that use ERA5 turbulent fluxes shows less positive anomalies in the central Arctic Ocean. Lastly, the heat gain estimates using turbulent fluxes from MERRA-2 show widespread negative anomalies across the central Arctic Ocean. These patterns follow the previous results that show ERA5 and MERRA-2 values are more similar to one another than CFSR and MERRA-2 (Figure 6.15). The anomaly patterns for 1996 show very similar large-scale negative values across the Central Arctic Ocean with positive anomalies along the coast lines. Upon closer look, there are different

regional patterns for all of these anomalies depending on which reanalysis' turbulent fluxes we used in the calculations.

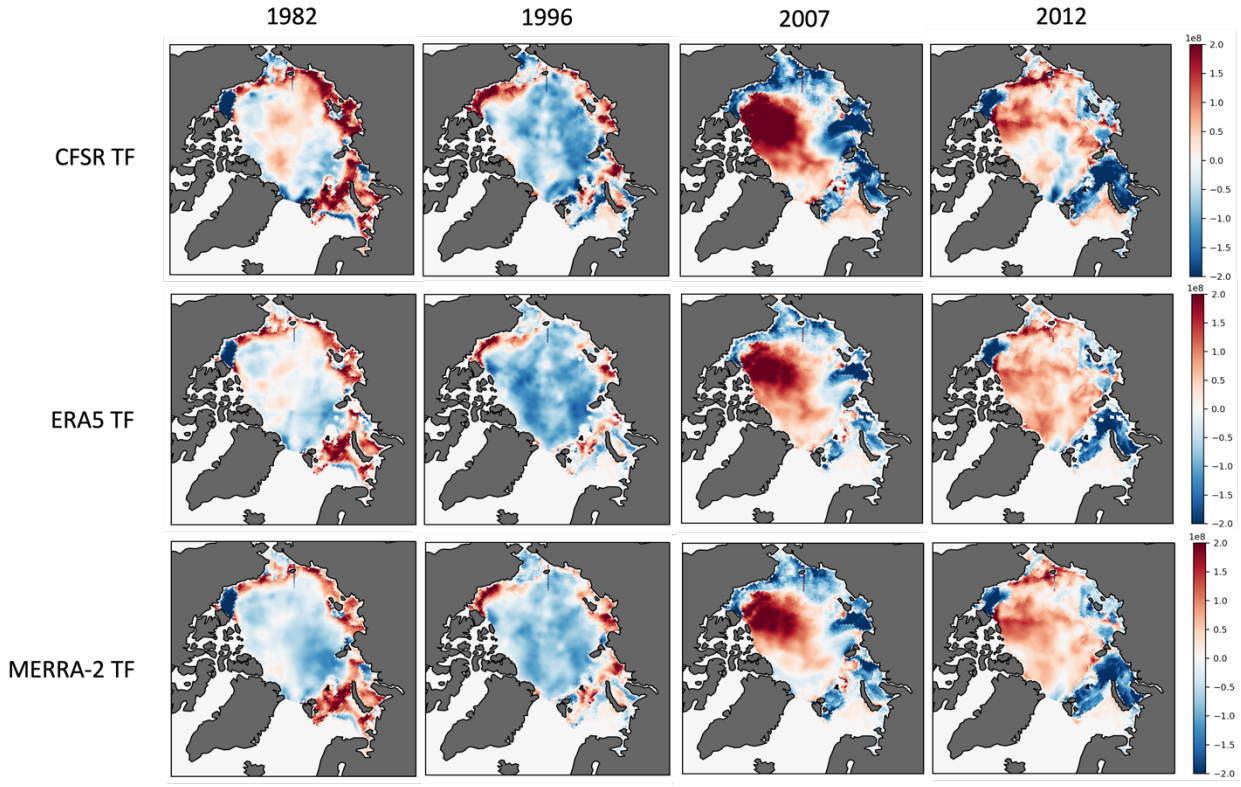

Figure 6.22: Spatial distribution of seasonal heat gain anomalies from the net surface heat flux over sea ice in MJ/m2 from April to August in 1982, 1996, 2007, and 2012 with turbulent flux (TF) values from CFSR, ERA5, MERRA-2.

Remember that 2007 and 2012 are the two years with the lowest September sea ice extent. A combination of conditions led to these two years holding the first and second places in the sea ice record, including a large storm in 2012 that broke up the sea ice cover. In 2007, a combination of high pressure over the Beaufort Sea and low pressure over northwestern Eurasia funneled warm air from the south into the Chukchi Sea sector and to the north, leading to strong melt. This manifested in the large and distinct positive anomaly in heat gain extending northward from the coast (Figure 6.22). The remainder of the Arctic Ocean and marginal seas have

negative anomalies. The Beaufort Gyre is very closely connected to the ocean's surface and thus has an intimate relationship with the sea ice cover (Timmermans and Toole, 2023). Timmermans and Toole (2023) found that in years where September sea ice extent is anomalously low, there is an increase in net surface heat flux, fresh water storage, and changes in salinity stratification. The change of these characteristics can be difficult to model, especially in a fixed physics model like reanalyses. Finally, 2012 shows the most widespread positive anomalies across the region. Although the anomalies are smaller than those seen in 2007, there are more areas with positive anomalies than in all previous years shown. Additionally, there are pronounced negative anomalies in the Kara and Barents Seas and along the coasts.

Table 6.4, shows the temporal correlations between the heat gain values based on adding the turbulent flux values from the three reanalyses to the net radiation that combines the flux terms from CFSR and MERRA-2. All correlations are significant at the 99% confidence level although some are not especially high for sea ice areas. Correlations are much stronger over the open ocean areas.

Table 6.4: Correlations between heat gain estimates using turbulent flux values from the three reanalyses and net radiation that combines the flux terms from CFSR and MERRA-2. TF stands for turbulent fluxes.

	CFSR TF			ERA5 TF			MERRA-2 TF		
	R^2	R	p	R^2	R	p	R^2	R	p
Over Sea Ice									
CFSR TF				0.5814	0.7625	**1.7e-8**	0.3575	0.5979	**5.83e-5**
ERA5	0.5814	0.7625	**1.7e-8**				0.6217	0.7885	**2.51e-9**
MERRA-2 TF	0.3575	0.5979	**5.83e-5**	0.6217	0.7885	**2.51e-9**			
Over Ocean									
CFSR TF				0.905	0.9513	**1.7e-20**	0.9473	0.9733	**3.0e-25**
ERA5 TF	0.905	0.9513	**1.7e-20**				0.9493	0.9743	**1.5e-25**
MERRA-2 TF	0.9473	0.9733	**3.0e-25**	0.9493	0.9743	**1.5e-25**			

Figure 6.23 shows spatial anomalies in the heat gain values using turbulent flux from the three reanalyses over open ocean for the four contrasting years. In 1982 and 1996, years with a large September sea ice extent, there are negative anomalies over most of the marginal seas. There are small positive anomalies in the Bering Strait, Chukchi Sea, and the Barents Sea. All calculations of open net surface heat flux for these two years are very similar to one another. The plots for 2007 and 2012 document positive anomalies over the majority of the marginal seas in both years; 2007 has the largest positive anomalies. One notable similarity with 1982 and 1996 is that there are negative anomalies over the Barents Sea in these plots as well.

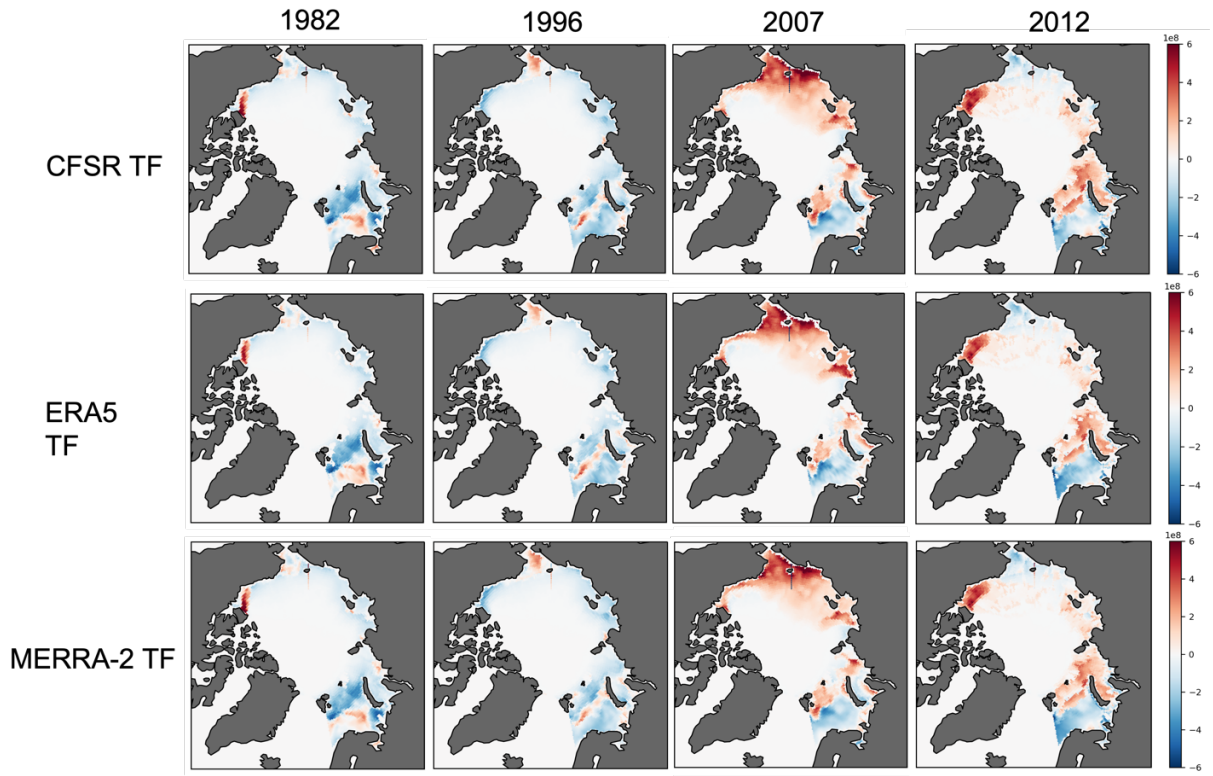

Figure 6.23: Spatial distribution of seasonal anomalies in heat gain from the net surface flux over ocean in MJ/m^2 from April to August in 1982, 1996, 2007, and 2012 with turbulent flux (TF) values from CFSR, ERA5, MERRA-2.

Again, these differences solely due to the different turbulent flux estimates. The anomaly patterns from each reanalysis are more consistent over open water as seen in Figure 6.21 and Table 6.3. One expects that since there will be only small vertical temperature and vapor gradients over open water, the turbulent fluxes will be small. Having said this, even though the only differences between the values are due to the turbulent fluxes, there is still spatial variation.

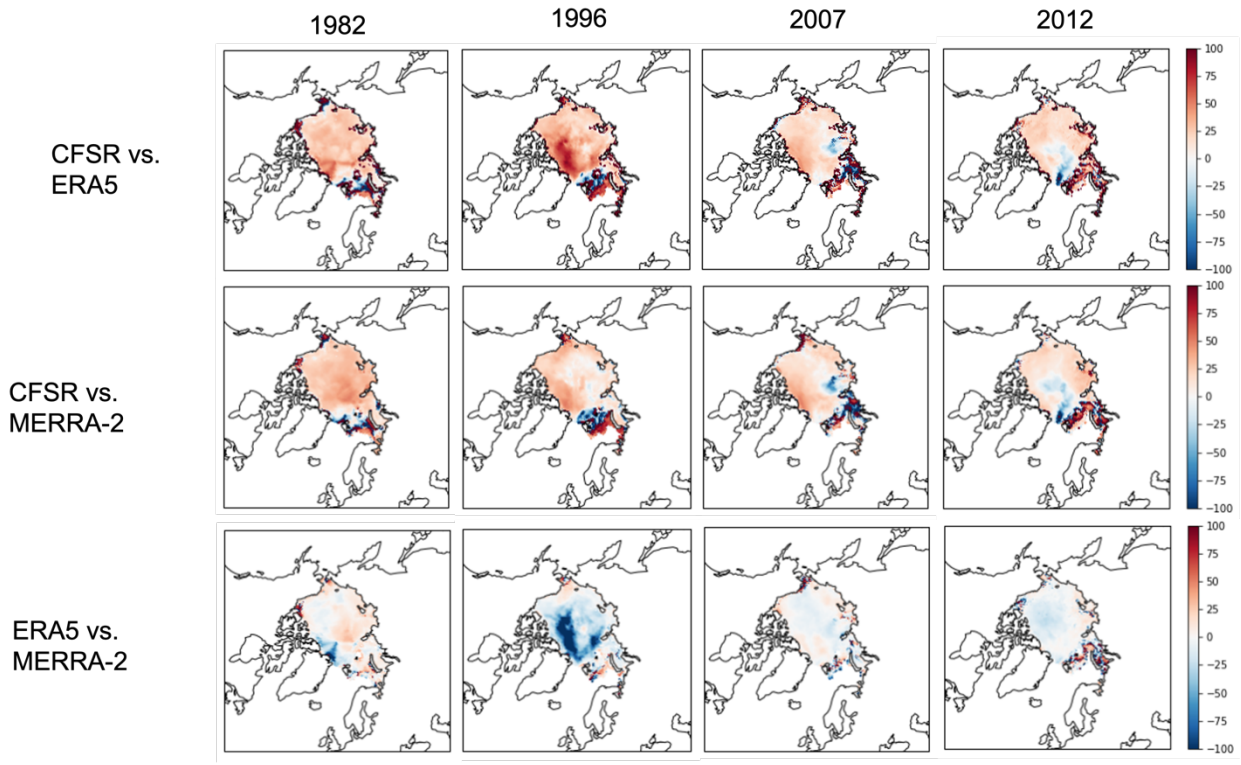

Figure 6.24: Percent differences in seasonal heat gain from the net surface heat flux over ice in 1982, 1996, 2007, and 2012 from CFSR, ERA5, MERRA-2.

Figures 6.24 and 6.25 show the percent differences between the three calculations. The percent differences between the heat gain estimates using the CFSR and ERA5 turbulent flux values are largest across the majority of the central Arctic Ocean and marginal seas. In 2007 and 2012 there are a few areas in the Laptev Sea and north of Svalbard, respectively, that have negative percentages. The year 1996 has the highest percentages. The differences between CFSR and MERRA-2 using their respective turbulent fluxes share similar patterns as the CFSR and ERA5 comparisons across the four years. There are lower percentages in 1982 and 1996, yet similar percentages in 2007 and 2012. Lastly, results using the ERA5 and MERRA-2 turbulent fluxes are the most similar. In 1996, there is a

swath along the north coast of Greenland and the Canadian Arctic Archipelago where estimates using the turbulent flux from ERA5 are smaller than those using the MERRA-2 turbulent flux data.

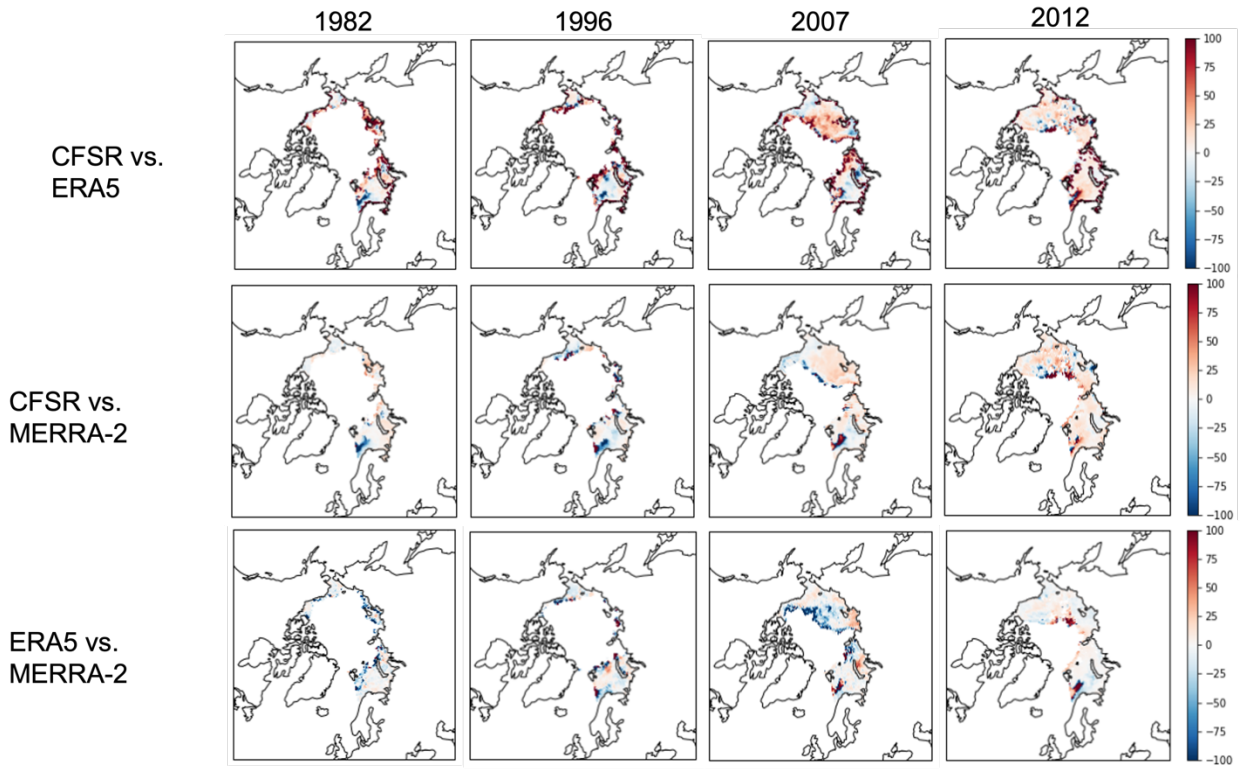

Figure 6.25: Percent differences in seasonal heat gain from the net surface heat flux over ocean in 1982, 1996, 2007, and 2012 from CFSR, ERA5, MERRA-2.

Lastly, Figure 6.25 shows the percent differences between the heat gain values using turbulent flux values from the three reanalyses. Mostly there are small negative or positive percentages across the marginal seas for all the comparisons. The one area with large percent differences is right along the ice edge as those are often different in each reanalysis. The comparisons between results using the CFSR and MERRA-2 turbulent fluxes are relatively similar.

What is to be made of the above results? The heat gain estimates from the three reanalyses differ widely, which manifests the effects of often very different

estimates of the individual flux terms. In some cases these will have offsetting effects, such that one might be getting something near the "right" (but unknown) net surface flux but for the wrong reasons, while in others cases, the biases in the individual terms will be additive. While the approach of getting the net radiation by combining the best individual terms from the reanalyses and then applying the turbulent fluxes from the different reanalyses has some merit, knowing which reanalysis has the best turbulent fluxes is problematic. However, it does seem that the turbulent fluxes from CFSR are not realistic. As such, the estimates using the turbulent fluxes from MERRA-2 and ERA5 are probably better.

Another approach to getting an estimate of the seasonal accumulated net surface flux is to form a "mini-ensemble" of six realizations: the three just discussed, using the "best" net radiation and swapping in the turbulent fluxes from the three reanalyses, and the three based on the reanalyses themselves, such as depicted in Figure 6.2 and 6.3. The average of the six members is taken as the one way to approach estimating the seasonal accumulated net surface flux while the maximum and minimum from the six is viewed as the spread, or uncertainty. This is essentially the same approach as used to depict (for example) projections of Arctic sea ice extent from the suite of CMIP6 climate models for a given emission scenario, but in this case the spread is a result of differences in both model structure and internal climate variability (for a given emissions scenario). It is acknowledged that the three estimates (or ensemble members in the present framework) based on swapping in the turbulent fluxes from each reanalysis are not independent as they

use the net radiation from the same combination of two reanalyses (MERRA-2 and CFSR).

Figure 6.26 and 6.27 show results for the ice covered and open water parts of the domain, respectively. Note how as assessed for the entire domain the low September sea ice years of 2007 and 2012 do not stand out in the mean and also the upper and lower bounds, as well as the high September sea ice year of 1996. In the ensemble mean and the Arctic Ocean as a whole, 1988-1991 stand out as having strong heat gains, while there appears to be a minimum in 2009. This minimum appears to be driven by small heat gains over open water, as does the 1989-1991 peak (Figure 6.27).

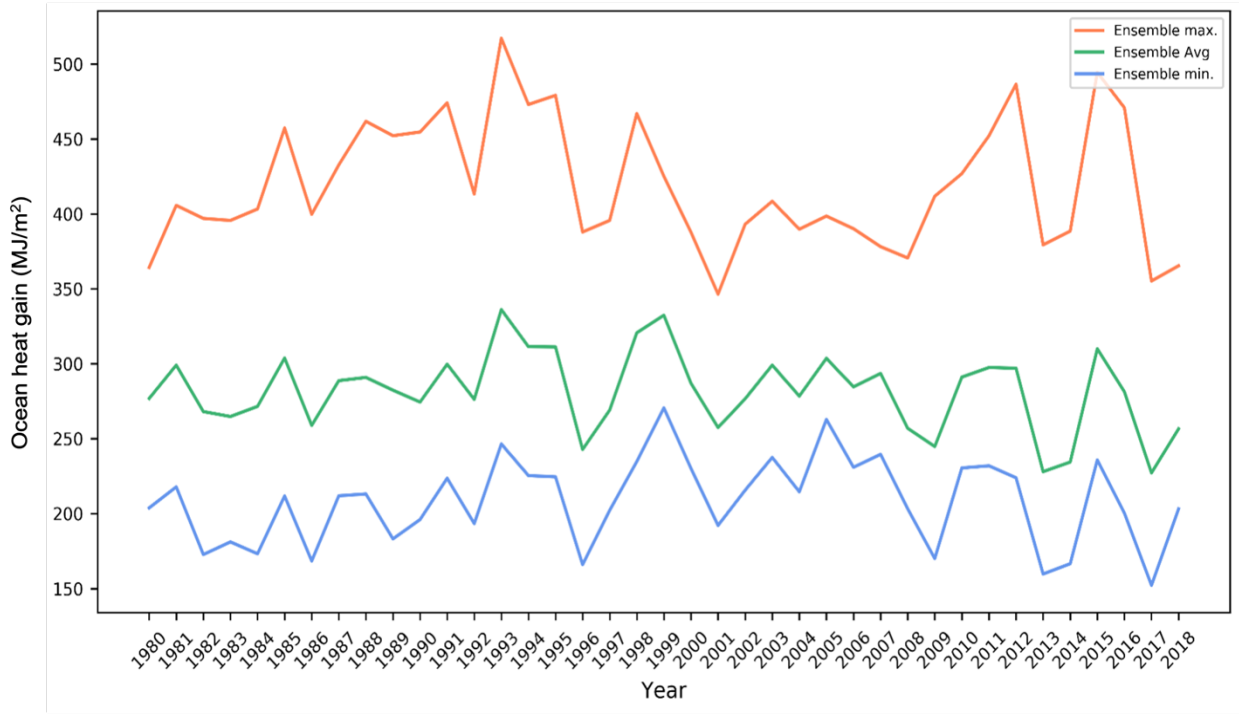

Figure 6.26: Ensemble seasonal heat gain estimates along with the minimum and maximum values over sea ice in MJ/m^2.

Building on earlier results, there are no obvious temporal trends in net surface heat flux over the 1980 to 2018 period. While this may seem

counterintuitive given that the Arctic is known to be strongly warming, a reasonable explanation is that most of the net surface heat flux from the net surface flux is accounted for by melt of ice. While the Arctic Ocean is increasing its latent heat energy content as ice turns to liquid, consistent with the observed decline in sea ice volume as depicted in the PIOMAS record (Schweiger et al., 2011), this will not be readily seen as a change in the net surface heat flux. There is also a negative feedback over open water; as the upper ocean and hence surface warms, longwave cooling increases, tending to decrease the net surface flux. Finally, because these values are only capturing the seasonal ocean heat gain over sea ice (Figure 6.26) and open water (Figure 6.27) separately they do not take the change in area of these two surface types over the study time period and therefore are not impacted by the change in sea ice extent.

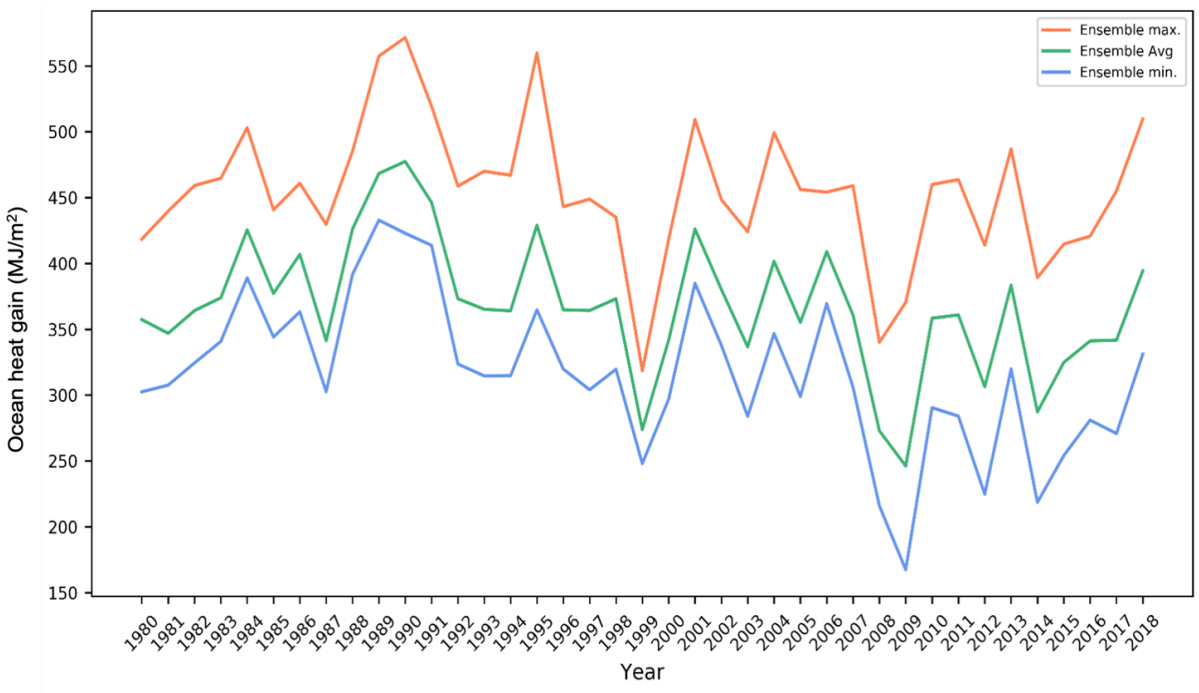

Figure 6.27: Ensemble seasonal heat gain estimates along with minimum and maximum values over open water in MJ/m^2.

Finally, and using the ensemble method, Figure 6.28 shows that seasonal heat gain values that were assessed over the entire Arctic Ocean study domain. The expected overall upward trend is readily apparent in all the data. The trend is the most apparent in the minimum ensemble values but are present in the average and maximum ensemble values. The maximum ensemble values are heavily influenced by CFSR data shown in Figure 6.2. The linear trend values for the ensemble maximum, average, and minimum over the analysis period are 8.5 x 10^{12} MJ and 9.3 x 10^{12} MJ and 2.4 x 10^{13} MJ respectively, but only the maximum values are statistically significant at the 95% level. Similar to Figure 6.2, the trends in Figure 6.28 are representative of the response in the surface energy budget to the decline in sea ice extent across the Arctic Ocean. The decline in sea ice cover replaces a highly reflective surface with a dark absorbent surface and thus leads to more heat/energy in the environment. This positive feedback loop leads to further sea ice melt and warming of the surface mixed layer.

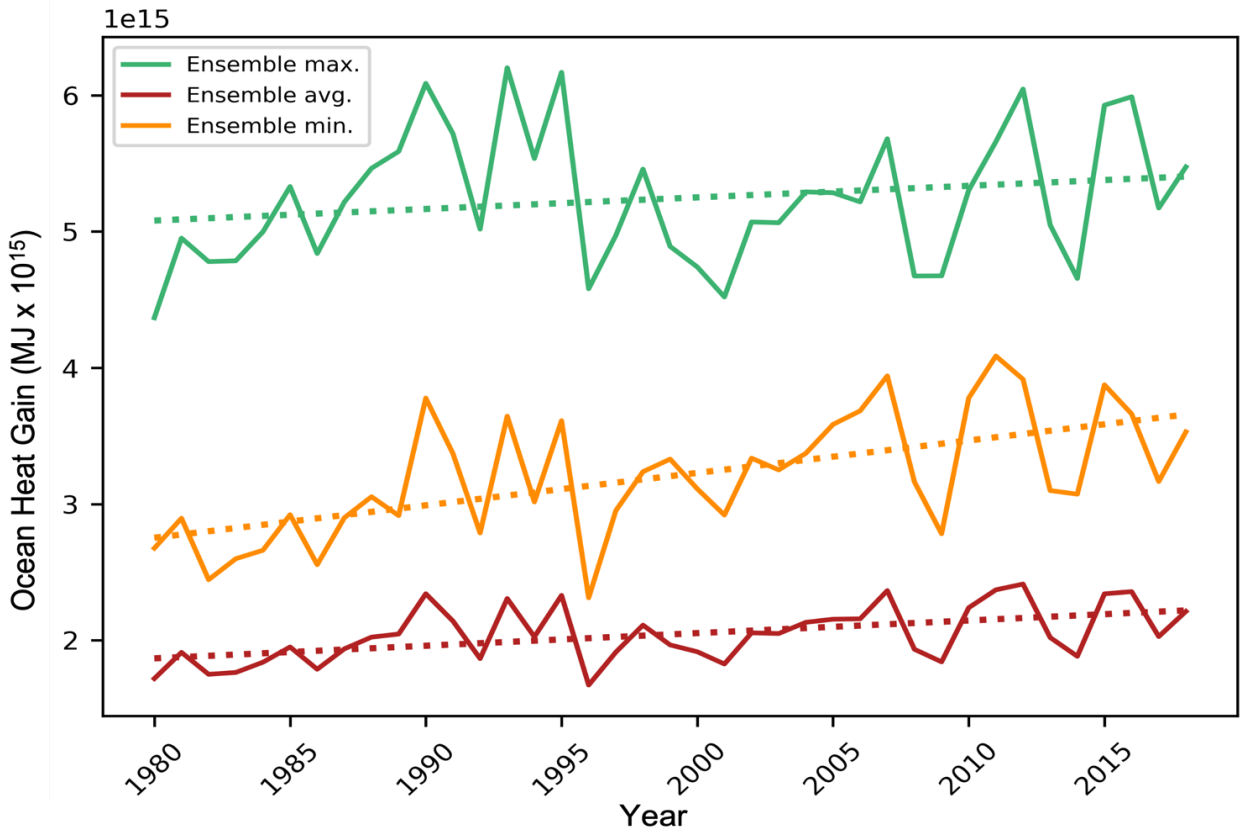

Figure 6.28: Ensemble seasonal heat gain estimates along with minimum and maximum values for the entire Arctic Domain in MJ x 10^{15}.

CHAPTER 7: CONCLUSION

7.1 Findings

The objective of this dissertation was to address the following:

Objective 1 Compare individual surface energy balance components (shortwave down, shortwave up, longwave down, longwave up, and sensible and latent heat) across three reanalyses (CFSR, MERRA-2, and ERA5) in a statistical assessment. Examined cloud cover as well. Efforts were guided by the following questions. *Does one reanalysis stand out in terms of its depiction of any or all components? Do cloud cover patterns agree with what we expect in terms of influences of downwelling shortwave and longwave radiation?*

Objective 2 Use observational datasets from the SHEBA expedition (1997-1998), the *RV Araon* (2018), and the MOSAIC expedition (2019-2020) to validate, to the extent possible, radiation components from the three different atmospheric reanalyses addressing the science questions: *How do fluxes from the reanalysis compare to the direct observations? Are the reanalyses doing a good job of capturing these values?*

Objective 3 Determine seasonal heat gain and loss patterns and long-term changes over the Arctic Ocean via the net surface flux and its components using reanalysis data. This final component of this study sought to answer the following questions: *Is there an increase in the total net surface heat flux from April-August over the 39-year*

period? Do periods of increased heat content at the surface occur in the same years as low sea ice concentration? How do the results vary between different reanalyses?

To address these questions, data from the three reanalyses and observational datasets were used to estimate differences between all datasets for upwelling and downwelling shortwave radiation and upwelling and downwelling longwave radiation. The reanalyses data was then used to calculate seasonal net surface heat flux and seasonal heat gain (April through August) across the Arctic Ocean from each reanalysis as well as time series using values from the reanalyses based on the results from the radiation comparison and validation efforts in Chapters 4 through 6.

CFSR has the largest upwelling and downwelling shortwave radiation values while MERRA-2 has the lowest values for those variables. Interestingly, MERRA-2 performs the best when those variables were compared to observations from three ship-based expeditions. There are statistically significant correlations between all the radiation components from the reanalyses and the SHEBA and MOSAiC datasets used in this study.

For upwelling and downwelling longwave radiation, ERA5 has the largest values over the central Arctic Ocean and the Chukchi Sea while CFSR has the highest values over Barents Sea, thus there are substantial regional differences in how the reanalyses also depict key variables such as cloud cover and its radiative properties. To the extent that one can validate the fluxes with the sparse

observational dataset it appears that MERRA-2 performs the best for upwelling and downwelling shortwave radiation and downwelling longwave radiation. CFSR performs the best for upwelling longwave radiation.

Results from the radiation comparisons implies that MERRA-2 has the greatest cloud cover and CFSR has the least cloud cover. However, results from the cloud comparison show that CFSR, in fact, has the highest percentage of medium cloud cover and low cloud cover and MERRA-2 has the lowest percentage. This is in opposition to what was expected because CFSR has the largest shortwave radiation values and the highest percentage of cloud cover. This points to differences in the treatment of cloud radiative properties and optical depth. The inverse is presented for MERRA-2; it has the least cloud cover and the lowest values of shortwave radiation. Differences in cloud type could contribute to how much radiation is emitted to the surface in CFSR. There is also a possibility that CFSR has a lot of cloud cover but the clouds are optically thin and transmit too much shortwave radiation through to the surface. In contrast, MERRA-2 may have a low cloud percentage but their optical depth is too large, allowing too little shortwave radiation to reach the surface.

Although there is good agreement between the reanalyses and the observations for some of variables, none of the reanalyses stood out as the best performing overall. Either CFSR or MERRA-2 performed the best for the radiation components that were evaluated against the observations and all correlations were statistically significant at the 95% confidence level. Interestingly, ERA5, which is

the newest reanalysis, was not highly correlated with any of the observational datasets.

The seasonal heat gain from the net surface flux calculated from each reanalysis as assessed for the Arctic Ocean domain as a whole shows upward trends over the 39-year period 1980-2018, expected as sea ice extent decreases and the open water fraction increases. However, no trends are apparent when the calculations are done separately for the sea ice and open water areas. Across the entire Arctic Ocean domain, the values range from 2.5×10^{15} MJ - 6.0×10^{15} MJ. CFSR has the highest numbers some of which are double the amount of what is shown by MERRA-2 (the reanalysis with the lowest ocean heat gain values).

Values calculated over sea ice range from 160 MJ/m^2 to over 500 MJ/m^2, which is enormous. Over sea ice, MERRA-2 has the lowest values and CFSR has the highest. Values over open water have a similar range in values but all the reanalyses values are across that range. The correlations between the time series from the reanalyses are all statistically significant at the 99% confidence level ($p<0.01$) except the relationship between MERRA-2 and ERA5 over open water.

Contrasting years of high September sea ice extent (1982, 1996) and low September sea ice extent (2007, 2012) were examined in greater detail in terms of the spatial structure of net surface heat flux anomalies. In years with high September sea ice (1982 and 1996), as expected, the heat gain is lower than average across the central Arctic Ocean. In years with low September sea ice (2007 and 2012), there is above average heat gain across the central Arctic Ocean. In 2007

there is a clear association between positive heat gain anomalies and an unusual summer atmospheric circulation pattern. This pattern was characterized by persistent strong high pressure over the Beaufort Sea and low pressure over northeastern Eurasia, leading to persistent warm winds from the south promoting extensive sea ice melt in the Chukchi Sea. By contrast, the summer of 1996 was known to be rather cold, and characterized by persistent low pressure over the central Arctic Ocean (Serreze et al., 2016). Even though there are spatial patterns in the years noted above, in the yearly averages, there are no noticeable differences.

As one approach to obtain a time series of net surface heat flux and heat gain, the net radiation was determined by using MERRA-2 downwelling shortwave, upwelling shortwave and downwelling longwave, and CFSR for upwelling longwave. These selections were based on the temporal correlations with the observed data sets. To this estimate of net radiation, the turbulent heat fluxes were plugged in from each reanalysis. This first set of heat gain estimates were more similar to one another, especially over open water because the only differences are due differences in the turbulent fluxes. These numbers range from ~150 MJ/m^2 to ~450 MJ/m^2 and have a much closer relationship over open water. The time series are strongly positively correlated and statistically significant at the 99% confidence level ($p<0.01$). However, based on physical considerations and limited data from SHEBA, the turbulent fluxes from CFSR seem to be much too large.

As another approach, values from the six calculations were simply averaged together, in the sense of a “mini ensemble”, viewing the mean as the the average

estimate and the maximum and minimum values from the three reanalyses as the uncertainty, or spread. This ensemble shows average values ranging from 250 MJ/m^2 to 460 MJ/m^2 with a full range from the spread of 175 MJ/m^2 to 575 MJ/m^2. It must be taken into account that averaging multiple net surface heat flux values together is not completely ideal because three of the estimates use the same net radiation.

A recent study by Li et al. (2022) found that there is an increase in summer net surface flux between 1979-2018, which aligns with the results in this study. Some differences between their study and the present one, though, are that their domain includes the Canadian archipelago and excludes the Barents Sea which may make the two studies incompatible and they do not separate their surface flux calculations over sea ice and open water. Additionally, this study includes April and May values while the Li et al. (2022) study only includes June, July, and August. This may mute the values in this study because April and May are still largely ice covered and those months may not be experiencing increasing net surface flux like the summer months. There may not be a visible trended in the ocean heat gain over the sea ice and open water only grid cells despite the loss of sea ice and decline in albedo because some of that energy is being advected away. Since this study only uses data at the surface and does not include advection in the calculation, that may be partially responsible for the lack of trend. Finally, there are no trends in the figures showing ocean heat gain over sea ice and open water because these number do not take into account the change in area for both of these surface characteristics.

This differs from the Li et al. (2022) study because they do not separate their surface heat flux values; they consider the whole area as one region.

7.2 Remaining Questions

As an overall statement, results from this analysis paint a rather sobering picture of the ability of the current generation of atmospheric reanalyses to depict surface fluxes. All of these fluxes are parameterized terms. Many factors contribute to inaccurate representations of surface radiation components. The main areas of concern are the depiction of cloud cover and its radiative properties, atmospheric aerosols, and surface albedo. One way to address these concerns is to conduct a similar analysis to this study focusing on aerosols and cloud cover characteristics. An additional deeper analysis into surface albedo and turbulent fluxes would also be helpful to addressing these issues.

7.3 Implications

If sea ice continues to decline, the light reflective ice surface is replaced with the dark water beneath, potentially leading to more energy in the surface mixed layer which delays sea ice freeze up in autumn. Comprehending what components of a reanalysis dataset are performing the best and ultimately what reanalysis is best to use to initiate models and use in other scientist endeavors is essential. This dissertation aimed to shed some light on that subject. The results shown in this dissertation imply that choosing one reanalysis (i.e. CFSR) over another one (ERA5) to initialize an ice ocean model may produce wildly different results and impact the conclusions made. To build on the research presented here, a project that can use

these results to address some larger questions is to construct a statistical model that incorporates all the net surface heat flux values, radiation and cloud cover components to predict seasonal sea ice extent.

References

Andersson, Tom R., J. Scott Hosking, María Pérez-Ortiz, Brooks Paige, Andrew Elliott, Chris Russell, Stephen Law, et al. "Seasonal Arctic Sea Ice Forecasting with Probabilistic Deep Learning." *Nature Communications* 12, no. 1 (August 26, 2021): 5124. https://doi.org/10.1038/s41467-021-25257-4.

Blanchard-Wrigglesworth, Edward, Kyle C. Armour, Cecilia M. Bitz, and Eric DeWeaver. "Persistence and Inherent Predictability of Arctic Sea Ice in a GCM Ensemble and Observations." *Journal of Climate* 24, no. 1 (January 1, 2011): 231–50. https://doi.org/10.1175/2010JCLI3775.1.

Bloom, S. C., L. L. Takacs, A. M. da Silva, and D. Ledvina. "Data Assimilation Using Incremental Analysis Updates." *Monthly Weather Review* 124, no. 6 (June 1, 1996): 1256–71. https://doi.org/10.1175/1520-0493(1996)124<1256:DAUIAU>2.0.CO;2.

Carmack, E., I. Polyakov, L. Padman, I. Fer, E. Hunke, J. Hutchings, J. Jackson, et al. "Toward Quantifying the Increasing Role of Oceanic Heat in Sea Ice Loss in the New Arctic." *Bulletin of the American Meteorological Society* 96, no. 12 (February 3, 2015): 2079–2105. https://doi.org/10.1175/BAMS-D-13-00177.1.

Cavalieri, D. J., and C. L. Parkinson. "Arctic Sea Ice Variability and Trends, 1979–2010." *The Cryosphere* 6, no. 4 (August 15, 2012): 881–89. https://doi.org/10.5194/tc-6-881-2012.

Cavalieri, Donald J., Barbara A. Burns, and Robert G. Onstott. "Investigation of the Effects of Summer Melt on the Calculation of Sea Ice Concentration Using Active and Passive Microwave Data." *Journal of Geophysical Research: Oceans* 95, no. C4 (1990): 5359–69. https://doi.org/10.1029/JC095iC04p05359.

Chakraborty, T., and X. Lee. “Large Differences in Diffuse Solar Radiation among Current-Generation Reanalysis and Satellite-Derived Products.” *Journal of Climate* 34, no. 16 (August 1, 2021): 6635–50. https://doi.org/10.1175/JCLI-D-20-0979.1.

Chaudhuri, Ayan H., and Rui M. Ponte. “An Evaluation of Surface Atmospheric Changes over the Arctic Ocean for 2000–09 Using Recent Reanalyses.” *Earth Interactions* 19, no. 2 (January 1, 2015): 1–18. https://doi.org/10.1175/EI-D-14-0012.1.

Clough, S. A., M. W. Shephard, E. J. Mlawer, J. S. Delamere, M. J. Iacono, K. Cady-Pereira, S. Boukabara, and P. D. Brown. “Atmospheric Radiative Transfer Modeling: A Summary of the AER Codes.” *Journal of Quantitative Spectroscopy and Radiative Transfer* 91, no. 2 (March 1, 2005): 233–44. https://doi.org/10.1016/j.jqsrt.2004.05.058.

Comiso, Josefino C., and Ron Kwok. “Surface and Radiative Characteristics of the Summer Arctic Sea Ice Cover from Multisensor Satellite Observations.” *Journal of Geophysical Research: Oceans* 101, no. C12 (1996): 28397–416. https://doi.org/10.1029/96JC02816.

Comiso, Josefino C., Claire L. Parkinson, Robert Gersten, and Larry Stock. “Accelerated Decline in the Arctic Sea Ice Cover.” *Geophysical Research Letters* 35, no. 1 (January 3, 2008). https://doi.org/10.1029/2007GL031972.

Cullather, Richard I., Sophie M. J. Nowicki, Bin Zhao, and Max J. Suarez. “Evaluation of the Surface Representation of the Greenland Ice Sheet in a General Circulation Model.” *Journal of Climate* 27, no. 13 (July 1, 2014): 4835–56. https://doi.org/10.1175/JCLI-D-13-00635.1.

Curry, Judith A. “Introduction to Special Section: FIRE Arctic Clouds Experiment.” *Journal of Geophysical Research: Atmospheres* 106, no. D14 (2001): 14985–87. https://doi.org/10.1029/2000JD900551.

Day, J. J., S. Tietsche, and E. Hawkins. "Pan-Arctic and Regional Sea Ice Predictability: Initialization Month Dependence." *Journal of Climate* 27, no. 12 (June 15, 2014): 4371–90. https://doi.org/10.1175/JCLI-D-13-00614.1.

Dee, D. P., S. M. Uppala, A. J. Simmons, P. Berrisford, P. Poli, S. Kobayashi, U. Andrae, et al. "The ERA-Interim Reanalysis: Configuration and Performance of the Data Assimilation System." *Quarterly Journal of the Royal Meteorological Society* 137, no. 656 (April 1, 2011): 553–97. https://doi.org/10.1002/qj.828.

Ding, Qinghua, Axel Schweiger, Michelle L'Heureux, David S. Battisti, Stephen Po-Chedley, Nathaniel C. Johnson, Eduardo Blanchard-Wrigglesworth, et al. "Influence of High-Latitude Atmospheric Circulation Changes on Summertime Arctic Sea Ice." *Nature Climate Change* 7, no. 4 (April 2017): 289–95. https://doi.org/10.1038/nclimate3241.

Divine, D. V., M. A. Granskog, S. R. Hudson, C. A. Pedersen, T. I. Karlsen, S. A. Divina, A. H. H. Renner, and S. Gerland. "Regional Melt-Pond Fraction and Albedo of Thin Arctic First-Year Drift Ice in Late Summer." *The Cryosphere* 9, no. 1 (February 9, 2015): 255–68. https://doi.org/10.5194/tc-9-255-2015.

Fetterer, F.; Knowles K.; Meier W.; Savoie M.; Windnagel A. "Sea Ice Index, Version 3." NSIDC, 2017. https://doi.org/10.7265/N5K072F8.

Francis, Jennifer. "8.5: CLOUD RADIATIVE FORCING OVER ARCTIC SURFACES." Accessed May 18, 2023. https://ams.confex.com/ams/older/99annual/abstracts/370.htm.

Gelaro, Ronald, Will McCarty, Max J. Suárez, Ricardo Todling, Andrea Molod, Lawrence Takacs, Cynthia A. Randles, et al. "The Modern-Era Retrospective Analysis for Research and Applications, Version 2 (MERRA-2)." *Journal of Climate* 30, no. 14 (July 15, 2017): 5419–54. https://doi.org/10.1175/JCLI-D-16-0758.1.

Graham, Robert M., Lana Cohen, Nicole Ritzhaupt, Benjamin Segger, Rune G. Graversen, Annette Rinke, Von P. Walden, Mats A. Granskog, and Stephen R. Hudson. "Evaluation of

Six Atmospheric Reanalyses over Arctic Sea Ice from Winter to Early Summer." *Journal of Climate* 32, no. 14 (July 15, 2019): 4121–43. https://doi.org/10.1175/JCLI-D-18-0643.1.

Guemas, Virginie, Edward Blanchard-Wrigglesworth, Matthieu Chevallier, Jonathan J. Day, Michel Déqué, Francisco J. Doblas-Reyes, Neven S. Fučkar, et al. "A Review on Arctic Sea-Ice Predictability and Prediction on Seasonal to Decadal Time-Scales." *Quarterly Journal of the Royal Meteorological Society* 142, no. 695 (2016): 546–61. https://doi.org/10.1002/qj.2401.

Hersbach, Hans, Bill Bell, Paul Berrisford, Shoji Hirahara, András Horányi, Joaquín Muñoz-Sabater, Julien Nicolas, et al. "The ERA5 Global Reanalysis." *Quarterly Journal of the Royal Meteorological Society* 146, no. 730 (2020): 1999–2049. https://doi.org/10.1002/qj.3803.

———. "The ERA5 Global Reanalysis." *Quarterly Journal of the Royal Meteorological Society* 146, no. 730 (2020): 1999–2049. https://doi.org/10.1002/qj.3803.

Iacono, Michael J., Eli J. Mlawer, Shepard A. Clough, and Jean-Jacques Morcrette. "Impact of an Improved Longwave Radiation Model, RRTM, on the Energy Budget and Thermodynamic Properties of the NCAR Community Climate Model, CCM3." *Journal of Geophysical Research: Atmospheres* 105, no. D11 (2000): 14873–90. https://doi.org/10.1029/2000JD900091.

Intrieri, J. M., C. W. Fairall, M. D. Shupe, P. O. G. Persson, E. L. Andreas, P. S. Guest, and R. E. Moritz. "An Annual Cycle of Arctic Surface Cloud Forcing at SHEBA." *Journal of Geophysical Research: Oceans* 107, no. C10 (2002): SHE 13-1-SHE 13-14. https://doi.org/10.1029/2000JC000439.

Ivanova, N., L. T. Pedersen, R. T. Tonboe, S. Kern, G. Heygster, T. Lavergne, A. Sørensen, et al. "Satellite Passive Microwave Measurements of Sea Ice Concentration: An Optimal Algorithm and Challenges." Preprint. Sea Ice, February 26, 2015. https://doi.org/10.5194/tcd-9-1269-2015.

Jakobsson, Martin. “Hypsometry and Volume of the Arctic Ocean and Its Constituent Seas.” *Geochemistry, Geophysics, Geosystems* 3, no. 5 (2002): 1–18. https://doi.org/10.1029/2001GC000302.

Jennifer E. Kay and Andrew Gettelman. “Cloud Influence on and Response to Seasonal Arctic Sea Ice Loss.” *Journal of Geophysical Research: Atmospheres* 114, no. D18 (September 19, 2009). https://doi.org/doi.org/10.1029/2009JD011773.

Johannessen, Ola M., Svetlana I. Kuzmina, Leonid P. Bobylev, and Martin W. Miles. “Surface Air Temperature Variability and Trends in the Arctic: New Amplification Assessment and Regionalisation.” *Tellus A: Dynamic Meteorology and Oceanography* 68, no. 1 (December 1, 2016): 28234. https://doi.org/10.3402/tellusa.v68.28234.

Jung, Thomas, Neil D. Gordon, Peter Bauer, David H. Bromwich, Matthieu Chevallier, Jonathan J. Day, Jackie Dawson, et al. “Advancing Polar Prediction Capabilities on Daily to Seasonal Time Scales.” *Bulletin of the American Meteorological Society* 97, no. 9 (September 1, 2016): 1631–47. https://doi.org/10.1175/BAMS-D-14-00246.1.

Kern, Stefan, Thomas Lavergne, Dirk Notz, Leif Toudal Pedersen, and Rasmus Tonboe. “Satellite Passive Microwave Sea-Ice Concentration Data Set Inter-Comparison for Arctic Summer Conditions.” *The Cryosphere* 14, no. 7 (July 28, 2020): 2469–93. https://doi.org/10.5194/tc-14-2469-2020.

Kleist, Daryl T., David F. Parrish, John C. Derber, Russ Treadon, Wan-Shu Wu, and Stephen Lord. “Introduction of the GSI into the NCEP Global Data Assimilation System.” *Weather and Forecasting* 24, no. 6 (December 1, 2009): 1691–1705. https://doi.org/10.1175/2009WAF2222201.1.

Kwok, R. “Outflow of Arctic Ocean Sea Ice into the Greenland and Barents Seas: 1979–2007.” *Journal of Climate* 22, no. 9 (May 1, 2009): 2438–57. https://doi.org/10.1175/2008JCLI2819.1.

Kwok, Ron. “Remote Sensing of Arctic Sea Ice.” https://dataverse.jpl.nasa.gov/file.xhtml?fileId=48226&version=1.0. Accessed May 18, 2023. https://dataverse.jpl.nasa.gov/file.xhtml?fileId=48226&version=1.0.

Landy, Jack, Jens Ehn, Megan Shields, and David Barber. “Surface and Melt Pond Evolution on Landfast First-Year Sea Ice in the Canadian Arctic Archipelago.” *Journal of Geophysical Research: Oceans* 119, no. 5 (2014): 3054–75. https://doi.org/10.1002/2013JC009617.

Langehaug, H. R., F. Geyer, L. H. Smedsrud, and Y. Gao. “Arctic Sea Ice Decline and Ice Export in the CMIP5 Historical Simulations.” *Ocean Modelling*, Arctic Ocean, 71 (November 1, 2013): 114–26. https://doi.org/10.1016/j.ocemod.2012.12.006.

Laurence C. Smith and Scott R. Stephenson. “New Trans-Arctic Shipping Routes Navigable by Midcentury.” *PNAS* 110, no. 13 (March 4, 2013). https://doi.org/doi.org/10.1073/pnas.1214212110.

Lenetsky, Jed E., and Mark C. Serreze. “Statistical Modeling of the Bering Strait Throughflow for Operational Sea Ice Forecasting in the Chukchi Sea.” *Geophysical Research Letters* 48, no. 10 (2021): e2021GL092939. https://doi.org/10.1029/2021GL092939.

Li, Zhe, Qinghua Ding, Michael Steele, and Axel Schweiger. “Recent Upper Arctic Ocean Warming Expedited by Summertime Atmospheric Processes.” *Nature Communications* 13, no. 1 (January 18, 2022): 362. https://doi.org/10.1038/s41467-022-28047-8.

Macdonald, R. W., T. Harner, and J. Fyfe. “Recent Climate Change in the Arctic and Its Impact on Contaminant Pathways and Interpretation of Temporal Trend Data.” *Science of The Total Environment*, Sources, Occurrence, Trends and Pathways of Contaminants in the Arctic, 342, no. 1 (April 15, 2005): 5–86. https://doi.org/10.1016/j.scitotenv.2004.12.059.

Markus, T., and S.T. Dokken. “Evaluation of Late Summer Passive Microwave Arctic Sea Ice Retrievals.” *IEEE Transactions on Geoscience and Remote Sensing* 40, no. 2 (February 2002): 348–56. https://doi.org/10.1109/36.992795.

Melinda A. Webster, Ignatius G. Rigor, Donald K. Perovich, Jacqueline A. Richter-Menge, Christopher M. Polashenski, and Bonnie Light. “Seasonal Evolution of Melt Ponds on Arctic Sea Ice.” *Journal of Geophysical Research. Oceans* 120, no. 9 (August 14, 2015). https://doi.org/doi.org/10.1002/2015JC011030.

Michael G. Bosilovich, Santha Akella, Lawrence Coy, RIchard Cullather, Clara Draper, Ronald Gelaro, Robin Kovach, et al. “Technical Report Series on Global Modeling and Data Assimilation, Volume 43.” National Aeronautics and Space Administration, September 2015. chrome-extension://efaidnbmnnnibpcajpcglclefindmkaj/https://gmao.gsfc.nasa.gov/pubs/docs/Bosilovich803.pdf.

Mlawer, E J, and S A Clough. “On the Extension of Rapid Radiative Transfer Model to the Shortwave Region,” n.d.

Msadek, R., G. A. Vecchi, M. Winton, and R. G. Gudgel. “Importance of Initial Conditions in Seasonal Predictions of Arctic Sea Ice Extent.” *Geophysical Research Letters* 41, no. 14 (2014): 5208–15. https://doi.org/10.1002/2014GL060799.

Notz, Dirk, and Julienne Stroeve. “Observed Arctic Sea-Ice Loss Directly Follows Anthropogenic CO ₂ Emission.” *Science* 354, no. 6313 (November 11, 2016): 747–50. https://doi.org/10.1126/science.aag2345.

Perovich, Donald K. “Sunlight, Clouds, Sea Ice, Albedo, and the Radiative Budget: The Umbrella versus the Blanket.” *The Cryosphere* 12, no. 6 (June 27, 2018): 2159–65. https://doi.org/10.5194/tc-12-2159-2018.

Perovich Donald K., Light Bonnie, Eicken Hajo, Jones Kathleen F., Runciman Kay, and Nghiem Son V. "Increasing Solar Heating of the Arctic Ocean and Adjacent Seas, 1979–2005: Attribution and Role in the Ice-albedo Feedback." *Geophysical Research Letters* 34, no. 19 (October 11, 2007). https://doi.org/10.1029/2007GL031480.

Persson, P. Ola G., Christopher W. Fairall, Edgar L. Andreas, Peter S. Guest, and Donald K. Perovich. "Measurements near the Atmospheric Surface Flux Group Tower at SHEBA: Near-Surface Conditions and Surface Energy Budget." *Journal of Geophysical Research: Oceans* 107, no. C10 (2002): SHE 21-1-SHE 21-35. https://doi.org/10.1029/2000JC000705.

Pohl, Christine, Larysa Istomina, Steffen Tietsche, Evelyn Jäkel, Johannes Stapf, Gunnar Spreen, and Georg Heygster. "Broadband Albedo of Arctic Sea Ice from MERIS Optical Data." *The Cryosphere* 14, no. 1 (January 22, 2020): 165–82. https://doi.org/10.5194/tc-14-165-2020.

Polyakov, Igor V., Andrey V. Pnyushkov, Matthew B. Alkire, Igor M. Ashik, Till M. Baumann, Eddy C. Carmack, Ilona Goszczko, et al. "Greater Role for Atlantic Inflows on Sea-Ice Loss in the Eurasian Basin of the Arctic Ocean." *Science*, April 6, 2017, eaai8204. https://doi.org/10.1126/science.aai8204.

Reichle, Rolf H., Clara S. Draper, Q. Liu, Manuela Girotto, Sarith P. P. Mahanama, Randal D. Koster, and Gabrielle J. M. De Lannoy. "Assessment of MERRA-2 Land Surface Hydrology Estimates." *Journal of Climate* 30, no. 8 (April 15, 2017): 2937–60. https://doi.org/10.1175/JCLI-D-16-0720.1.

Reichle, Rolf H., Q. Liu, Randal D. Koster, Clara S. Draper, Sarith P. P. Mahanama, and Gary S. Partyka. "Land Surface Precipitation in MERRA-2." *Journal of Climate* 30, no. 5 (March 1, 2017): 1643–64. https://doi.org/10.1175/JCLI-D-16-0570.1.

Rösel, A., L. Kaleschke, and G. Birnbaum. "Melt Ponds on Arctic Sea Ice Determined from MODIS Satellite Data Using an Artificial Neural Network." *The Cryosphere* 6, no. 2 (April 3, 2012): 431–46. https://doi.org/10.5194/tc-6-431-2012.

Saha, Suranjana, Shrinivas Moorthi, Hua-Lu Pan, Xingren Wu, Jiande Wang, Sudhir Nadiga, Patrick Tripp, et al. "The NCEP Climate Forecast System Reanalysis." *Bulletin of the American Meteorological Society* 91, no. 8 (April 23, 2010): 1015–58. https://doi.org/10.1175/2010BAMS3001.1.

Saha, Suranjana, Shrinivas Moorthi, Xingren Wu, Jiande Wang, Sudhir Nadiga, Patrick Tripp, David Behringer, et al. "The NCEP Climate Forecast System Version 2." *Journal of Climate* 27, no. 6 (September 25, 2013): 2185–2208. https://doi.org/10.1175/JCLI-D-12-00823.1.

———. "The NCEP Climate Forecast System Version 2." *Journal of Climate* 27, no. 6 (March 15, 2014): 2185–2208. https://doi.org/10.1175/JCLI-D-12-00823.1.

Schneider, Tapio, and Isaac M. Held. "Discriminants of Twentieth-Century Changes in Earth Surface Temperatures." *Journal of Climate* 14, no. 3 (February 1, 2001): 249–54. https://doi.org/10.1175/1520-0442(2001)014<0249:LDOTCC>2.0.CO;2.

Screen, James A., and Ian Simmonds. "The Central Role of Diminishing Sea Ice in Recent Arctic Temperature Amplification." *Nature* 464, no. 7293 (April 2010): 1334–37. https://doi.org/10.1038/nature09051.

Serreze, M. C. and Barry, R.G. *The Arctic Climate System*. 2nd ed. 32 Avenue of the Americas, New York NY 10013-2473, USA: Cambridge University Press, 2014.

Serreze, Mark C., Andrew P. Barrett, Andrew G. Slater, Michael Steele, Jinlun Zhang, and Kevin E. Trenberth. "The Large-Scale Energy Budget of the Arctic." *Journal of Geophysical Research: Atmospheres* 112, no. D11 (June 16, 2007). https://doi.org/10.1029/2006JD008230.

Serreze, Mark C., and Roger G. Barry. "Processes and Impacts of Arctic Amplification: A Research Synthesis." *Global and Planetary Change* 77, no. 1 (May 1, 2011): 85–96. https://doi.org/10.1016/j.gloplacha.2011.03.004.

Serreze, Mark C., Alex D. Crawford, Julienne C. Stroeve, Andrew P. Barrett, and Rebecca A. Woodgate. "Variability, Trends, and Predictability of Seasonal Sea Ice Retreat and Advance in the Chukchi Sea." *Journal of Geophysical Research: Oceans* 121, no. 10 (October 1, 2016): 7308–25. https://doi.org/10.1002/2016JC011977.

Serreze, Mark C., and Jennifer A. Francis. "The Arctic Amplification Debate." *Climatic Change* 76, no. 3 (June 1, 2006): 241–64. https://doi.org/10.1007/s10584-005-9017-y.

Serreze, Mark C., Julienne Stroeve, Andrew P. Barrett, and Linette N. Boisvert. "Summer Atmospheric Circulation Anomalies over the Arctic Ocean and Their Influences on September Sea Ice Extent: A Cautionary Tale." *Journal of Geophysical Research: Atmospheres* 121, no. 19 (October 16, 2016): 2016JD025161. https://doi.org/10.1002/2016JD025161.

Shupe, Matthew D., and Janet M. Intrieri. "Cloud Radiative Forcing of the Arctic Surface: The Influence of Cloud Properties, Surface Albedo, and Solar Zenith Angle." *Journal of Climate* 17, no. 3 (February 1, 2004): 616–28. https://doi.org/10.1175/1520-0442(2004)017<0616:CRFOTA>2.0.CO;2.

Shupe, Matthew D., Markus Rex, Byron Blomquist, P. Ola G. Persson, Julia Schmale, Taneil Uttal, Dietrich Althausen, et al. "Overview of the MOSAiC Expedition: Atmosphere." *Elementa: Science of the Anthropocene* 10, no. 1 (February 7, 2022): 00060. https://doi.org/10.1525/elementa.2021.00060.

Shupe, Matthew D., Taneil Uttal, and Sergey Y. Matrosov. "Arctic Cloud Microphysics Retrievals from Surface-Based Remote Sensors at SHEBA." *Journal of Applied Meteorology and Climatology* 44, no. 10 (October 1, 2005): 1544–62. https://doi.org/10.1175/JAM2297.1.

Sigmond, M., J. C. Fyfe, G. M. Flato, V. V. Kharin, and W. J. Merryfield. "Seasonal Forecast Skill of Arctic Sea Ice Area in a Dynamical Forecast System." *Geophysical Research Letters* 40, no. 3 (2013): 529–34. https://doi.org/10.1002/grl.50129.

Smedsrud, L. H., A. Sirevaag, K. Kloster, A. Sorteberg, and S. Sandven. "Recent Wind Driven High Sea Ice Area Export in the Fram Strait Contributes to Arctic Sea Ice Decline." *The Cryosphere* 5, no. 4 (October 14, 2011): 821–29. https://doi.org/10.5194/tc-5-821-2011.

Smith, Laurence C., and Scott R. Stephenson. "New Trans-Arctic Shipping Routes Navigable by Midcentury." *Proceedings of the National Academy of Sciences* 110, no. 13 (March 26, 2013): E1191–95. https://doi.org/10.1073/pnas.1214212110.

Steckling, Julia, Markus Ritschel, Prof Dr Johanna Baehr, and Prof Dr Dirk Notz. "Evolution of Heat Fluxes at the Arctic Sea-Ice Edge." Copernicus Meetings, February 22, 2023. https://doi.org/10.5194/egusphere-egu23-12844.

Steffen, Konrad, and Axel Schweiger. "NASA Team Algorithm for Sea Ice Concentration Retrieval from Defense Meteorological Satellite Program Special Sensor Microwave Imager: Comparison with Landsat Satellite Imagery." *Journal of Geophysical Research: Oceans* 96, no. C12 (1991): 21971–87. https://doi.org/10.1029/91JC02334.

Stroeve, J. C., T. Markus, L. Boisvert, J. Miller, and A. Barrett. "Changes in Arctic Melt Season and Implications for Sea Ice Loss." *Geophysical Research Letters* 41, no. 4 (February 28, 2014): 1216–25. https://doi.org/10.1002/2013GL058951.

Stroeve, Julienne C., Vladimir Kattsov, Andrew Barrett, Mark Serreze, Tatiana Pavlova, Marika Holland, and Walter N. Meier. "Trends in Arctic Sea Ice Extent from CMIP5, CMIP3 and Observations." *Geophysical Research Letters* 39, no. 16 (August 28, 2012): L16502. https://doi.org/10.1029/2012GL052676.

Schweiger, Axel, Ron Lindsay, Jinlun Zhang, Mike Steele, Harry Stern, and Ron Kwok. "Uncertainty in Modeled Arctic Sea Ice Volume." *Journal of Geophysical Research: Oceans* 116, no. C8 (2011). https://doi.org/10.1029/2011JC007084.

Timmermans, Mary-Louise, John Toole, and Richard Krishfield. "Warming of the Interior Arctic Ocean Linked to Sea Ice Losses at the Basin Margins." *Science Advances* 4, no. 8 (August 1, 2018): eaat6773. https://doi.org/10.1126/sciadv.aat6773.

Timmermans, Mary-Louise, and John M. Toole. "The Arctic Ocean's Beaufort Gyre." *Annual Review of Marine Science* 15, no. 1 (2023): 223–48. https://doi.org/10.1146/annurev-marine-032122-012034.

Tokinaga, Hiroki, Shang-Ping Xie, and Hitoshi Mukougawa. "Early 20th-Century Arctic Warming Intensified by Pacific and Atlantic Multidecadal Variability." *Proceedings of the National Academy of Sciences* 114, no. 24 (June 13, 2017): 6227–32. https://doi.org/10.1073/pnas.1615880114.

Trenberth, Kevin E., and David P. Stepaniak. "Covariability of Components of Poleward Atmospheric Energy Transports on Seasonal and Interannual Timescales." *Journal of Climate* 16, no. 22 (November 15, 2003): 3691–3705. https://doi.org/10.1175/1520-0442(2003)016<3691:COCOPA>2.0.CO;2.

Uttal, Taneil, Judith A. Curry, Miles G. Mcphee, Donald K. Perovich, Richard E. Moritz, James A. Maslanik, Peter S. Guest, et al. "Surface Heat Budget of the Arctic Ocean." *Bulletin of the American Meteorological Society* 83, no. 2 (February 2002): 255–75. https://doi.org/10.1175/1520-0477(2002)083<0255:SHBOTA>2.3.CO;2.

Wang, Gongjie, Lijing Cheng, John Abraham, and Chongyin Li. "Consensuses and Discrepancies of Basin-Scale Ocean Heat Content Changes in Different Ocean Analyses." *Climate Dynamics* 50, no. 7 (April 1, 2018): 2471–87. https://doi.org/10.1007/s00382-017-3751-5.

Wang, Xuguang. “Incorporating Ensemble Covariance in the Gridpoint Statistical Interpolation Variational Minimization: A Mathematical Framework.” *Monthly Weather Review* 138, no. 7 (July 1, 2010): 2990–95. https://doi.org/10.1175/2010MWR3245.1.

Wayand, N. E., C. M. Bitz, and E. Blanchard-Wrigglesworth. “A Year-Round Subseasonal-to-Seasonal Sea Ice Prediction Portal.” *Geophysical Research Letters* 46, no. 6 (2019): 3298–3307. https://doi.org/10.1029/2018GL081565.

Wei, Jianfen, Xiangdong Zhang, and Zhaomin Wang. “Reexamination of Fram Strait Sea Ice Export and Its Role in Recently Accelerated Arctic Sea Ice Retreat.” *Climate Dynamics* 53, no. 3 (August 1, 2019): 1823–41. https://doi.org/10.1007/s00382-019-04741-0.

York, Ashley V., Frey, Karen E., and Young, Luisa N. C. “Changes at the Edge: Trends in Sea Ice, Ocean Temperature and Ocean Color at the Northwest Atlantic/Southern Arctic Interface | Annals of Glaciology | Cambridge Core.” *Annals of Glaciology* 61, no. 83 (September 24, 2020): 426–40. https://doi.org/10.1017/aog.2020.66.

Zhang, Zhi-Lun, Feng-Ming Hui, Timo Vihma, Mats A. Granskog, Bin Cheng, Zhuo-Qi Chen, and Xiao Cheng. “On the Turbulent Heat Fluxes: A Comparison among Satellite-Based Estimates, Atmospheric Reanalyses, and in-Situ Observations during the Winter Climate over Arctic Sea Ice.” *Advances in Climate Change Research*, April 17, 2023. https://doi.org/10.1016/j.accre.2023.04.004.

Zheng, Lei, Xiao Cheng, Zhuoqi Chen, and Qi Liang. “Delay in Arctic Sea Ice Freeze-Up Linked to Early Summer Sea Ice Loss: Evidence from Satellite Observations.” *Remote Sensing* 13, no. 11 (January 2021): 2162. https://doi.org/10.3390/rs13112162.

APPENDIX I: GLOSSARY

Acronym	Full Names
CFSR	Climate Forecast System Reanalysis
ECMWF	European Centre for Medium Range Weather Forecasts
ERA5	ECMWF Reanalysis Project, 5th Generation
MERRA-2	Modern Era Retrospective Analysis for Research and Applications, Version 2
MOSAiC	Multidisciplinary drifting Observatory for the Study of Arctic Science
NASA	National Aeronautics and Space Administration
NCEP	National Centers for Environmental Prediction
NSF	National Science Foundation
RV	Research Vessel
SHEBA	Surface Heat Budget of the Arctic Ocean

APPENDIX II: ADDITIONAL CHAPTER 4 PLOTS

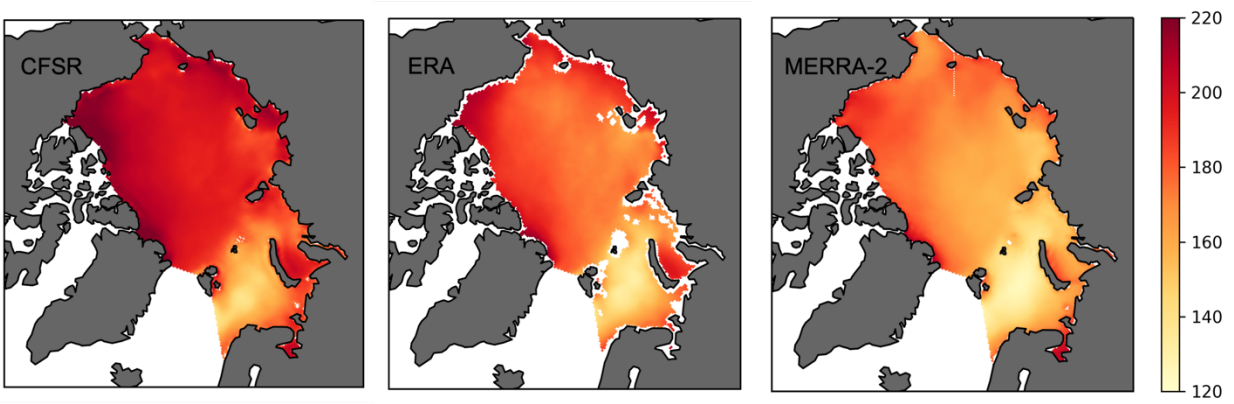

Figure 1: Seasonal downwelling shortwave radiation values in W/m2 from CFSR, ERA5, and MERRA-2 between April-August 2009-2012.

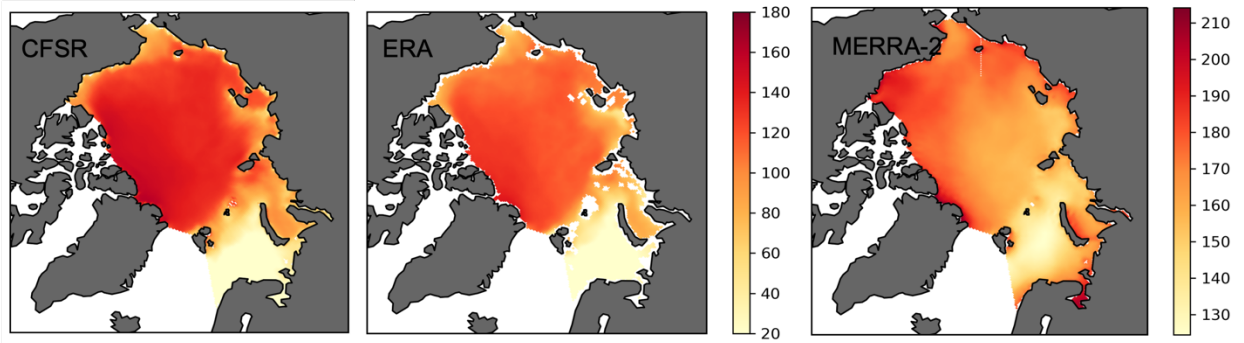

Figure 2: Seasonal upwelling shortwave radiation values in W/m^2 from CFSR, ERA5, and MERRA-2 between April-August 2009-2013.

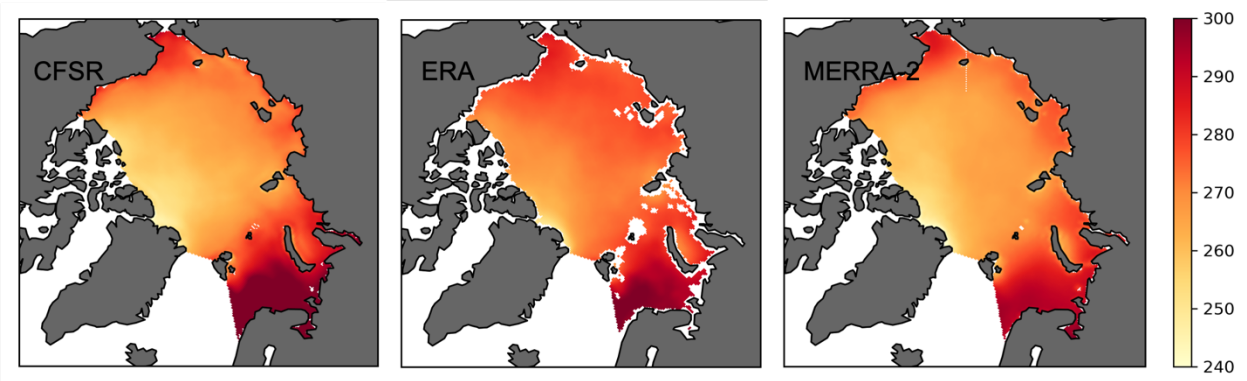

Figure 3: Seasonal downwelling longwave radiation values in W/m2 from CFSR, ERA5, and MERRA-2 between April-August 2009-2013.

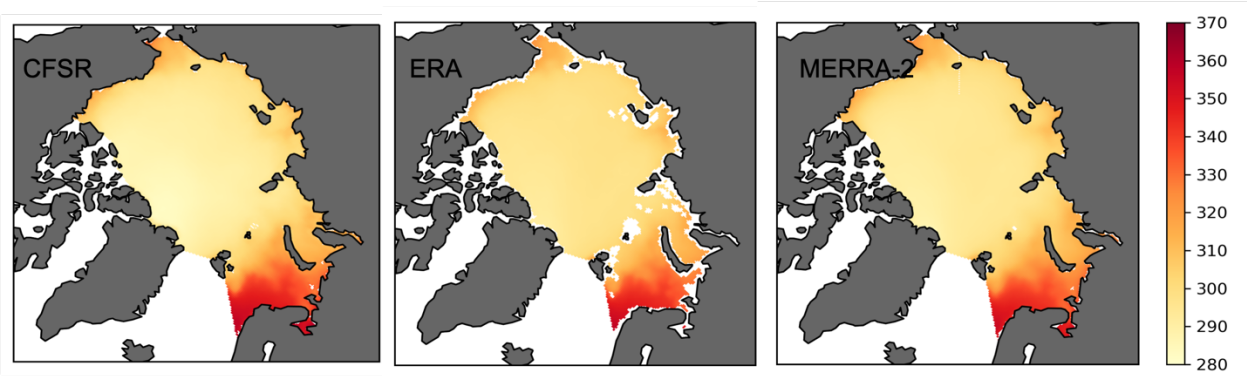

Figure 4: Seasonal upwelling longwave radiation values in W/m2 from CFSR, ERA5, and MERRA-2 between April-August 2009-2013.

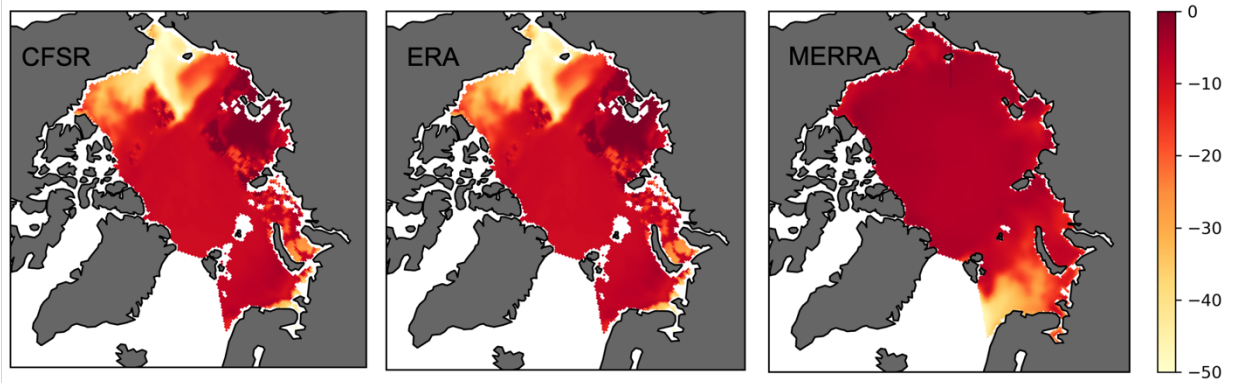

Figure 5: Seasonal latent heat values in W/m2 from CFSR, ERA5, and MERRA-2 between April-August 2009-2013.

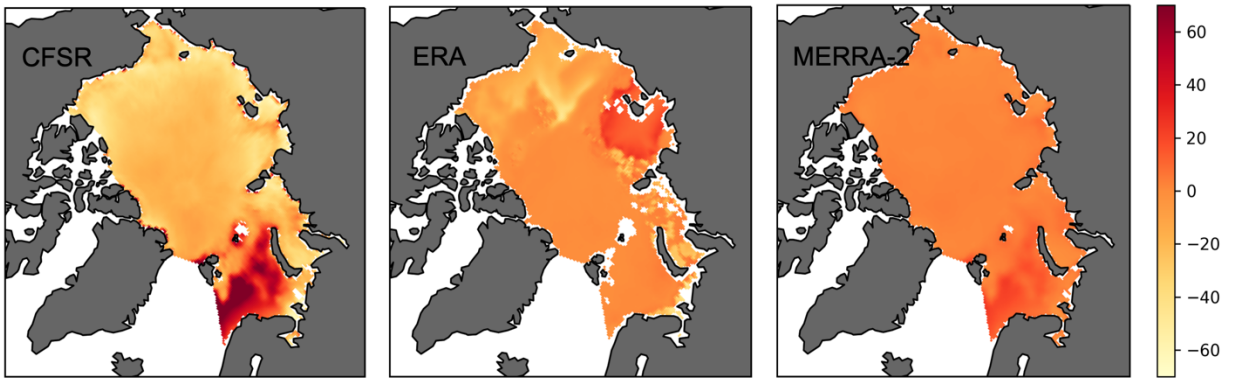

Figure 6: Seasonal sensible heat values in W/m2 from CFSR, ERA5, and MERRA-2 between April-August 2009-2013.

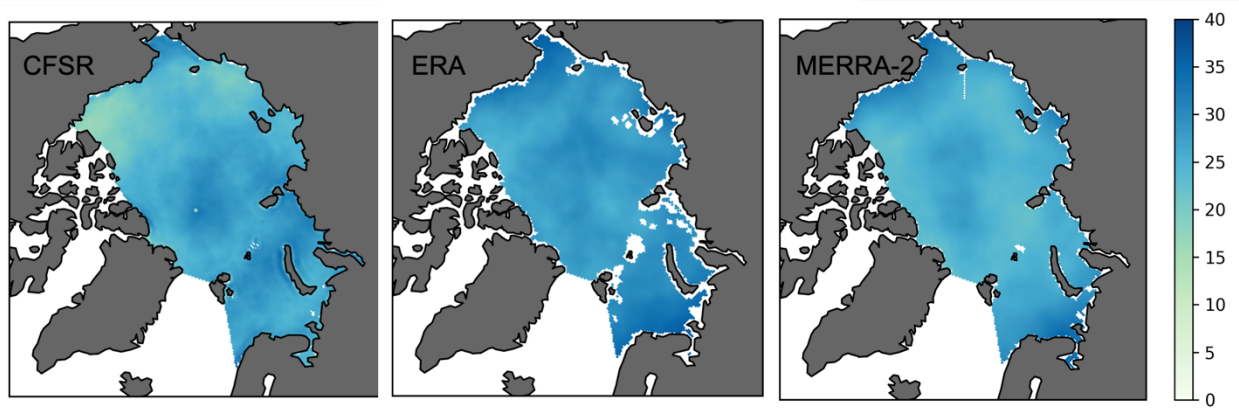

Figure 7: Seasonal high level cloud cover in percentage of 100 from CFSR, ERA5, and MERRA-2 between April-August 2009-2013.

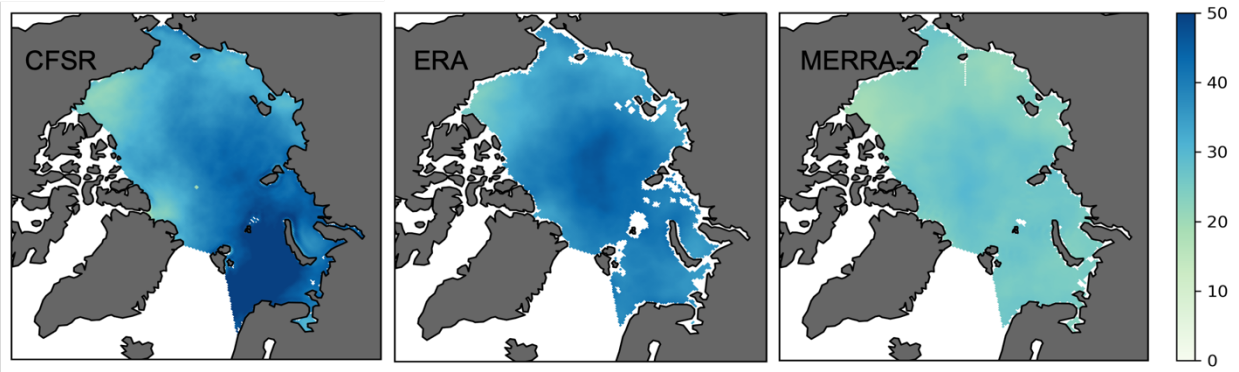

Figure 8: Seasonal medium level cloud cover in percentage of 100 from CFSR, ERA5, and MERRA-2 between April-August 2009-2013.

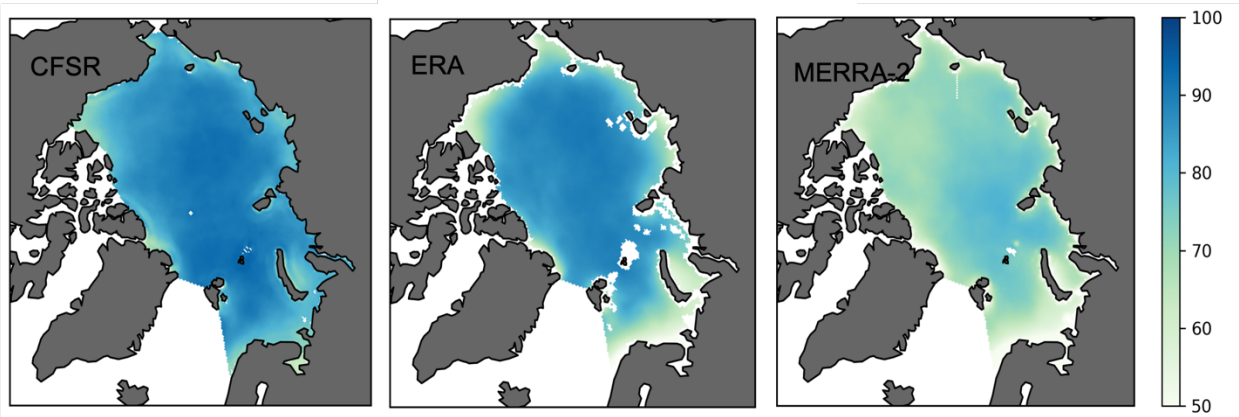

Figure 9: Seasonal low level cloud cover in percentage of 100 from CFSR, ERA5, and MERRA-2 between April-August 2009-2013.

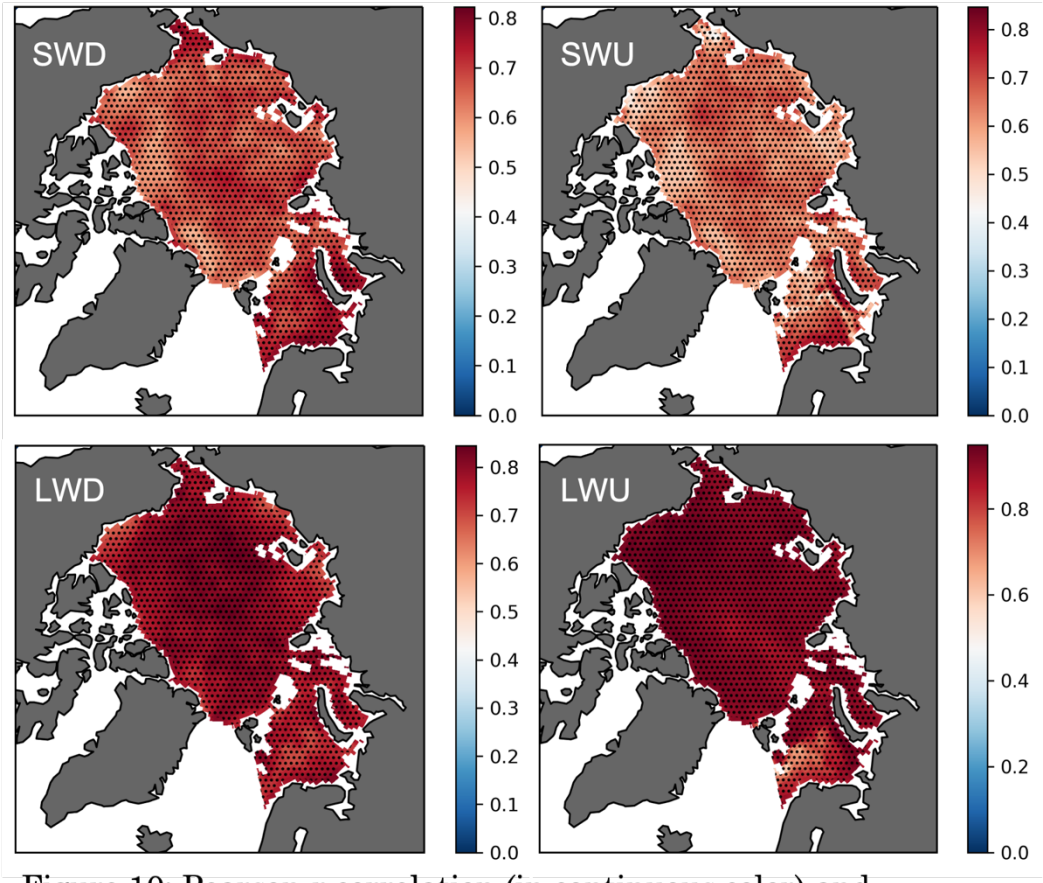

Figure 10: Pearson-r correlation (in continuous color) and statistical significance at the 95% confidence interval (points) for downwelling shortwave radiation (SWD), upwelling shortwave radiation (SWU), downwelling longwave radiation (LWD), and upwelling longwave radiation (LWU) from daily values from April-August between 1993 and 1997 for CFSR and ERA5.

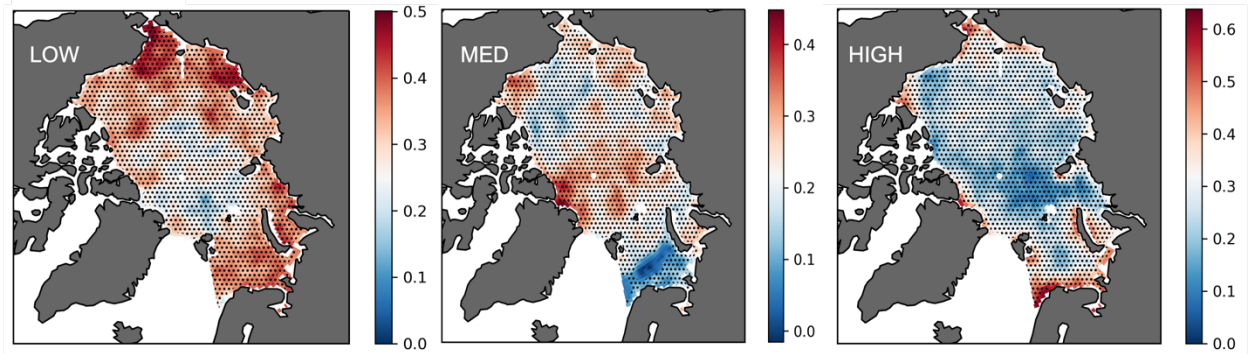

Figure 12: Pearson-r correlations and statistical significance at the 95% confidence interval (points) for high level, medium level, and low level cloud cover from April-August between 1993 and 1997 for CFSR and MERRA-2

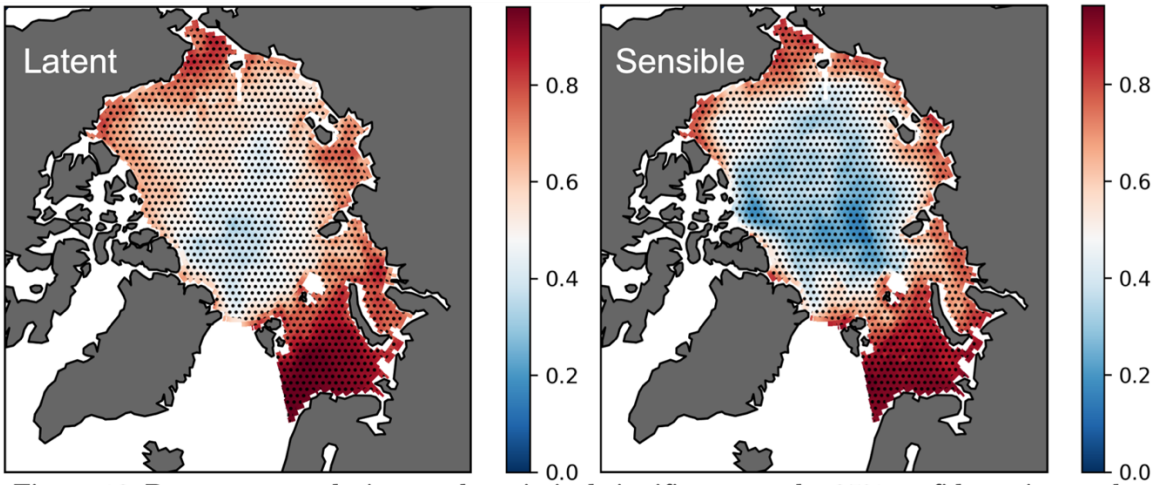

Figure 13: Pearson-r correlations and statistical significance at the 95% confidence interval (points) for latent and sensible heat flux from CFSR and MERRA-2 from detrended daily values from April-August between 1993 and 1997

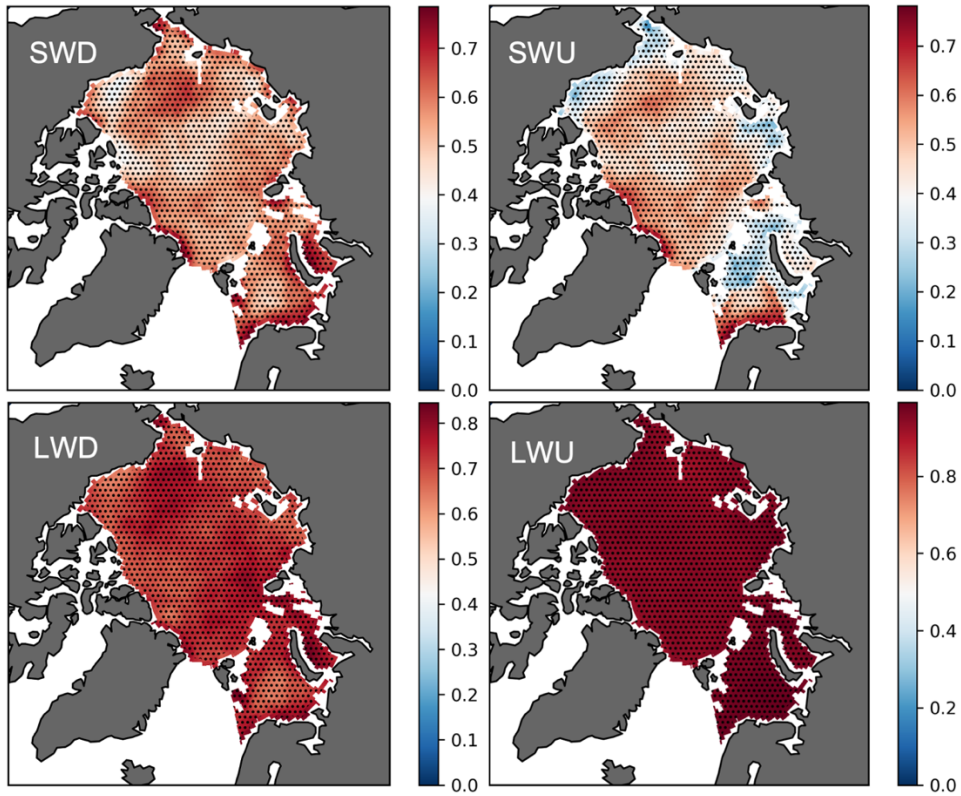

Figure 14: Pearson-r correlation (in continuous color) and statistical significance at the 95% confidence interval (points) for downwelling shortwave radiation (SWD), upwelling shortwave radiation (SWU), downwelling longwave radiation (LWD), and upwelling longwave radiation (LWU) from daily values from April-August between 1993 and 1997 for ERA5 and MERRA-2.

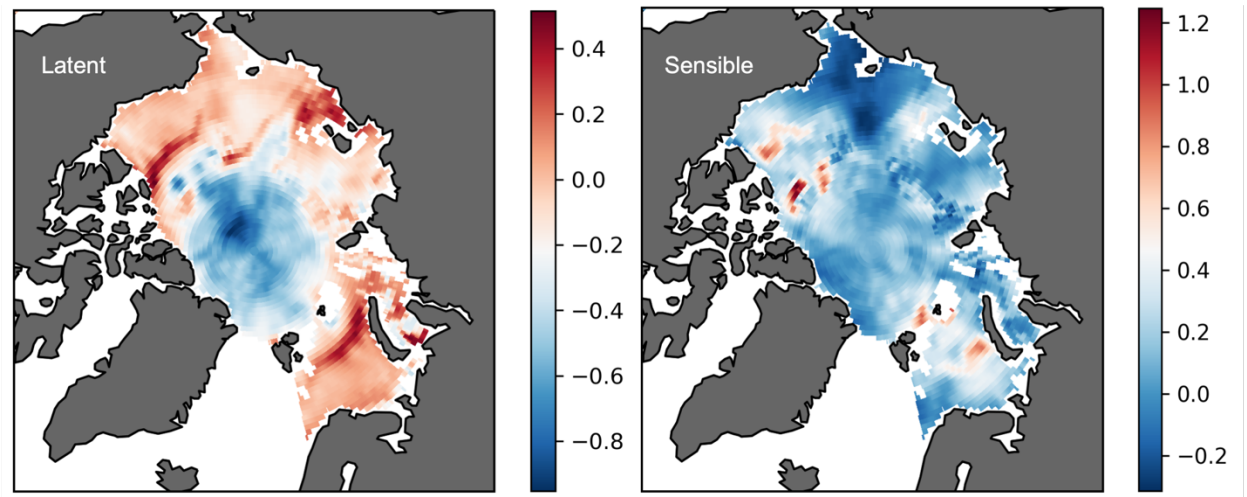

Figure 15: T-test results (continuous color) and statistical significance at the 95% confidence interval (points) for latent and sensible heat flux from ERA5 and MERRA-2 from detrended daily values from April-August between 1993 and 1997

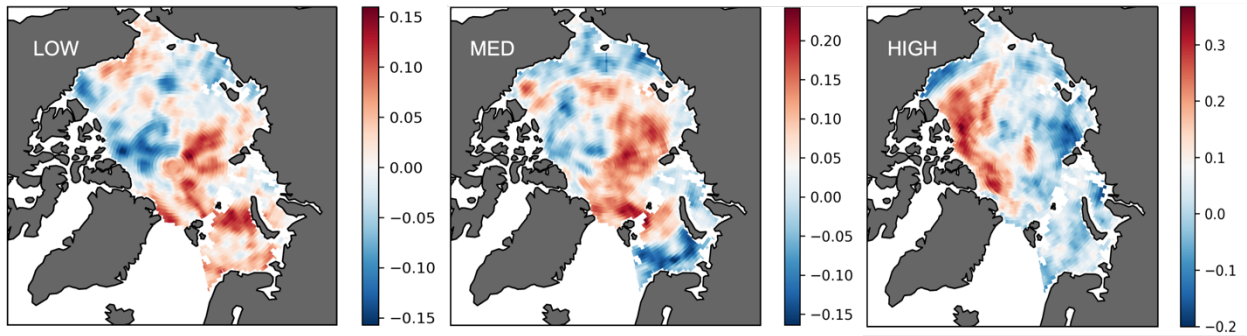

Figure 16: T-statistics (in continuous color) and statistical significance at the 95% confidence interval (points) for high level, medium level, and low level cloud cover from April-August between 1993 and 1997 for ERA5 and MERRA-2.

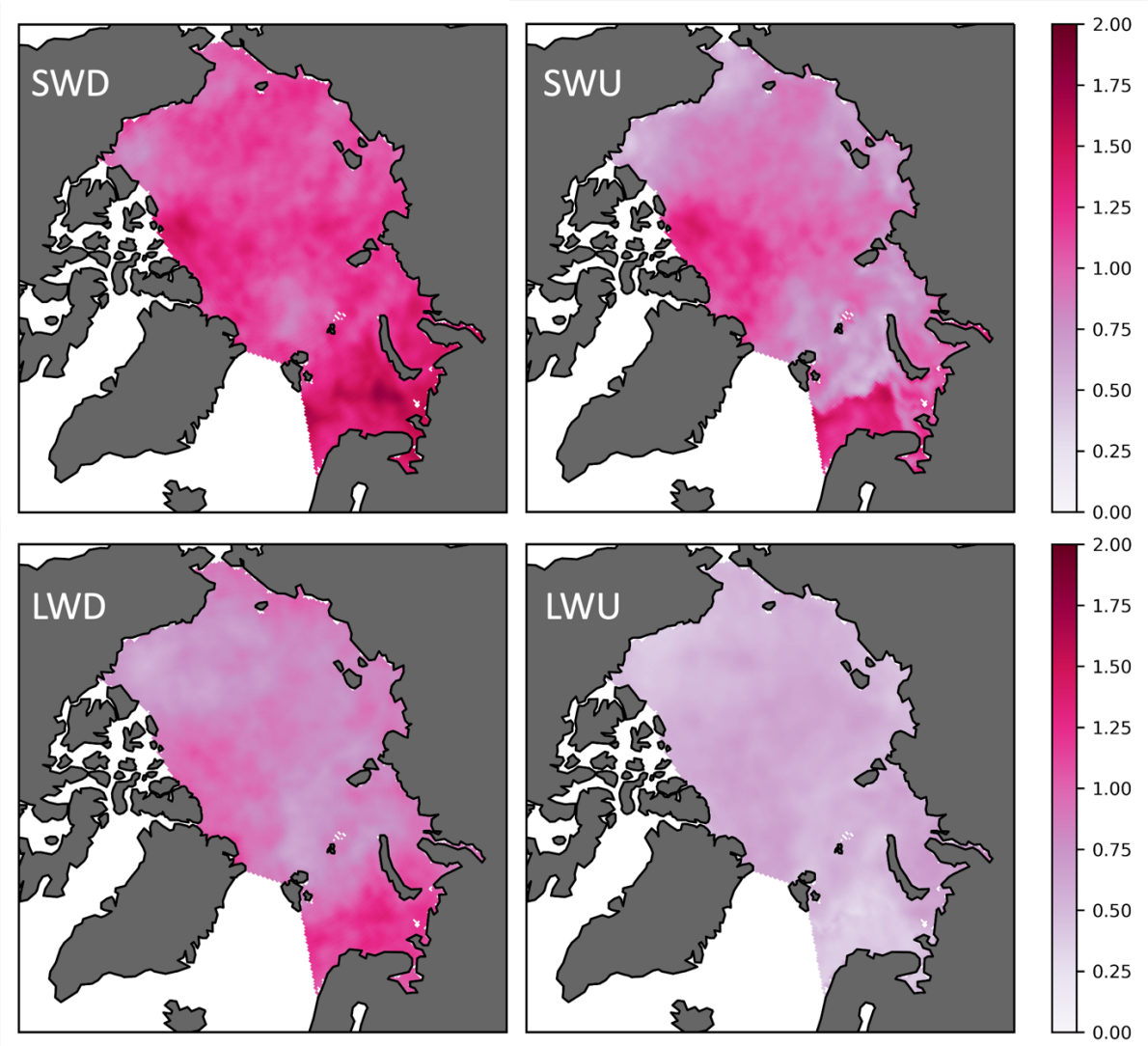

Figure 17: Results from a Durbin Watson (DB) test per grid cell for the four radiation components from CFSR across the Arctic Ocean study area. The values used to calculate the autocorrelation results are detrended daily values between 1993 and 1997.

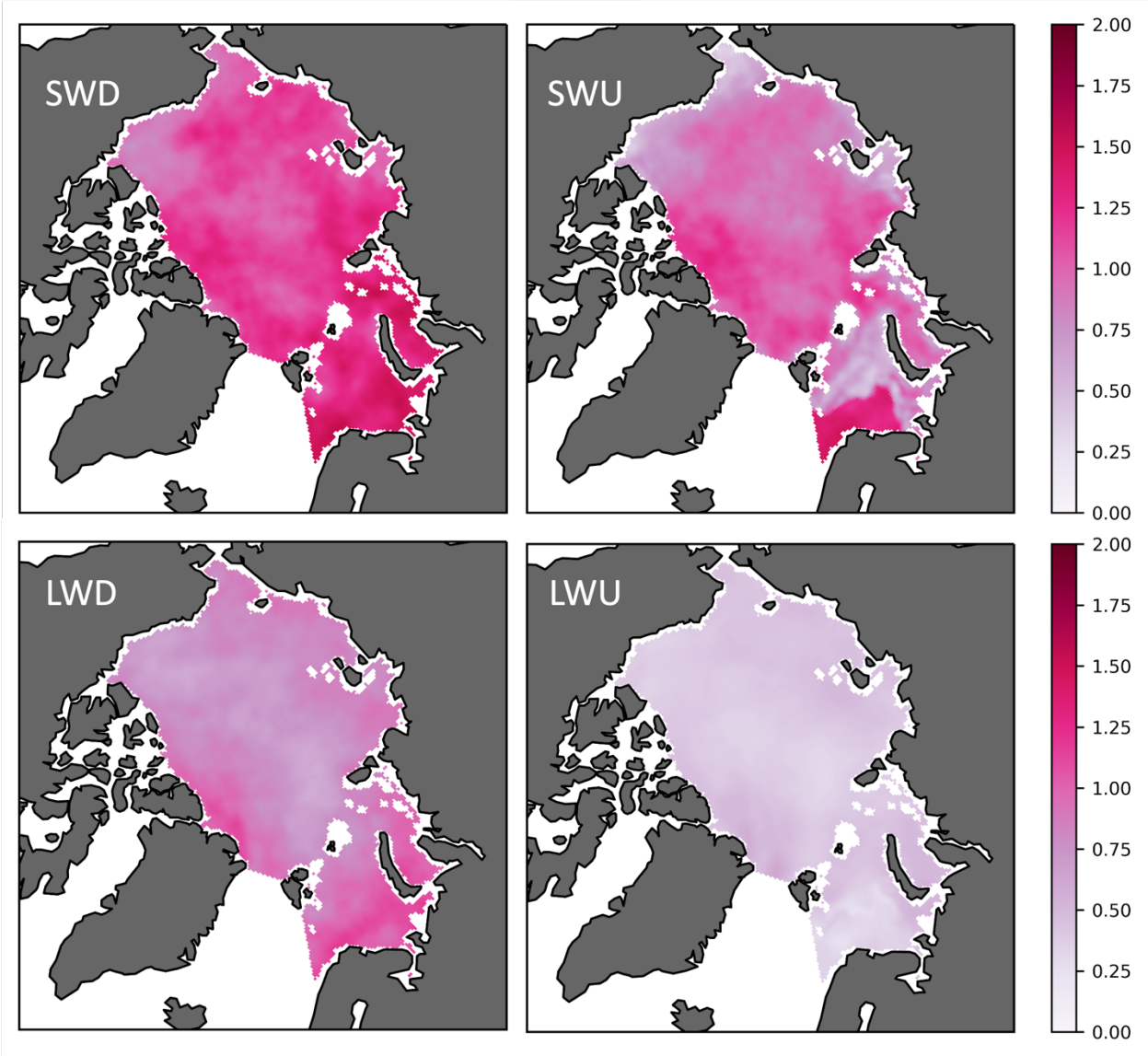

Figure 18: Results from a Durbin Watson (DB) test per grid cell for the four radiation components from ERA5 across the Arctic Ocean study area. The values used to calculate the autocorrelation results are detrended daily values between 1993 and 1997.

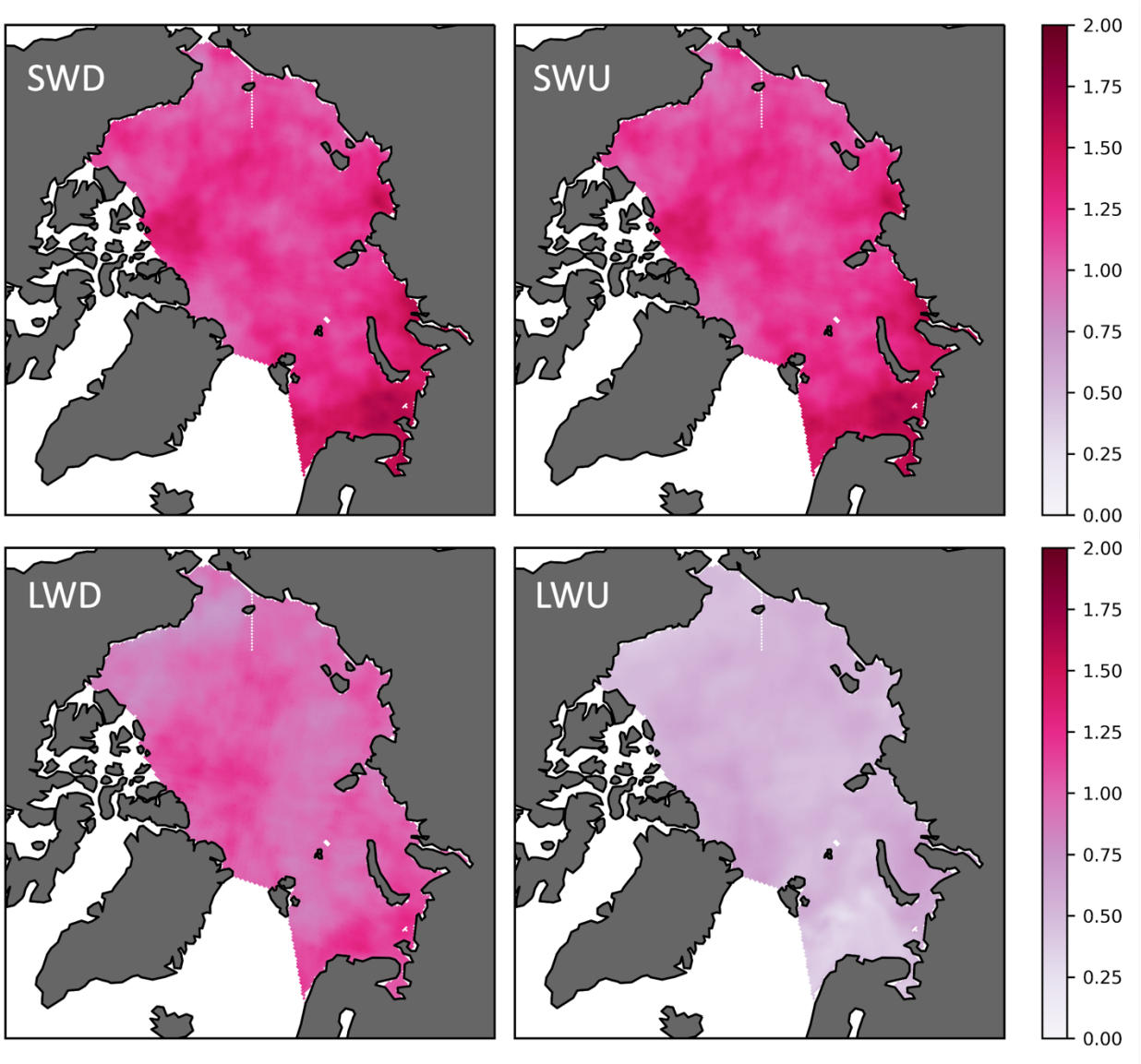

Figure 19: Results from a Durbin Watson (DB) test per grid cell for the four radiation components from MERRA-2 across the Arctic Ocean study area. The values used to calculate the autocorrelation results are detrended daily values between 1993 and 1997.